EXPERIMENTAL INVESTIGATIONS

IN

ELEMENTARY PARTICLE PHYSICS

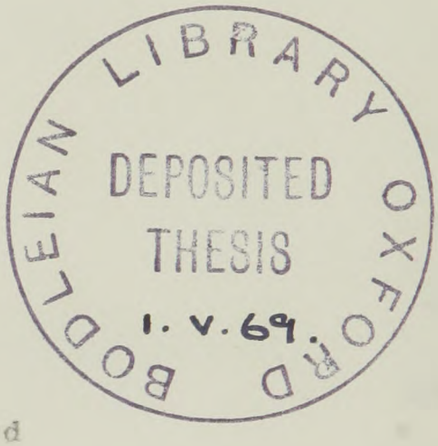

BY

B. T. MEADOWS

Trinity College, Oxford

A Dissertation Submitted to the

University of Oxford

for the

Degree of Doctor of Philosophy

October, 1966

INDEX

Page No.

CHAPTER IV cont.

Page No.

CHAPTER VI cont.

CHAPTER VII Cont.

ABSTRACT

In the separation of final states contributing to the simple two prong and four prong topologies created by K^-p collisions (K^- beam momentum 3.5 Gec/c) considerable kinematic ambiguity has been found. A device capable of measuring mean gap length has been constructed and used in an attempt to resolve such ambiguities. The limitation of the application of the device is found to be largely attributable to too high an ionization in the primary tracks and some conclusions regarding this quantity have been arrived at. A method of ionization estimation other than that of mean gap length measurement is suggested and shown to lead to better statistical accuracy.

In the three body final states, strong $\bar{K}^{*0}(890)$ and $\bar{K}^{**0}(1400)$ have been observed and their production and decay properties reviewed in the light of the peripheral model. The $\bar{K}^{**}(1400)$ isotopic spin assignment of $\frac{1}{2}$ has been confirmed as has its spin-parity. Spins higher than 2 were not, however, considered.

Evidence has been found for production of the same resonance in final states of higher multiplicity and estimates of the decay rates of the negatively charged boson into $\bar{K}^{*}\pi$, $\bar{K}\rho$, $K^-\pi^+\pi^-$ and $\bar{K}\omega$ as well as into $\bar{K}\pi$ have been made. The results have been compared with the predictions

of SU_3.

The cross-sections of both single and double resonance productions as well as that of the decay of the $\bar{K}^{**}(1400)$ into $\bar{K}^{*}\pi$ have been determined by a maximum likelihood method, and the former processes found to dominate the $K^{-}p\pi^{+}\pi^{-}$ final state. One of these involving $\bar{K}^{*o}(890)$ production has been found to have some qualitative features characteristic of the Drell process.

PREFACE

The work described in this thesis was carried out at the Nuclear Physics Laboratory, Oxford under the supervision of Dr. W. T. Davies.

The film was obtained from bubble chamber exposures made at C.E.R.N., Geneva and the scanning and measuring performed at Oxford, Imperial College, Birmingham University, Glasgow University and the Rutherford High Energy Laboratory. The processing of the measurements was carried out at the Deutches Rechenzentrum, Darmstadt, and at Imperial College, London using IBM 7090 computers.

Much of the initial part of the analysis - described in Chapter I - had already been carried out when the author became involved in the experiment, but the separation into final states of all the Oxford two prong and four prong events and the preparation of the data in the form of data summary tapes suitable for use by the statistics programme was the work of the author.

In the development of a device such as that described in Chapter IV, the ideas that result from discussions with many people are bound to contribute. However, with the exception of the mechanical design which was due to Dr. W. T. Davies, the main responsibility for the growth of the mean gap length machine from an idea originally conceived

by Dr. D. J. Crennell can be claimed as that of the author. The method suggested in Appendix B for extracting ionization information from film is original.

The analysis of the two prong events reported in Chapter VI is a personal one. An independent analysis has however, been carried out previously by Dr. A. Segar and the results obtained in this thesis are of a confirmatory nature. Chapter VII contains an account of the analysis of four prong events which is the sole responsibility of the author and the method adopted throughout to maximize functions of many variables - though similar in outline to one seen elsewhere - is claimed to contain several original features.

I hereby declare that this dissertation is not substantially the same as any other submitted by me to this or any other University.

B. T. Meadows.

Department of Nuclear Physics

Oxford

ACKNOWLEDGEMENTS

Embodied in the work reported in this thesis are contributions from many people who all deserve thanks.

The author is indebted to his supervisor, Dr. W. T. Davies for his support and guidance in many stages of the work. He would also like to thank Professor D. H. Wilkinson for allowing him to work at the University Nuclear Physics Laboratory, and the Science Research Council for a Research Studentship during part of the time.

It is a pleasure to the author to thank his friends and fellow group members for their share in much of the ardour of scanning and all night computing, and for many stimulating discussions. In particular, his thanks are due to Mr. Derek Locke and Drs. Louis Lyons and Mike Bowler for many valuable suggestions, and to Dr. J. H. Mulvey for his encouragement.

He would also like to thank Dr. A. Segar for several useful discussions and for his willing advice and co-operation on several important matters connected with a variety of aspects of the thesis.

Much of the work has been carried out in the workshops and the author's thanks are due to their staffs under the supervision of Mr. S. Tolan and Mr. A. Gilgrass to whom the

author is truly in debt. Special thanks are also due to Mr. S. Stevens and Mr. N. Webb for their infinite patience and skill, and in particular for their personal interest without which a worse than mediocre result could have been achieved.

The author also wishes to thank Mr. Cyril Band and the members of the photographic department of the Clarendon Laboratory for technical assistance and advice on many occasions; and Mr. D. Smith of the electronics department for the benefit of his experience on some matters, and in particular for the suggestion of the use of a shift register in the design of the gap length device.

For many hours spent scanning and measuring, and for the efficient channelling of data to the computers, the author is grateful to the scanners under the supervision of, successively, Anne Pitts and Pat Aidley. Though thanks are expressed to all the scanners for their conscientious assistance, the help of Kay, Liz and Helen in preparing many of the diagrams is particularly appreciated.

The co-operation and strenuous efforts of the computing staffs of DRZ Darmstadt, Imperial College Computing Unit, the SMP7044 installation (Glasgow University) and the Atlas Computing Laboratory are also gratefully acknowledged.

The author would also like to thank Miss Janet Hiscox for the careful insertion of Greek letters, and Miss Angela Payne for the majority of the beautifully drawn diagrams.

Finally, the author's personal gratitude and indebtedness are expressed to his wife, Carol, to whom he owes thanks for far more than the typing of the whole thesis.

"I have nothing to offer but blood, toil, tears and sweat."

Sir Winston Churchill
Speech, House of Commons,
13th May, 1940

INTRODUCTION

The 3.5 Gev/c K^- Experiment

At the time this experiment was first run - February 1963 - it was nowhere possible to obtain a K^- beam with a momentum greater than 3.5 Gev/c, SU(3) was still an exciting speculation,[1,2] and quarks were still literary concoctions. It is therefore interesting perhaps to consider some of the changes brought about either directly by or during the course of the present experiment as some of the points raised may help to verify the relevance of this thesis which is concerned with particular parts of the experiment.

The Ω^- Particle

Unitary symmetry was suggested as a possible extension to the idea of charge independence. Here, particles instead of being grouped together in multiplets of isotopic spin, were to be grouped in a more general way which would include hypercharge ($Y = B + S$ where B = baryon and S = strangeness quantum numbers). The result would be that supermultiplets instead of multiplets should occur. The presence of these depends upon the supposed symmetry of the strong interaction under unitary transformations which belong to the group SU(3). In this way, several particles are thought to be merely substates of one eigenstate of a Hamiltonian symmetrical under these transformations, and the only

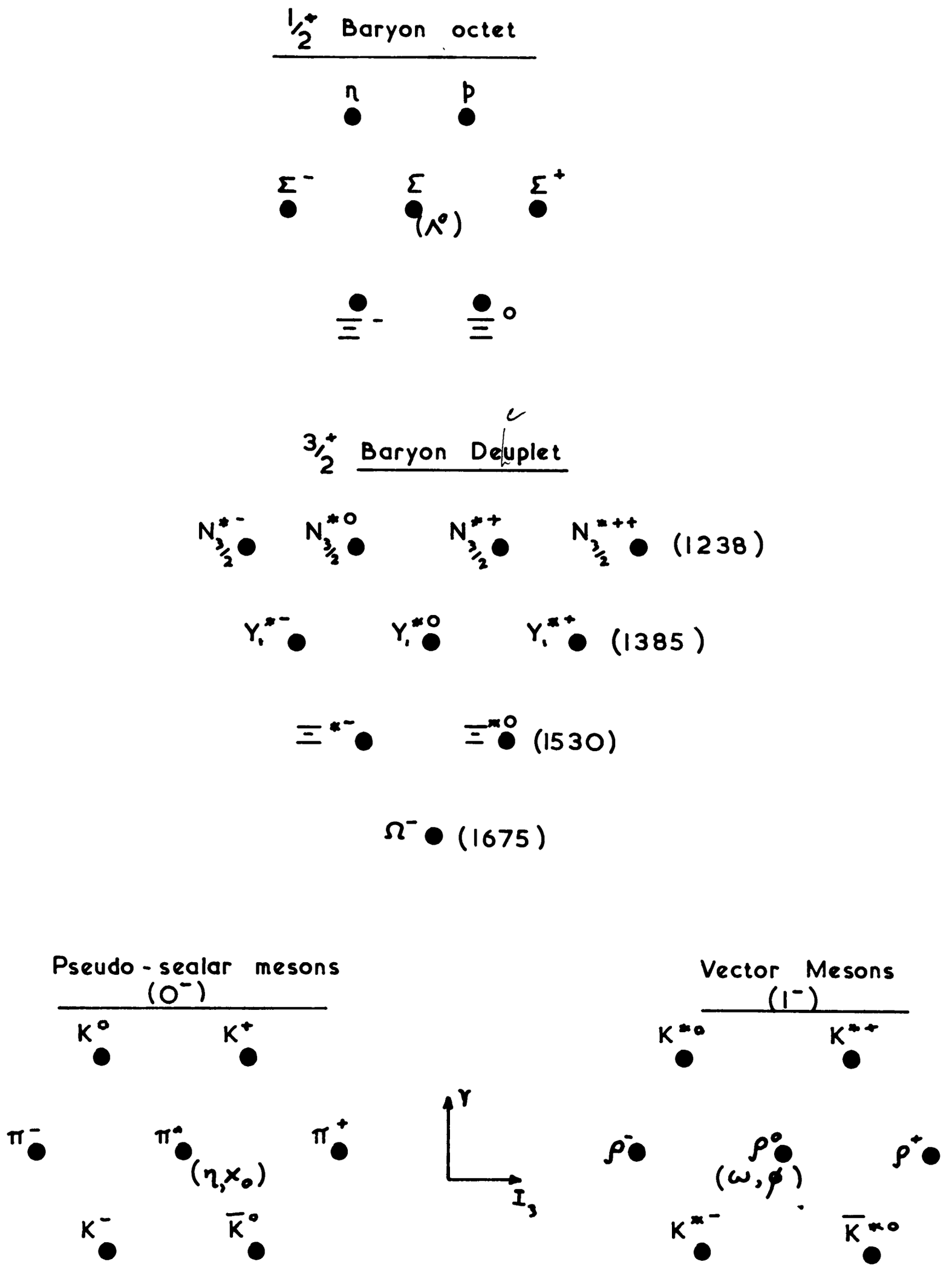

FIG. 1 Some established super multiplets.

reason that they are distinct is because there exists some 'medium strong' interaction which removes the natural degeneracy. In this way, the medium strong interaction is analogous to the magnetic field which causes the energy levels of electrons in atoms to split.

In the case of strong interactions, the symmetry chosen is known as SU(3) and the perturbing force causing the mass splittings is assumed to have some definite symmetry of its own. On these assumptions, one can predict the existence of various types of supermultiplet and to first order, calculate a formula governing the mass splittings within these multiplets. [3]

Some such well known "representations" are illustrated in Fig.1. It will be noticed that all these are either singlets, octets or decuplets and that the spin-parities (J^P) of all members within a multiplet are the same. Extensions have been made to the SU(3) assumption mentioned previously to include some symmetry with respect to these variables, but they will not be discussed here.

In the 3/2+ decuplet of baryons, a noticeable omission was that of the Ω^- at the time that the theory was produced. The Gell-Mann-Okubo mass formula [3] governing this decuplet is of the form:

$$M = M_o\left\{1 + aY + b\left[I(I+1) - Y^2/4\right]\right\} \qquad \ldots.(1)$$

where M_o, a and b are constants. From the known masses of the other particles, one can derive

$$a = -0.105, \quad b = -7.2 \times 10^{-4}, \quad M_o = 1.386 \text{ Gev}$$

giving expected value of m_{Ω^-} at 1675 Mev. The search for this particle in the reaction:

$$K^- + p \rightarrow \Omega^- + K^+ + K^o \qquad \ldots.(2)$$

in which the required centre of mass energy is at least 2.660 Gev corresponding to beam momentum of 3.15 Gev/c was the main reason for using as high an energy K^- beam as possible in this experiment. However, it has become apparent that 3.5 Gev/c was too near the threshold required as no event has been found corresponding to reaction (2) followed by any of the decays:

$$\Omega^- \rightarrow \Lambda^o + K^-$$

$$\Xi^o + \pi^-$$

$$\Xi^- + \pi^o$$

where the products were visible.

The Ω^- was subsequently found at Brookhaven[4] using a 5 Gev/c K^- beam, but this was approximately one year later.

The actual importance of the discovery of this particle may have been overestimated, of course, but it is certainly exciting that the existence of an object which only decays by weak interaction and which is nearly twice as heavy as a proton should be accurately predictable. Perhaps it is as a consequence

of this new found confidence in the idea of higher symmetry that has led to the even more audacious schemes that have been proposed.[5,6,7]

Baryon Resonances

Some interest in this experiment has been centred around the Y*(1660) region. The main reaction in which this resonance was studied was:

$$K^- p \Rightarrow (\Sigma^- \pi^+ \pi^+)\, \pi^- \qquad \text{....(3)}$$
$$\quad Y_1^*(1660)$$

The peak in the $\Sigma^- \pi^+ \pi^+$ mass distribution occurs at a part where the non-resonant "phase-space" expectation is very small, so that little background is present. Further, by selecting only events in which the four-momentum transfer to the $\Sigma^- \pi^+ \pi^+$ mass is small, most of the peak remains, indicating a production mechanism that could be simply one meson exchange. In this particular case, the exchanged system must be a K* with isotopic spin $\frac{1}{2}$. As a result of the foregoing, a reasonably pure sample of $Y_1^*(1660)$ events was available, and after combining these with similar events from the 3.0 Gev/c K^-p experiment being analysed by the Saclay-Ecole Polytechnique groups, an analysis of the decay Dalitz plot was undertaken. The result was that consistency with the spin-parity assignment $3/2^+$ was found. However, the situation regarding this resonance remains one of the many unsolved mysteries of experimental elementary

particle physics, for another group, performing a similar analysis [8] obtained the result that the 1660 had spin-parity $3/2^-$, whilst later experiments also favour this assignment.

$Y_0^*(1645)$

It was also found that, in the reaction:

$$K^- p \rightarrow \Sigma^{\pm} \pi^{\mp} \pi^0$$

a further peak at about 1645 Mev was present in the $\Sigma^{\pm} \pi^{\mp}$ mass spectrum. That this corresponded to the decay of a new isotopic singlet state with mass at 1645 Mev and width 40 Mev was believed for several reasons:[9]

1. No corresponding enhancement was noticed in the charged $\Sigma\pi$ combinations in the $K^- p \rightarrow \Sigma(2\pi)$ reactions. If it were the $Y_1^*(1660)$ this would have been surprising.
2. The centre of mass production angular distribution for the resonance showed a forward peaking corresponding to a baryon exchange production mechanism. No such peaking was obvious in the background events.
3. One can calculate from the fact that reaction (3) probably proceeds via K* exchange how much neutral Y* should be produced. Then from the known branching ratio [10]

$$\frac{Y_1^* \rightarrow \Sigma\pi\pi}{Y_1^* \rightarrow \Sigma\pi} \sim 1$$

an estimate of the expected number of 1660 events in $\Sigma^{\pm}\pi^{\mp}$

is obtained. The result is that, where 11 events would thus be expected 42 exist.

Production Mechanisms

In the study of the production and decay of baryon and boson resonances, a simple theoretical model which has had a limited success is the so called Peripheral Model and much work has recently been done on the sophistication of it especially during the course of this experiment and many reactions have been analysed by reference to it. As some of the results which are presented in this thesis are discussed within the framework of the model, a brief account is given here.

Phenomenologically, one can think of the target proton being surrounded by a cloud of mesons. On the average, most K^- mesons in the beam strike the proton in this cloud with fairly large impact parameter and scatter off the mesons therein. In many of these instances, the K^-p interaction can be described in terms of "one meson exchange" leading to a quasi two body final state. The scattering which takes place causes the emerging meson (sometimes a resonance) to be polarized in general, in a predictable way. The subsequent decay (of the resonance) therefore provides a check on the assumed exchange.

Meson-Meson Scattering

The only way that boson resonances can be produced is by

Table I - Meson Nonets.

Spin-Parity	Members	Mixing Angle.
0^-	π, K, η, X^0	
1^-	ρ, K^*, ω, ϕ	
2^+	$A_2, K^{**}(1400)$	
	f_0, f'	

some such peripheral scattering, as this is the nearest approximation that one can imagine to having meson target. Consequently, the detailed analysis of these particles usually relies to a certain extent upon the assumed production mode.

Within the framework of SU(3) the main meson resonances now seem to fit conveniently into three nonets .

The inclusion of ninth particles in the basic octets is necessary in order to satisfy the Gell-Mann-Okubo mass formula within the octet. The eighth member then becomes a "mixture" of two particles with mixing angle θ defined by:

$$\mathrm{Tan}^2\theta = \left(\frac{M_8^2 - M_8^{o2}}{M_8^{o2} - M_1^2} \right)$$

where: M_8 = physical mass of octet member with I = 0

M_8^o = bare mass of octet member with I = 0

M_1 = physical mass of singlet

Then using the values for the masses quoted in Ref. 10, we obtain the "mixing angles" given in Table .

The study and classification of such resonances could be regarded as a special case of the more general problem of trying to understand the dynamics of meson-meson interactions. Perhaps the more fundamental problem is that of trying to describe the interactions between quarks - if indeed they exist, for it has even been suggested by Gell-Mann that they may merely be mathematical

entities.[11] Thus, just as the K*(890) is a pole in the $K-\pi$ scattering amplitude, perhaps the K itself is an analogous phenomenon in the quark-antiquark amplitude. However, whatever the outcome of such theoretical investigations, the observation and analysis of the properties of these resonances and the accumulation of data on meson-meson scatterings are essential to progress. This may be one of the justifications for experiments like the present one in which K^- mesons are aimed at protons in such a way that the many peripheral interactions which result provide such data.

The K*'(1400)

A notable feature of the 3.5 Gev/c experiment was the discovery of this resonant state. It was first noticed in the reaction:[12]

$$K^- + p \Rightarrow \bar{K}^0 + \pi^- + p$$

Neither of the two body systems π^-p or $\bar{K}^0p$ were found to resonate strongly, but the $\bar{K}^0\pi^-$ invariant mass had a very noticeable enhancement at 890 Mev corresponding to production of that well known resonance. However, a bump was also noticed in the same distribution at about 1400 Mev., and no acceptable fit to the data could be made by ignoring it. The fact that the population of points on the Dalitz plot showed a band of higher density at this mass added confidence to the suggestion that this was a resonance.

Almost at the same time, Hardy et al[13] who studied $\pi^- p$ interactions at 3.9 and 4.2 Gev/c observed the anti-particle in the reactions:

$$\pi^- p \longrightarrow \Sigma^0 (K^+ \pi^-)$$
$$\Lambda^0 (K^+ \pi^-)$$

where they also were troubled little by interference (or competition) from excited baryon states.

That this phenomenon should occur in two such different reactions must be conclusive evidence for the existence of the particle, which has now been reported in several other experiments.[14,15]

The original observation[12] permitted an analysis of the decay correlations of the K** on the assumption that the production process:

$$K^- + p \longrightarrow K^{**-} + p$$

proceeded dominantly by one particle exchange. The result was a closer adherence of the data to spin-parity 2^+ than to 1^- by 2 standard deviations. No conclusive estimate of the isotopic spin (T) was available, but Hardy et al expressed a weak preference for $T = \frac{1}{2}$ on the basis of the observed rates:

$$\frac{K^{**} \rightarrow (\Sigma^+) \pi^- K^0}{K^{**} \rightarrow (\Sigma^0) \pi^- K^+} \quad \text{and} \quad \frac{K^{**} \rightarrow (\Lambda) \pi^0 K^0}{K^{**} \rightarrow (\Lambda) \pi^- K^+}$$

Their data was also more consistent with a spin-parity of 2^+

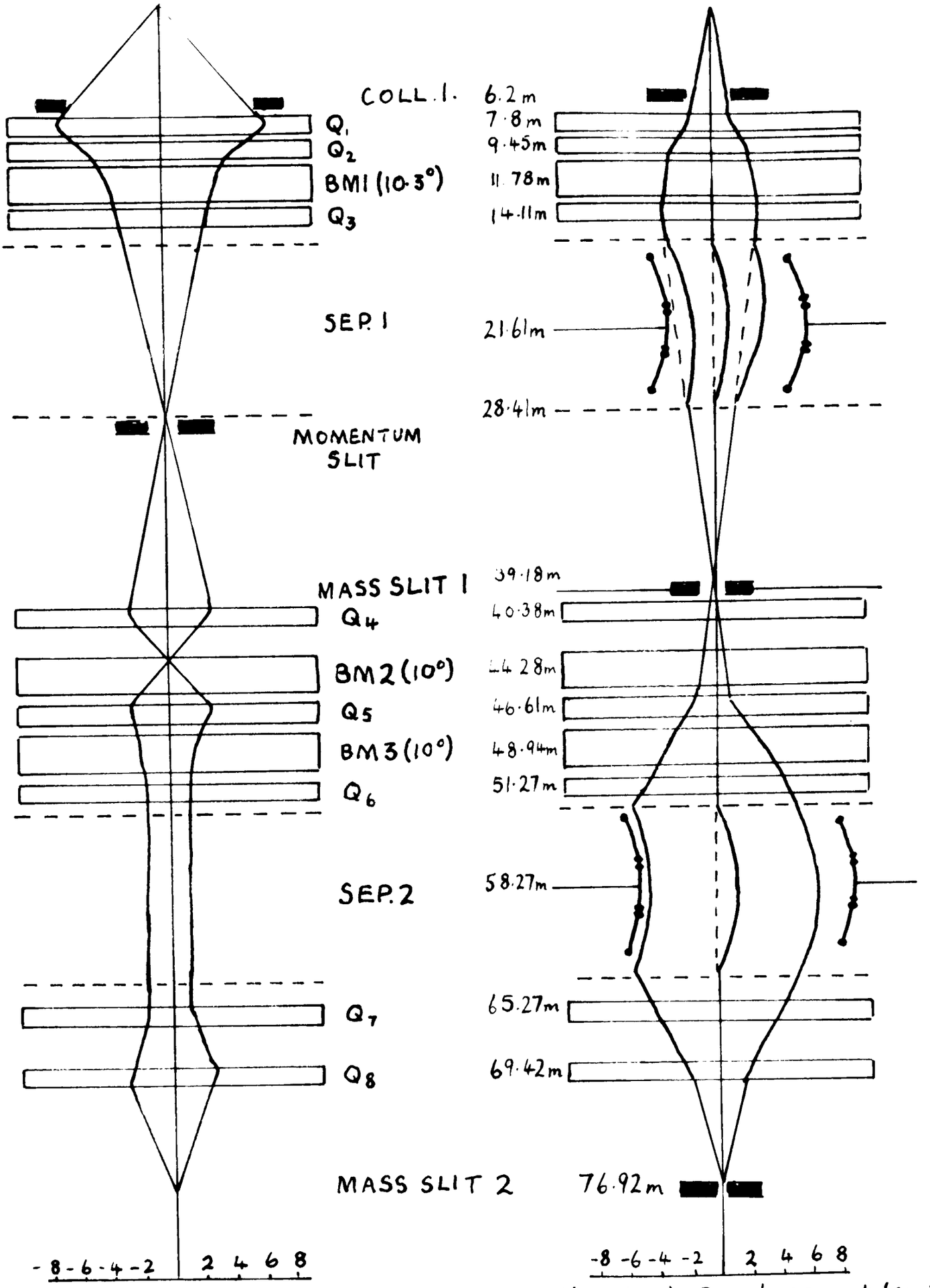

Fig 4(a)

Fig 4(b)

BEAM PROFILES

than 1^-.

The Experiment

As already mentioned, to obtain a beam of K^- mesons without too high a pion contamination at 3.5 Gev/c was a technical triumph when this K^-p experiment was first run in January/February of 1963.

The M2 beam was built in the South Hall at C.E.R.N. and was used to provide separated beams of $K^{\pm}$ particles at 3.0 Gev/c and K^- at 3.5 Gev/c. As a result of 3 runs during that year - the other two taking place in October and December respectively - over half a million photographs were produced: 100,000 K^+ at 3.0 Gev/c, 300,000 K^- at the same momentum and 310,000 K^- at 3.5 Gev/c. The latter film was distributed among the members of a British collaboration - Birmingham University, Imperial College London, National Institute - Rutherford Laboratory (N.I.R.N.S.), Glasgow University and Oxford who took approximately half the total 3.5 K^- film. It is with the analysis of this film that this thesis is primarily concerned.

The M2 Beam

The layout is shown schematically in Figs. .4(a) and .4 (b) which make the optical arrangement apparent.

Injection was provided by a copper target at 8.5° production angle placed in a straight section of the PS. The first

collimator collected the particles from a solid angle of 0.6×10^{-4} steradians and filtered them into the momentum defining stage which consisted of a bending magnet (BM_1) - whose current defined the momentum of the resulting beam - and the momentum slit whose resolution was set at (4%). The purpose of the quadrupoles Q_1, Q_2, Q_3 was to produce a horizontal focus on the momentum slit and a vertical focus on the first mass slit whilst the separator number one caused a bending in a vertical direction and a resulting separation of π and K images of 3mm. The size of these was about 1.3mm at the first mass slit which thus allowed a somewhat purified sample of K-mesons of the required momentum through to the second separation system that followed. This consisted of quadrupoles Q_4, Q_5 and Q_6 and bending magnets BM_2 and BM_3 which performed a momentum recombination (after the first separation) and produced a collinated beam to pass through the second electrostatic separator. This then resulted in an image size of less than 1mm and an expected beam of K's with about 10% π's at the 2nd mass slit. In practice, this was scanned across the image, and the particles passing through were counted. The profile being thus judged enabled a final setting to be made as near to the K end of the image as possible, consistent with obtaining a flux of approximately 10-20 K's ($+\pi$'s and μ's)

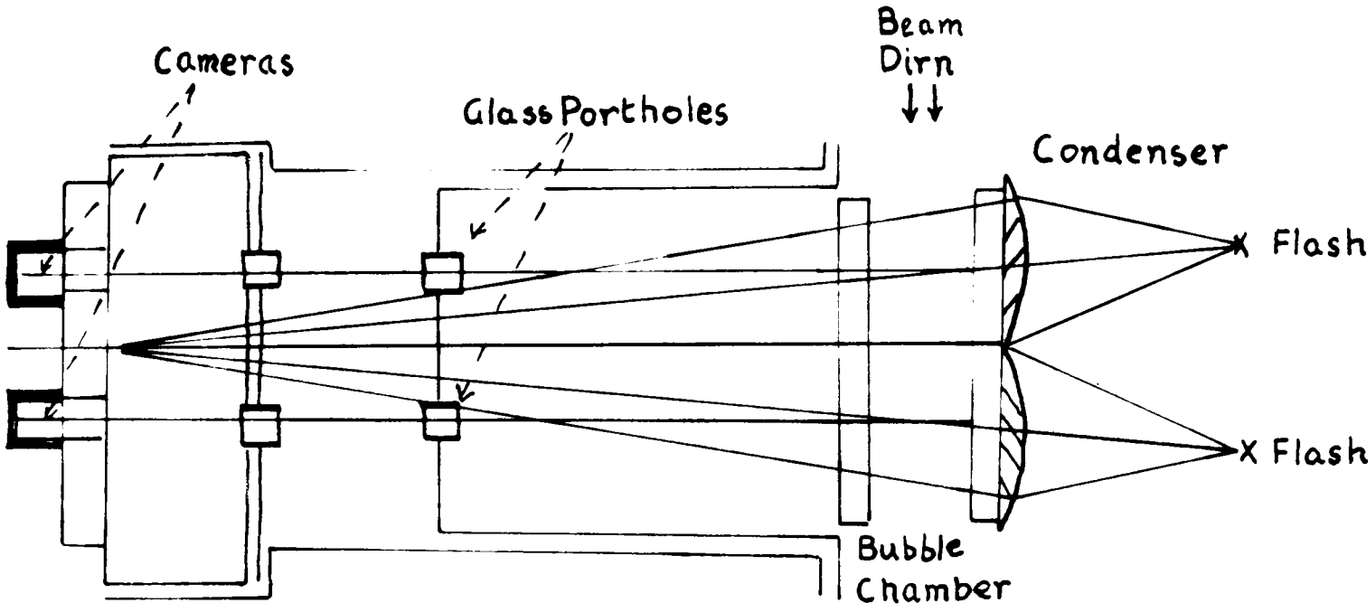

Plan (not to scale)

Fig 5 Saclay 81 cm. Chamber

per pulse. Two further quadrupoles were used to provide a reasonable spread of beam tracks throughout the chamber.

The 81cm Saclay Bubble Chamber (See Fig. .5)

The main part of this was a tank measuring 81cm by about 30cm in depth which was suspended in a large vacuum enclosure which in turn was surrounded by a liquid nitrogen shield. There were three cameras mounted on the outside of the structure and these were allowed a view of the main chamber by means of glass portholes in the vacuum jackets. Both sides of the main tank that were face on to the cameras (whose axes were all parallel) were made of glass, and contained diagonal engraved crosses which served to define a co-ordinate system (discussed in Chapter I). On the side of the chamber remote from the cameras were two flash tubes whose separate condensing systems produced a focus of each situated between the cameras such that the only light received by these came from objects in the chamber (or fiducial marks on the windows) which scattered the main illumination.

The magnet coils were wound around the windows in such a way that the axis of the field was parallel to the camera axes. In order to obtain a uniform magnetic field of 20 K Gauss over the whole volume of the chamber, a very large current was required and kept at a stabilized level throughout the whole of

each run. The compression and expansion of the chamber were effected by a piston whose connection with the visible portion of the liquid hydrogen container was through a conical neck which helped to reduce turbulence.

The Illumination System

The sources were 2 electronic flash tubes whose triggering could be delayed by a variable amount relative to a syne pulse generated by the PS. Each of these had its own condensing system, and some uncertainty due to non-synchronisation of the flashes occasionally arose. The bubble sizes were usually about 0.20mm in the chamber which was comparable with the resolving power of the camera lenses, though a little larger (camera resolution corresponding to aperture of 1cms at wavelength of 5,000 $\mathring{A}$ is about 0.07mm). Hence, the images on the film had a considerable diffraction halo and their size, though fairly insensitive to the actual bubble size, depended to a large extent on the intensity of illumination.

Chamber Parameters

The process of "tuning the chamber" was a never ending one. The temperature drifted slightly as did the expansion cycle. Normally, the liquid was under pressure which was released a moment before the proton bunch in the PS struck the copper target. Some variables were:-

1. The expansion delay

2. The compression ratio

3. Temperature

4. Flash delay

5. Flash intensity

The first three affected the pressure of the hydrogen when the beam entered and so how sensitive it was to boiling. The last two controlled the picture quality by varying the actual bubble size (which was more effectively changed by the first two variables) and the film exposure respectively.

Control of these quantities was the job of the chamber crew but was brought about by physicists whose responsibility it was to inspect samples of film which were snipped from the end of each roll as it was taken off the chamber. Such things as: 1. Number and type of interaction;

2. Number of γ decays;

3. General film quality including advance between frames on each of the views;

4. Bubble density of minimum ionizing tracks;

were checked and recorded. The feed-back time for this was, however, far too long to be very useful but did serve some purpose in seeing that things were not going too badly wrong. A more immediate check on position (or even presence) of beam

tracks in the chamber was provided by an inspection window which was designed to receive a polaroid camera. In one experiment a potential Ω^- candidate was found in this way!

Topologically, the reactions described in this thesis are those producing a simple two or four prong event, with no visible decay. These reactions are therefore distinct from all but the rarest in that they usually involve a negative K-meson, or occasionally an unseen $\bar{K}^o$? Unfortunately, the presence of π's in the beam resulted in some difficulty in distinguishing final states with these simple topologies, and ambiguities remained in many events. In this connection, the possibility of using an ionization measuring device was investigated, and some description of it, and the conclusions regarding its usefulness form Part I of the remainder of this dissertation. Included in this section is an account of the methods adopted which lead eventually to the separation of the final states:

$$K^-p \rightarrow K^-p$$

$$K^-p \rightarrow K^-p\pi^o$$

$$K^-p \rightarrow \bar{K}^o p\pi^-$$

$$K^-p \rightarrow K^-\pi^+ n$$

$$K^-p \rightarrow K^-p\pi^+\pi^-$$

$$K^-p \rightarrow K^-p\pi^+\pi^-\pi^o$$

$$K^-p \rightarrow K^-\pi^+\pi^+\pi^-n$$

Part II than describes the analysis of some of these.

REFERENCES TO INTRODUCTION

1: M. Gell-Mann: Phys.Rev.125,1067(1962)

2. Y.Ne'eman; Nuclear Physics 26,419(1961)

3. S.Okubo: Prog.Th.Phys.(Kyoto) 27,949(1962)

4. V.E.Barnes et al,P.R.L.12,204(1964)

5. G.Sweig: "An SU_3 Model for Strong Interaction Symmetry and Its Breaking".C.E.R.N.Report 8419/TH.412(1964)

6. M.Gell-Mann: Phys.Letts. 8,214(1964)

7. R.E. Marshak & S.Okubo,Phys.Rev.Letters,13,818(1964)

8. Berley et al

9. "Two Body Final States in K^-p Collisions at 3.5 Gev/c" - N. Haque et al (Unpublished)

10. A. H. Rosenfeld,A.Barbaro-Galtieri,W.H.Barkus,P.L.Bastien, J.Kirz and M.Roos: UCRL - 8030

11. Talk given by M.Gell-Mann in Oxford - May 1966

12. N. Haque et al: Phys.Lett.14,338(1965)

13. Hardy et al: Phys.rev.Letters 14,401(1965)

14. S.Focardi et al: Phys.Letters,16,351(1965)

15. S.Goldhaber et al; UCRL 16332

PART ONE

3.3 Ge It is an unfortunate characteristic of bubble chamber experiments that, though the actual running time on the accelerator may be a matter of a few weeks, the time required to sift and analyse the thousands of photographs which result may well be months or even years. The difficulties involved in triggering the chamber actions only when useful events are observed are considerable, and - except for the case of the flash tube - impossible, for the expansion cycle occupies many milliseconds whilst the bubble formation mechanism is probably only potent for a few microseconds. Consequently, the chamber sensitization must be ensured for every incident beam pulse. Further, the lack of particles emerging from the dense liquid target of the chamber anyway makes the job of arranging a system of counters to look for a particular type of interaction difficult. As a result, a large part of bubble chamber photograph analysis consists of the scanning for useful events and rejection of wasted exposures. The next section describes this part of the analysis.

Scanning Procedure

An estimate of the topologies required for the types of interactions which were to be studied was first made.

For instance, if one wished to study final states involving

charged Σ hyperons made by collisions between K^- and p at 3.5 Gev/c (as in the present experiment) one realised that the decay length of a Σ^- at this momentum (or less) was 15cms (or less). As the visible region of the chamber was about 45 cms. in length, the majority of Σ's would be observed to decay.

For other reasons, if one wished to observe neutral K's or Λ hyperons, an obvious place to look was in the events which had an associated V^o.

The events of interest to the author involved a charged K meson (negative) and so excluded either of the above possibilities. This was because, in order to conserve strangeness, a reaction:

$$K^- + p \rightarrow K^- + X^+$$

where X^+ was some combination of particles having overall charge +1, was unlikely to involve any further strange particles which would probably give a visible decay, as these would have to occur in pairs of opposite strangeness. It is true that the K^- meson could decay but the mean free path of a fast K^- meson (3.5 Gev/c) is 1070cms., making the ratio of the number of charged decays that were K's to those that were Σ's very small for most observed momenta.

Definition of Topology

A simple code has been used in this (and some subsequent)

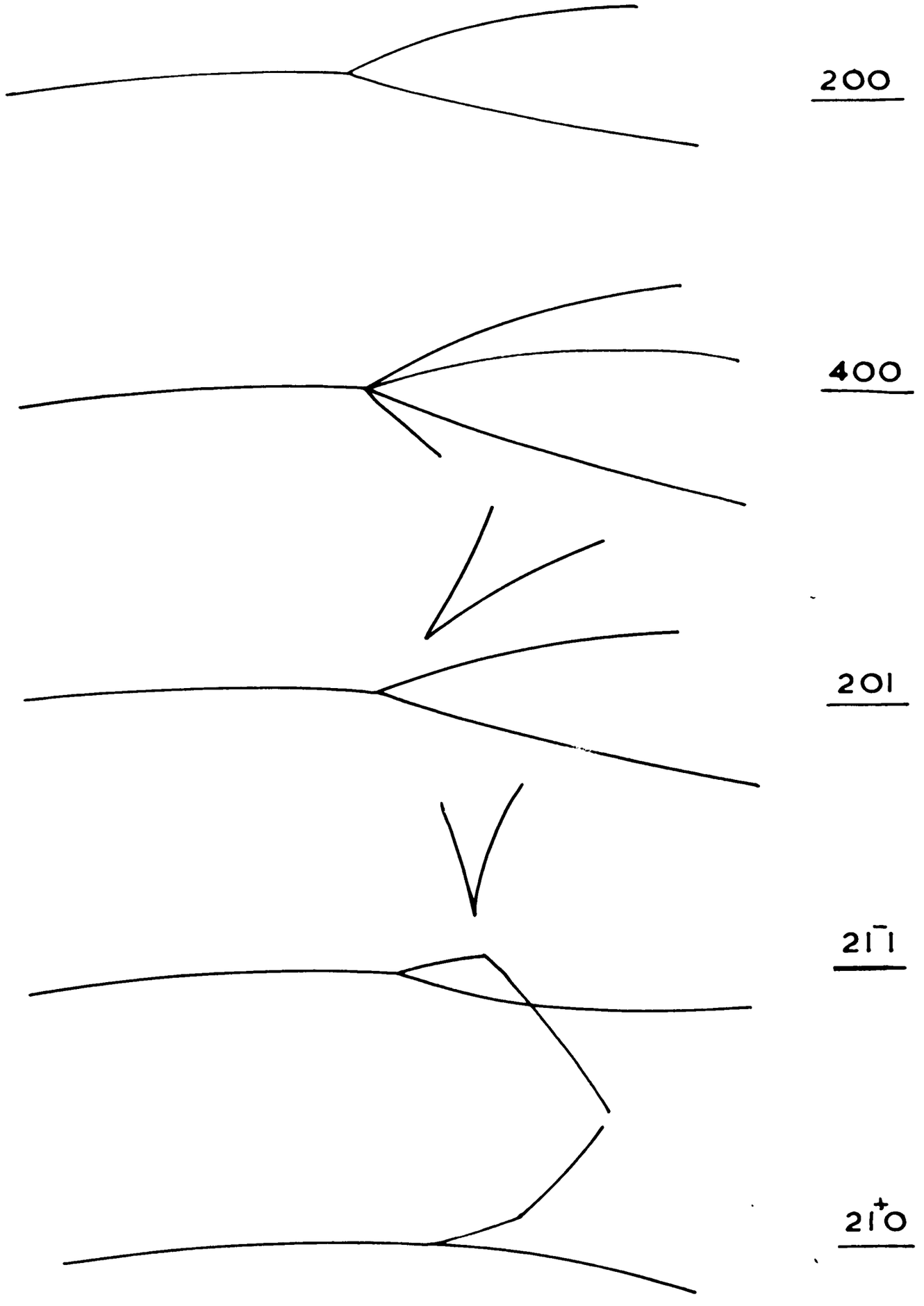

FIG 1.1 Examples of Topology Code.

experiments to specify the topology of the various events. It is of the form "lmn" where:

l = number of charge prongs associated with the first interaction (production vertex).

m = number of visible charged decays (evidenced by a kink in a track).

n = number of visible V^0s (neutral track decays).

Some examples of this code are given in Fig. 1.1.

From what has been said before, the events of principal interest to the author were the 200 and 400 topologies.

Structure of the Scans

The whole of the 1st run film was scanned four times. The first time involved looking for rare events (defined to have topology more complex than 200, 400, 001, 201). This was then repeated in order to estimate a scanning efficiency. The process was repeated looking for common events (i.e. 400, 201, 001 - not 200). It was thought at this time that the 2 prong events (200) would merely slow down the scanning too much. It was only with the subsequent discovery of the K**(1400) resonance that any analysis of 2 prongs was envisaged.

After the common and rare rescans, those events which were given a different interpretation on two previous scans were looked at again. Several factors could contribute to these

differences, for instance a 001 event could easily be mistaken for a 200 if the V^o were separated from the end of a beam track by only one mean gap length.

The 2nd and 3rd run film was of much poorer quality, although the beam purity for the second run was thought to be better than elsewhere. Consequently, in the first place, these films were only scanned for rare events. Later, however, to boost the statistical significance of the results obtained from the first run, the 201s from the second run film were analysed and later the 200s.

The latter events were taken only from this film as it was decided by the collaboration that the beam quality was the most important factor. The actual figures for the latter are given below (Table V., Chapter II) calculated from the Oxford film. These figures are discussed in more detail in Chapter II but it may be noted that the difference between the two runs is quite small and the importance attached by the author to making ionization measurements (see Chapter IV) together with the better visual quality of the first run film led him to prefer taking the four prong events from this. No ionization measurements were attempted on the other film at all. The two prong sample was, however, extracted from the second run film, where it enjoyed a special two prong scan. In the interests of

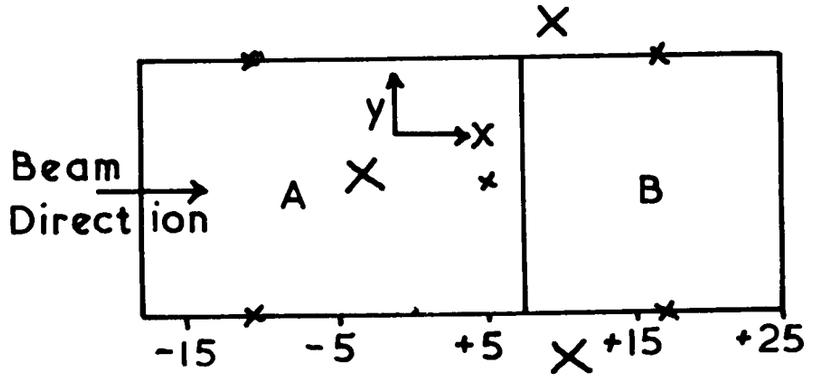

FIG. 1.2 (a) Scanning boxes

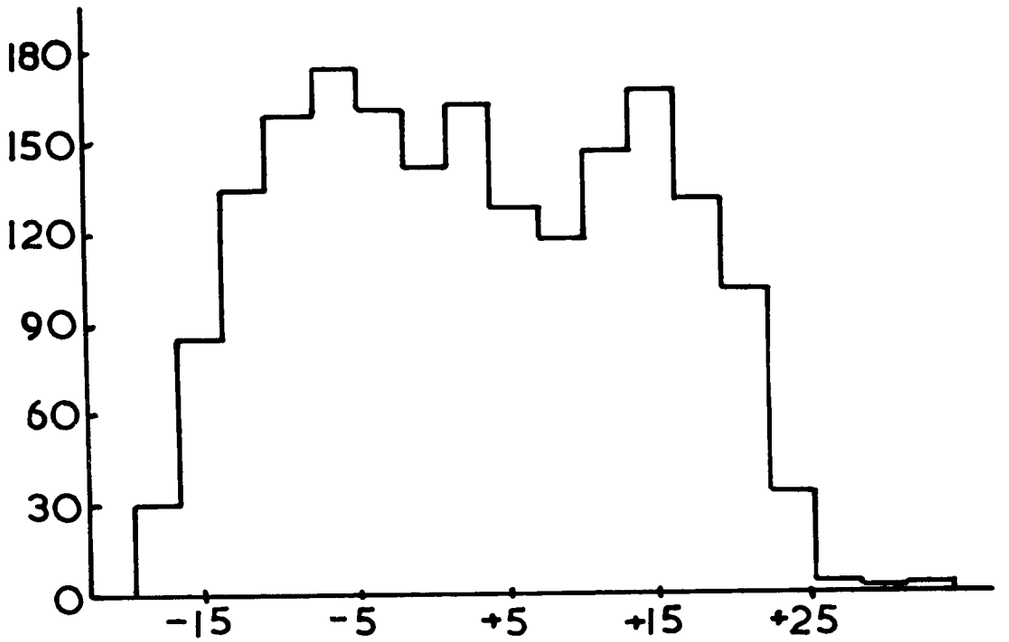

FIG. 1.2 (b) 2-prong vertex x-co-ordinates.

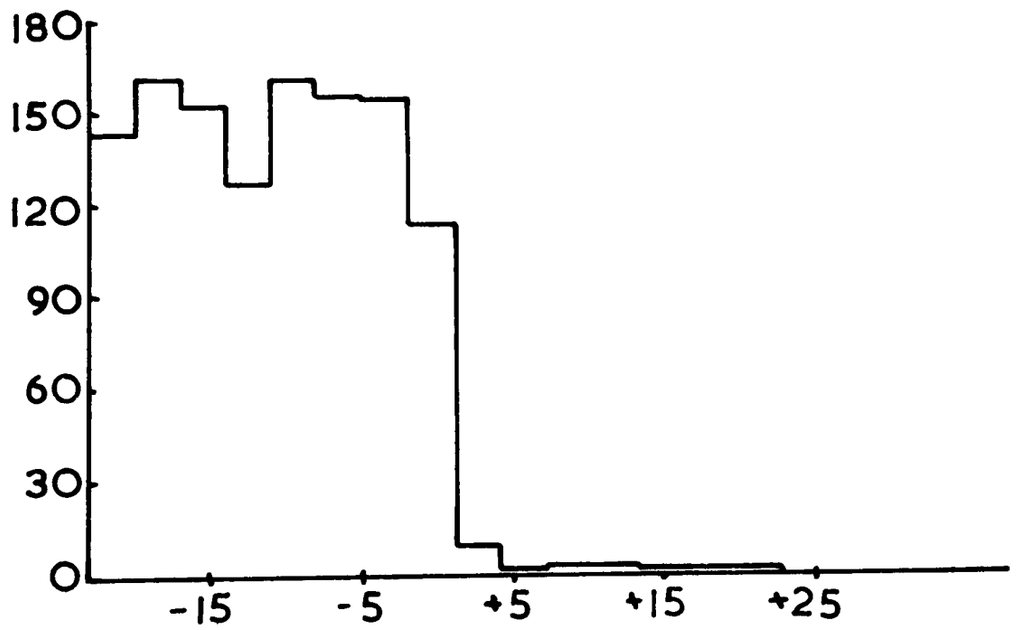

FIG. 1.2 (c) 4-prong vertex x-co-ordinates.

haste only three out of the seventeen Oxford rolls were rescanned to make some estimate of the efficiency of the main scan. This was thought, in view of the large number of events on three rolls (about 500), to be a sufficiently good estimate.

Scanning Boxes

In order to reduce erratic loss of events due to poor illumination near the edges of the chamber a fiducial region was defined to cover the centre and upstream ends of the chamber. The actual dimensions of this scanning box are shown in Fig. 1.2(a). The dimensions and fiducial positions are illustrated for a 10 x magnified image of the film for view two. As seen, the box was divided into two regions (A and B in the diagram). The common events were only scanned for in region A for the first run film in order to reduce the number of V^0 events for which large corrections would have to be applied. It was simply more convenient at the time to confine the four prong scan to the same region, as there was certainly no shortage of events with this topology.

The lack of any systematic scanning bias when using these boxes is illustrated in Figs. 1.2.(b) and (c) which show respectively 200 and 400 x-distributions to be isotropic. The z distribution in Fig. 1.3(a) and (b) should be representative of the beam profile; so approximately Gaussian in form.

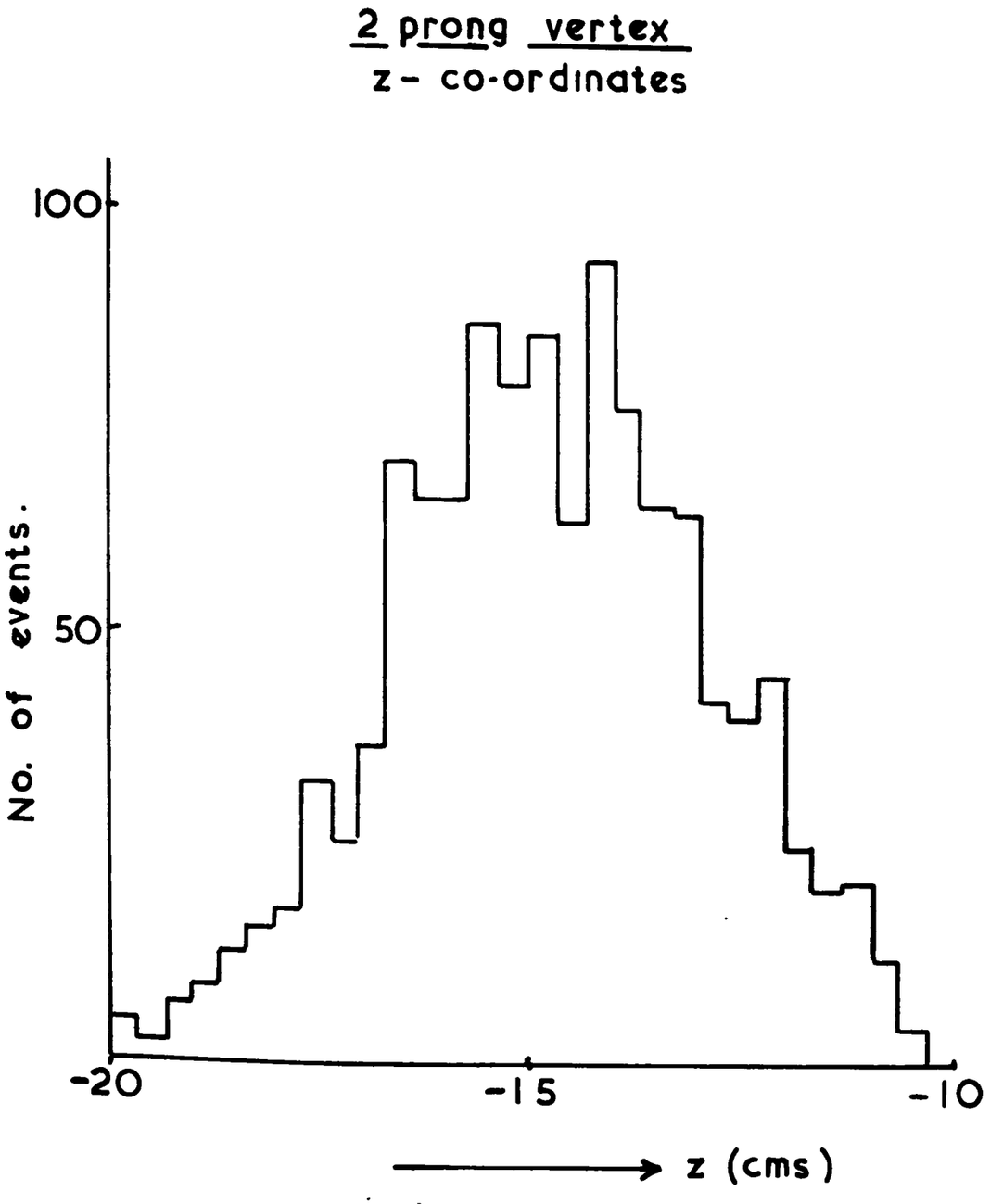

FIG. 1.3 (a)

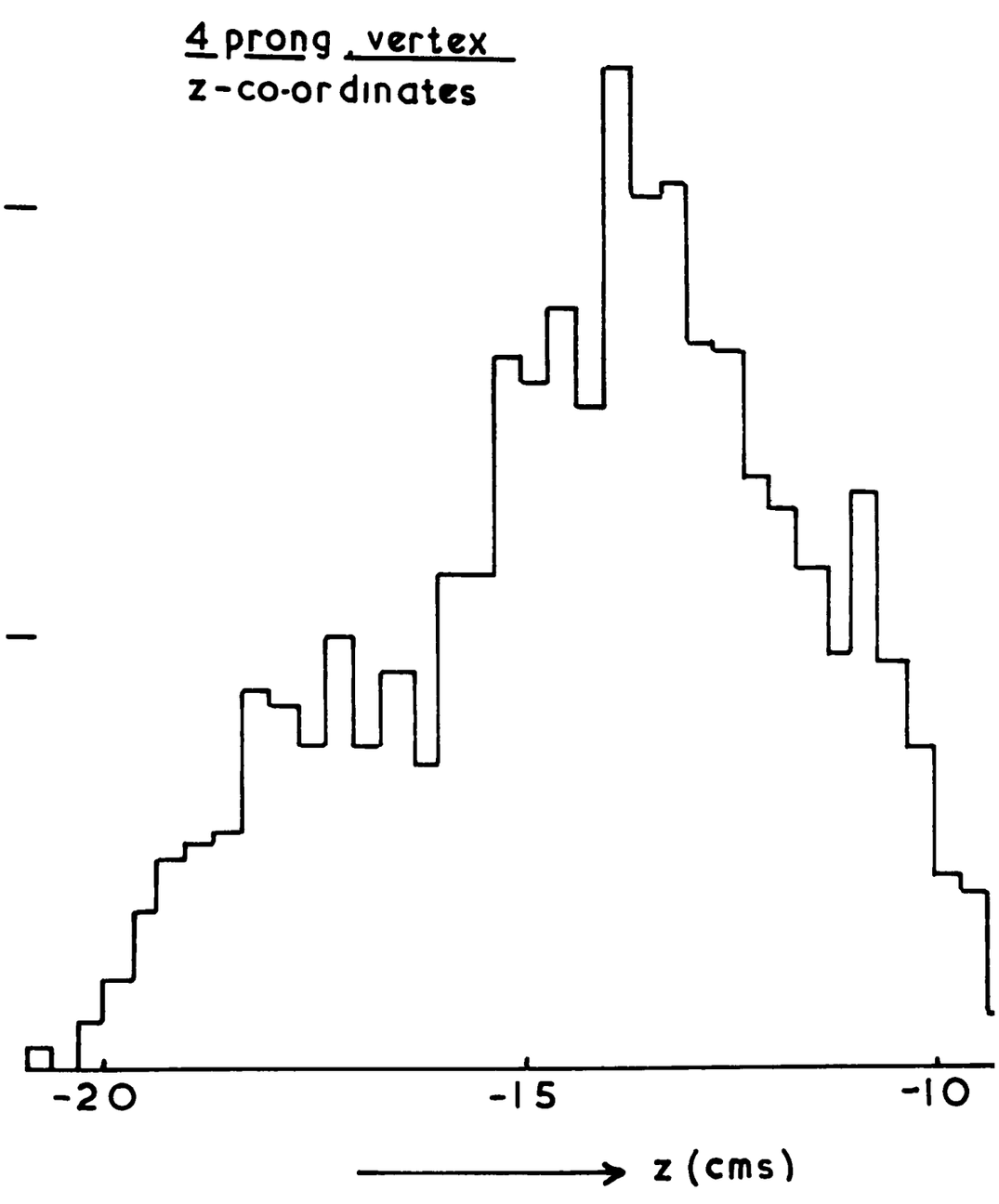

FIG. 1.3 (b)

Measuring the Film

In order to obtain a geometrical reconstruction of each event, (x,y) co-ordinate pairs of points along tracks, and at vertices, etc., were measured on each of the three available views, using both home-made and commercially built measuring machines which provided this information in the form of 5-hole paper tape ready for direct input to a computer. These machines have been well described elsewhere.[1,2] However, it is probably worthy of note here that all the machines which were used had well built measuring stages with Ferranti Moiré fringe digitizers. The diffraction grating ruling used was one micron.

Though it would appear that the machines were accurate to one micron in the film plane, it should be remembered that a track width in this is approximately 25 μm. Hence an r.m.s. scatter of points of up to about 15 μm was expected. The counters and digitization were checked on each view measured by returning to some fixed point at the end of the measurements. The counters were required to read what they started at to within setting accuracy.

At the time of writing, the work of putting the existing machines under the constant supervision of an on-line computer is at an advanced stage. Four machines are at present under such control. The computer checks the format of the symbols

typed by the operator to signature the various parts of film measured and at the end of each track checks for badly measured points causing a REMEASURE directive to be made if necessary. It is gratifying to note that those tracks persistently rejected by the computer are often found to have a very slight decay or scatter on them - a fact which encourages the author in the belief that no such events, measured as four prongs, e.g. actually pass the rigorous scrutiny of the geometry programme about to be described.

The Reconstruction Programme

This was written by members of the Rutherford High Energy Laboratory and has been described in considerable detail elsewhere.[3] Consequently, only a brief account is given here emphasizing the main points in the personal use made of it.

The programme was protected against varying input by the requirement of a set format. To present such a format to the IBM 7090 computerson which all the author's events were processed (see Acknowledgements) a buffer input translation process was first used. This also checked the raw data from the machines for obvious mistakes.

Some fixed data containing information on camera positions; position, thickness and refractive indices of windows; etc; was also fed to the computer which carried out some preliminary

transformations on the data to allow for film shrinkage (fx in the x-direction and fy in the y-direction) and for any rotation (θ) with respect to the measurement axes. In order to do this, the measurements of several fiducial marks were used. In carrying out the transformation, all measurements also had their origin changed to the position of a central fiducial mark on the front glass; consequently measurement of at least three fiducials was required. In the present experiment a habit of measuring four was adopted.

Some assumptions regarding the reconstruction process adopted by the programme used by the author were as follows:

1. That the camera axes were parallel;
2. That the film plane was parallel to both the front and back glasses of the chamber;
3. That pinhole optics could be applied to the cameras;
4. That the measuring axes of the machines were orthogonal.

The justification for these assumptions lay entirely in the fact that a good reconstruction of the space positions of all fiducials (on both front and back glass) was obtainable. Assumption (3) at least could not be made, for instance, in the case of the British National Hydrogen Bubble Chamber as the wider angle of the optical system (approximately one and

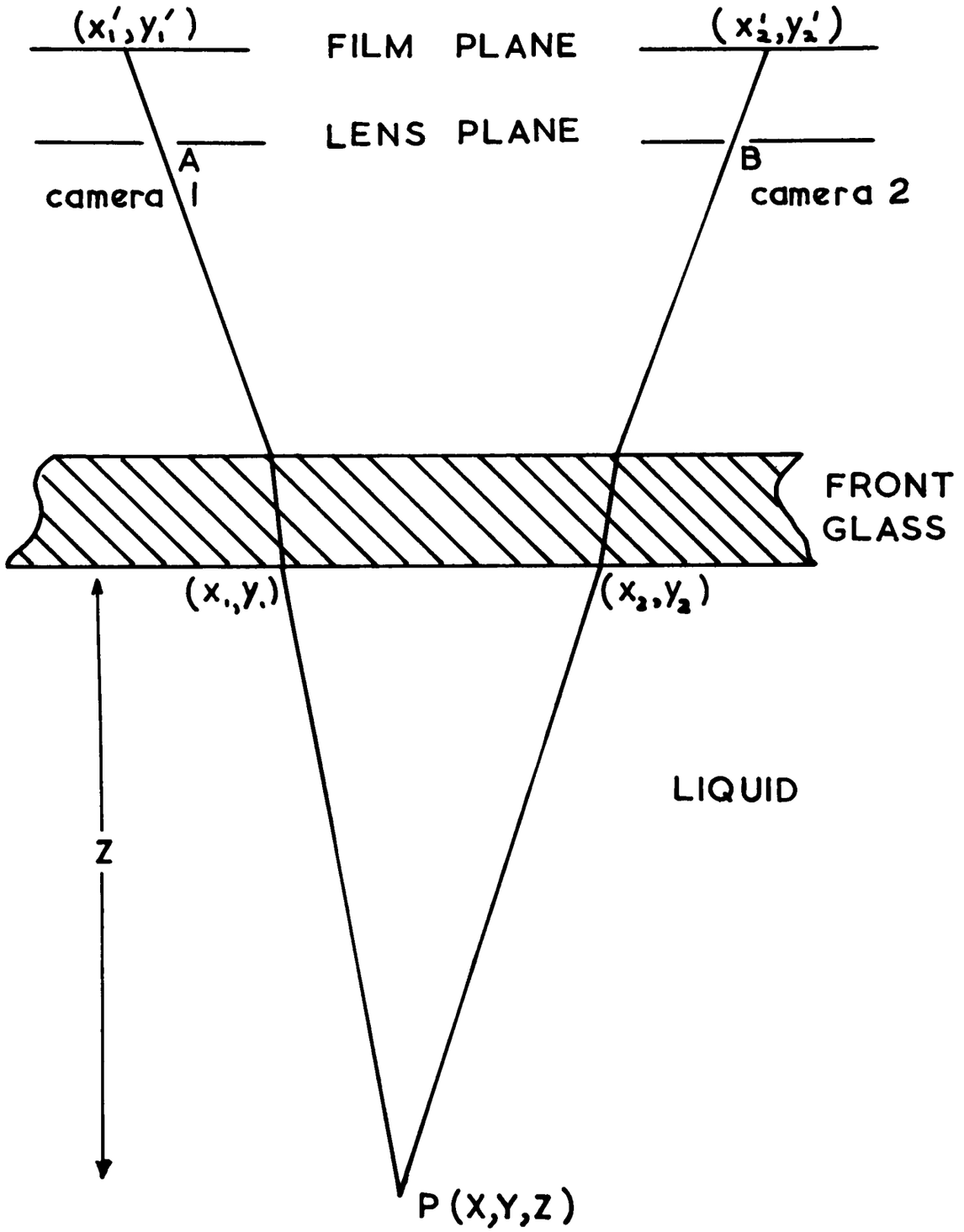
(x_1', y_1')
FILM PLANE
(x_2', y_2')
LENS PLANE
A
camera 1
B
camera 2
FRONT GLASS
(x_1, y_1)
(x_2, y_2)
LIQUID
Z
P (X,Y,Z)

FIG. 1.4

a half that of the Saclay chamber) did not allow the neglect of lens imperfections.

The reconstruction of points in the chamber was obviously overdetermined as Fig. 1.4. illustrates. The Point P (Fig.1.4.) is assumed to have measurements on the two views indicated by A and B at positions (x_1', y_1') and (x_2', y_2'). In fact these positions were not necessarily correctly measured and a two view reconstruction was possible and even provided an error estimate. However, corresponding points along a track were not always measured and the necessary interpolation between measured points added uncertainty and lead one to prefer a 3 view reconstruction. All events were, therefore, measured on three views where possible. The reconstruction of tracks was then carried out by a least squares procedure. By hypothesizing a helix of the form:

$$\begin{aligned} x &= \alpha + \rho \cos\theta + c_x(\theta) \\ y &= \beta + \rho \sin\theta + c_y(\theta) \\ z &= \gamma + \rho\theta \tan\lambda \end{aligned} \qquad \ldots.(1)$$

where θ was a convenient parameter specifying the angle that the track had turned through at position (x,y) relative to position (α, β), the programme calculated the apparent trajectory projected back onto a nominal film plane constructed by ignoring the front glass refraction. This is illustrated in Fig.1.5.

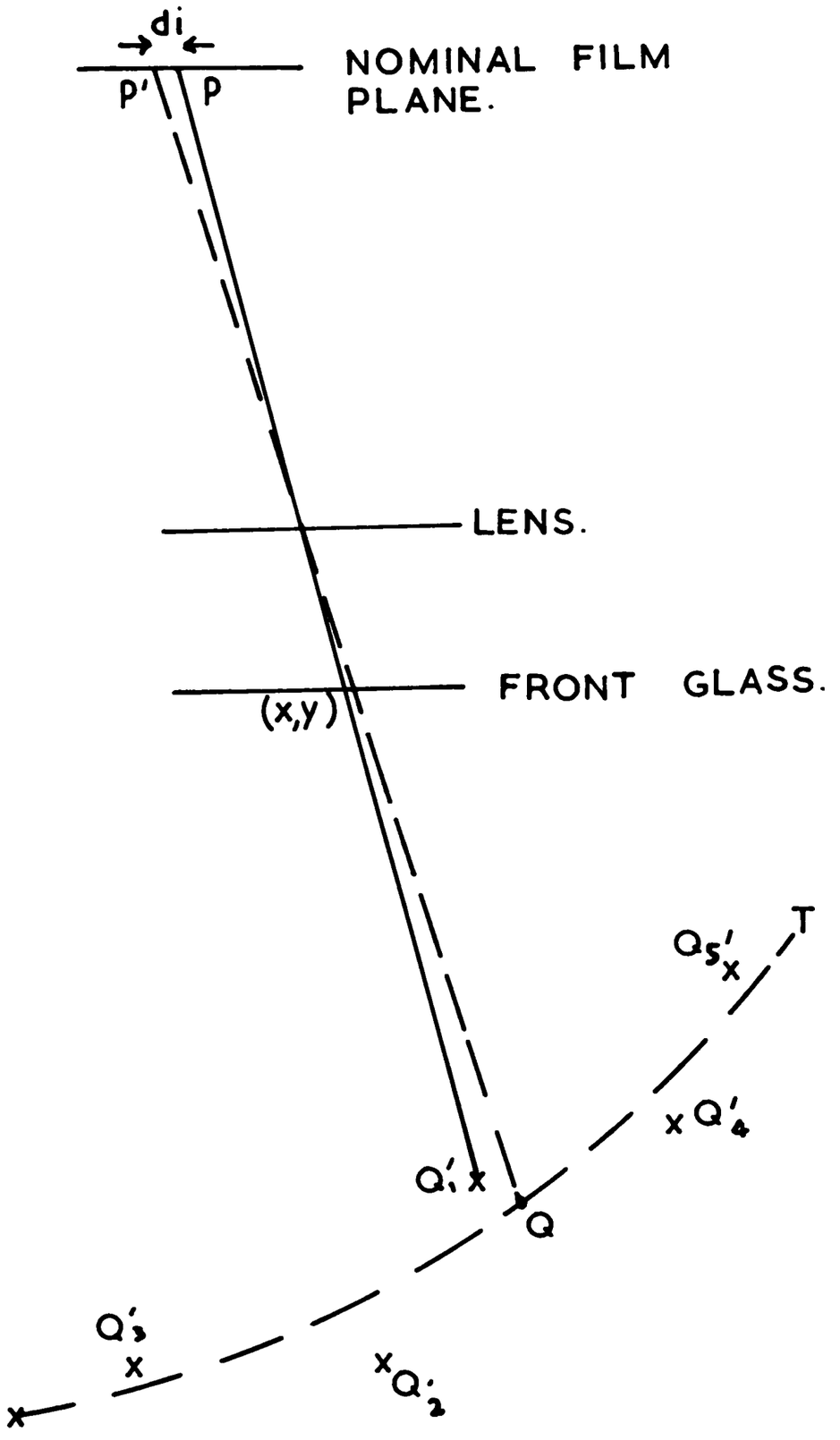

FIG. 1.5

where the hypothetical track T has measured "rays" such as P'Q' which pass near the helix such that their points of nearest approach to it are represented by crosses. (Q_1', Q_2', Q_3' ,....). The rays are calculated at an early stage by the programme and effectively allow one to forget the front glass. They are specified by their point of intersection with this glass and their direction. The least squares procedure then consisted of a variation of the parameters α, β, ρ and those involved in C in order to minimize the quantity:

$$M = \Sigma d_i^2$$

where d_i was the distance between points P and P' corresponding to the ends of "hypothetical" and "real" rays PQ and P'Q', as in Fig. 1.5. along a direction (PP') perpendicular to the projected helix on the film plane. The quantities C_x and C_y represented the effect of slowing of the particle, and depended upon the track curvature and position in the chamber. As a consequence the expressions (1) were non-linear in the parameters to be found and the least squares procedure had to be an iterative one. The error matrix was calculated by

$$\langle \delta\alpha_\lambda{}^* \, \delta\alpha_\mu{}^* \rangle = \sigma_F^2 \, H_{\lambda\mu}^{-1}$$

where

$$H_{\lambda\mu} = \tfrac{1}{2} \sum_{i=1}^{N} \frac{\partial^2 d_i^2}{\partial\alpha_\lambda \, \partial\alpha_\mu}^*$$

and where $\alpha_\lambda{}^*$, $\alpha_\mu{}^*$ were the best values for the λth and μth parameters; N = total number of points measured on each track

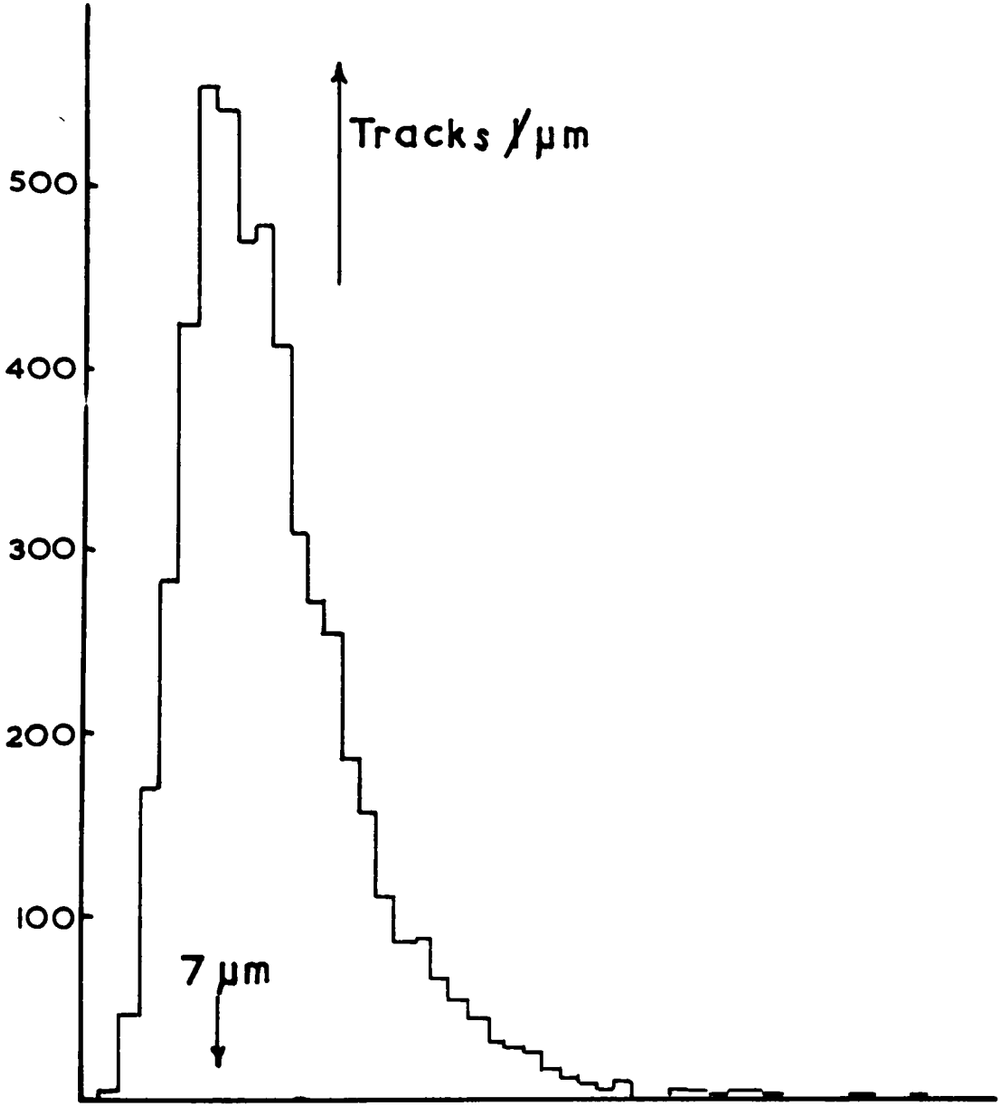

FIG. 1.6 (a) Helix fit R.M.S. errors 2-prongs.

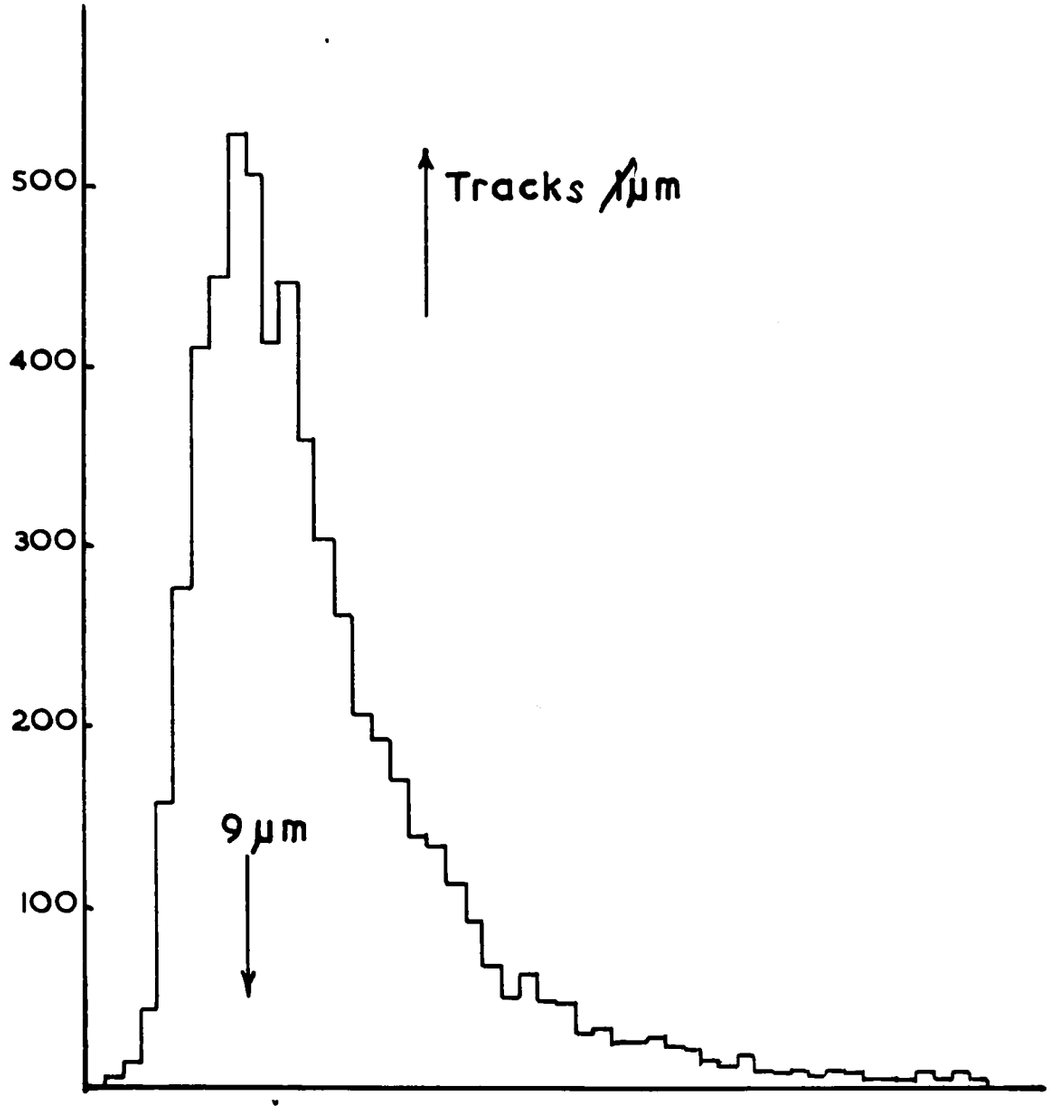

FIG. 1.6 (b) Helix fit R.M.S. errors 4-prong

and σ_F = a standard measuring error.

In order to determine σ_F, use was made of the fact that, for normally distributed measured variables, the χ^2 for the helix fit had expectation value:

$$\langle \chi^2 \rangle = \frac{1}{\sigma_F^2} \sum_{i=1}^{N} d_i^2 = N-5$$

as there are 5 unknowns ($\alpha, \beta, \gamma, \rho, \lambda$) and N measurements.

The distribution of the quantity:

$$\sigma_p^2 = \frac{1}{N-5} \sum_{i=1}^{N} d_i^2$$

shown in Fig. 1.6. indicates a reasonable value for σ_F of 9 μm for the 400 and 7 μm for the 200 measurements.

Mass Dependent Helices

For slower tracks (less than about 1 Gev) it was always found necessary to fit three helices to a track - one each for a K, for a π and also a p mass. This was because the slowing down corrections became increasingly distinct for the three cases. As the momentum lessened, the resulting errors calculated also became markedly different. This could be used to identify slower tracks, especially when their ionization became too large to estimate at all accurately. However, a serious consideration was that an increased error estimate for what was probably the wrong mass for the track merely simplified the task of the kinematics programme to assign that wrong mass to it.

Constants Required for Reconstruction

These could be classified as follows:-

1. Information on the magnetic field throughout the chamber.
2. Optical constants including camera positions, fiducial positions on the film for each of three views and details of any optical components between the camera and the liquid in the chamber.

The Magnetic Field

The magnetic field in the Saclay 81cm. chamber had been accurately surveyed. The resulting three dimensional lattice of values was fitted to an empirical polynomial expression [4] which was used in the geometry programme to calculate the average value of the field along a track. The polynomials described the variation of B/B_o where B was the value of the z component of field, and B_o that at the centre of the field gap. The latter value was held accurately constant throughout the experiment by a current stabilising circuit. The absolute value did, however, need to be accurately known.

A method suggested by M. Derrick was implemented by J. G. Loken[5]. At an early stage in the experiment, some rare events having more than one V^o associated with them were measured. A χ^2 fit was made, by varying the measured momenta of the V^o prongs such that:

$$\underline{p}_1 + \underline{p}_2 = k\underline{p} \qquad \ldots.(1)$$

Where $\underline{P}_1$, $\underline{P}_2$ are the momenta of the prongs and $\underline{P}$ a unit vector joining the V^o and the production vertices. This was thus a two constraint fit (equation (1) represents three equations with one unknown - k)

The mass (M) associated with the V^o was given by:-

$$M^2 = \left(\sqrt{\underline{P}_1^2 + m_1^2} + \sqrt{\underline{P}_2 + m_2^2}\right)^2 - \left|\underline{P}_1 + \underline{P}_2\right|^2$$

where $m_1 = m_2 = m = 0.1396$ Mev if a K^o - V and

$m_1 = m_p = 0.938$ Mev

$m_2 = m_\pi = 0.1396$ Mev if a Λ^o - V

A Gaussian Ideogram of these masses was made when the V^o was identified as being due to the decay of a K^o meson. The central value of the ideogram turned out to be 494.9 Mev. The value of B_o was therefore changed by 0.9% which, on repeating the process gave the central value at 497.6 Mev. The reason for restricting the method to K^os was simply due to the fact that variations in magnetic field have a larger influence on the mass of the K^o than the Λ^o Vs. This can be seen if one considers the centre of mass of the V^o.

Here, the mass is given by:

$$M = \sqrt{p^2 + m_1^2} + \sqrt{p^2 + m_2^2}$$

Where m_1 and m_2 are the masses of the decay products, and p their relative momentum.

In the Λ^o rest system:

$m_1 + m_2 = m_p + m_\pi = 1077.8$

$= m_\Lambda - 37.4$

Where the 37.4 Mev depends on the momentum.

In the case of the $\bar{K}^o \rightarrow \pi^+ \pi^-$ decay

$m_1 + m_2 = 2m_\pi = 279.3 = m_{K^o} - 217.84$

Taking an extreme case, where all momenta were apparently a large factor too small, because of an error in the magnetic field value, it is clear that the effect of the K^o mass would be much greater than on the Λ^o. This fact, together with the fact that the momenta in the two cases are not very different ($p_\Lambda = 148$ Mev/c; $p_K = 206$ Mev/c) leads one to suppose that this is so for any field variation.

Optical Constants

The z co-ordinates of the cameras were well measured by direct means, but the same cannot be said of the x,y co-ordinates because the exact positions of the camera axes relative to the chamber were not easy to define. In order to obtain these, photographs of the chamber fiducials (whose absolute space positions were measured with a theodolite) were taken and measured repeatedly on a measuring machine. The resulting measurements were then taken as standard and all subsequent film shrinkages made the same as on this piece of film.

A correction was made to the theodolite measurements to

allow for any rotation of the front glass relative to the back, or any shrinkage, due to lowering the temperature of the glasses containing the fiducials.

The thicknesses of portholes and the front glass itself were determined and the Böck[6] camera constant programme used. This took the measured fiducial positions on the three views, compared them with calculated positions allowing for film shrinkage and refraction at the various surfaces and by varying the camera co-ordinates in x and y directions, minimized the quantity $\sum_{i=1}^{N} d_i^2$ where d_i was the distance of the ith fiducial from its calculated position.

In the case of the February run, it was found that satisfactory results could only be obtained by this procedure if two fiducials were rejected (presumably having been incorrectly surveyed).

Beam Tracks

In most cases, the beam tracks were too short to have accurately measurable curvature. As the beam momentum was, in fact, held within fairly close limits, it seemed unnecessary to rely upon inaccurate measurements. Consequently, a large number of long beams were measured and processed by the geometry programme using the best constants obtained - including the magnetic field - and the resulting momenta ideogrammed. The mean value, together with a standard error were then used

for all events.

The value for momentum used was 3.460 ± 0.020 Gev/c making the centre of mass energy 2.771 ± 0.007 Gev.

REFERENCES TO CHAPTER I

1. D. J. Crennell: D.Phil. Thesis, Oxford (1963)

2. Ferranti-Sogenique Technical Manual FSP 249

3. J. W. Burren & J. Sparrow: "The Geometrical Reconstruction of Bubble Chamber Tracks", R.H.E.L. Reprint RHEL/R/14, H.M.S.O. (1963)

4. C. J. B. Hawkins: Nucl.Instr.and Methods. 20,455,(1963)

5. J. G. Loken: D.Phil. Thesis,Oxford Univ. (1964)

6. R. Böck, C.E.R.N. Reprint 60-7 (1960)

CHAPTER II

In order that the results of different experiments may be compared it is important to eliminate effects due to differing beam fluxes (both in quality and quantity), bubble chamber sizes and experimental biases as far as possible and to convert numbers of events into cross-sections.

Overall Scanning and Geometry Losses

As previously mentioned in Chapter I, scanning was confined to events lying within a fiducial volume defined by a template placed on the scanning table. Two prongs and 's were required to lie within a larger region than the four prongs and the isotropic distribution in x - co-ordinate of the vertices for 2 and 4 prongs, illustrated in Figs. 1, 2(b) and (c) (Chapter I) relative to these 2 boxes can be taken as evidence for the lack of dependence of scanning efficiency upon position of the events in the chamber. This is to be expected for the more common topologies not requiring the observation of visible secondary decay within the same fiducial region. However, the negative requirement that such a decay be not observed represents the necessity for some further overall correction to be applied to events involving, for instance, a neutral K meson. This will be discussed later.

Scanning Efficiency

Some estimate of the loss of events due to genuine

omission may be obtained from a repeated scan. The usual way of calculating the overall efficiency of two scans is as follows:-[1]

Let E_1 and E_2 be the efficiencies of the two scans separately estimated from the number of events seen (N_1 and N_2 respectively) by the relations:

$$E_1 = \frac{N_1}{N} \quad ; \quad E_2 = \frac{N_2}{N} \qquad \ldots.(1)$$

where N is the supposed total number which could have been seen. By making the assumption that all events are equally likely to be seen, the number observed on both scans may be expressed as:

$$N_{12} = E_1 E_2 N \qquad \ldots.(2)$$

Then, if N_{TOT} is the number seen altogether, A_1 the number seen on the first but not the second scan, A_2 the corresponding number on the second but not the first,

$$N_{TOT} = NE_1 + NE_2 - NE_1E_2 = NE$$

where E is the overall efficiency;

$$E = E_1 + E_2 - E_1E_2$$

where:

$$E_1 = 1 - \frac{A_2}{N_2} \quad ; \quad E_2 = 1 - \frac{A_1}{N_1} \qquad \ldots.(3)$$

Application to 4 prongs

The whole of the four prong sample of film was scanned twice. Formulae (3) were used to estimate an overall efficiency

of 99.5% giving a possible total number of events of 1433. Altogether, 1427 events were measured three times where necessary yielding a total geometry pass rate of 79%. It seems likely, from the fact that tracks which, on closer inspection, turn out to have small angle decays are rejected by the computer now on line to the measuring machines, that some of these failures may have been due to such decays. The number of missed decays has been estimated in connection with the analysis of the 410 topology, and is 30 events when normalized to the same quantity of film. This gives the result that, assuming they all appear among the four prongs that failed geometry, 80.5% of pure 400s with no decay passed geometry. Thus the factor $f_{400} = 1.25$ must be applied to allow for scanning and measuring losses.

Two Prongs

In this case only 3 out of 17 of the rolls of film were rescanned. The large number of events thus rescanned was thought to justify this procedure. The values $N_1 = 419$; $N_2 = 411$; $A_1 = 92$; $A_2 = 84$ were substituted in (3) to give the overall efficiency 95.5% for two scans and 79.5% for E_1. Thus, the estimated total number of events is $2303/E_1 = 2900$ and a further 470 could have been observed by a complete rescan.

A similar calculation of geometry loss after two measurements using the estimated number of missed 210s of 25 gives

the geometry and scanning loss factor of $f_{200} = 1.65$.

3 Prong Decays

It is important that the number of τ decays (characteristic only of K-mesons) should be carefully measured in order to estimate the beam purity. Consequently, as already mentioned, four scans were carried out on the first run of film - corresponding to the source of four prongs - and two on the two prong sample, with the finding of such decays in mind.

In the analysis of the scanning efficiency for the former case of four scans it is possible to use formula (3) by first combining the scans in pairs as follows:-[2]

Calling the four scans A, B, C and D a summary of events seen is given in Table I, where for instance AB denotes the number of events seen on both A and B but not on any other combination of scans. Thus, it is easy to calculate that, treating A and B as a single scan, the number seen on this scan alone is:

$AB + A + B = M_{AB}$ say and those seen on this scan at all is

$N_{AB} = \text{Total} - M_{CD}$ where M_{CD} is defined analogously to M_{AB}.

By calculating M_{CD}, N_{AB} and N_{CD} in this way, the two pairs may be combined by use of (3) where $A_1 = M_{AB}$, $A_2 = M_{CD}$ $N_1 = N_{AB}$, $N_2 = N_{CD}$ to give overall efficiency = 97.3%.

The similar results of 99.0% and 98.9% were obtained using the other pairs (AC, BD, and AD, BC) respectively. The

TABLE I

τ's - Number of times seen

1	2	3	4
A = 30	AB = 29	ABC = 22	ABCD = 91
B = 4	AC = 20	ABD = 10	
C = 9	AD = 7	ACD = 22	
D = 1	BC = 3	BCD = 7	
	BD = 4		
	CD = 3		
TOTAL	TOTAL	TOTAL	TOTAL
$N_1 = 44$	$N_2 = 66$	$N_4 = 61$	$N_4 = 91$

average value of 98.4% may be taken to give a total number of τ s of 266.2. In the two prong case the simple result of 102 τ s is achieved.

Criticism of Formula (3)

Several doubtful assumptions are made in deriving equation (3) the worst of which is probably that all events are equally likely to be seen. However, if one estimates the number not satisfying this criterion (e.g. short tracks not visible, etc.) separately, this is not too serious as the probability for seeing an event is probably only different in such cases. Another assumption is that the efficiencies of each scan are truly represented by the actual number of events seen. That different scans are subject to differing efficiencies is undoubted but the generalization to, for instance, the four scan case where one would need to define four efficiencies:

$$E_1 = N_1/N, \qquad E_2 = N_2/N, \quad \text{etc.}$$

is somewhat cumbersome whereas the simplified procedure adopted above lacks both symmetry and accuracy.

A slightly more symmetrical treatment of four scans can be made as follows:-

Instead of differing efficiencies, we define the probability for seeing an event as p where:

$$p = \lim_{n \to \infty} \left(\frac{n'}{n}\right)$$

where n' is the number of times it is seen after looking at it n times. The p replaces both E_1 and E_2 in the two scan case, for instance, so that the fact that the numbers of events seen (N_1 and N_2) are different, may be regarded as a statistical fluctuation. Then p represents the value that the E's would attain if the scanning were repeated an infinite number of times.

On this basis, if s scans were performed on the film, it is only of interest to know how many events were seen once, twice, etc. and not on which scans they were seen. The probability for these numbers to be N_1, N_2, ...N_s may easily be calculated. It is:-

$$P(N,p) = \left[\frac{N!}{(N-n)!\prod_{r=1}^{s} N_r!}\right] \times \prod_{r=1}^{s} (C_r)^{N_r} \times (1-p)^{s(N-n)} \times \prod_{r=1}^{s}\left[p^r(1-p)^{s-r}\right]^{N_r}$$

(where $n = \sum_{t=1}^{s} N_r$ is the number seen at all and N is the total number of events which could be seen with probability p)

The multinomial expression in square brackets allows for permutations amongst the events (assumed identical) whilst the factor $\prod_{r=1}^{s} (C_r)^{N_r}$ is to allow for the identity of the scans.

It is then reasonable to suppose that the best values of N and p describing these results are those which maximize the probability P. Using the more convenient logarithmic probability:

$$W = \ln.P = \ln\frac{\Gamma(N)}{\Gamma(N-n)} + s(N-n)\ln.(1-p) + \sum_{r=1}^{s} N_r\left[r\ln.p + (s-r)\ln.(1-p)\right] + \text{CONST.}$$

where the Gamma functions replace the factorials of the continuous quantities N and N-n, the problem becomes that of solving:

$$\frac{\partial W}{\partial N} = \frac{\partial W}{\partial p} = 0$$

If we approximate $\ln.\frac{\Gamma(N)}{\Gamma(N-n)}$ by $\sum_{m=0}^{n} \ln(N-m)$ we obtain

$$\sum_{m=0}^{n} \frac{1}{(N-m)} + s\ln.(1-p) = 0 \qquad \ldots.(4)$$

$$\sum_{r=1}^{s} N_r \left[\frac{r}{p} - \frac{(s-r)}{(1-p)} \right] - \frac{s(N-n)}{(1-p)} = 0$$

Furthermore the errors on these quantities may be estimated from the second derivatives of W in the usual way.[3]

Equations (4) have been solved numerically for the case of the 4τ scans giving the result of 263.7 decays instead of the previously calculated value of 266.2.

It is thought better to allow some difference between efficiencies in the simpler case of two scans only since it is obvious from Table I that such a difference could be genuine. It is clear that the method described is as incorrect as the first one. However, its sole virtue is the applicability to any number of scans. Strictly, if one were to have a large number of independent scans, it would be better to attempt to infer some detail of the distribution of detection efficiency for different events, and possibly for different scans. However, a comparison between the two methods described is

TABLE II

Scanning Efficiencies

Type of Event	Number of Scans	Number Seen	Corrected Number		Efficiency				
			Method I	Method II	Method I			Method II	
					E_1%	E_2%	E%	p%	E%
2 Prong	2	502	526	529±5	79.5	78.2	95.5	74.0±1.0	95.0±1.0
4 Prong	2	1427	1433	1437±2	76.2	99.2	99.5	86.2±0.3	99.3±0.2
τ	4	262	266.2	263.7±1.2			98.4	67.0±0.7	99.5±0.5

made in Table II where the final results are also summarized. Method 1 is use of equation (3) and method II of equation (4).

Other Biases

In addition to the losses calculated above, some allowance may be required for the following factors:-

1. Events involving a charged K-meson are lost from the two and four prong samples if the meson decays within the chamber fiducial volume. No analysis of these was undertaken as it was considered better to correct for them.
2. Events involving a $\bar{K}^0$ or Λ^0 require corresponding correction. However, as no channels involving a Λ^0 were of interest to this analysis only the former case will be considered.
3. The presence of Dalitz pairs corresponding to the decay of a π^0 could produce some contamination.
4. Some short proton tracks may be lost.

Charged Decays

Suppose that, in the laboratory, a fraction $f(p,L)dpdL$ of events have a K^- particle which travels a length between L and L + dL with momentum between p and p + dp where the differentials have the usual significance. If the particle has a proper lifetime (in its own rest frame) of τ, then only a fraction $e^{-L/\lambda(p)}$ will actually survive the full length L without decay. Here, $\lambda(p)$ is the decay length given by:-

$$\lambda(p) = \frac{pc}{M_o \tau}$$

where p = momentum

$c = 3 \times 10^{10} cm.sec^{-1}$ (= velocity of light)

M_o = particle rest mass

Consequently, if one expects to see any tracks of length L where K^- has this momentum, one will only see a fraction $f'(p,L)dpdL$ of the events where $f'(p,L)=f(p,L)e^{-L\lambda(p)}$

Hence, the corrected number will be N given by:

$$N/N_{seen} = \int_0^{pmax} \int_0^{Lmax} f'(p,L)e^{L\lambda(p)} dpdL$$

where N_{seen} is the number seen.

For each event, the momentum p and length L were noted for the track of interest for a given hypothesis. This event was given the weight $e^{L\lambda(p)}$. The corrected number of events satisfying that hypothesis was then computed to be:

$$N = \sum_{i=1}^{N_{seen}} \exp(L_i \lambda_{K^-}(p_i)) = RN_{seen}$$

Most events had weighting factors of unity and only five in all reactions required a weight of more than 2.0. It is clear, therefore, that the value of R produced by summing these is not strongly influenced by statistical fluctuations in the small number having large weight. Further, it is apparent that the weighting of individual events is hardly necessary - merely the application

of an overall factor R to the cross-sections. Similar conclusions apply to all other final states involving a K^-.

Neutral Decays

Only one case needs to be considered, that is the two prong reaction $K^-p \rightarrow \bar{K}^o p \pi^-$. The correction is slightly different from the case of the charged decays since only one third of the $\bar{K}^o$'s are expected to give a visible decay.

Thus, we need to compute g where $1/g = \sum_{i=1}^{N_{seen}} \exp(L/\lambda_{K_1}(p_i))$ (where L is taken as the average distance from production vertex to the end of the scanning box.) Then g is the fraction of events having the K_1^o lifetime which do not decay.

If the correct number of $\bar{K}^o$'s is N, it is given by:

$$N_{seen} = \tfrac{2}{3}N + \tfrac{1}{3}gN$$

i.e. $$N = \frac{3N_{seen}}{(2+1/g)} = GN_{seen}$$

It is noted that N_{seen} refers to the number of unobserved $\bar{K}^o$ decays.

Dalitz Pairs

Some estimate of the seriousness of these as a potential source of contamination may be arrived at in the following way. Consider the four prongs.

The reactions $K^-p \rightarrow K^-p\,\pi^+\pi^-$ (i)

$K^-p\,\pi^+\pi^-\pi^o$ (ii)

may well be contaminated by the two prong reactions

$$K^- p \rightarrow K^- p \pi^0 \qquad \text{(iii)}$$

$$\rightarrow K^- p \pi^0 \pi^0 \qquad \text{(iv)}$$

$$\rightarrow K^- p \pi^0 \pi^0 \pi^0 \qquad \text{(v)}$$

where one π^0 decays in the Dalitz mode. Using the cross-sections estimated for reactions (i), (ii) and (iii) and assuming that those for (i) and (iv) are alike, and also for (ii) and (v) it is apparent that (iii), (iv) and (v) collectively may contribute up to 3.6% to reaction (i) or 5.7% to reaction (ii). In order to obtain these estimates, the branching ratio $\pi^0 \rightarrow \gamma e^+ e^- / \pi^0 \rightarrow \gamma\gamma$ of about 1/80 has been used. However, it is clear that many of the Dalitz pair events, though simulating four prongs, would be removed at the scanning stage since the electron pair is usually unmistakable by its characteristics of zero opening angle and somewhat curved but minimum ionizing tracks. Further, it is unlikely that all events escaping such detection would be able to satisfy the constraints of energy and momentum balance necessary for reactions (i) and (ii). Consequently, contamination from this source has been neglected.

Slow Protons

In order to determine the loss of slow protons the useful parameter is the track length projected onto the film. An approximation to this is the projection onto a plane parallel to the front glass and the distribution of this quantity was investigated

for all events involving a proton. It is clear that any such loss is only important in the case of the lowest momentum transfers to the proton (which occur in the elastic events -). In all other cases, a noticeable depletion of events commences at about 1.5 cms (easily visible). In this thesis, no analysis of elastic events is given so that this loss is ignored.

Estimation of Total K Flux

Three Prong Decays

It is expected that a considerable negative pion and μ^- meson contamination exists in the beam. However, decay rates for these particles producing three charged tracks are negligibly small, whereas several are summarized [4] in Table III for the K-mesons. In practice, it is difficult to distinguish these different decays, so no attempt was made. Using the K^- lifetime of $1.229 \pm 0.008 \times 10^{-8}$ sec., the K length corresponding to the observation of N_3 three prong decays is L where:

$$L = N_3 \times \frac{cp}{m_o} \times \frac{(1.229 \pm 0.008) \times 10^{-8}}{(0.0593 \pm 0.009)}$$

where $p = 3.46$ Gev/c, $m_o = 0.494$ Gev, $c = 3 \times 10^{10}$ cm.sec^{-1}

One may then express the cross-section per interaction as:

$$\sigma = \frac{M}{N_o \rho L} \times f$$

where M = molecular weight of hydrogen = 1

TABLE III

3 Prong Decays of K^--Mesons

Mode	Rate
$K^-_\tau \rightarrow \pi^- \pi^+ \pi^-$	
$K^-_\theta \rightarrow \pi^- \pi^0$, $\pi^0 \rightarrow e^+e^-\gamma$	$1/80 \times 0.213 = 0.0027$
$K^-_{\pi 3} \rightarrow \pi^- \pi^0 \pi^0$, one $\pi^0 \rightarrow (e^+e^-\gamma)$, other $\pi^0 \rightarrow e^+e^-\gamma$	$2/80 \times 0.017 = 0.0004$
$K^-_{\mu 3} \rightarrow \mu^- \nu \pi^0$, $\pi^0 \rightarrow e^+e^-\gamma$	$1/80 \times 0.034 = 0.0004$
$K^-_{e3} \rightarrow e^- \nu \pi^0$, $\pi^0 \rightarrow e^+e^-\gamma$	$1/80 \times 0.049 = 0.006$
Total 3 prong	$= 0.0593 \pm 0.0009$

w: N_o = Avogadro's number = 6.02×10^{23}

and ρ = density of hydrogen = 0.0614 ± 0.004 gms.cm^{-3}

Using f = geometry and scanning factor

tota In this way, the results obtained are summarised in Table IV., where the errors include uncertainties in the density of hydrogen, the number of τ's and the K^- lifetimes. The largest of these is in the number of τ s. The error in f is neglected.

Pion Contamination in the beam

It is supposed that the only particles in the beam are negative Ks, πs and μ s. The latter are no cause for concern since their interaction cross-section is negligibly small. However, the pions have a total cross-section at this energy ($\sigma_\pi \simeq$ 30mb) comparable with that of the Ks ($\sigma_K \simeq$ 30mb).[5]

An estimate of the pion fraction can be obtained by measuring the total cross-section of the beam with hydrogen (σ_{TOT}) This is done by measuring: (a) total number of interactions

$= N_{TOT}$

(b) total number of beam tracks

= n (on the number of frames scanned)

If the scanning box has length l, the total beam length is $L_{TOT} = nl$. One may then express σ_{TOT} in two ways:

$$\sigma_{TOT} = \frac{N_{TOT}}{N_o \rho L_{TOT}} \quad ; \qquad \sigma_{TOT} = k\sigma_k + \pi\sigma_\pi + \mu\sigma_\mu$$

where k, π, μ are respectively fractions of K π and μ in the beam, and the subscripts refer to the relevant total cross-sections. Using the values for length of K in the beam and the known total cross-sections assuming that σ_{μ} = 0 one obtains the figures quoted in Table V.

Summary of Cross-Sections

In Table IV are given the various microbarn equivalents of events taken to represent the reactions studied in this thesis. Slight differences are the result of the presence, or otherwise, of charged or neutral K meson in the final state. The symbols used in Column 3 are defined in the previous pages, and their values are often different for different hypotheses because of differing momentum and length spectra.

TABLE IV

Two Prong & Four Prong Cross-Sections (Oxford Events)

Final State	No.of Events	Number Ambiguous	Correction Factors	μb/event	Total Cross-Section (μb)
$K^- p \pi^0$	105	17	$f_{200}{}^R$	11.9±1.2	1250±177*
$\bar{K}^0 p \pi^-$	129	20	$f_{200}{}^G$	17.5±1.8	1535±205*
$K^- \pi^+ n$	209	25	$f_{200}{}^R$	11.9±1.2	2430±295*
$K^- p \pi^+ \pi^-$	276	47	$f_{400}{}^R$	5.38±0.4	1359±136**
$K^- p \pi^+ \pi^- \pi^0$	169	87	$f_{400}{}^R$	5.38±0.4	909±99*
$K^- \pi^+ \pi^- \pi^+ n$	94	52	$f_{400}{}^R$	5.38±0.4	506±65*

* These figures ignore ambiguities, so represent upper limits

** In this case the only serious ambiguity is with the corresponding π-induced reaction $\pi^- p \rightarrow \pi^- p \pi^+ \pi^-$ so that such events are given a weight of $\frac{1}{2}$.

TABLE V

Beam Purity

Run	%K	%π	Total K Length in Film Sample
Feb. 1963	60±1	26±8	62.2±5 km
Oct. 1963	57±1	23±7	39.2±4 km

REFERENCES FOR CHAPTER II

1. J. G. Loken: D.Sc.Thesis, Oxford Univ.(1962)

2. A. R. Atherton: D.Phil Thesis, Oxford Univ.(1965)

3. D. J. Hudson: Statistics Lectures II,C.E.R.N. 64-18

Page 143

4. A. H. Rosenfeld et al: U.C.R.L. 8030

5. J. H. Field; D.Phil.Thesis, Oxford Univ.(1964)

CHAPTER III

The Estimation of Ionization

Introduction

Although considerable success has been achieved in the identification of elementary particle reactions by momentum measurement alone, kinematic ambiguity often remains and one needs to resort to the film for further objective information. Such information is to be obtained from the ionization of the tracks caused by the particles and yields in favourable cases, an estimate of the particle velocity. This chapter is devoted to a discussion of the methods which were considered by which this quantity could have been extracted from the film with the special requirements of a machine in mind. The machine built by the author, its calibration and its application to the four prong events are described in the following chapter.

Velocity Dependence of Ionization

As all estimates of ionization are basically of the quantity:

$$g = \frac{\text{number of bubble nucleation centres in track}}{\text{length of track}}$$

we will adopt this as the definition.

A simple model for the formation of bubbles in a bubble chamber regards the actual formation as the result not of ionization but of a thermal process brought about by the heat given out by a stopping δ ray. Some calculations of the effect

have been made[1,2] and indicate that an energy of a few hundred electron volts is sufficient for the δ ray corresponding to a range of a few microns in hydrogen, comparable with observed scattering of bubble centres about a smooth trajectory. The cross-sections(4) for coulomb scattering of free electrons by other charged particles may be expressed as a function of the velocity of the particle ($\beta = v/c$) and the final energy of the δ ray (w) in the form:[3]

$$\sigma(\beta, w)dw = \frac{2\pi Z^2 r_o^2 m^2 c^2}{\beta^2}\left(1 - \frac{w(1-\beta^2)}{2mc^2}\right)\frac{dw}{w^2}$$

where m = electron mass; r_o = electron radius

Z = charge number of moving particle

The liquid of the bubble chamber then behaves as a detector with energy dependent efficiency E(w). A simple form for E(w) assumes that δ rays with energy less than w_1 or greater than w_2 do not cause bubbles to form on a recognizable trajectory at all, whilst E assumes the value of unity between these values for w. Consequently, the number of bubbles formed only depends upon the number of useful δ rays. Denoting the bubble density by $g(\beta)$ therefore:

$$g(\beta) = n\int_o^{\infty} E(w)\sigma(\beta, w)dw$$ (n= density of electrons per unit length) which becomes:

$$g(\beta) = \frac{2\pi n Z^2 r_o^2 mc^2}{\beta^2}\left(\frac{1}{w_1} - \frac{1}{w_2} - \frac{(1-\beta^2)}{2mc^2}\right)\ln\frac{w_2}{w_1}$$

i.e. $\sigma(\beta w) \sim 1/\beta^2 w^2$ for $\beta w \gg 1$.

This is only approximately true in liquid hydrogen since the integration over w extends, effectively, over the range w_1 to w_2. If w_1 is at all comparable with the binding energy of the electron, then the expression used for $\sigma(\beta, w)$ is no longer valid. In fact, w_1 is of order a few hundred ev whilst the ground state binding energy for hydrogen is only about 13 ev. As can be seen, the measurement of ionization could be a sensitive means of determining β when it is not too close to unity. The precise range of its usefulness will, it is hoped, become clearer in the following chapter where the application to the 4 prong events is described.

The Statistical Nature of Bubble Formations

An analogy may be made between the traversal of a charged particle through a superheated liquid and a molecule in a gas. The gas kinetic theory provides a prediction of the free path distribution of such molecules in the gas. The analogy here is between a molecule - molecule collision and a charged particle interaction causing a bubble to form and so one expects an exponential distribution of gap lengths between bubble centres.

Thus the probability for a gap of length at least x is given by:

$$P(x) = Ae^{-gx} \qquad \ldots.(1)$$

It is shown in Appendix A that the constant g can be

identified with the ionization and that it is also the inverse mean gap length of gaps $> \alpha$ any arbitrary length α.

Gap Geometry of an Ideal Track

An ideal track is considered to consist of round bubbles whose separations obey the distribution law (1). In Appendix A some formulae are derived which relate various physical aspects of such tracks with the quantities g and α where α is identified with the effective bubble diameter. Each relationship could be used to estimate g and we number these estimates with a subscript. The quantities of interest are:-

$\bar{y}$ = mean gap length

$H(\alpha)$ = density of gaps $> \alpha$

$L(\alpha)$ = lacunarity = total length of gaps ($>\alpha$) ÷ total track length

$\bar{b}$ = mean blob length

all of which provide a clue to the value of g. The problem is to decide which (if any) is the most reliable for the tracks we have to deal with. The formulae of Appendix A may then be adapted to give:

Bubble density = g_0 A.1'

$$\bar{y} = g_1^{-1} \qquad \text{A.2'}$$

$$L(\alpha) = e^{-g_2 \alpha} \qquad \text{A.3'}$$

$$g_3 = \frac{\ln H(\alpha) - \ln H(\beta)}{(\beta - \alpha)} \qquad \text{A.4'}$$

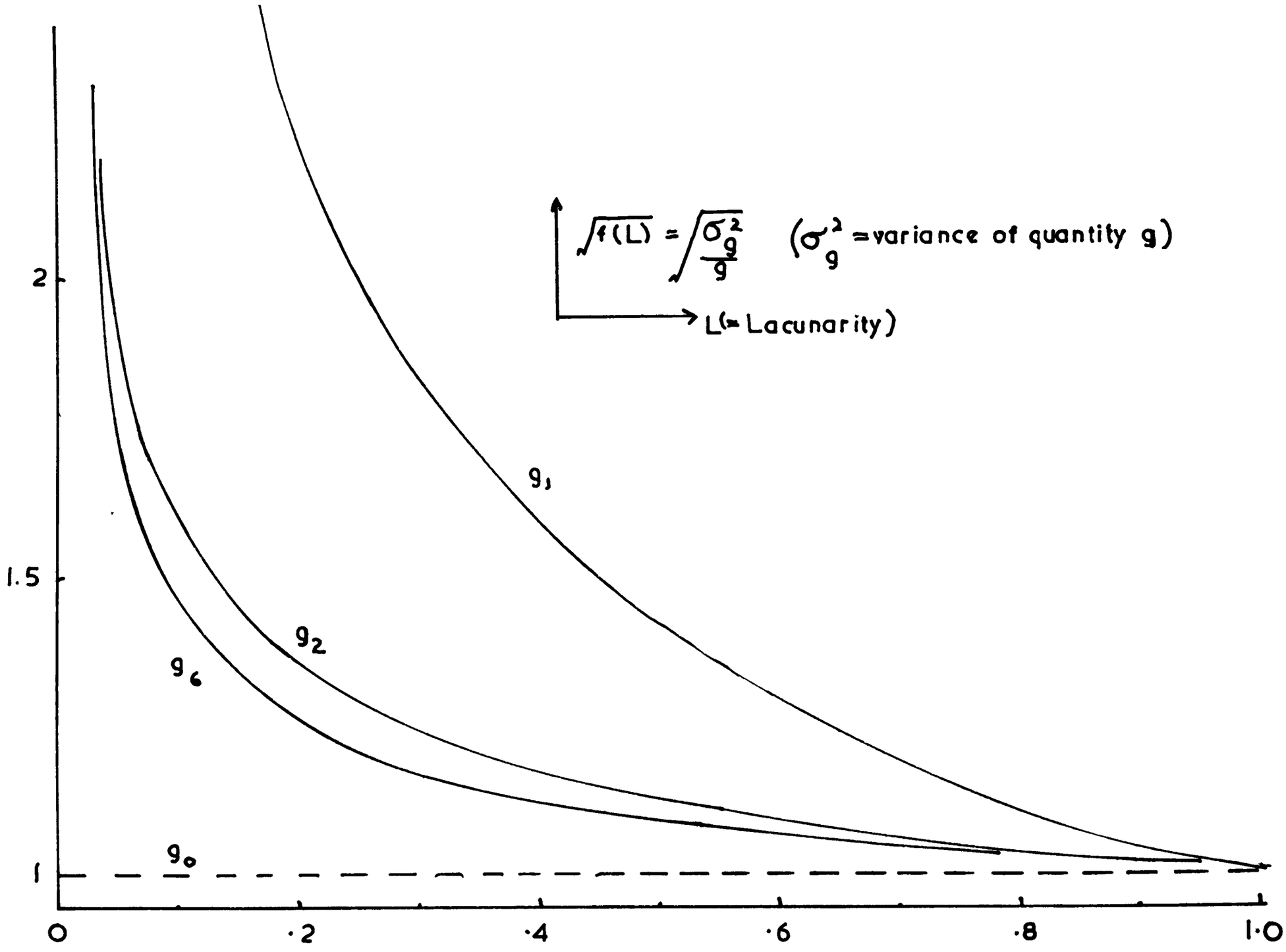
$\sqrt{f(L)} = \sqrt{\frac{\sigma_g^2}{g^2}}$ (σ_g^2 = variance of quantity g)
L (= Lacunarity)
2
1.5
1
0
·2
·4
·6
·8
1·0
g_1
g_2
g_6
g_0

FIG 3.1

$$\bar{b} = \frac{e^{\alpha g_4} - 1}{g_4} \qquad \text{A.5'}$$

Another method of determining g is from the slope of the gap length distribution (which may be fitted by maximum likelihood 4 to the form (1)) and we call this g_5.

Statistical Accuracy of g

In Appendix A expressions are also derived for the errors on the estimates g_1, g_2, g_3, and g_4. It is pointed out that the number of bubbles in a given length of track is a Poisson variable having a distribution function:-

$$P(m) = \frac{n^m e^{-n}}{m!} \qquad \ldots.(2)$$

which gives the probability for there actually being m when n were expected. Thus the variance of g_o is = g_o, and represents the ultimate statistical accuracy which can be achieved. Usually, however, one is extracting information from the visible gaps (greater than α) and this is less than the number of bubbles by a factor $L = e^{-g\alpha}$. Hence, the expressions for the variance of $g(\sigma_g^2)$ for unit track length are all of the form:-

$$\langle \sigma_g^2 \rangle = gf(L) \gg g \qquad \ldots.(3)$$

Curves of $\sqrt{f(L)}$ are shown in Fig. 3.1. with subscript referring to the estimate of g concerned. It appears that the mean gap length estimate is the poorest of all, though in practice it is difficult to draw any definite conclusions from f alone.

Plate I

The Structure of Real Tracks - Cells

So far, the formulae derived have been concerned with gap lengths defined as the distance between bubble centres and no restriction on their smallness has been made. In reality, the bubbles have a finite size which is effectively increased by diffraction when an image of them is produced on the film. A comparison may be made with the tracks formed by the path of a charged particle through nuclear emulsion. In that case, individual grains become developed and show up clearly under a microscope with sharp boundaries and are easily resolvable. In bubble chamber photographs however, the corresponding entities are usually formed by a fairly small flux of light focussed from a distant object (a real bubble). The resulting image is several grains in size and formed by a random density of developed grains. Consequently, bubbles separated by little more than a bubble diameter ($\sim 25\mu m$ on the film) produce images that are blurred together to form blobs. It is just this blurring which makes the method of counting bubbles almost impossible in most cases. Plate I is a reproduction of an actual minimum ionizing track image. It can be appreciated from this that, were the bubble density much higher, individual bubbles would be hard to resolve, especially for a machine. Even the more intelligent human eye would sometimes be deceived

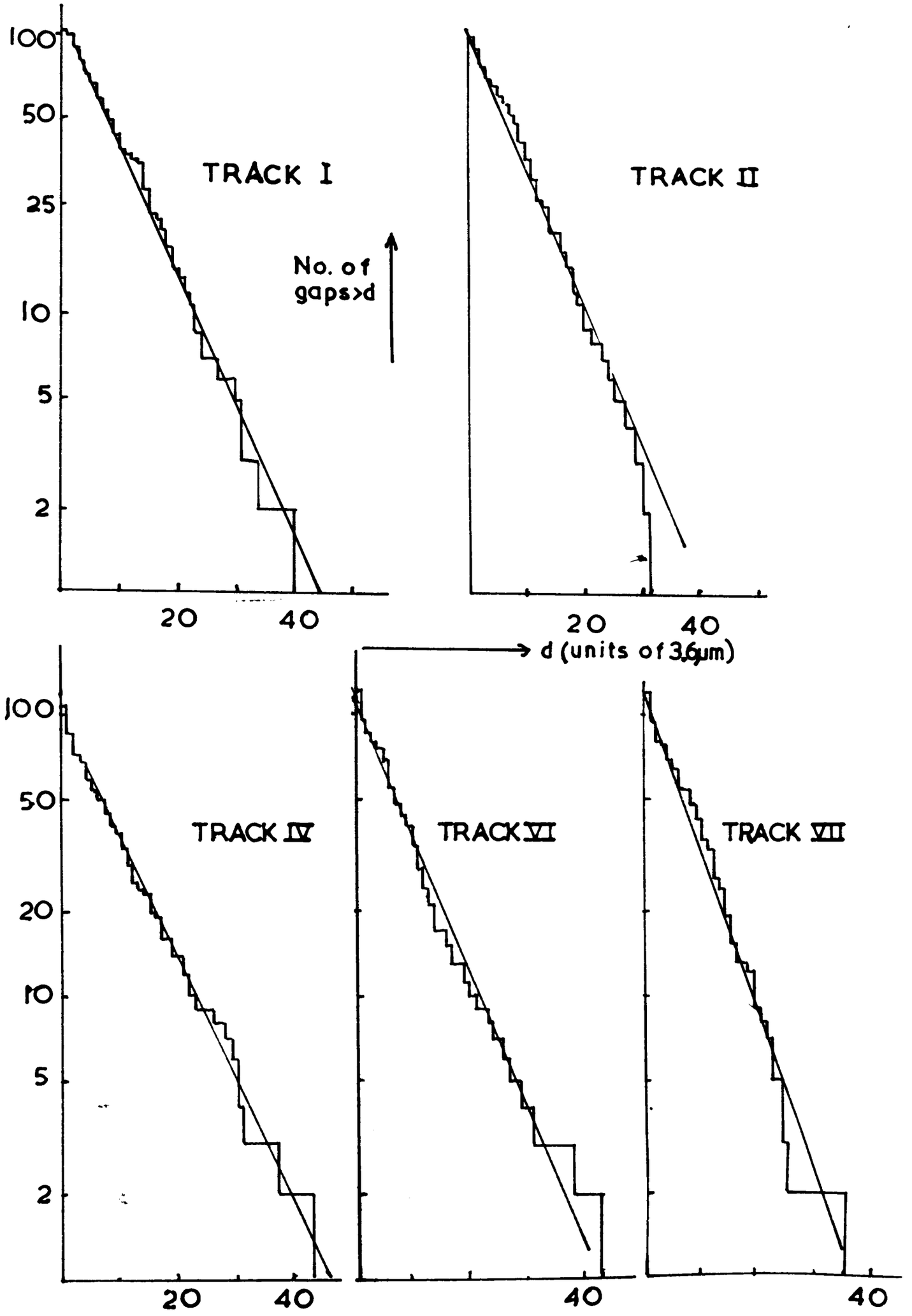

FIG 3.2 Gap Length Distributions

when asked to guess how many bubbles there were in a blob. A consequence of this blurring is that the track is more realistically divided into 'blobs' and gaps rather than bubbles and gaps, and it is convenient to refer to one blob with neighbouring gap as a cell. The cells are then the units of information available to us.

Another distinction which can be made between emulsion and bubble chamber tracks concerns the range of values of L that are used. In the latter case, L is much smaller than in the former to facilitate scanning and is usually less than 0.5 even on relativistic tracks. Thus, the number of cells is always less than one half of the number of bubbles and a decrease in statistical accuracy results.

The Distribution Law on Real Tracks

In order to check the validity of the formulae A(1'-5') on the film whose analysis is here described, microscope measurements of the gap lengths (defined from blob edge to edge) belonging to some beam tracks were made. Using the newly defined variable ($y = x - \lambda$) the distribution law (1) should still hold with A replaced by $Ae^{-g\lambda}$. The resulting plot of $\log_e$(number of gaps $\geq y$) against y is shown for some such measured tracks in Fig. 3.2. A satisfactory straight line fit by maximum likelihood is made and shown on the same figure.

TABLE I

Microscope Measurements

Track Number	Measured Length (cms. in chamber)	g(cm^{-1})					δ (μm)
		g_o	g_1	g_2	g_4	g_5	
I	8.1	173	280±30	278	274	271±25	29±2
II	8.1	190	340±36	337	333	275±44	32±3
III	8.1	192	252±32	254	256	300±30	33±3
IV	8.1	165	266±30	256	246	273±27	35±2
V	8.1	183	282±35	282	282	270±25	30±3
VI	8.1	190	309±40	300	291	295±30	33±3
VII	8.1	195	340±50	335	330	300±35	32±3

The agreement with relation (1) is a conclusion drawn by several authors.[5,6] The total length of track (l_{tot}) was measured and the bubbles counted. By using the normalization condition that the number of gaps > zero length should be $g_0 l_{tot}$, a value for α was determined simultaneously. Using this in equation (2) a value for g_1 was also obtained. Results of seven such tracks are displayed in Table I. It is noticed how persistently low the value of g_0 is, and how consistent the other estimates. The low value of g_0 could be the result of finite bubble size. When two bubble nucleation centres are produced very close together, it is possible that the bubbles coalesce to form only one and in some cases actually form separately but expand themselves at the expense of a slight displacement from their original position. This movement will affect the smaller gaps mainly but the larger ones to a lesser extent. The overall effect would be a decrease in mean gap length and also in the number of bubbles (two opposing effects) which could explain the discrepancy observed. A more extensive investigation by Morrison et al[7] showed that the relative ionization (g_0/g_0^s) where g_0^s was the bubble density for a standard track, showed a dramatic departure from the $1/\beta^2$ law expected and indeed found from their mean gap length measurements. That this effect is due to finite bubble size is made plausible in the following way. To take a simple case, suppose

that no bubble centre-to-centre gaps greater than the minimum visible (α) are affected by the bubble size and that within a blob, all gaps are equal to α. It is likely, in fact, that this is very near reality, for actual bubble images have a diffraction halo causing some genuine gaps to be obscured. If one excludes this halo from the definition of α it is probable that only very few visible gaps will be altered by physical bubble size, the only effect being a slight adjustment of bubble positions within a blob. If we assume, further, that nucleation centres occurring less than a bubble diameter apart do not all produce bubbles, then - to a good approximation - all gaps within a blob are nearly equal to α.

On this simple interpretation, an estimate of the effect can be made. The density of bubbles per unit length with separations less than α instead of being $< d_{expected}$ where $d_{expected} = g(1-L)$ will be $d_{observed} = \frac{\bar{b}}{\alpha} \times H(\alpha)$ where $\bar{b}$ = mean blob length and $H(\alpha)$ = blob density. Thus, the observed bubble density $g_{observed}$ is $g_{observed} = d_{observed} + ge^{-\alpha g}$ the last term being the number of gaps/unit length

$$\text{Therefore} \quad R \left(= \frac{g_{observed}}{g} \right) = \frac{1-L}{\alpha g} + L \qquad \ldots.(4)$$

It will be noticed that as $g \to 0$, $R \to 1$, and as $g \to \infty$, $R \to 0$ as expected.

The effect is illustrated in Fig. 3.3. (a) where the ratio

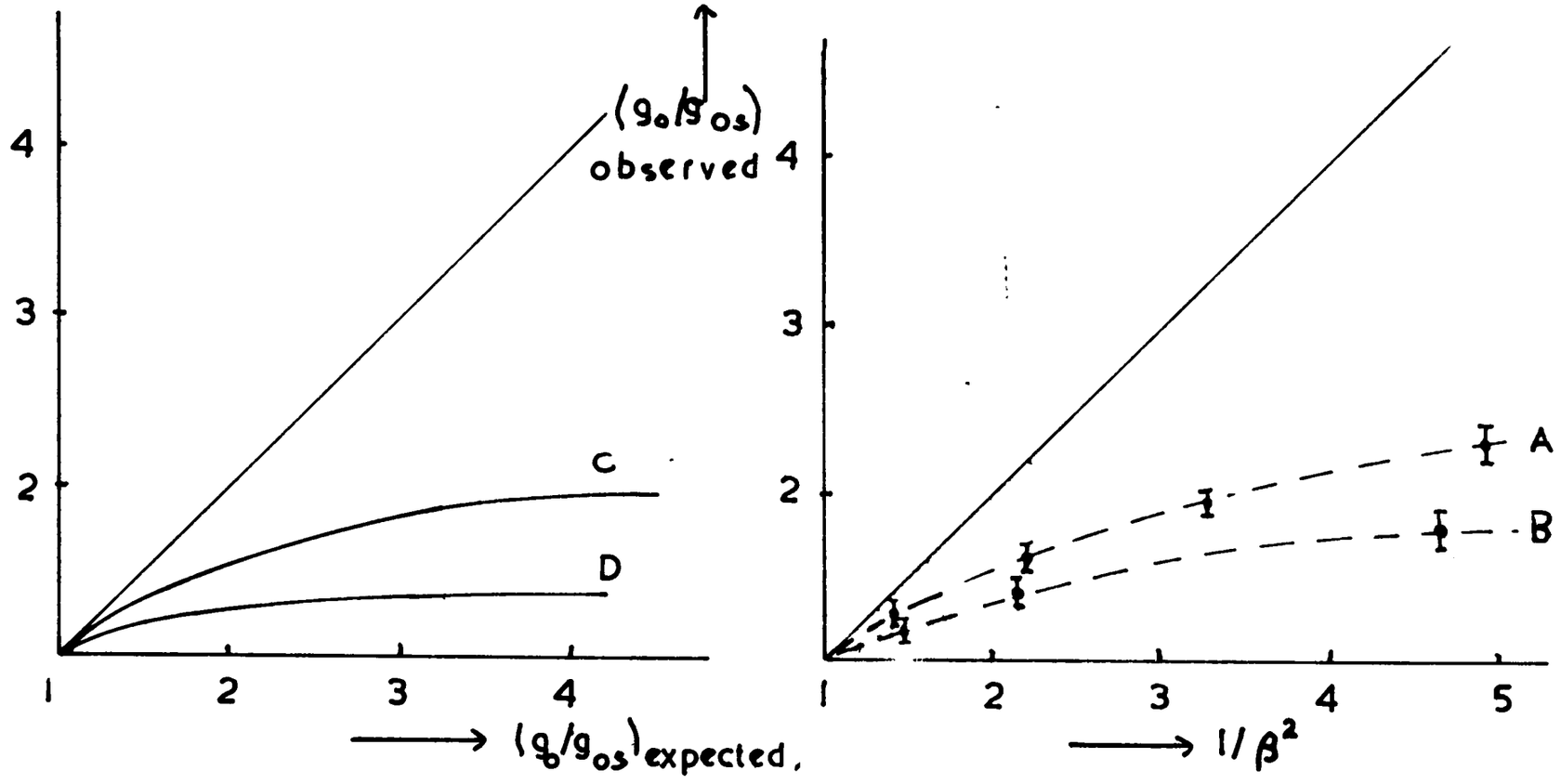

(a) (b)

FIG 3.3

A,B = Experimental points taken from ref.7-page 1440.

A for mean gap length of standard tracks of 350-450 μm (bubble diam.~160μm)

B " " " " " " " " 100-300 μm (" " ")

C calculated using m.g.l. 400 (" " =150μm)

D " " " 200 (" " ")

g_o/g_{os} (g_{os}= bubble density on standard track) is plotted against the value calculated from equation (4) for a variety of typical values of g_s. The curves are compared with those found experimentally by Morrison[7] and at least show the correct kind of behaviour.

It would seem, therefore, that bubble counting is not only very difficult and subjective, but almost certainly misleading. The distribution of gap lengths, the mean blob and gap lengths are, however, probably faithful estimators of the intended ionization, and this is the assumption that is hereafter made. A further basis for this arises from the result of Morrison that the mean gap length varies in the expected $1/\rho^2$ manner. A similar conclusion regarding the mean gap length has also been reached by other workers.[8,9,10] We therefore assume that real tracks can be regarded as ideal so long as we do not enquire too closely into the behaviour of the distribution law within the blobs.

Machine measurement of ionization

It appears from the foregoing that the image of one cell of a bubble chamber track has three quantities that may be measured: (a) gap length;

(b) blob length;

(c) blob width(α)

Measurement of (a) is sufficient to estimate the ionization, though either of the others provide additional information.

An inspection of Plate I leads one to consider the ways in which a set of rules may be applied by an automatic device, in deciding, for instance, the length of a particular gap. Two extreme possibilities are:

(i) the provision of a preset threshold with which the film transparency may be compared;

(ii) use of a more complex system in which the device surveys the film transparency over a finite area about the gap in order to decide its own criterion.

Clearly, the former is the simpler and the one that has been used in the present case. With sufficient care, it has been found possible to achieve some success in the form of an answer to the question: "bubble or gap?" at any point along a track. However, use of a system such as this leads to difficulties if a value for quantity (c) is required, as discovered in practice, and one is therefore left with a choice of the following methods of ionization measurement:

(i) mean gap length;

(ii) lacunarity;

(iii) gap-length distribution.

Lacunarity measurement is the simplest to perform as it does not depend critically upon the unambiguous identification of the blob-gap boundary. Consequently, this was tried first. It's success was limited by the requirement of a standard track having the same value for α (estimated from blob width) which reduced the meaning of a quantitative ionization estimate. The method finally adopted, therefore, was that of measuring the mean gap length (quantity (a)) though a method is described in Appendix B which could also be used. This uses the gap length distribution to determine the value for α which is then used, together with the mean blob length, to estimate the ionization. Reasons are presented in the analysis of the results obtained from the machine for a preference for this method.

The machine is now described.

REFERENCES TO CHAPTER III

1. D. V. Bugg: Proc. Nucl. Phys. 7, 1 (1959)

2. F. Seitz: Physics of Fluids. 1, 1 (1958)

3. Barkas: U.C.R.L. Report 9420

4. R. D. Fortune: C. E. R. N. 62-31 (1962)

5. W. J. Willis, E. C. Fowler & D. C. Rahm: Phys. Rev. 108 1046 (1957)

6. C. Dilworth, G. Mambriani, D. R. O. Morrison: Report by Ch. Peyrou: Int. Conf. on Instr. for High Energy Physics (Berkely, 1960)

7. C. Dilworth, G. Mambriani, D. R. O. Morrison: Nuovo Cimento X, vol. 32, 1432 (1964)

8. C. O'Ceallaigh: C. E. R. N. Report BS 11 (1954)

9. E. C. Fowler & D. H. Perkins: Phil. Mag. 46, 587 (1955)

10. B. S. Zorn & G. T. Zorn: Nuovo Cimento Suppl. 26 197 (1962

CHAPTER IV

The Gap Length Machine

Introduction

Though, as has been pointed out, the measurement of lacunarity ($L = \frac{\text{gap length}}{\text{all length}}$) was an unsuccessful way of estimating ionization, the method by which the measurements were achieved forms a logical introduction to the description of the machine. The evidence leading to the necessity to count gaps is then presented followed by the description of the way in which this was done. Results of mean gap length measurements are then presented and discussed.

In order to measure L, one needs a value of the total length of track (l_{tot}) and the integrated gap length (l_{gap}). Then the ionization should be proportional to Y where:

$$Y = \ln\left(\frac{l_{tot}}{l_{gap}}\right) = kg \qquad \ldots\ (1)$$

Two points should be noticed about (1). The first is that the constant of proportionality (k) contains two factors: one is α (see previous chapter) and the other depends on the chamber operating conditions. As neither of these quantities is measured, the results rely upon their constancy. Therefore measurements have to be standardized to beam tracks on the same frame (assuming that all beam particles are minimum

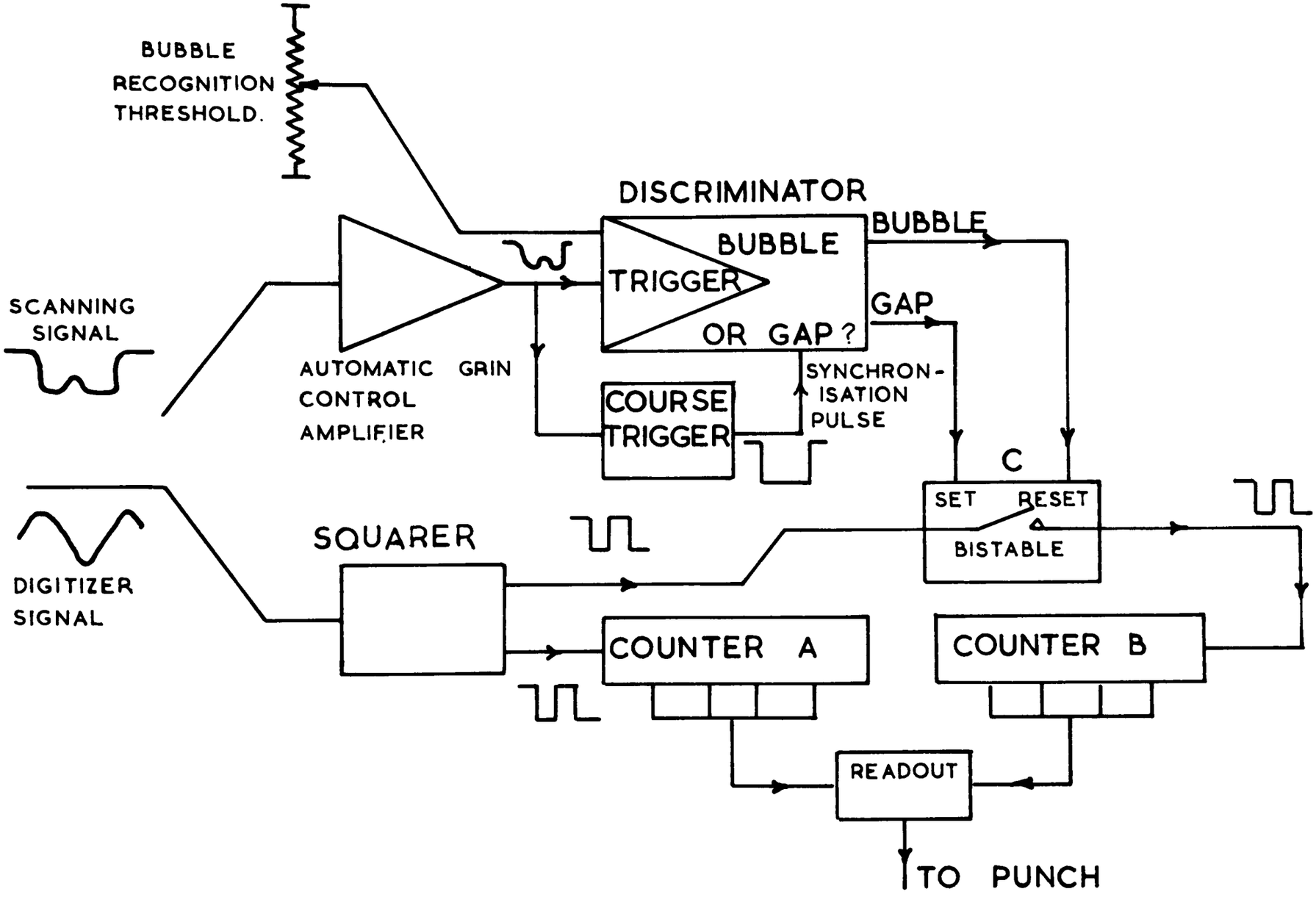

FIG. 4.1 LAYOUT OF MACHINE SYSTEM.

ionizing) when the two factors should cancel. The second point concerns λ. One may regard α as the apparent bubble diameter; in other words, if a gap can only just be seen between adjacent bubble circumferences, the distance between the centres of those bubbles is α. Further disregard of any gap of physical length x_o (distance between bubble centres $= \lambda + x_o$) necessitates the subtraction of a length x_o from all the other gaps when computing l_{gap} in order to preserve the validity of (1). The effective value of λ is then really $\lambda + x_o$. In the case of a machine, no such problem should arise since, it is hoped, the "eye" of the device should have to pass a distance $x_o/2$ from the nearest bubble circumference before recognizing the beginning of a gap at all, and the value of x_o should depend entirely upon the resolution between bubbles and gaps. It is therefore expected that (1) is relevant. It may also be noted that, if n_{gap} is the number of gaps comprising l_{gap}, an alternative estimate of ionization is:

$$g = \frac{n_{gap}}{l_{gap}} \qquad \ldots\ (2)$$

This is also only true with the above restrictions on λ but should hold good for a machine.

The Layout of the Machine

Fig. 4.1 illustrates in block form the operation of the device set up to measure l_{gap} and l_{tot} only. A scanning

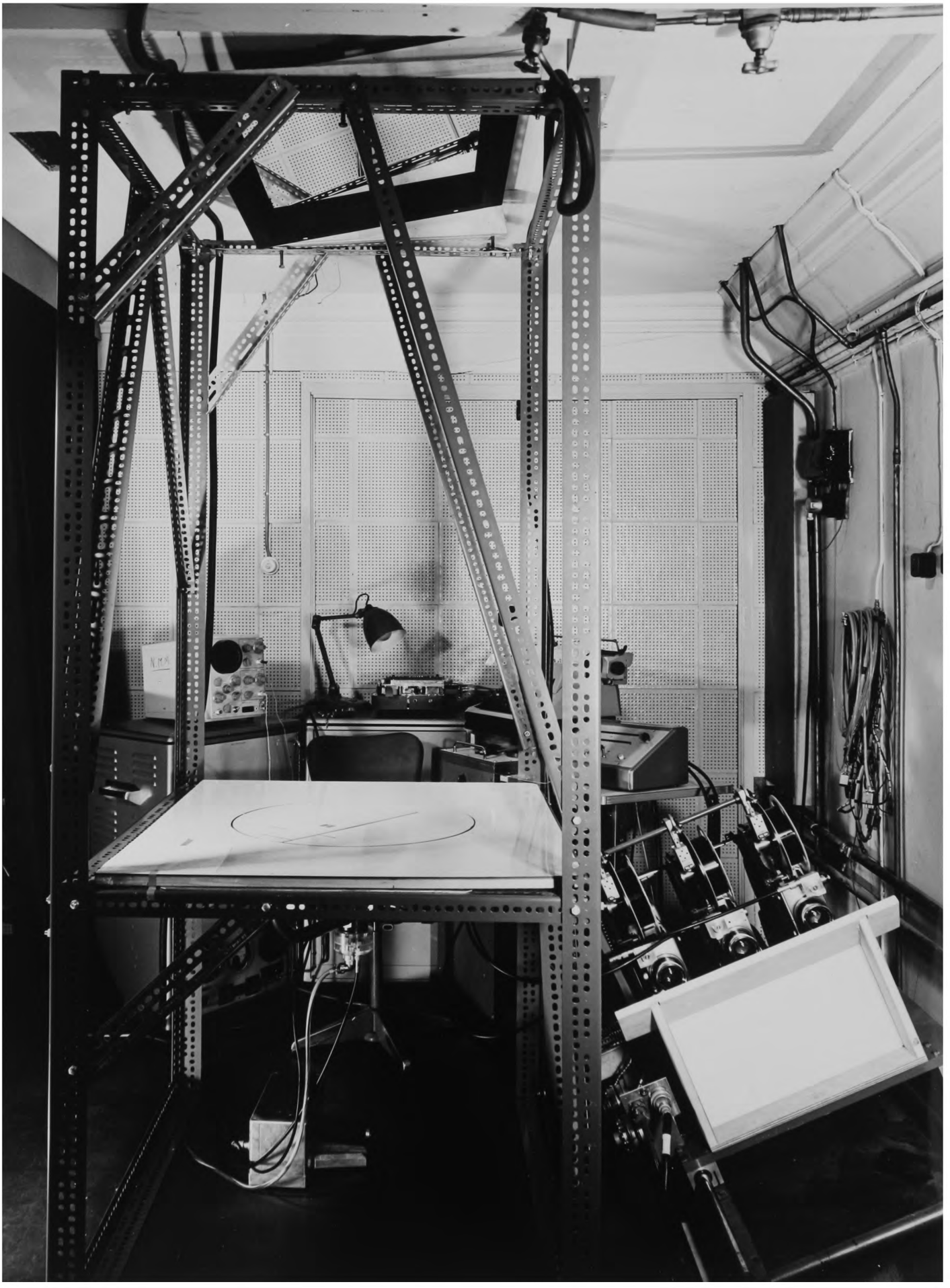

Plate I

head is driven along the projected image of the track on a digitized carriage. The digitizer generates a sine wave signal which is squared and provides the source of length measurement when pulses are stored in the counters. The scanning head scans the track approximately every millisencond, independently of the motion of the stage on which it is mounted. This rate is greater than that at which digits are ever generated, so that the head provides a quasi-continuous source of information. Counter A stores all counts as the scanning head is driven, but B is only allowed to accept signals when the information received from the head indicates that gap is being observed. Plate I illustrates the physical arrangement of the projection system where an image of the film - magnified about 25 times - is focused on a horizontal table. The machine is mounted at the centre of this table and is capable of rotation about a fixed vertical axis such that the digitized motion passes through it in any desired direction. In order that the cables may be passed from the machine to the electronic racks, rotation is restricted to 365°.

To drive the machine along a selected section of track, it is necessary to adjust the image position until the track passes through the axis of rotation at the beginning of the section. Rotation of the machine about its fixed axis now

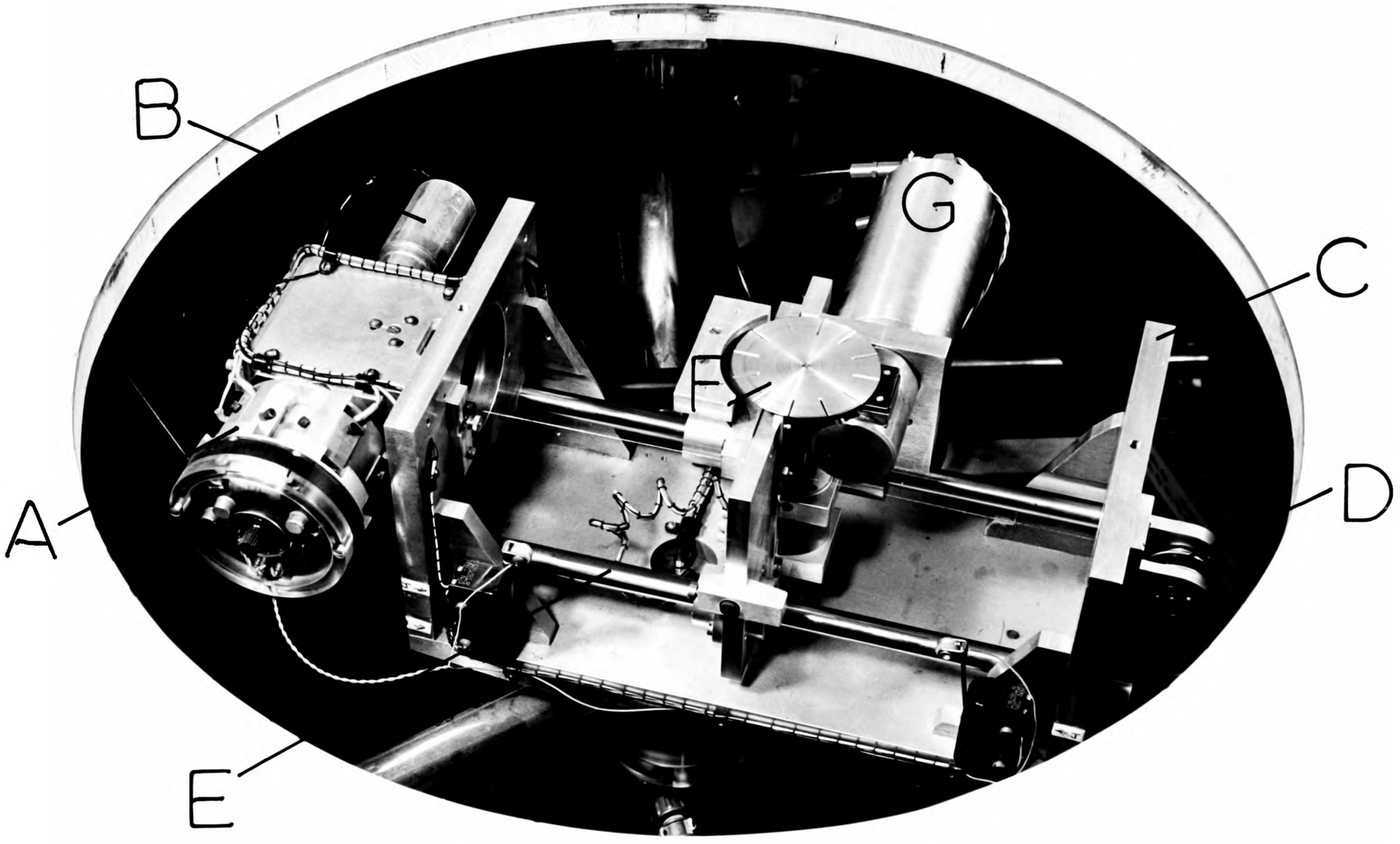

Plate II

enables the operator to drive the scanning head along the required direction, slight adjustments being necessary to allow for the curvature of the track. This is illustrated in Fig.4.2 where it will be apparent that the resulting measurements are effectively along a chord of track. The difference between arc and chord length is, however, not appreciable compared with the statistical error in one machine length of track ($\sim$15%). Movement of the film image is made possible through an electrically driven lead screw by moving the projector assembly bodily relative to the scanning table. Adjustment in the perpendicular direction is provided by a lateral movement of the projection lenses relative to the film.

The Digitized Drive

Plate II shows the digitizer (A) mounted on the end of the main frame (C) which supports the linear drive. Motion is powered by a 24 volt D.C. fixed field motor (B) whose speed is varied by a footpedal which controls (through a potentiometer) a D.C. voltage applied after a current gain stage of amplification, to it. Through an Oldham flexible coupling, the motor drives a worm and the digitizer. The worm, in turn, drives a wheel attached to a drum which unwinds or winds up a taut wire pulling directly on the moving stage. This is supported on high quality linear bearings (E) and is

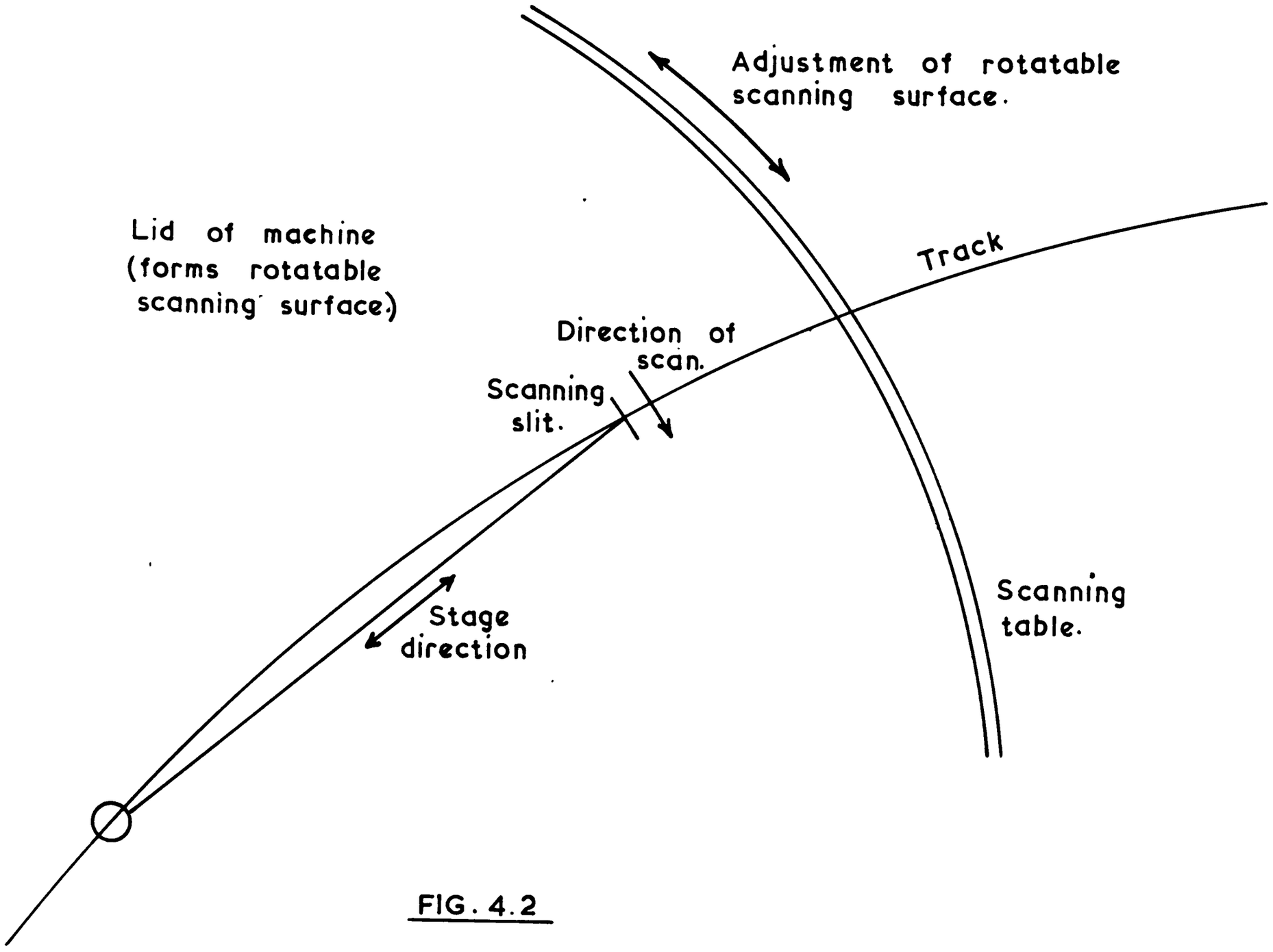
Adjustment of rotatable scanning surface.
Lid of machine (forms rotatable scanning surface)
Track
Direction of scan.
Scanning slit.
Stage direction
Scanning table.

FIG. 4.2

pulled one way by the drum referred to and the other way by a wire under a constant tension of about 2lb.wt. produced by the tensator spring motor (D).

The Digitizer

This consists of a pair of circular dural discs approximately 10cms. in diameter, placed concentrically and a few mms. apart. One contains 75 radial slots of equal area (about 3mm x 1mm linear dimensions) arranged around a circle (close to the circumference) having a uniformly angular displacement of 4.8^{o} and is driven about an axis through its centre by the D.C. motor (B) - see Plate II. The other disc is fixed and contains two slots geometrically identical to the others and disposed at such positions that one coincides with a moving slot whilst the other lies exactly between two further ones. It should be mentioned that the area of the slots is such that the "mark space" ratio on the rotating disc is approximately equal to unity. Light (produced by 6V bulbs which are under-run from a D.C. supply) is shone through the combined discs and the signals resulting from two solar-diodes placed behind the apertures in the fixed disc are roughly sinusoidal. Two diodes in antiphase are used (through a differential amplifier) in this way in order to reduce D.C. drift to a negligible amount.

The worm and wheel referred to has a ratio of 50:1 which together with the fact that one rotation of the drum (attached to the wheel) gives the stage its full movement of 15cms. means that a digit length of about 20μm is available if peaks and troughs of the sine wave are counted - as is the case. This corresponds to approximately 25 counts per bubble diameter giving ample resolution. In view of the size of gap to be measured (about 25μm on the film) and in order to make the best use of the digitization available, it is important to keep vibration to a minimum. The machine is therefore mounted in a basement room on a concrete floor.

The Scanning Head

In order to detect the presence of a bubble image in the scanning table, a mechanism capable of comparing the illumination on the track trajectory with that beside it is required. A possible means of doing this is to use two photosensitive devices placed in suitable positions. However, in order to reduce the effect of varying illumination and particularly to reduce the sensitivity of the machine to the accuracy of setting on the track, an A.C. scanning method has been adopted.At first a sambatron was used to sweep (by refraction) the focused image of the track across

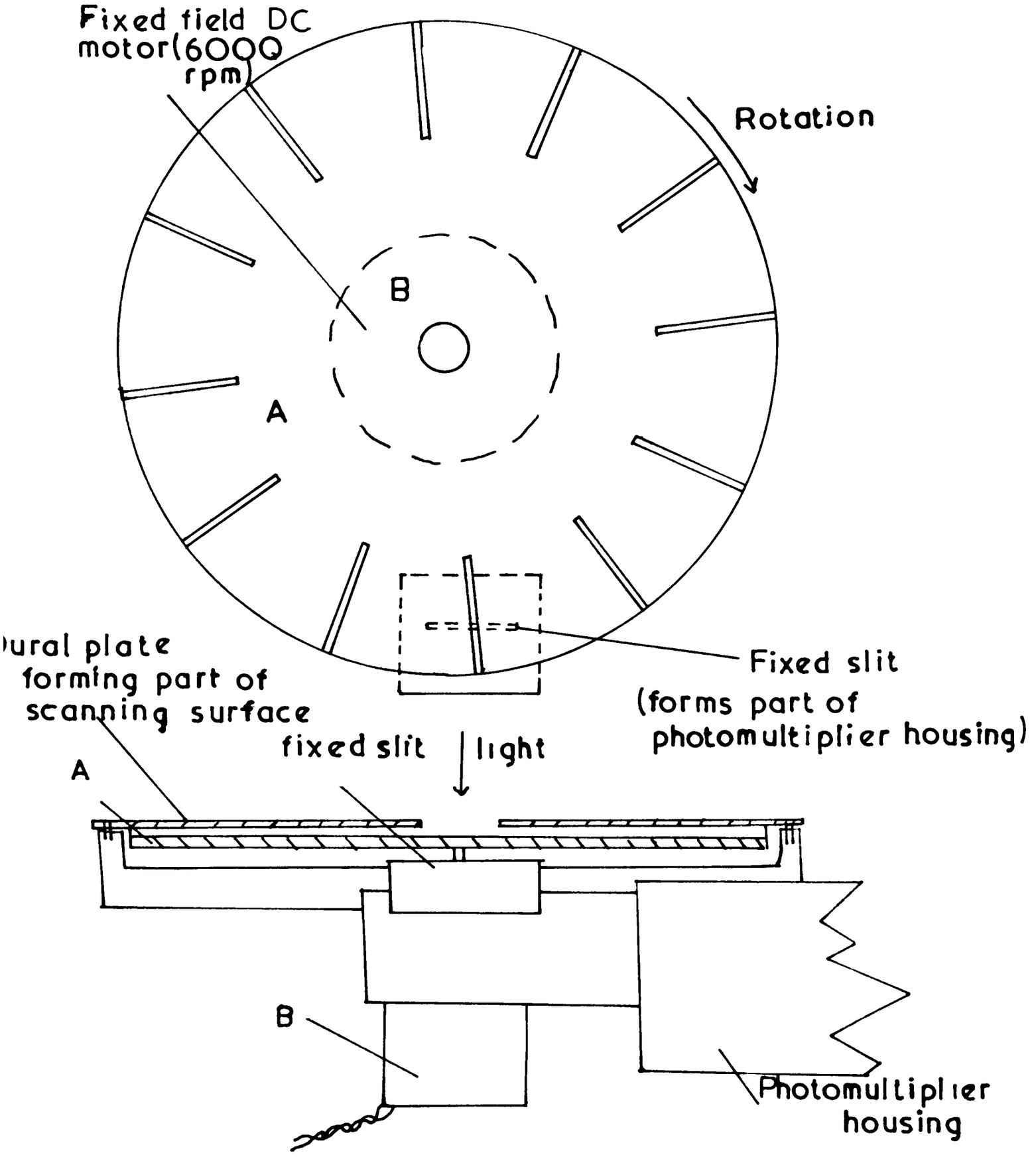

Fig. 4. 3- Rotating disc scanning system. (diagrammatic)

a fixed pinhole whose dimensions were small compared with track diameters. The sambatron (a rectangular section block of glass) was rotated at high speed about an axis parallel to the track and placed just above the scanning table. Though the device worked quite well, it was difficult for the operator to see which part of the track was being scanned at any time. Further, in order to obtain a scanning rate of 1,000 per second, since it was only found possible to use a two sided sambatron with ease, a motor with a speed of 24,000 r.p.m. had to be used. The necessary indirect drive (through a rubber belt) also proved to be an inconvenience at this speed!

To overcome these difficulties, a rotating slit method was used; Fig.4.3 illustrates this. A disc (A) having 12 slots equal in width (0.020 $\pm$ 0.005" - comparable with a track diameter) cut in the circumference with a slitting saw rotated in the plane of focus of the track image above a fixed slit whose direction lay perpendicular to the track. A D.C. motor (B) was used to drive the disc at 6,000 r.p.m. providing a scanning rate of about 1,200 per second. The actual relationship between this and the digitizer frequency depended on the speed of drive along the track. All relative sizes are illustrated in Fig.4.4 for the maximum

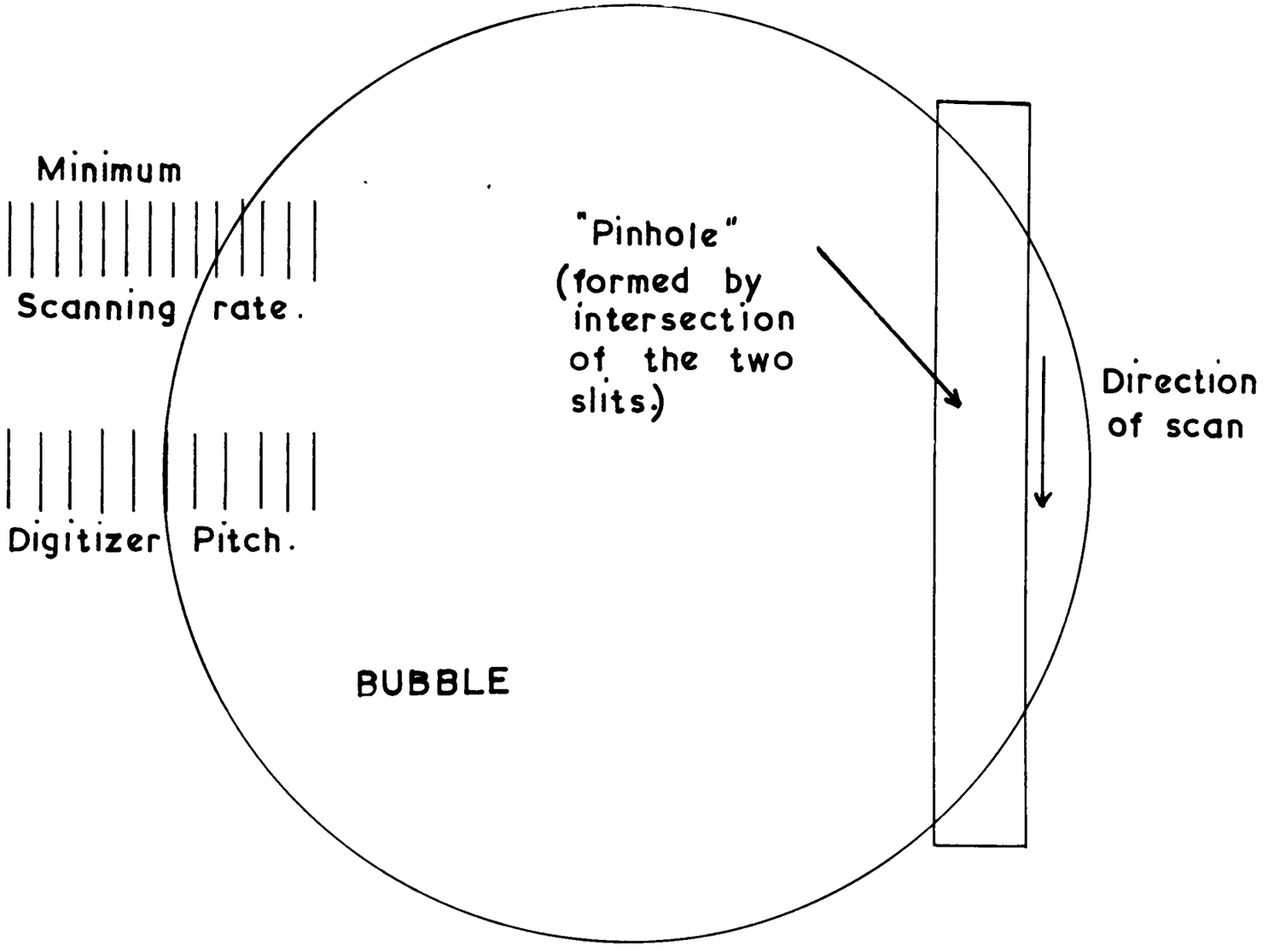

FIG. 4.4 Showing relative sizes for bubble of average diameter.

FIG 4.5 (a)

FIG 4.5(b)

driving speed. The width of the fixed aperture was set at about 0.0025" (about 1/10 track diameter) and placed as close to the plane of focus as possible. The perpendicular intersection of the two slits formed a pinhole of suitable dimensions that was drawn across the image of the track for a distance defined by a course aperture cut in a thin dural plate situated just above the scanning disc but still approximately in the focal plane. This served both to render the image visible (as it formed part of the scanning table surface) and to provide a boundary for the scan unaffected by parallax caused by varying angles of illumination. The arrangement is illustrated in Fig.4.3 and shown in Plate II (with the scanning surface removed) where (F) is the scanning disc. A photomultiplier (housed in the box (C)) which allowed light in only through the fixed slit analysed the light coming through the "pinhole".

The Photomultiplier Signal

Typical signals which resulted from this system are shown in Fig.s 4.5(a) and (b). The first is the kind resulting from a bubble and the second from a gap. In order to detect the presence of a bubble or otherwise, the voltage waveform from the photomultiplier collector is compared with a preset D.C. level. Thus it was important that the bottom

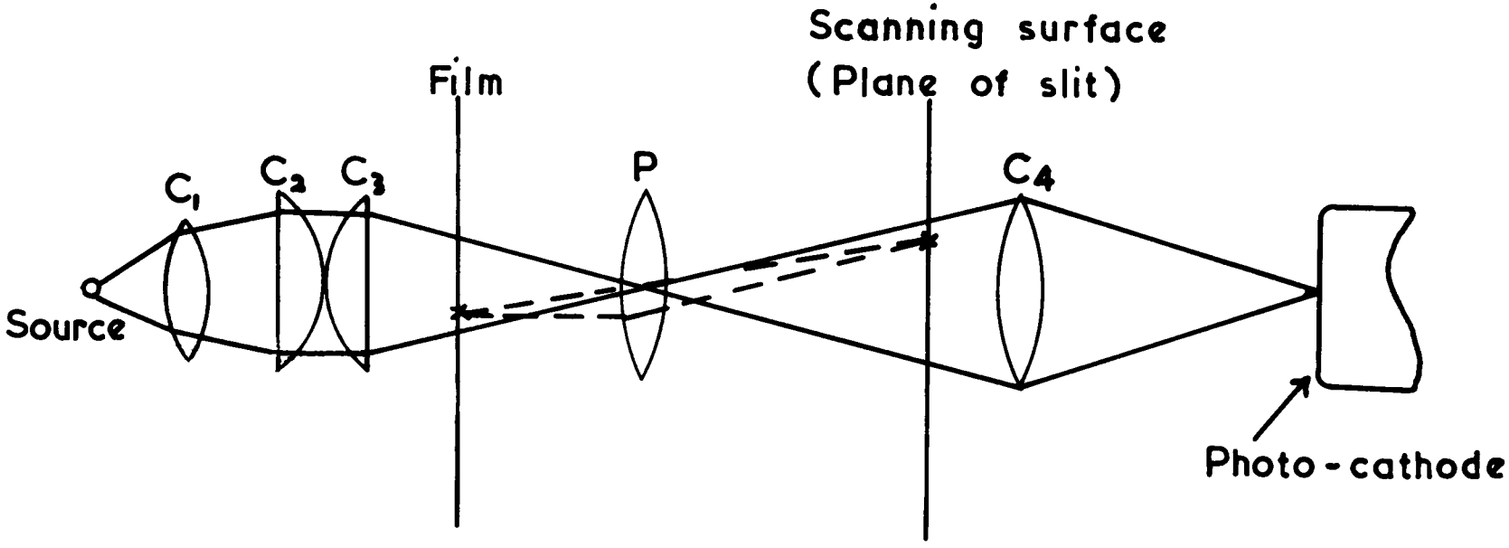

FIG. 4.6(a) General Optical Arrangement.

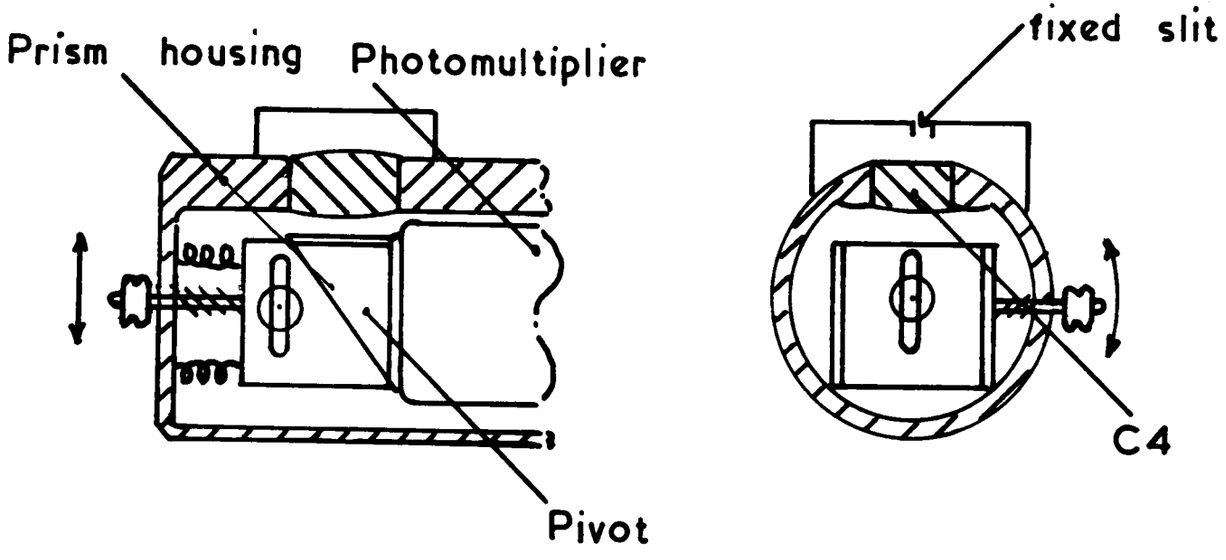

FIG. 4.6 (b) Prismadjustment.

of the signal (which was clamped) should be as flat as possible. Great difficulty was experienced in achieving this but its importance cannot be underestimated. The main contribution to unevenness came from the shape of the fixed slit whose width needed to be constant to within a few percent of 2 thousanths of an inch. Mechanical slits were abandoned as was one photo-etched in copper sheet 0.002" thick; but simple photographic reduction of a straight line of thickness 1/64" onto a fine emulsion with glass plate backing, proved to be quite successful.

Optical Arrangement

Fig. 4.6 shows the simple geometrical optics of the machine. Two main features should be noticed. It was important to channel as much light as possible into the photomultiplier since the small pinhole size meant that shot noise was a considerable problem. Consequently, the lens system C_1, C_2, C_3 was used to produce an image of the filament of the Aldis projector 500W bulb near to the principal plane of the projection lens P. This image was then refocused onto the photocathode by a small perspex converging lens C_4 turned down to fit into the photomultiplier housing. The result of this was that, to a good approximation, the position of the pinhole with respect to the photocathode

made little difference to the signal current, and variations in sensitivity across the photosurface were unimportant. In order that the electronic scanning should be effective, lens P (focal length 208 cms. at f 5.6)produced a focused image of the film in the slit plane (i.e. the scanning table).

Careful adjustment was made to ensure that the plane of P was exactly parallel to the film; for any slight tilt would be magnified 25 times (the linear magnification of the system). The photomultiplier used was type 9524S made by E.M.I.Limited and was chosen for its very small dark current. It was an end window tube which, for physical reasons, had to be placed horizontally in the machine necessitating the insertion of a small 45° prism between C_4 and the cathode. Silicone grease was used to form an optical junction between the tube and prism, and adjustment of the position and angle of it (illustrated in Fig.4.6(b) were found to be desirable.

The Electronic System

The description of the electronic system consists of two parts: The counter and readout systems and the analysis of scanning.

The counters were of standard "ripple carry" design

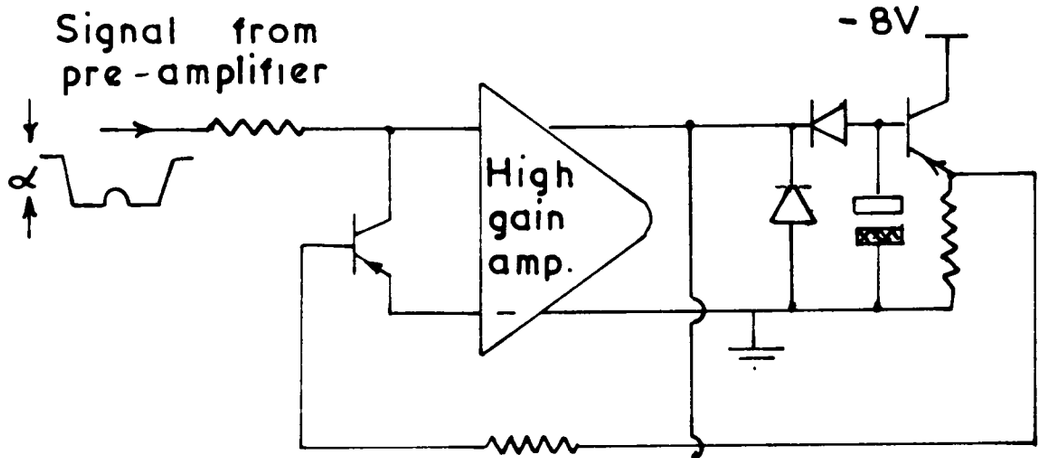

FIG. 4.7 (a)

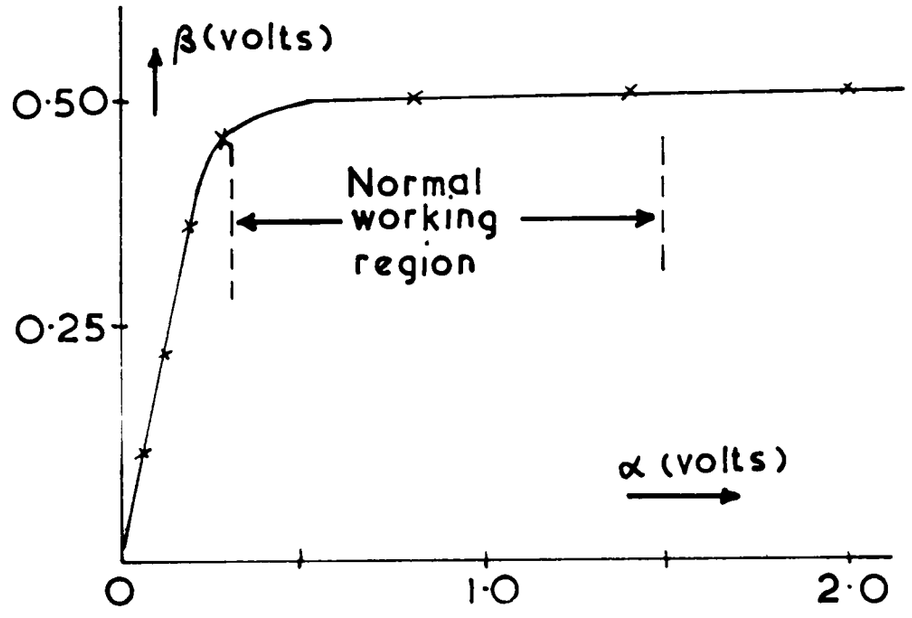

FIG. 4.7 (b)

similar to those used on the conventional measuring machines. The readout system did, however, have some original features which are omitted for brevity.

Fig.4.1 indicates the various electronic operations that were performed on the basic signal from the photomultiplier. In the early stages, careful handling was required as the collector of the tube behaved as a source of very high impedance. After preamplification, the stages immediately following were aimed directly at "cleaning up" the signal by squaring with a Schmidt squarer having very low backlash so that even a small bubble signal would cause triggering.

In order to achieve this, considerable amplification was required. Overall variation of light intensity was appreciable in practice and so presented a problem. This was overcome by the crude kind of automatic gain control illustrated in Fig.4.7(a). Amplification of the signal was followed by a full wave rectifying circuit which measured the height of the output. The D.C. level resulting was fed back in a negative sense onto the base of a transistor which formed one arm of a potential divider at the input to the amplifier. In practice, two such stages were employed in series, and the resulting gain control is demonstrated in

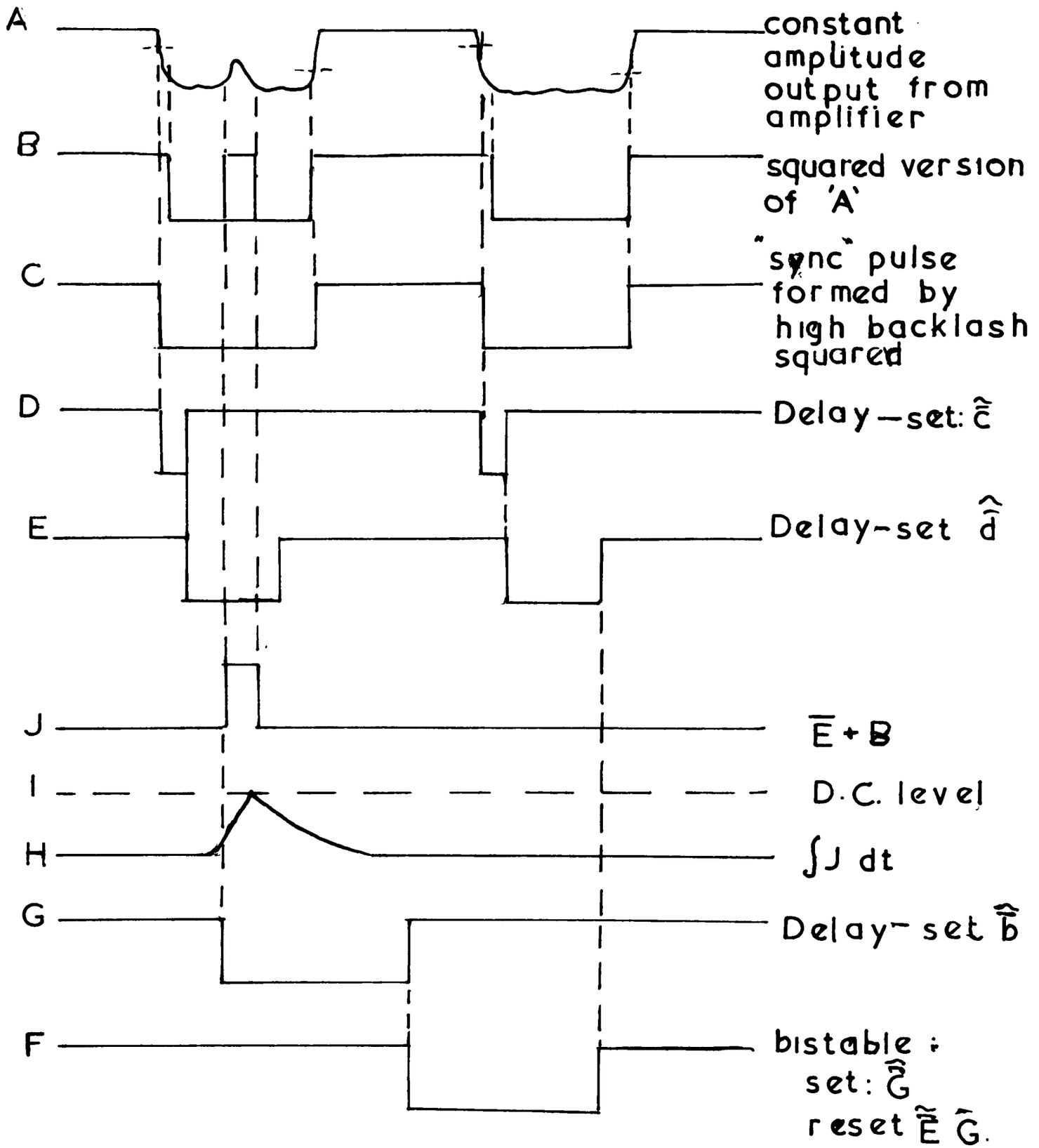

FIG. 48 -DISCRIMINATOR LOGIC

Fig.4.7(b) where the input voltage amplitude versus output is shown. Typical input signals varied in voltage from about 0.3 to 1.5V amplitude for optimum E.H.T. setting on the photomultiplier, so it is seen that the output was easily kept constant at 0.5V amplitude. For input signals above about 2.5V, however, considerable distortion of the higher voltage part of the waveform became apparent.

Bubble Discrimination

Fig. 4.8 illustrates the further means by which the bistable circuit (C of Fig. 4.1) was set or reset according to the presence or not of a bubble in the scan, after the final amplification and squaring of the raw signal. An explanation of the Boolean symbols used in Fig.4.8 is required. The product of two signals (e.g. A.B) implies the logical AND and the addition implies OR. Negative logic is assumed, in other words a signal having a low potential is assumed to be present. A tilde above a symbol indicates its A.C. leading edge, and a bar and tilde the falling (i.e. rising potential) edge. A contrast may be noticed between signals B and C which were both squared up versions of the basic input A.B attempted to reproduce details of the trace whilst C was merely generated as a synchronization pulse and therefore simulated only the gross

features of the signal. Its sole purpose was to provide a gating signal E which focused further attention upon the expected bubble region of the scan. As D and E which defined this region were produced by monostable circuits with a preset time constant, the machine was, to some extent, at the mercy of variations of scanning frequency. However, modulation of as much as 20% could be borne without serious consequences, where 10% was the largest that was ever noticed in practice.

Measurements of Lacunarity

In order to test the machine's performance, use was made of the fact that the ionizations of all beam tracks on one frame should be equal within statistical expectation. Any deviation would be due to either a variation in chamber conditions of temperature and pressure, or in a systematic unreliability in the sensitivity of the detection apparatus. Fluctuations in bubble density were to be expected from frame to frame, so measurements of beam tracks were all normalized to the average for the frame. It may be remembered that the illumination of the chamber occurred in two halves with one flash tube serving each. As a result, therefore, film exposure usually was less for the region furthest from the camera. Thus, four machine sections of beam were measured

FIG. 49(a)

Distribution of Ln(L)

(L=lacunarity)

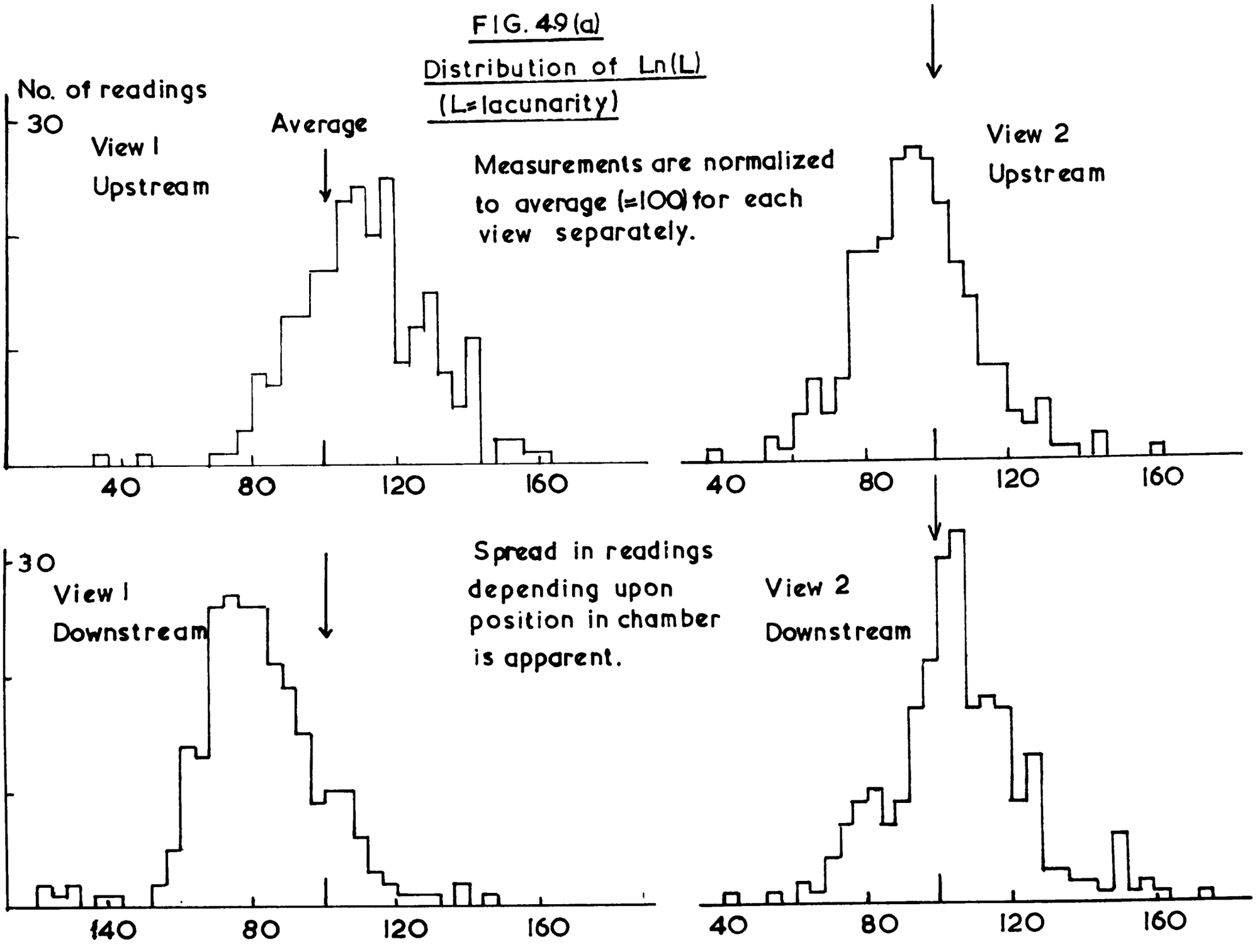

FIG. 4 9 (b)

Mean gap length measurements.

Distributions are normalised to the average for the view.

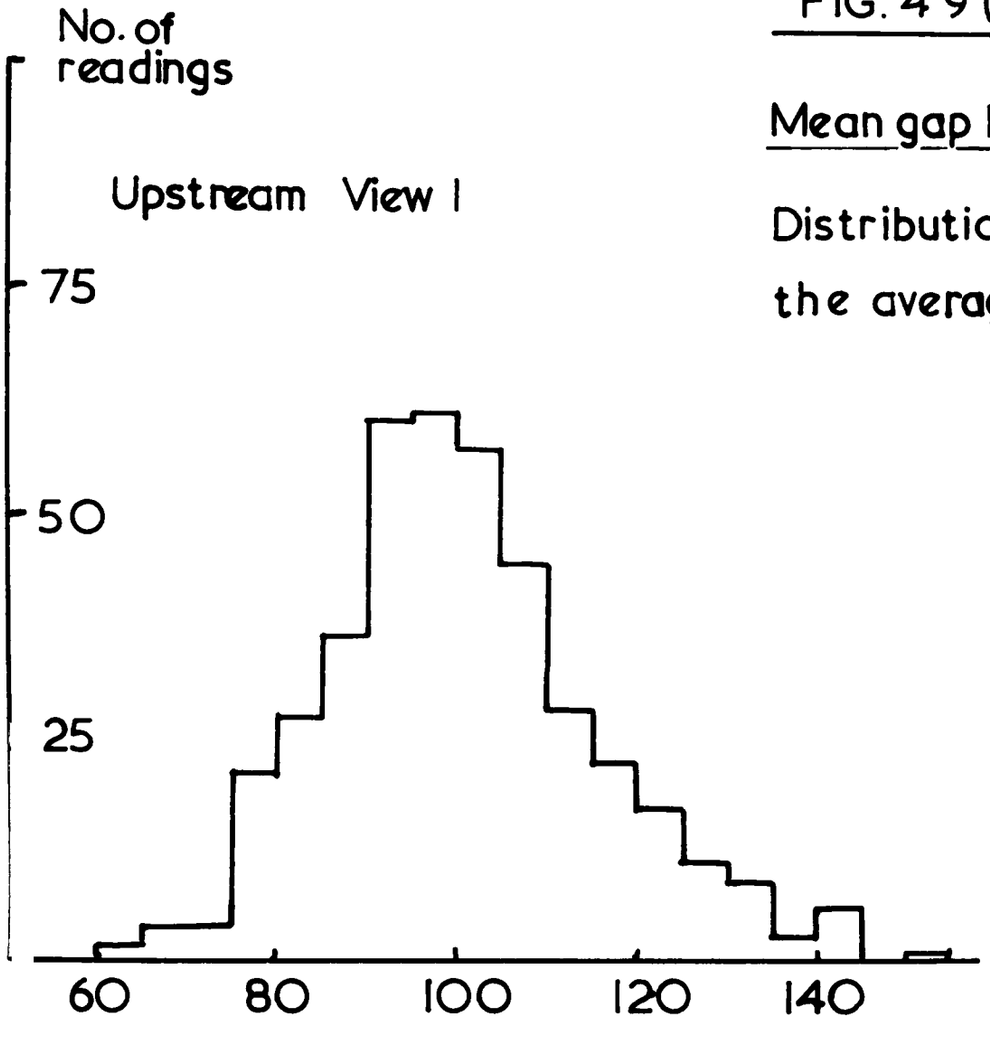

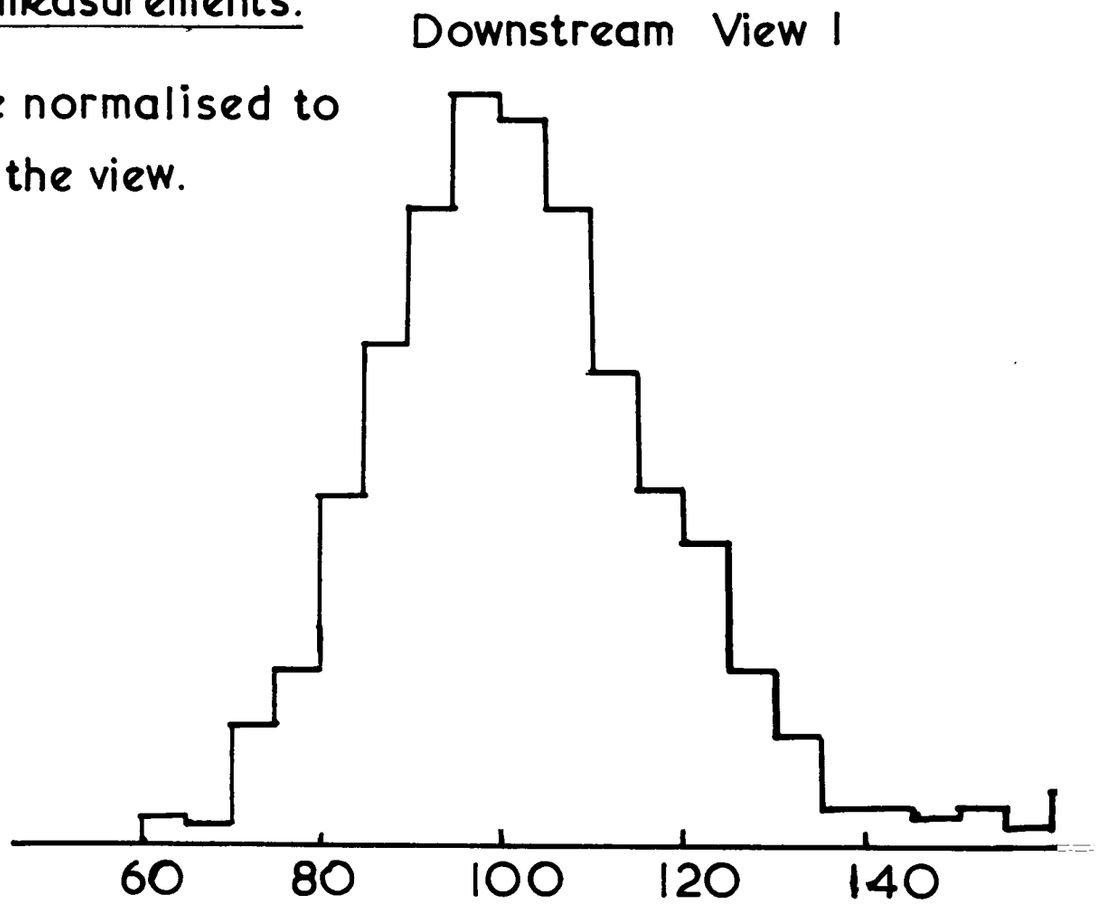

in each half separately in order to attempt to ascertain the effect of any such variation. In all 68 frames were measured and the resulting distributions presented in Figs.4.9. In Fig.4.9(a) the"downstream" and "upstream" tracks are drawn separately for each of views 1 and 2.

Measurement of λ

From this, and from the fact that many odd results for secondary tracks (relative ionizations of 0.6 or less) were often obtained - notably for tracks near the edges of the illuminated region - it became clear that measurement of lacunarity was insufficient without some estimate of the parameter λ. It was thought possible to do this by measuring the track width as illustrated in Fig.4.8 (signals H and I). A Miller operational integration amplifier was driven by the squared up bubble signal to produce a waveform whose height was proportional to its duration, and therefore to the effective track width. The D. C. level (I) measuring this height was displayed on a voltmeter and allowed to vary with time constant determined by a resistance and capacitor. However, two main difficulties arose:

(i) The introduction of such a time constant was inconsistent with the philosophy of variable speed of stage drive

(ii) In order to utilize the information provided, an analogue to digital conversion would be necessary.

Some attempt to overcome varying track width was made by feeding the voltage I in a negative sense directly onto the bias input of the trigger circuit producing signal B such that the apparent width of track remained within controlled limits. This did not overcome the fundamental difficulty implicit in (i) whose effect was particularly noticeable on short sections of track containing mostly gap. In view of this, hope of measuring α directly was abandoned. A method of determining ionization independently of α is by mean gap length as discussed in the previous chapter and was the method finally accepted.

Counting Gaps

It should be pointed out that the decision of the machine on the state of track (bubble or otherwise) has so far been by means of the bistable circuit C in Fig.4.1 whose waveform is represented by F in Fig.4.7. This was set or reset on every scan (i.e. up to 1,200 times per second) independently of movement along the track of the scanning head and at the edges of blobs, therefore, any hesitation between conflicting decisions was bound to cause many changes of state. In order to measure mean gap length, it

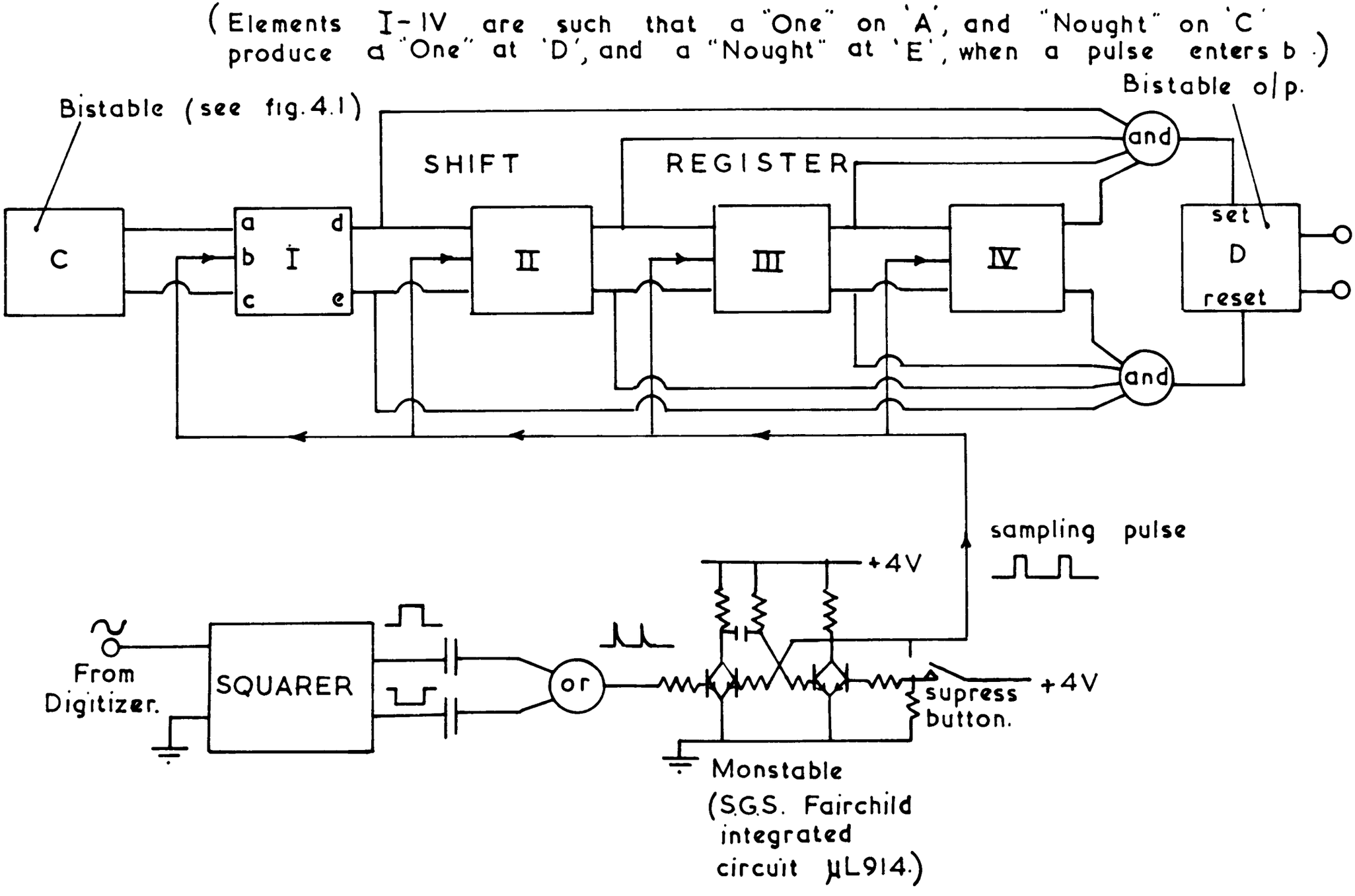

FIG. 4.10 Shift register and driving circuit.

was necessary to count gaps (a severely quantized measurement) and a profile of the track had to be made available with only one change of state at each blob-gap boundary. To achieve this, a coupling of information from the gate F (Fig.4.8) with the digitizer was brought about. The logical demand that a gap only be recognized when n consecutive digitizer signals occur during gap type scans, and the converse for recognition of a bubble was fulfilled by a shift register. A simple representation is given in Fig.4.10. Digits were fed into each of the n bistable elements simultaneously, but their effect upon a particular stage was governed by the state of the previous stage. At the input end, gating was effected by C itself. Thus, with C in the bubble position, a "one" was fed into the chain, and all other states were pushed along one place. If n consecutive "ones" occurred, coincidence (all stages set) resulted in the setting of the output bistable D in Fig.4.10.

With this arrangement, the digitizer signal behaved as a sampling pulse generator which also formed the basic drive for the whole electronic system. Thus, at a movement of one digit (20μm) the state of the track was inspected, and the result stored in the shift register. As long as no movement took place, no change in D could occur. It was found satisfactory to use a value for n of 4. (It may be noted that a

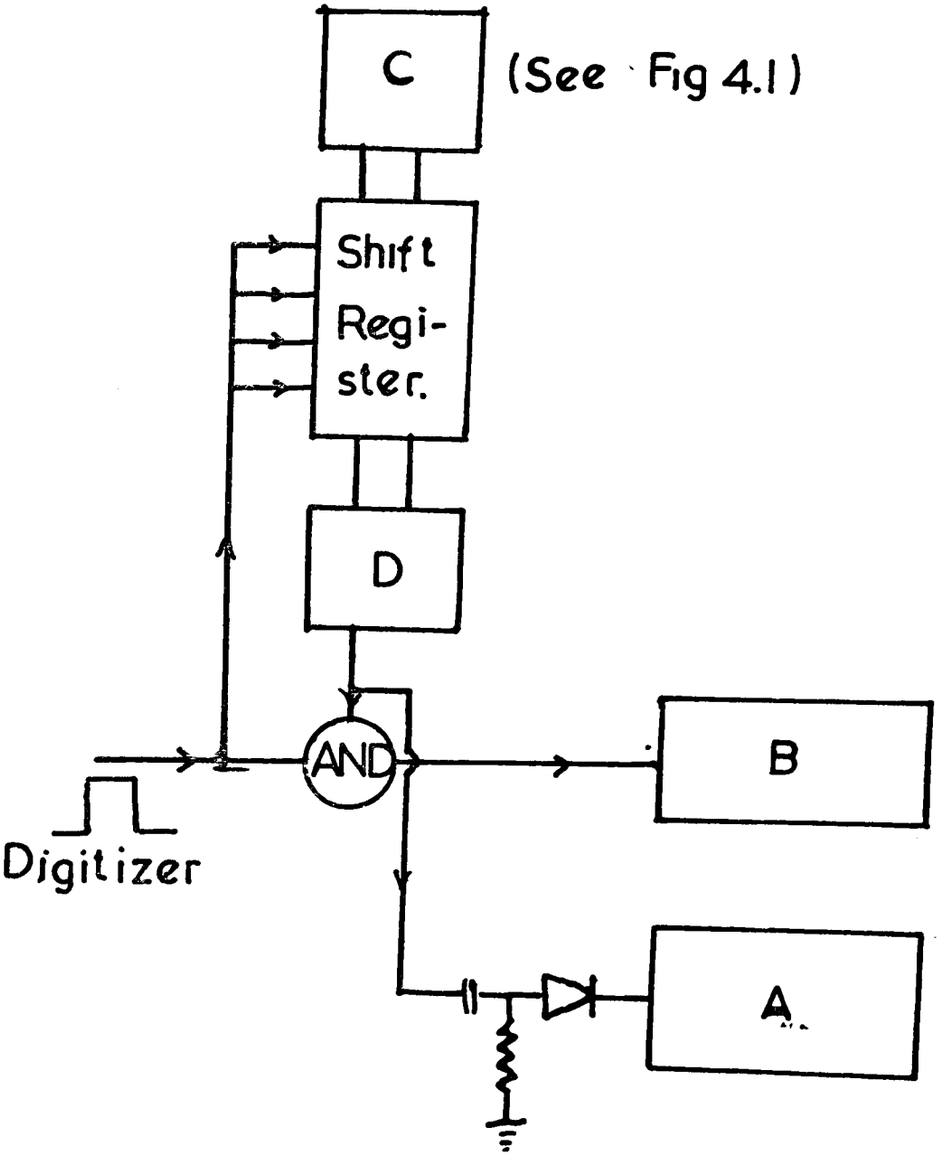

FIG 4.11

bubble diameter was approximately 30 counts.)

The present layout of the machine is shown in Fig.4.11 where it is seen that counter A simply registers the number of changes of state of bistable D (giving n_{gap} in A).

Calibration of internal errors

A simple way of testing the consistency of the readings obtained from the device was to make several measurements of the same section of track. For this purpose, a beam track of good quality was selected and measured 25 times. The resulting mean gap length of 59.3 counts had a standard deviation of $\pm$ 2 counts which is satisfactory when one considers that four counts are required to identify both beginning and end of each gap. The number of gaps was 45.

A further test of the accuracy of the measurements was carried out as follows: each section of track was measured when the machine was driven in each direction. Two answers (x_1 and x_2) for the mean gap length resulted along any one section. The plot of $\frac{1}{2}(x_1-x_2)$ is shown in Fig.4.12 where the Gaussian curve superimposed has a width of 2 counts. This is in agreement with the previous result, and it is seen from the distribution that most measurements agree within six counts. As an average value for the mean gap length is at least 50 counts, the error is less than 4%

TABLE I

Gap by Gap Measurement of Beam Track

Gap	Length *M_1	M_2	M_3	M_4
1	22	42	48	25
2	58	31	27	25
3	42	49	59	70
4	7	9	46	52
5	88	91	83	87
6	279	266	(32 (239	31 239
7	121	130	119	114
8	13	10	Missed	14
9	55	57	58	50
10	17	31	18	17
11	38	36	47	51
12	18	14	Missed	
13	Missed	7	8	Missed
14	126	133	131	130

Gap	Length M_1	M_2	M_3	M_4
15	162	162	152	153
16	54	56	53	55
17	57	50	53	44
18	74	) (	67	64
19	Missed	)110(	Missed	3
20	50	) (	50	50
21	90	85	81	89
22	18	19	23	14
23	21	25	17	17
24	24	37	23	17
25	61	53	58	58
26	44	45	39	32
27	36	34	40	38
28	14	14	14	10

	Length M_1	M_2	M_3	M_4
29	136	139	135	137
30	28	27	15	28
31	56	59	54	51
Number of gaps	29	30	30	30
Length of gaps	1709	1821	1794	1765
Mean gap Length	59	61	60	59

*M_1 = First measurement, etc.

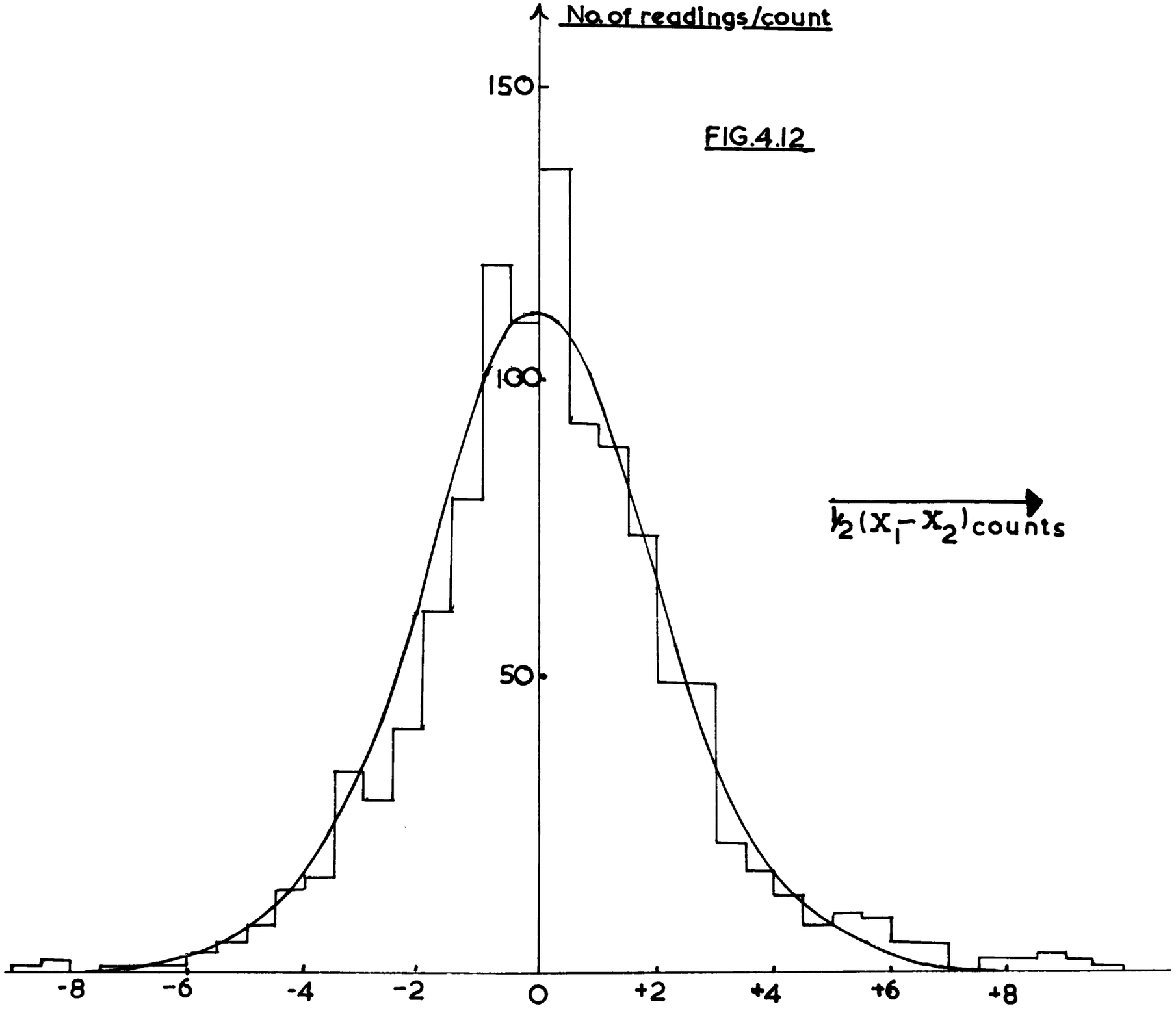

FIG.4.12

The symmetrical nature of the distribution in Fig.4.12 is evidence that no significant hysteresis exists in the stage drive.

The most serious source of error was in the inconsistency in the number of gaps. The origin of this was investigated by measuring a section of track gap by gap. The counters were read out onto tape after each gap, and the process repeated four times in all. The results are summarized in Table I where it is seen that the measurement of any one gap is quite reproducible in most cases. Lapses amounting to 25 counts in a gap occasionally arose and sometimes resulted in the complete loss of gaps as short as this. Such inconsistencies certainly arise in microscope measurements, but the similar occurrance in an objective device of this nature is puzzling. It is possible that the shadowy - somewhat uncertain - grain structure that is evident in the shorter gaps may account for this loss since the positions at which the track is sampled vary from measurement to measurement.

Calibration of external errors

The spread in measured mean gap length on a single frame gives a meaningful estimate of the error of measuring one section of track, since - provided chamber conditions of

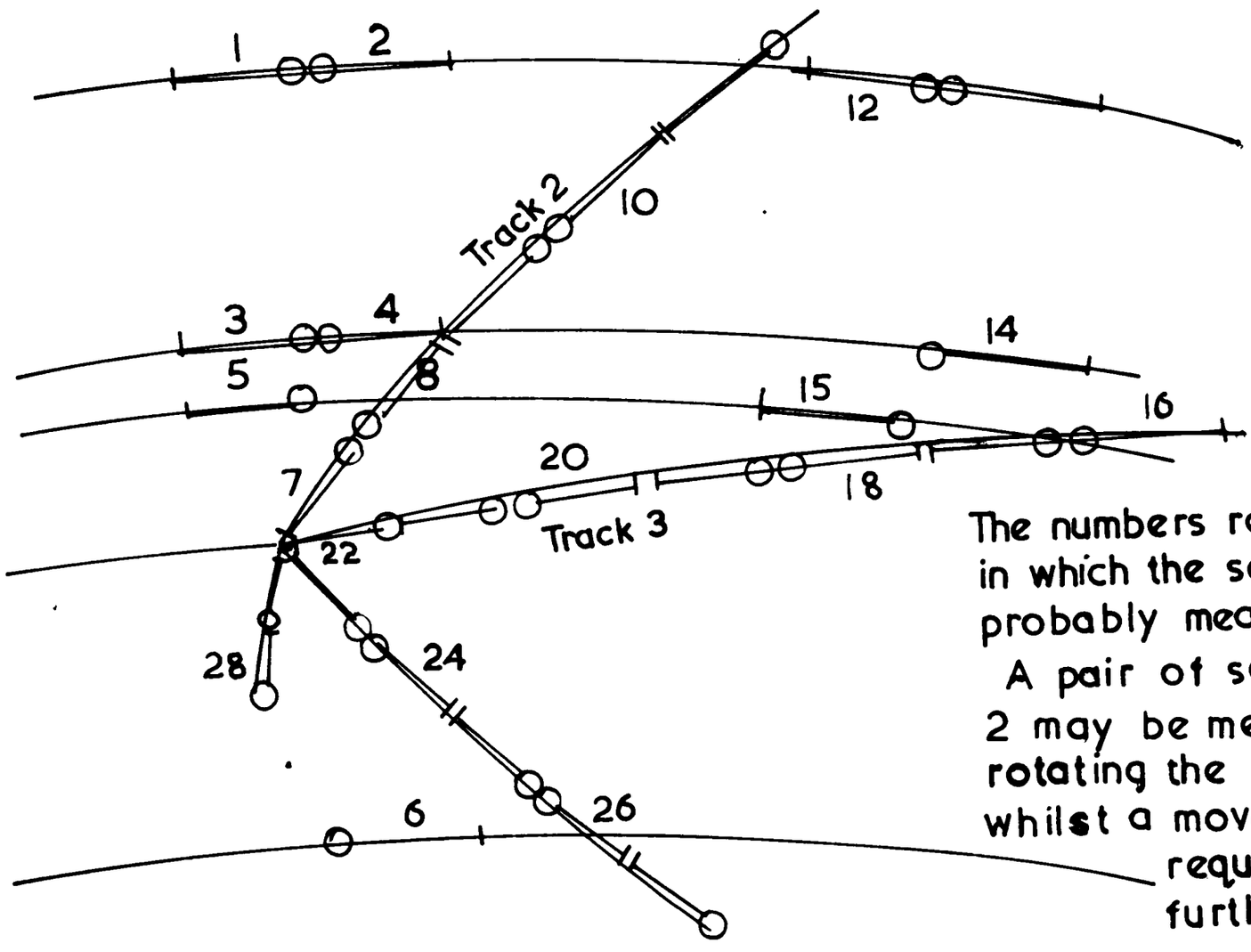

The numbers represent the order in which the sections are probably measured.

A pair of sections such as 1 and 2 may be measured by rotating the device though 180° whilst a movement of the film is required to measure any further sections.

Fig 4.13 - Measurement of a four prong event.

temperature and pressure do not vary with position - the expectation value for this quantity is the same on all tracks. Tracks were selected from both ends of the chamber and their measurements - normalized to the average value for the whole frame - plotted separately. The distributions are shown in Fig.4.9(b) where they may be compared with the lacunarity measurements of 4.9(a). The width is noticeably reduced and this is probably a consequence of the absence of the effect of a spread in α. It is further noticed that the measurements from either end of the chamber peak at the same value which suggests that the effect of varying illumination is insignificant.

Errors were calculated from the observed spread in the repeated measurement of sections of track and from the number of gaps. The average value for beam tracks estimated in this way was about 15%. This figure appears to agree quite well with the observed spread of Fig.4.9(b).

Measurement of the Four Prong Events

Measuring Procedure

Fig.4.13 illustrates the order in which the various track sections were measured on a typical event. The circle represents the centre of the rotatable part of the machine and the bar is the far end of the stage drive. Each section

was measured twice, and the process always commenced at the centre (circle end). In this way, any hysteresis effect resulting either from a machine fault or a greater difficulty in following the track in one direction would have shown up. At least six beam track sections were measured at the upstream end of the chamber and four at the other. This was purely a matter of convenience, though the input programme which processed the results allowed for interruption of measuring at any time in order to measure a beam track. Every track was measured on the best view (that is the one on which the number of crossing tracks was least, or where the flash gap was least significant) and any secondary track whose identity was sought was measured on one other view together with a further four beam track sections. Where a track was impossible to measure (because of crossing tracks etc.) a symbol was typed onto the output tape to signify its omission. A complete set of such symbols was available for indicating the change of section, track or view, etc, and the processing programme checked the format of each event carefully so that no misidentification of tracks was possible. Momentum measurements had taken place at a previous time so that the correct matching of the ionization measurements with these was of paramount importance. The

former had taken place in an order which depended upon the presence of stops, scatters, etc. on the various tracks. For simplicity and convenience, the rule adopted in the latter measurements was that tracks should be taken in strict clockwise order (at the production vertex) on the best view (i.e. the first measured). Appendix C describes the method of stereo sorting which was adopted as well as the corrections that were subsequently employed to allow for track dip, foreshortening and depth in the chamber.

Crossing Tracks

The selection of beam tracks was usually quite simple as there were usually more than the required minimum number of 10 good clear sections. The same situation did not exist for the secondary tracks, of course, where one had to use as much of them as possible in order to maintain statistical accuracy. It was therefore necessary to be able to suspend measurement whilst traversing crossing tracks, dirty marks, flash gaps, etc. This was achieved by a push-button held in the hand which would impose an inhibit upon the digitizer circuitry when pressed as illustrated in Fig.4.10.

Faint Tracks

The photomultiplier signal was on display to the

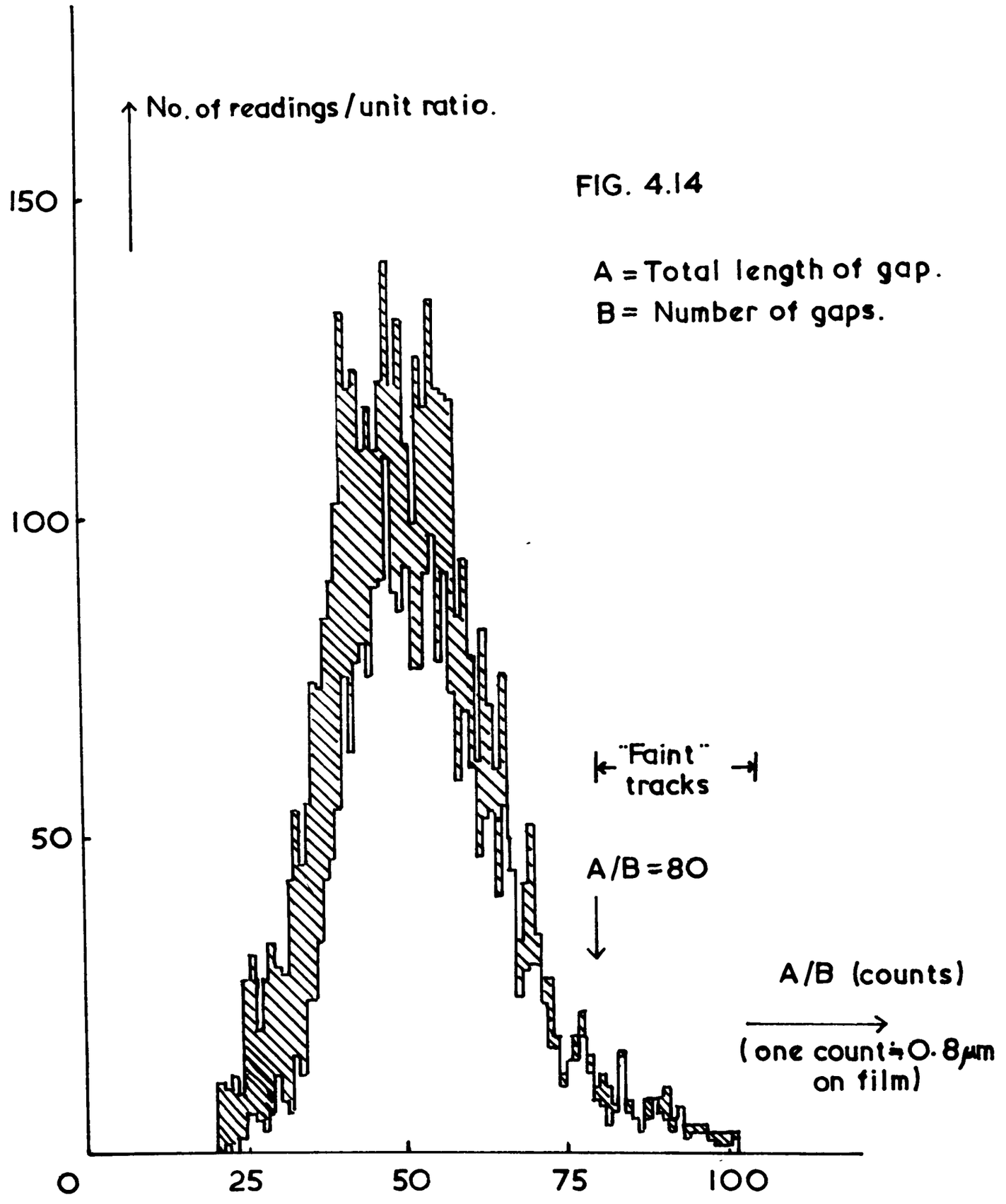
No. of readings / unit ratio.
150
100
50
0
25
50
75
100
A = Total length of gap.
B = Number of gaps.
"Faint" tracks
A/B = 80
A/B (counts)
(one count ≒ 0.8 μm on film)

FIG. 4.14

the operator throughout the measurements. Gross malfunction of the apparatus was occasionally indicated by its behaviour. Some check on performance was also provided by the state of the counter display after measuring a section of beam track. However, the estimation of whether a given section of track was too faint for the machine was somewhat arbitrary.

The effect of faintness would be to cause a drastic decrease in the apparent number of gaps (or rather - blobs) and a similar increase in total length of gap. A histogram of the ratio of these two quantities for every measurement made was formed in the computer by the data processing programme. It is shown in Fig.4.14. The shaded area represents the secondary tracks which are, as expected biassed very slightly toward the smaller average gap length end. It is noticed, however, that a very long tail in the distribution is present and populated by a minority of measurements amongst which the more outrageous results (projected relative ionizations < 0.85) were more prominent. More satisfactory results were obtained when a cut-off of 80 ms applied to this ratio. This meant that a few tracks were unmeasurable, but most of the rejects occurred at the ends of tracks and considerably more confidence in the results was felt.

Velocity Variation of the Measurements

The results of the ionization measurements are

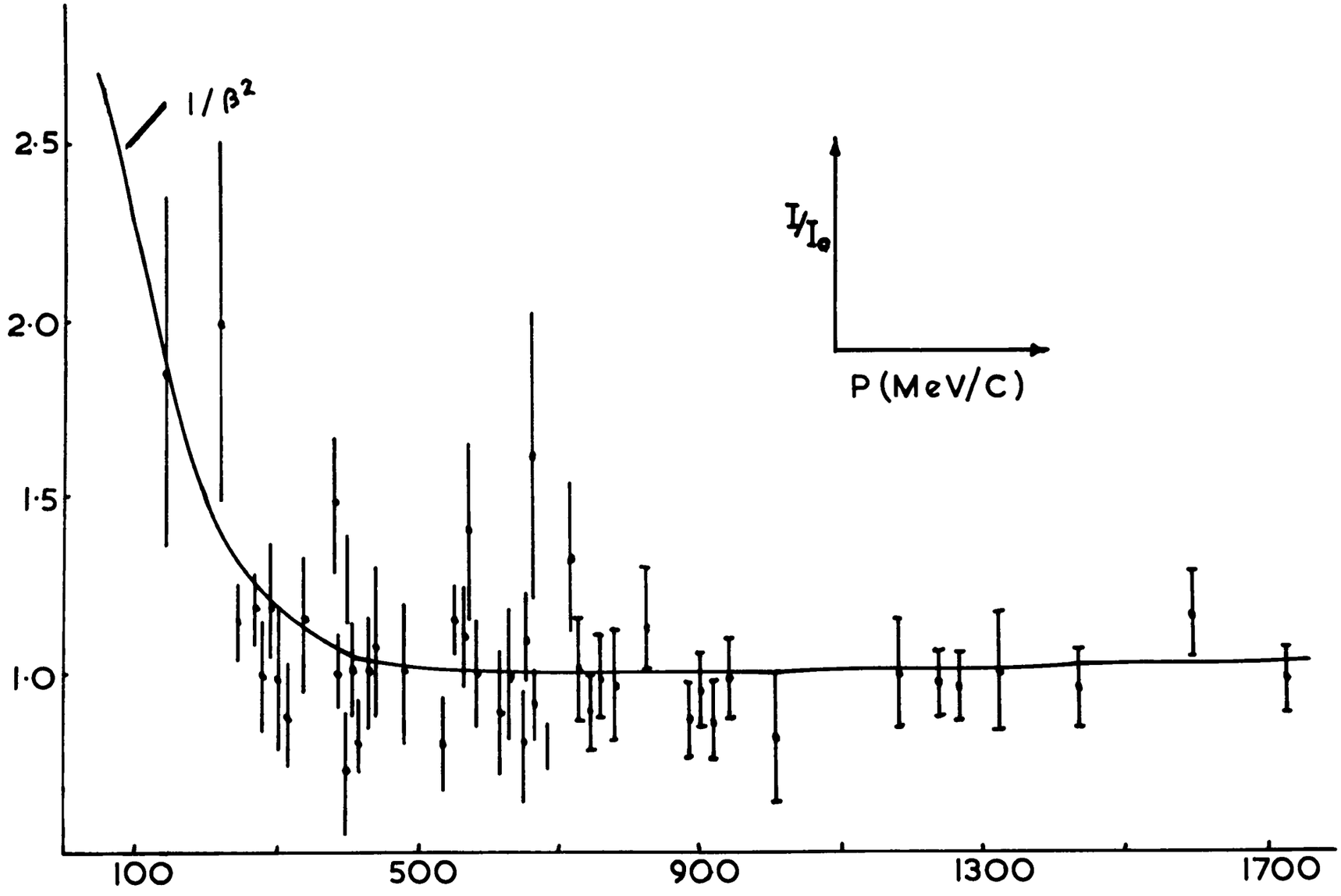

FIG. 4.15 (a) Unique π's

summarized in Fig.4.15(a)-(d). These display the relative ionization of various types of track as a function of their implied momentum. Though the errors are quite large and the uncertainty in the abscissae not shown, one cannot fail to observe that the results do not show the expected $1/\beta^2$ distribution (indicated by the continuous curves on the various plots). The pi-meson curve of Fig.4.15(a) seems to be more closely adhered to than the others, but this is probably because the majority of these particles travel at relativistic speeds and so have mean gap lengths similar to the beam tracks. The heavier particles, however, which have characteristically lower speeds, seem to exhibit measured ionizations systematically below expectation. It is likely that this is the result of the inability of the machine to register the smaller gaps reliably.

Distribution of Gap Lengths

Fig. 4.16 shows the distribution of gap lengths along several sections of beam tracks measured by the machine. In Fig.4.16(a) the distribution for one of these sections measured by a microscope is superimposed (dotted line) and indicates that much smaller gaps are visible by its use. It is further noticed that the distribution ceases to be exponential below about 30 counts ($\sim$ 25μm on the film)

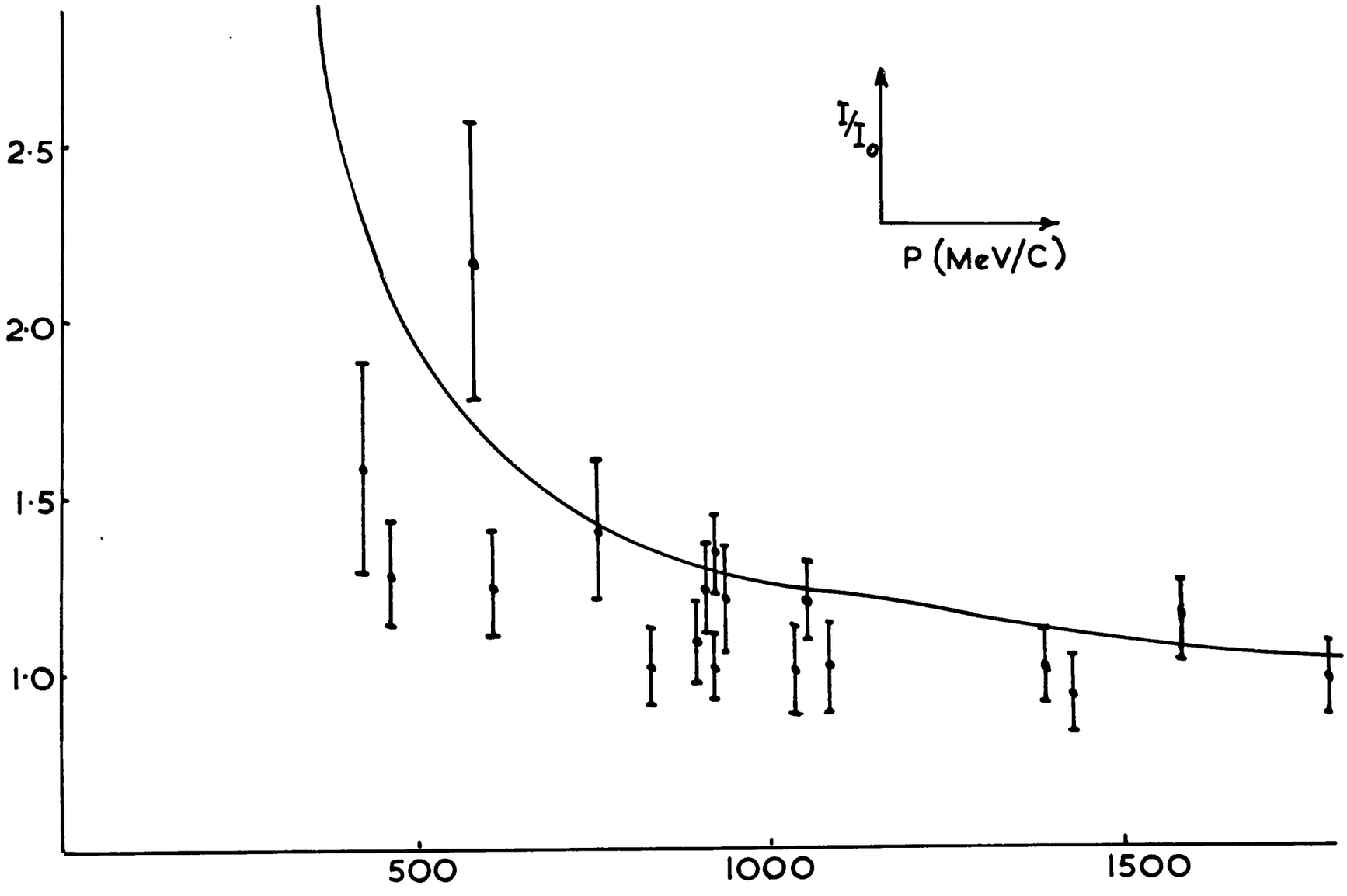

FIG. 4.15 (b) Unique K's.

which corresponds to about one bubble diameter clear gap between bubble circumferences. In such gaps shading of the negative was apparent, and the failure of the machine to recognize them unambiguously probably the result of the fact that the eye was capable of more intelligent interpretation.

With the failure to follow the exponential distribution, it is not surprising that the mean length of the gaps was not proportional to $1/\beta^2$. The smallest gap length consistent with the exponential distribution appears to be about 25-35 counts for most tracks (20-28μm on the film or$\sim$ 1 bubble diameter). This may be compared with the result of Morrisson et al[1] who found that by using a microscope, the mean gap length provided an estimate of $1/\beta^2$ for mean gap length down to about 9μm on the film. In the present case, the average mean gap length for beam tracks was about 50 counts which meant that one third of the gaps were inconsistently measured. The resulting low value for the exponent in the velocity dependence is not, therefore, difficult to understand. The film used by Morrisson, though coming from the same chamber, had two main differences. The chief one was that the beam tracks had a slightly longer mean gap length. The other was that the bubble diameter was smaller (16μm

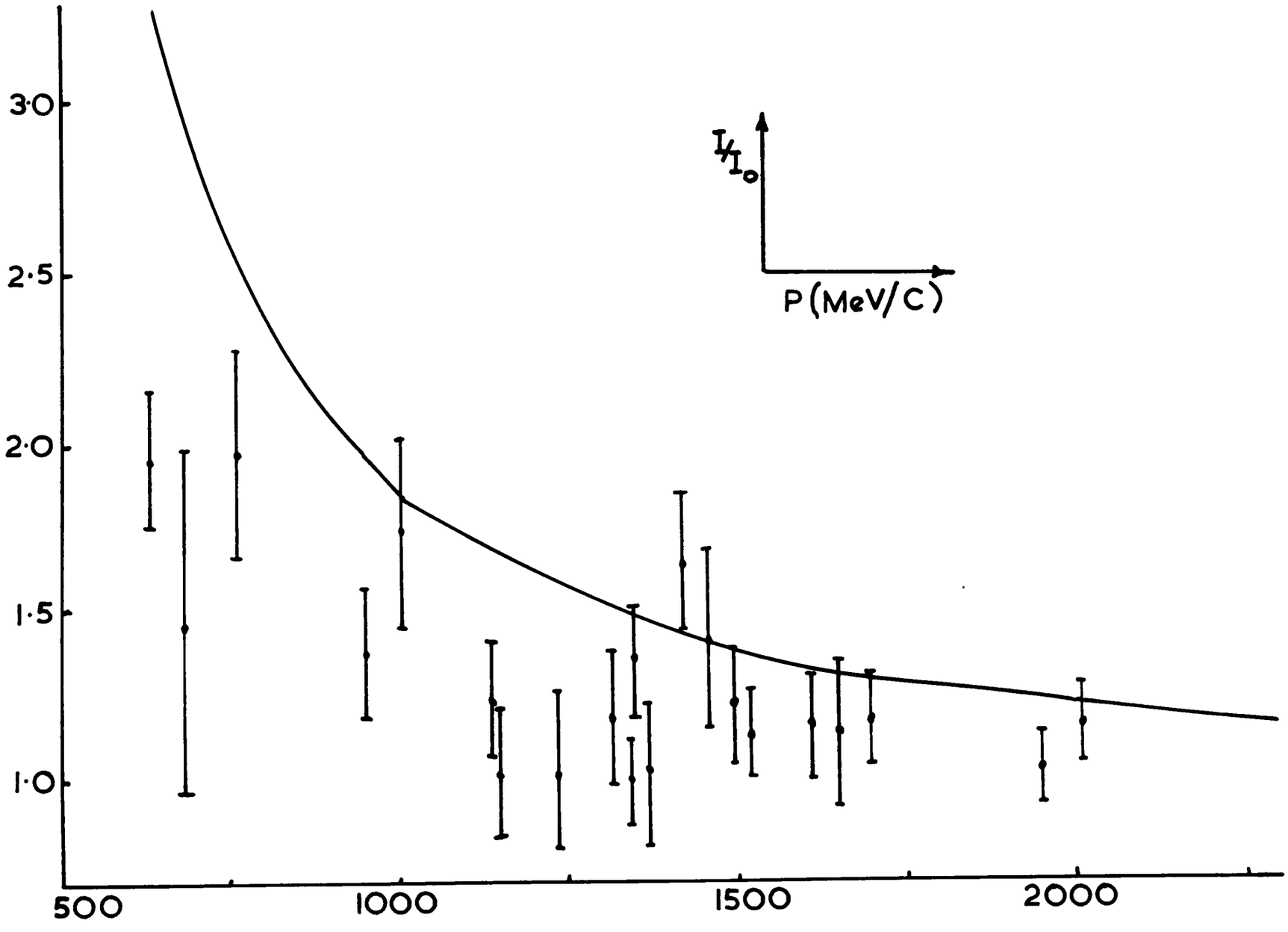

FIG. 4.15 (c) Unique Protons.

instead of 20-25μm).

An attempt was made to reduce the sensitivity of the device to the diffraction haze surrounding the bubble images by adjusting the bubble discrimination level. The result was that better distributions were obtainable on the film having good contrast, though more erratic readings were obtained from the (more usual) poorer quality film. The alternative of removing all gaps less that 35 counts from the measurements would have resulted in a grave loss of statistical accuracy, particularly on the tracks of higher ionization. Consequently, it was decided to accept the less sensitive velocity dependence displayed in Figs. 4.15. The fourth of these (4.15 (d) indicates the measurements made of tracks ambiguous between K's and π's and exhibits a reasonable separation of points onto two trajectories.

The resolution of Ambiguities

The machine was mainly used on events where such an ambiguity existed (between a K or π hypothesis for a track) and where the difference in $1/\beta^2$ was less than or equal to a ratio of 1:1.4. Under such conditions, the $1/\beta^2$ law was not expected to be too badly violated as the mean gap lengths were all fairly large. Consequently, the following rules were adopted in deciding which hypothesis to take.

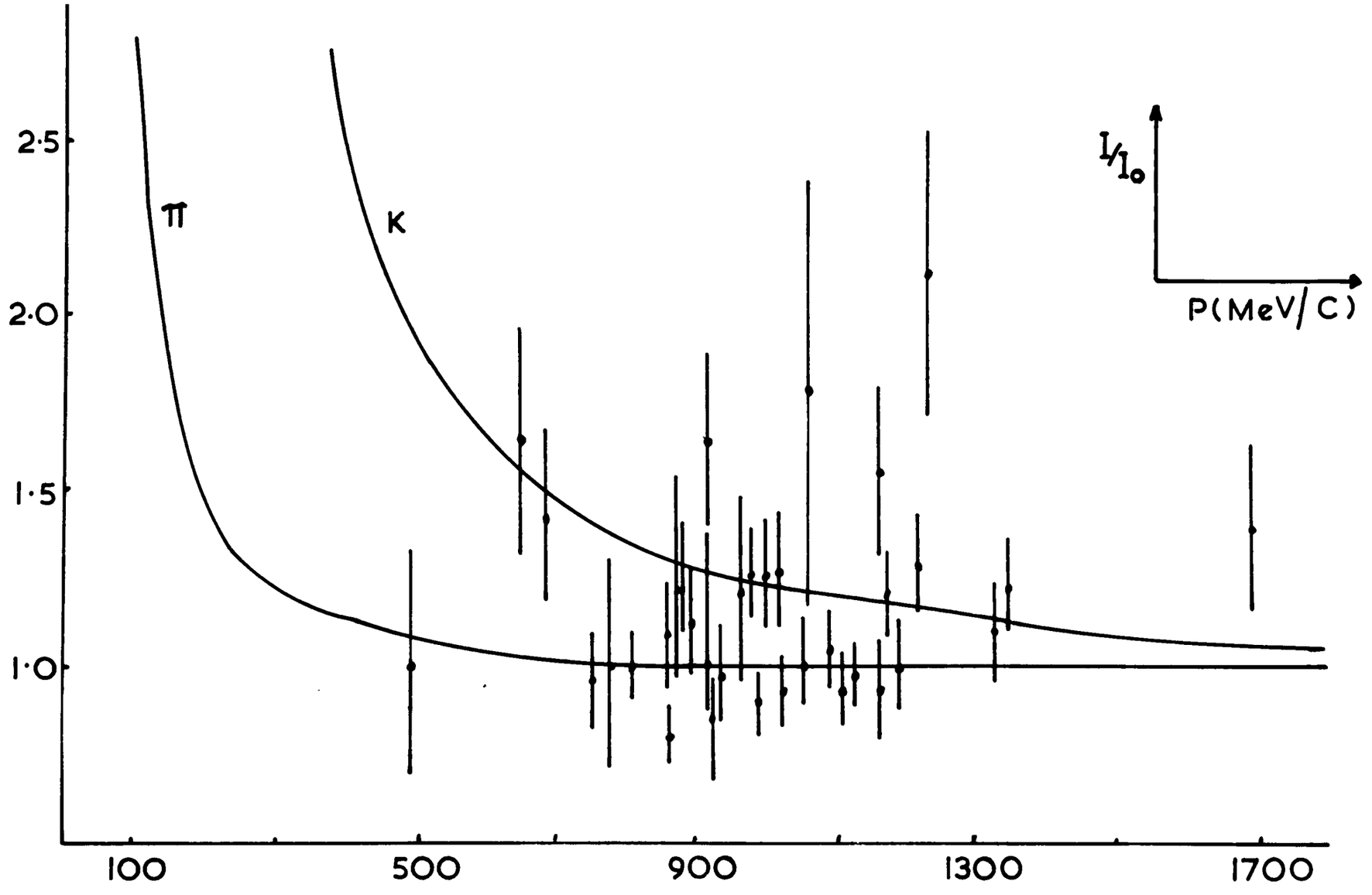

FIG. 4.15 (d) Ambiguous K-π.

A measured value:

(a) within one standard deviation of $1/\beta^2$ for one hypothesis and more than one standard deviation from the other was taken as resolved in favour of the former (31 examples);

(b) more than one but less than two standard deviations from one hypothesis but more than two from the other was also taken as decided (4 examples);

(c) more than one but less than two standard deviations from both hypotheses was regarded as still ambiguous (10 examples);

(d) more than two standard deviations from both hypotheses was rejected (positive tracks) or taken as ambiguous (negative tracks) (4 examples).

Applying these criteria to the unique K and π tracks with momentum $>$ 500 Mev/c indicated that 8 out of 16 K's would thus be wrongly assigned though all but 3 (out of 48) π's would be correctly identified.

Discussion

The results presented indicate that ionization measurements are possible on the film from the Saclay 81cm. bubble chamber using the mean gap length method, and an automatic scanning device. A velocity dependence of $1/\beta^2$ was, however, not found, and this was thought to be largely the result of somewhat unfavourable chamber conditions.

Fig. 4.16

Gap length distribution.

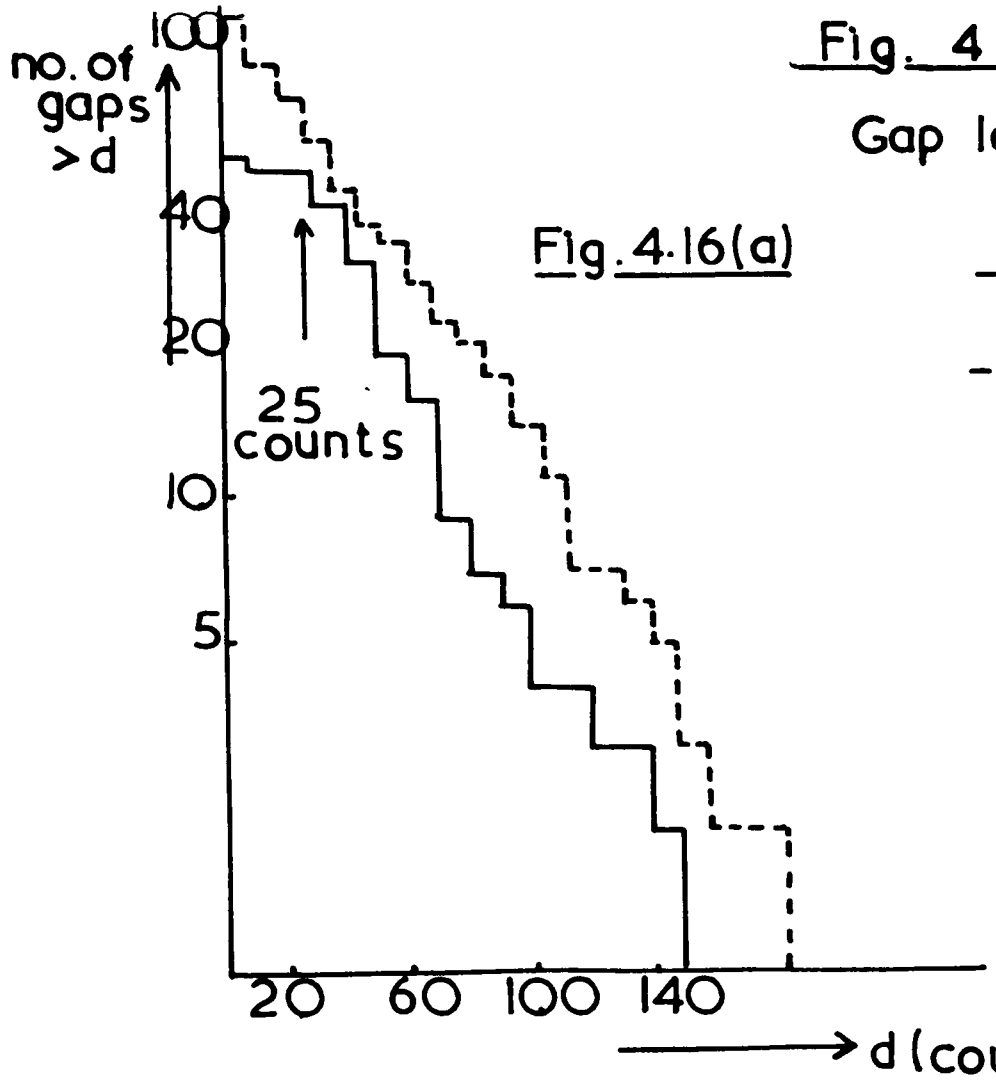

Fig. 4.16(a)

——— measured by machine. (bins of 10 counts)

- - - - measured by microscope. (bins of 2 eyepiece divs = 9.2 counts.)

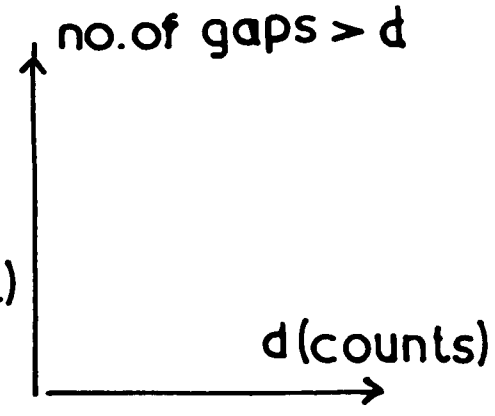

Fig. 4.16(b)

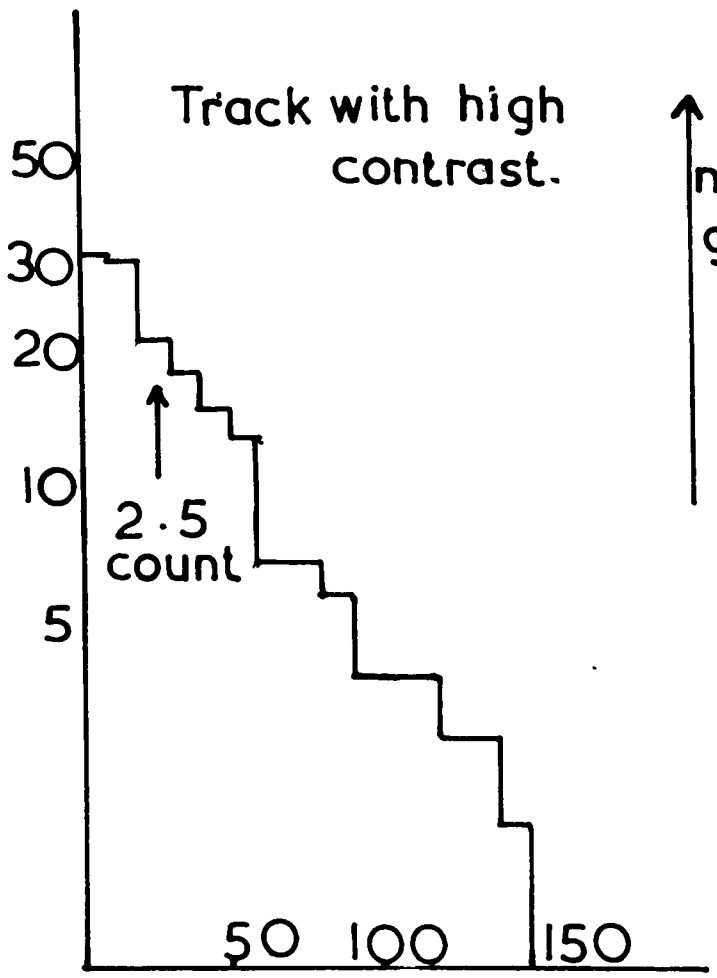

Fig. 4.16(c)

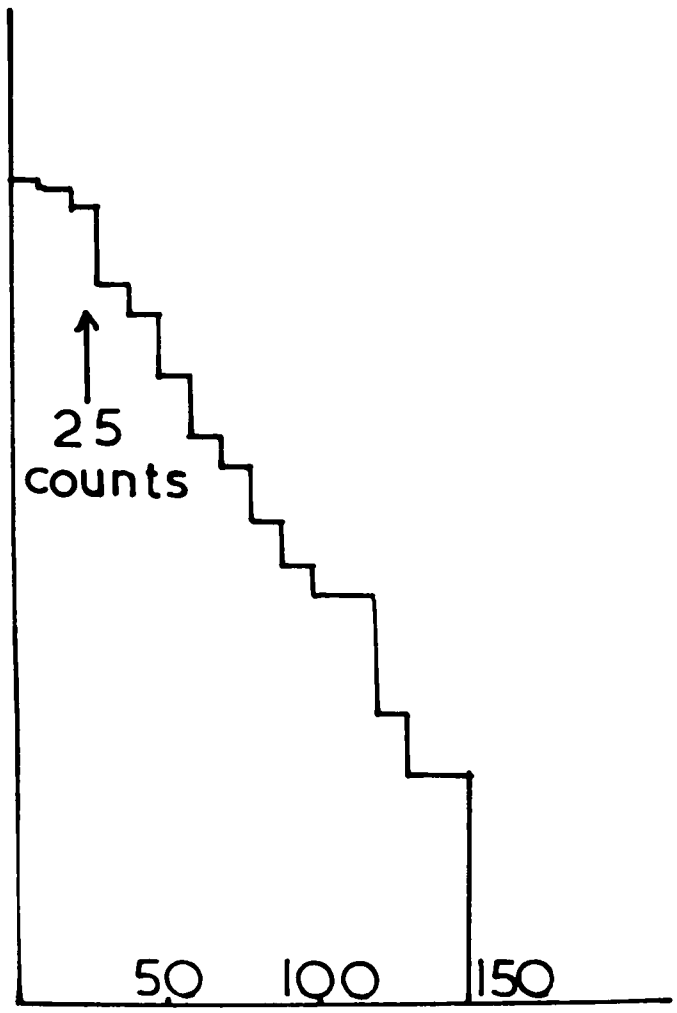

no. of gap > d

d (counts)

Better film contrast would have allowed some adjustment of the sensitivity of the device to make the recognition of smaller gaps more reliable. Failing this, a larger mean gap length would have been desirable as the relative importance of the smaller gaps would have been reduced. Maximum statistical accuracy is obtainable from mean gap length measurements when the value for this quantity is equal to the minimum observable gap length. In order to preserve the exponential character of the distribution of gaps, a reasonable estimate for the latter quantity for the device described is two bubble diameters ($\sim 500\mu m$ in the chamber). The average value for the present film was about $400\mu m$. Though this is not far from optimum, the necessary rejection of gaps $< 500\mu m$ would have lead to an average number of gaps of ~ 36 in one machine section of beam track and a similar number for one of relative ionization 1.4. As it was possible to measure three such sections on most tracks, the statistical accuracy could not, therefore, be expected to be better than approximately 10%.

A considerable improvement would also have been to have had smaller bubbles. The minimum observable gap appears to be related to the bubble size since the limitation on the recognition of small gaps is the "diffraction shadow" around the bubble image.

REFERENCES TO CHAPTER IV

1. C. Dilworth, G. Mambriani, D.R.O. Morrison; Nuovo Cimento 32,1432(1963)

CHAPTER V

Assignment of Events to Final States

After obtaining a satisfactory geometrical reconstruction of each event, the next important step is to test various hypotheses for its origin against the measured momenta. The hypothesis which most nearly satisfies the conservation of energy and momentum is often to be preferred. In order to perform this test, the kinematics programme (which forms part of the Rutherford Laboratory bubble chamber analysis system[1]) carried out the minimization - by an iterative process - of the quantity:

$$\chi^2 = (X - \bar{X})^T G (X - \bar{X}) \qquad \ldots\ (1)$$

subject to the conditions of energy and momentum balance. In equation (1) X is a vector containing the measured values (p = momentum, λ = angle of dip and ϕ = angle of azimuth) for all of the tracks in the fit. $\bar{X}$ is the vector containing the set of values nearest to the X which satisfy the kinematic constraint equations and G is the inverse of the error matrix for the measured quantities. Basically, minimization of (1) is equivalent to variation of the measured values of X in order to satisfy the constraint equations and the hypotheses requiring the smallest variation has the smallest χ^2. Therefore, the use of kinematic fitting was two-fold:

(a) to test one hypothesis against another (through the value achieved for χ^2)

(b) to obtain a set of variables which satisfied the conditions of energy and momentum conservation.

For a correct hypothesis, the probability (P) that χ^2 will be greater than a given amount (x_o) may be calculated on the assumption that the variables are normally distributed. It is:

$$P = \frac{1}{2^{(n/2+1)}\,\Gamma(n)} \int_{x_o}^{\infty} x^{(n/2-1)}\, e^{-x/2}\, dx$$

and depends upon the number of constraints (n). The programme automatically rejected events that had a probability after two iterations of less than 0.1%

The fact that only four constraint equations were available meant that n was never larger than 4. This was the case for events where the presence of no missing particles was assumed so that all the variables were measured. When, however, the presence of a neutral particle was assumed, the introduction of 3 unmeasured quantities corresponding to the invisible track momentum components became inevitable, and n was therefore reduced to 1. Finally, those events where one of the tracks was either steeply dipping, short or in any way of uncertain curvature, such that its momentum remained unmeasured whilst its direction was known, contributed

TABLE I

Hypothesis Name	Reaction	
20001	$K^- p \rightarrow K^- p$	(elastic scattering)
20002	$\rightarrow K^- p \pi^0$	
20003	$\rightarrow \pi^- p \bar{K}^0$	($\bar{K}^0$ not seen)
20004	$\rightarrow K^- \pi^+ n$	
20005	$\rightarrow \pi^- \pi^+ \Lambda^0$	(Λ^0 unseen)
20006	$\rightarrow \pi^- \pi^+ \Sigma^0$	(Σ^0 unseen)
20007	$\pi^- p \rightarrow K^- p K^0$	
20008	$\rightarrow \pi^- p$	
20009	$\rightarrow \pi^- p \pi^0$	
20010	$\rightarrow \pi^- \pi^+ n$	

to hypotheses involving n = 0 and 3. It is usual to refer to an n-C hypothesis where n in our case takes the values 0,1,3 and 4, and this we shall do henceforth. It may be noticed that hypotheses involving more than one missing particle were underconstrained and were, therefore, unable to be kinematically fitted at all.

Separation of the Two Prong Events

The hypotheses tried on the two prongs are summarized in Table 1.

A common feature of the two and four prongs was that no hint of the reaction apart from the occasional presence of a stopping proton (or more rarely a K^-) or perhaps a $\pi^- - \mu^- - e$ or $K^- - \pi^- - \mu^- - e^-$ decay was given at the scanning stage, and one had to depend upon the kinematic fitting programme to a large extent. As a result, considerable ambiguity between the various hypotheses was found.

The main object of the two prong experiment was the investigation of the three final states represented by 20002, 20003, 20004 in Table I, whilst some interest also fell upon the elastic scattering channel, 20001. Consequently, we shall not be concerned with any event not having a reasonable fit to one of these hypotheses. It may also be observed that, apart from 20001 and 20008, all

reactionswere of the 1-C type (occasionally 0-C) whilst the former were 4-C.

After the fitting, a sample of events was inspected on the scanning table to check the consistency of the results with ionization estimates made by eye. The prediction made for comparison with this estimate was $\sec\lambda/\beta^2$ where λ is the track dip angle and β the relativistic velocity which depends upon the hypothesis. As a result, the following criteria were decided upon by the collaboration for the separation of final states.

1. All 4-C fits (elastic events) were given priority, and accepted if the probability for the fit was greater than 1%.
2. 1-C fits with χ^2 probability $<$ 5% were rejected. This removed many ambiguities.
3. Events fitting with probability 5 times (or more) that of the next most likely fit could safely be regarded as unique. Only fits having probability $>$ 1/5th of the largest were considered.
4. Ambiguities resolvable by ionization estimates where the predicted difference was larger than a factor of 1.5 were resolved by inspection on the scanning table.
5. Any remaining ambiguity was awarded to one (or more) of

TABLE II

Two Prong Ambiguities

Hypothesis	Ambiguous With						Unique
	20001	20002	20003	20004	Two of 2, 3 & 4	Λ^o, Σ^o	
$K^- p \rightarrow K^- p$							
$\rightarrow K^- p\pi^o$			16	1	0	7	81
$\rightarrow \pi^- p\bar{K}^o$		16		4	0	12	97
$\rightarrow K^- \pi^+ n$		1	4		0	78	116

the hypotheses 20002, 20003, 20004.

On this basis, the number of final fits for Oxford events is summarized in Table II.

A few events were ambiguous with one or more of the wanted hypotheses, whilst those which fitted more than three before the imposition of condition (5) were remeasured.

The rather arbitrary decision to ignore incoming π^- and Λ^o, Σ^o production channels requires some comment.

Some events having - in addition to two prongs - a visible V^o had already been analysed and uniquely identified[2]. By refitting some of these with the kinematics programme and scanning for ionization (both whilst ignoring the presence of the V^o) the results in Table III were obtained.

From this it is seen that the most highly contaminated final state was $K^-\pi^+n$ which received the majority of its misidentified events from the reaction:

$$K^-p \rightarrow \Lambda^o\pi^+\pi^-\pi^o$$

whilst, apart from genuine hypothesis 20003 events, the remaining hypotheses were virtually unaffected by Λ^o or $\bar{K}^o$ reactions. However, of the 26 $\Lambda^o 3\pi$ events, only 3 also fitted the 3 body channel: $K^-p \rightarrow \Lambda^o\pi^+\pi^-$ so that they appear to represent an entirely additional source of contamination from outside any two prong hypothesis.

TABLE III

Number of Fits to 2-Prong Hypotheses

Reaction	20002	20003	20004	20002 & 3	Any Other 2,3,4 comb	Neither 2,3,or 4
$K^- p \rightarrow \Lambda^0 \pi^+ \pi^-$			3			7
$\rightarrow \Lambda^0 \pi^+ \pi^- \pi^0$			12			14
$\rightarrow \Sigma^0 \pi^+ \pi^-$			1			2
$\rightarrow \bar{K}^0 p \pi^-$		7		4		1
$\rightarrow \bar{K}^0 p \pi^- \pi^0$	1					8
$\rightarrow \bar{K}^0 \pi^+ \pi^- n$			2			10

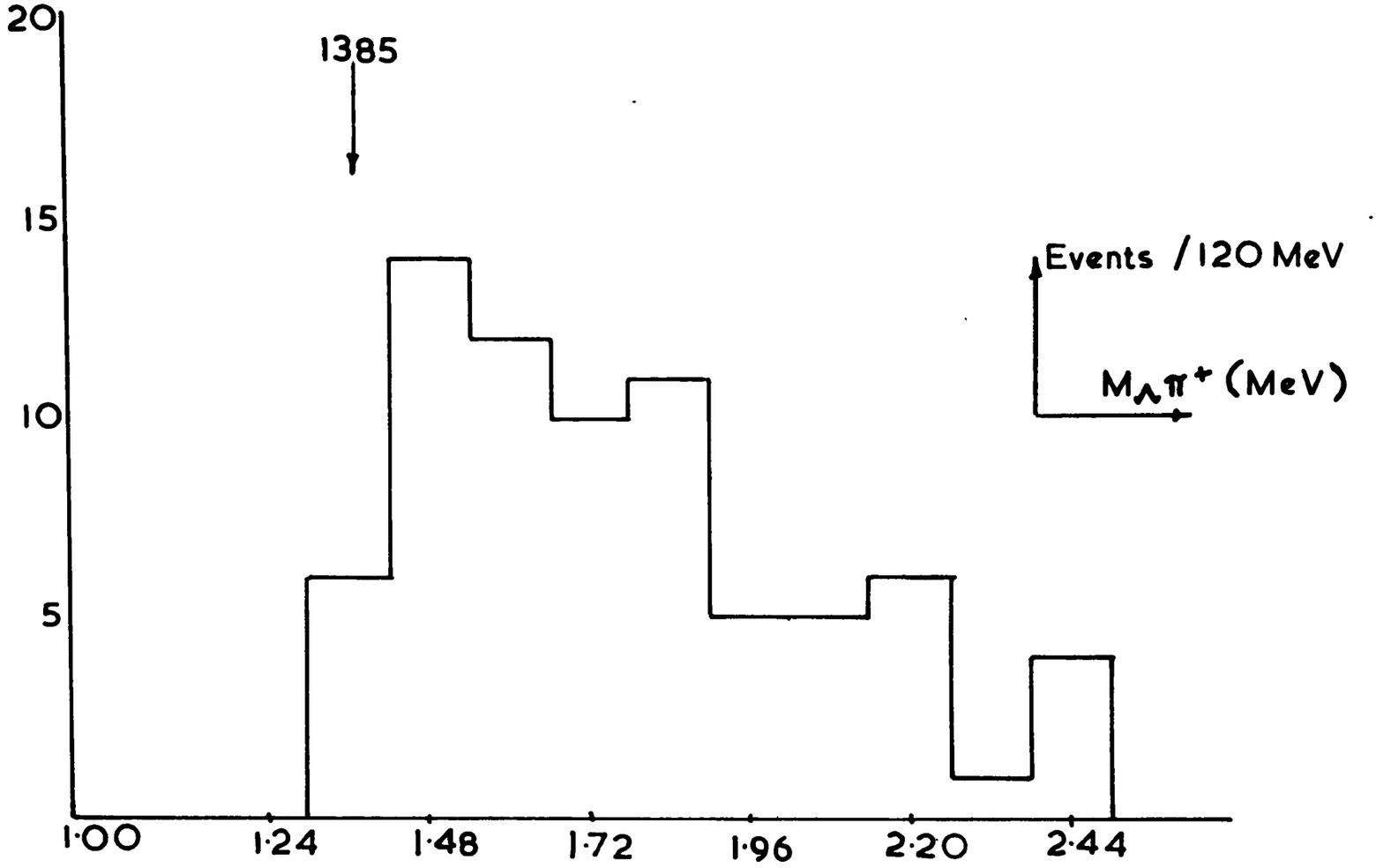

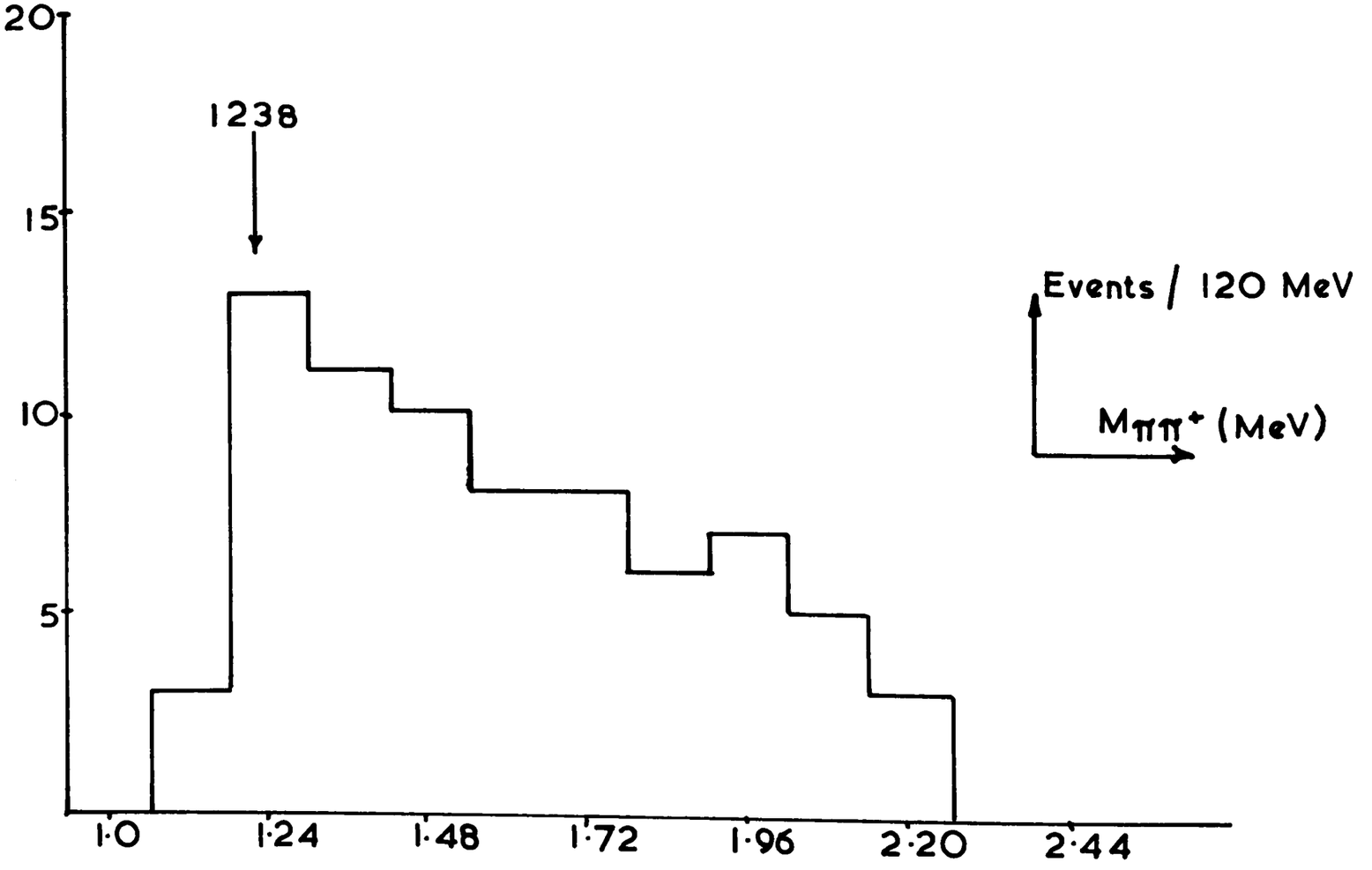

FIG. 5.1 Events ambiguous between hypotheses 20004 & 20005.

Converting the figures in Table III into numbers of two prong events by using the ratio of microbarn/event equivalents between the 201 and 200 event samples and the known cross sections for the reactions:

$K^o p \rightarrow \Lambda^o \pi^+ \pi^-$ $\quad 462 \pm 30 \mu b$

$\rightarrow \Lambda^o \pi^+ \pi^- \pi^o$ $\quad 1216 \pm 40 \mu b$

$\rightarrow \Sigma^o \pi^+ \pi^-$ $\quad \sim 600 \mu b$

$\rightarrow \bar{K}^o p \pi^- \pi^o$ $\quad 1180 \pm 150 \mu b$

$\rightarrow \bar{K}^o \pi^+ \pi^- n$ $\quad 1250 \pm 150 \mu b$

one may estimate that a contamination of as much as 50% in reaction (4) (26% of which could come from the $\Lambda 3\pi$ final state) and 8-9% in reaction (3) (from the hypothesis having an extra π^o) could have resulted from the present criteria.

In the case of $\Lambda \pi^+ \pi^-$, an independent check on the contamination was available. This reaction is known to proceed dominantly via the production of $Y^*_1(1385)$

$$K^- p \rightarrow Y^{*+}(1385) \pi^- \quad (3.5 \text{ Gev/c})$$
$$\hookrightarrow \Lambda^o \pi^+$$

Taking for instance, the ambiguous 20004 events suspected of harbouring such contaminants, inspection of the $n\pi^+$ invariant mass distribution Fig.5.1 shows the presence of N^{*+} with a broad width, but little, if any, concrete evidence for the expected Y^*_1 events which should show up

as a somewhat narrower peak centred at a little below 1385 Mev. This serves to show that the previous contamination figure can be, at worst, an overestimate. However, the existence of some pion induced events would tend to decrease the importance of the Y*.

Effect of Pion Contamination in the Beam

As already mentioned, no attempt was made to remove the incoming pion events from the sample. As the main purpose of carrying out the two prong experiment was to study the K*(890) and K*(1400), this was not too serious a shortcoming since any event contribution to a "$\bar{K}\pi$" invariant mass enhancement near to either of these resonances was unlikely to be pion-induced. The fractions of K* resonances in these final states are found in the next chapter, and they appear to be substantially represented - indicating that pion contamination was not too serious. A consequence of the contamination, however, was that the absolute cross-sections of any of the reactions 2,3 or 4 were unknown.

Contamination from Events Having Multiple Missing Neutrals

It may be regarded as significant that the figures in Table III indicate no noticeable contamination of reaction (2) from any of the final states involving heavy missing particles. It is also rather satisfactory to note that

TABLE IV

Missing Mass Cut-offs

Hypothesis	Missing System	Missing Mass Range
20002	π^o	0 - 300 Mev
20003	$\bar{K}^o$	350 - 650 Mev
20004	n	800 - 1100 Mev

TABLE V

"Faked" Multiple Missing ^{o} Events

Identity	Number having no Fits to Hypothesis 20002	Number of Fits To Hypothesis 20002	Number of Fits with Missing Mass within 0-300 Mev
$K^-p \rightarrow K^-p\pi^+\pi^-$	64	12	2
$K^-p \rightarrow K^-p\pi^+\pi^-\pi^o$	69	5	1

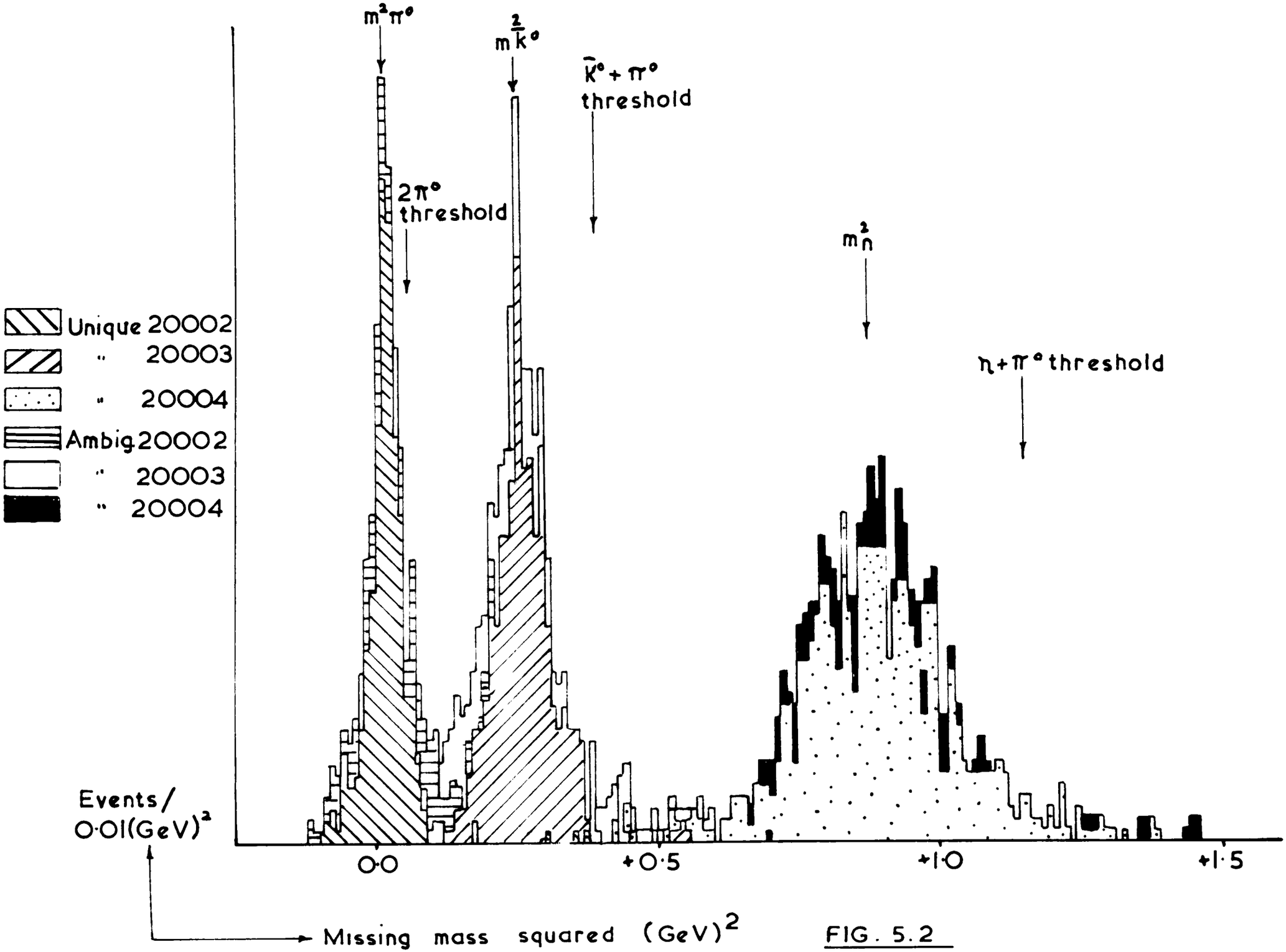
$m^2_{\pi^0}$
$m^2_{\bar{K}^0}$
$\bar{K}^0 + \pi^0$ threshold
$2\pi^0$ threshold
m^2_η
$\eta + \pi^0$ threshold
Unique 20002
" 20003
" 20004
Ambig 20002
" 20003
" 20004
Events / 0·01(GeV)²
0·0
+0·5
+1·0
+1·5
Missing mass squared (GeV)²

FIG. 5.2

reaction (3) was only fitted by one out of nine events known to represent the same reaction with one extra π^0. The missing mass plots of Fig.5.2 for the three reactions (2,3 and 4) are instructive. The actual quantity plotted is the squared invariant mass of the missing system calculated from the energy and momentum unbalance of the measured variables. The uniquely fitting events are indicated. In order to reduce the effect of extra π^0 hypotheses affecting the final states, cuts were applied to the missing masses as listed in Table IV. It is clear from Fig. 5.2 that it was reaction (2) that was most likely to be affected by final states such as $K^-p \rightarrow K^-p\pi^0\pi^0$, so that a test of the effectiveness of these cut-offs was made as follows. Some four prong events whose identity was known to be one of the following: $K^-p \rightarrow K^-p\pi^+\pi^-$

$\rightarrow K^-p\pi^+\pi^-\pi^0$

were selected, and some two prong events "faked" by selecting the K^- and p tracks, and removing the information relevant to the others. After testing these events with the kinematics programme against the two prong hypotheses, the fits that were obtained are summarized in Table V. It would appear from this that the missing mass selctions were very efficient, and that one might have expected a very small contamination from multiple π^0 events.

TABLE VI

Hypothesis Name		Final State	No. of events fitting	No. after Ionization Scanning	Final No. U	Final No. A
K-induced	40001	$K^- p \pi^+ \pi^-$	302	281	276	93
	40003	$\bar{K}^0 p \pi^+ \pi^- \pi^0$	415	177	169	87
	40007	$\bar{K}^0 p \pi^+ \pi^- \pi^-$	243			
	40011	$K^- \pi^+ \pi^+ \pi^- n$	256	101	94	52
	40021	$\pi^- \pi^+ \pi^- \pi^+ \Lambda^0$	193			
	40031	$\pi^- \pi^+ \pi^- \pi^+ \Sigma^0$	151			
π-induced	40051	$\pi^- p \pi^+ \pi^-$	171			
	40052	$\pi^- p K^+ K^-$	26			
	40053	$\pi^- p \pi^+ \pi^- \pi^0$	360			
	40054	$\pi^- p K^- \pi^+ K^0$	58			
	40055	$\pi^- p \pi^- K^+ \bar{K}^0$	22			
	40056	$\pi^- p K^+ K^- \pi^0$	85			
	40061	$\pi^- \pi^+ \pi^- \pi^+ n$	213			
	40062	$\pi^- \pi^+ K^- K^+ n$	71			
	40071	$\pi^- \pi^+ \pi^- K^+ \Lambda^0$	100			
	40081	$\pi^- \pi^+ \pi^- K^+ \Sigma^0$	64			

U = Unique

A = Ambiguous

Separation of the Four Prong Events

Table VI contains the list of hypotheses against which the four prongs were tested. Column three contains the number of events having at least one fit to one of the reactions of interest. A large sample of events were inspected on the scanning table for consistency with ionization estimates in a similar way to the two prongs. As a result of this it was found justifiable to reject any fits to a "1-C" hypothesis having χ^2 probability of less than 5%

Ionization Scanning

With this proviso, all events fitting any of the reactions of interest (hypotheses 40001, 40003 or 40011) were then inspected for consistency with ionization predictions and an attempt to resolve some of the more obvious ambiguities was made. It is seen from the figures in column 4 of Table VI that very few fits to the first reaction were ever rejected in this way. The reason is probably that the four constraints imposed upon such events were difficult to satisfy so that few accidental fits occurred. A frequent occurrence was that an event fitting 40001 with low probability had - by permuting proton and positive pion mass assignments - produced a very good fit to hypothesis 40003 or sometimes 40053. The difference was usually obvious in such cases.

Use of the Ionization Machine

The method of guessing ionizations as above was quite successful on the present film. It was often found, for instance, that writing down the guesses for this quantity on each track provided a set of numbers which often matched at least one set of predicted figures rather well. However, this was dangerous, especially when the ionizations were below about 1.3 or 1.4 relative to minimum (1.0) as in those cases, a guess of 1.25 say, for a track which was for example either a K^- (1.28) or a π^- (1.18), could temptingly be accepted as the former. It would really be desirable to have an ionization estimate with error for every track.

In those cases where the predicted projected ionization was either in the range (1.20 - 1.40) or minimum depending on the hypothesis, the assistance of the gap length device described in the previous chapter was invoked. In most cases, this meant that a distinction between a π^- or K^- was sought. Only events occurring on film of reasonable quality were selected for measurement. This should have introduced no bias into the ambiguous events - merely to have reduced their number. Some uniquely identified events from the better quality film were also selected for measurement

TABLE VII

Ambiguities Resolved by Ionization Machine

Hypothesis		Ambiguous With									Multiply Ambiguous
		40001	40003	40007	40021	40031	40051	40053	40061	Others	
40001	Resolved	1						59			
	Rejected							4			1
	Unresolved	1					2	1		2	
40003	Resolved		2	1							3
	Rejected		1	2				3			2
	Unresolved			3				1			
40011	Resolved				3	1			1		
	Rejected				3	1			1		2
	Unresolved				3	1					

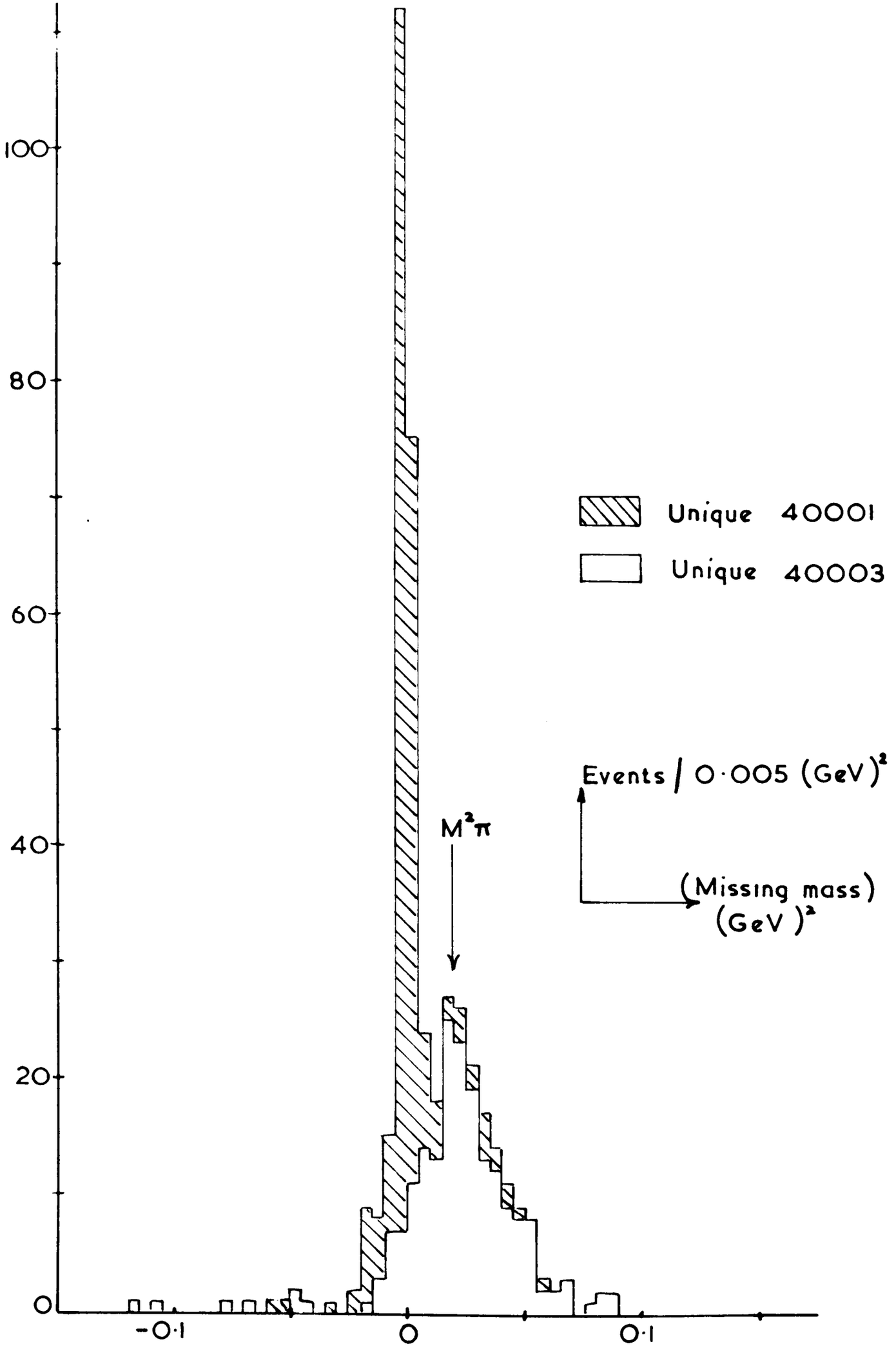
100
80
60
40
20
0
-0·1
0
0·1
Unique 40001
Unique 40003
Events / 0·005 (GeV)²
(Missing mass)
(GeV)²
M²π

FIG. 5.3

in order to calibrate the machine's performance. In this way, 104 events were measured, of which 52 involved an ambiguity of the nature specified above. The interpretation of the measurements is given in the previous Chapter, and a summary of the types of ambiguities resolved given in Table VII. The term "resolved means resolved in favour of the hypothesis indicated. The final numbers of events are summarized in columns 5 and 6 of Table VI where it is observed that the influence of the machine upon the results is only of mild significance. It is now thought that more success could have been achieved had the experimental running conditions been a little more suitable (larger mean gap length and smaller bubbles so that the smallest gaps - unfortunately often in shadow - would have been less significant). Fig.5.3 shows the missing mass distributions for hypotheses 40001 and 40003 where the resolution of the π^0 peak appears to be satisfactory.

Remaining Ambiguities

A few ambiguities remained in the 40001 sample. The 93 events still not resolved had the $K^-\pi^+$ invariant mass distribution shown in Fig.5.4. The presence of $K^{*0}(890)$ is observed and indicates that at least a large fraction of the events amongst them belong to 40001. (See Fig.7.2)

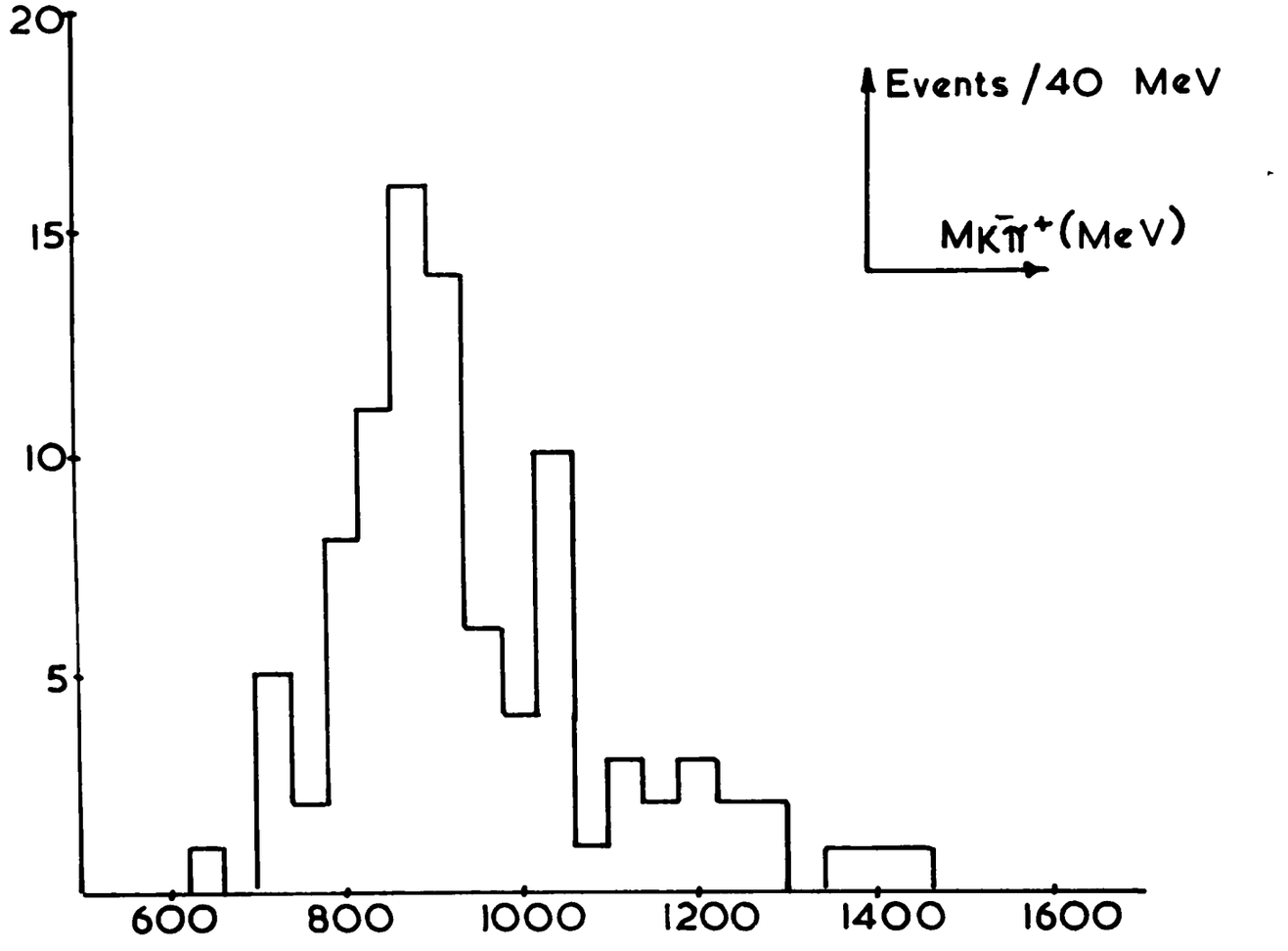

FIG. 5.4 Ambiguous 40001 events.

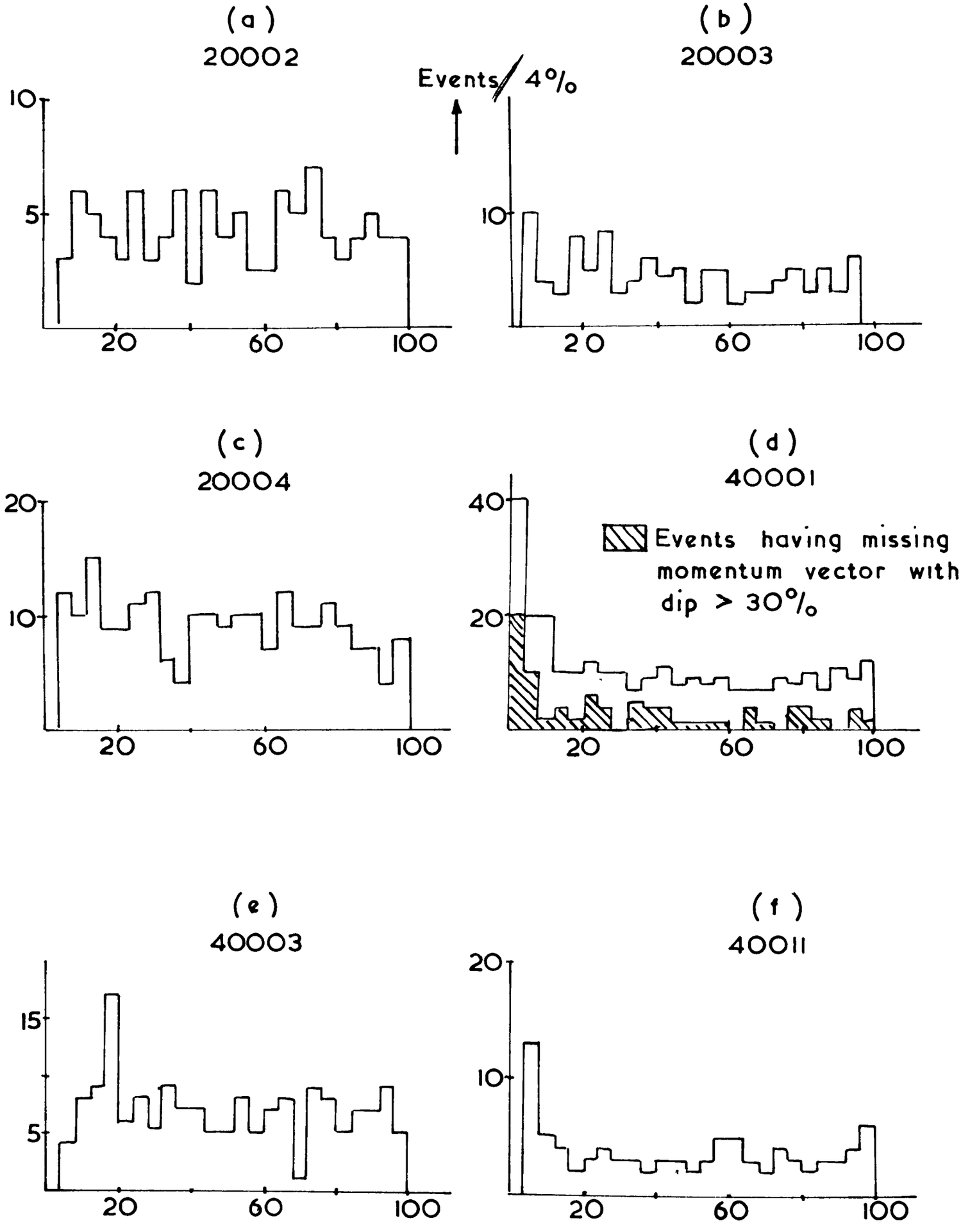

FIG. 5.5 PROBABILITY DISTRIBUTION

Half of the ambiguities were with 40051 - also a 4-C hypothesis. All remaining ambiguities were resolved in favour of 40001.

Judging by the small number of cases in which an ionization estimate led to an assignment to one of the incoming pion associated production reactions any four prong events ambiguous only with these were included in the unique sample.

Low Probability Events

The probability distributions for all the reactions discussed in this chapter are presented in Figs.5.5(a)-(f). The peak in the distribution at the low probability and for the 4-C events ($K^-p \rightarrow K^-p\pi^+\pi^-$) is striking.To investigate this, various quantities of physical interest have been examined, and it is seen from Fig.5.5(d) that the spike was correlated with events having a small "missing momentum" entirely in the z-direction. It was found, in fact that there was no preference for positive (or negative) values in this direction, and it appeared likely that the anomaly was the result of inaccurate measurement.Fig.5.6 illustrates that - among the low probability events - an excess of events having steeply dipping missing momentum was present. The events of low probability were therefore retained as they appeared to satisfy the ionization requirements reasonably well.

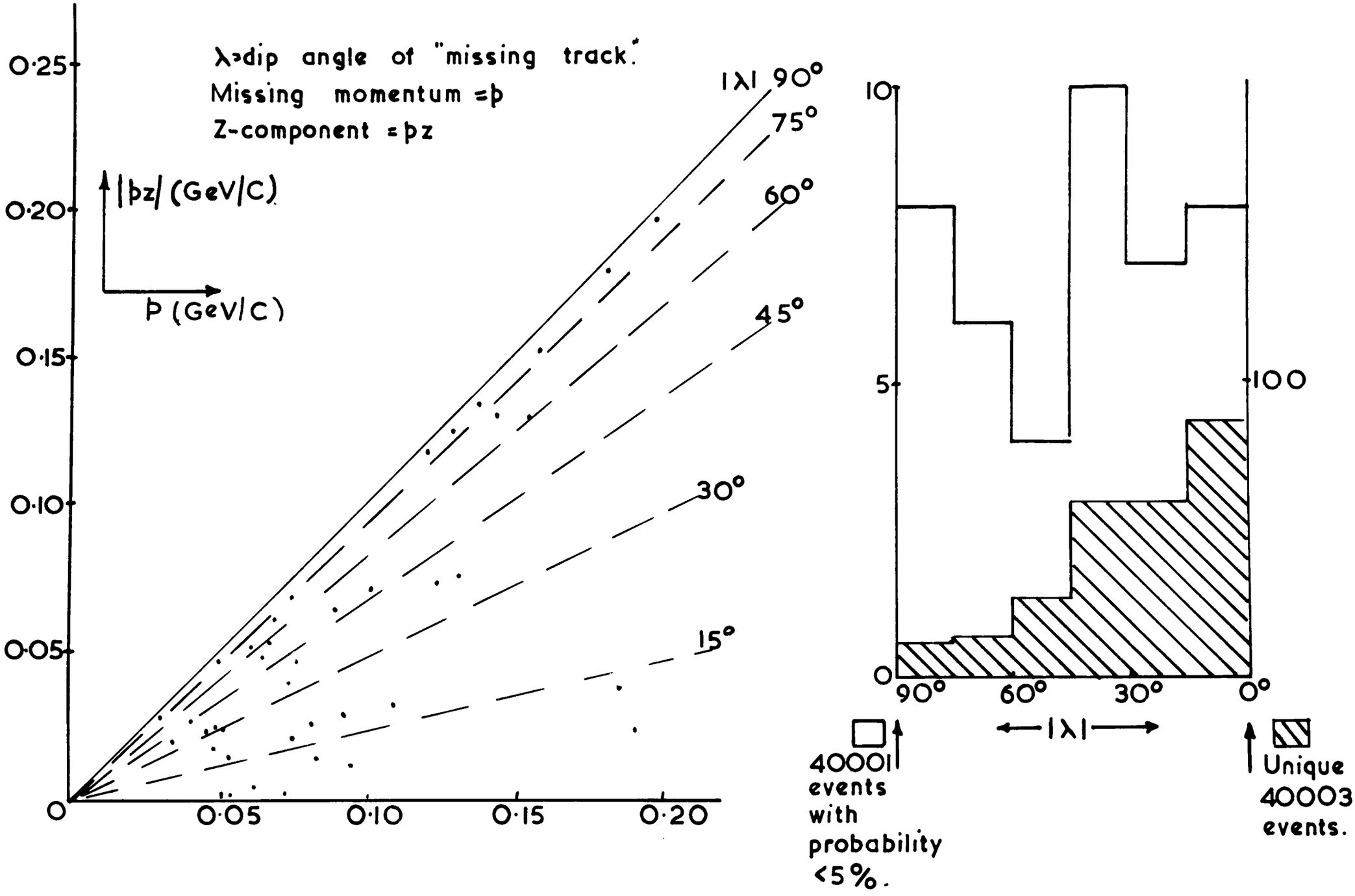
λ=dip angle of "missing track."
Missing momentum =p
Z-component =pz
|pz| (GeV/C)
P (GeV/C)
|λ|
90°
75°
60°
45°
30°
15°
0·25
0·20
0·15
0·10
0·05
0
0·05
0·10
0·15
0·20
10
5
0
100
90°
60°
30°
0°
|λ|
40001 events with probability <5%.
Unique 40003 events.

FIG. 5.6

A correction of 5% was applied to other final states in the estimation of cross-sections to allow for the removal of events fitting with probability below this.

Four Prong Collaboration

Only two groups measured four prong events at 3.5 Gev/c - N.I.R.N.S. and Oxford. As different criteria were used in their separation, only the 4-C fits have been combined.

REFERENCES TO CHAPTER V

1. A Kinematical Fitting Programme for the Analysis of Bubble Chamber Events. A. G. Wilson NIRL/M/38

2. J. H. Field - Private Communication

PART TWO

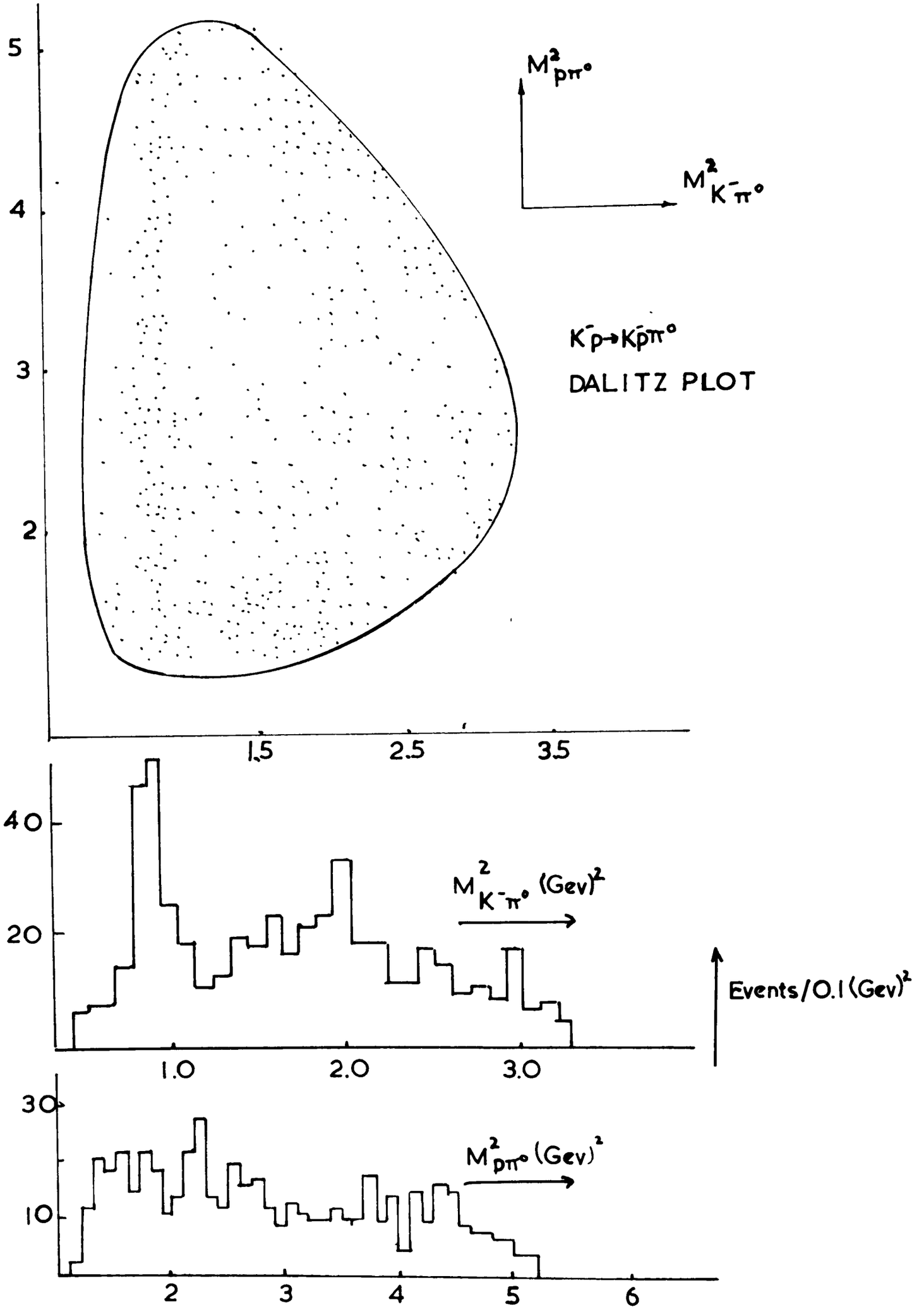
5
4
3
2
$M^2_{p\pi^0}$
$M^2_{K^-\pi^0}$
$K^-p \to K\bar{p}\pi^0$
DALITZ PLOT
1.5
2.5
3.5
40
20
$M^2_{K^-\pi^0}$ (Gev)^2
Events/0.1 (Gev)^2
1.0
2.0
3.0
30
10
$M^2_{p\pi^0}$ (Gev)^2
2
3
4
5
6

FIG 6.1(a)

CHAPTER VI

The Analysis of the Two Prong Events

The discovery of the K**(1400)[1] occurred in the isotopic spin substate $T_z = -\frac{1}{2}$ in the reaction

$$K^- p \rightarrow \bar{K}^0 p \pi^- \qquad (\bar{K}^0 \text{ visible}) \qquad \ldots\ (1)$$

so that no clue to its isotopic spin (which could be $\frac{1}{2}$ or 3/2) was given. The subsequent confirmation of its existence[2] was also accompanied by a weak preference for $T = \frac{1}{2}$ based on the absence of K** production in any but the zero charge state. For exchange of an isospin $\frac{1}{2}$ particle (implying a peripheral production mechanism) the relative production cross-sections in the two states $\dfrac{\pi^- p \rightarrow \Sigma^+ \pi^- K^0}{\pi^- p \rightarrow \Sigma^0 \pi^- K^+}$ would be 27. Consequently, the study of the two prong reactions

$$K^- p \rightarrow K^- p \pi^0 \qquad \ldots\ (2)$$

$$\rightarrow \bar{K}^0 p \pi^- \qquad \ldots\ (3) \qquad (\text{unseen } \bar{K}^0)$$

$$\rightarrow K^- \pi^+ n \qquad \ldots\ (4)$$

was of interest. During the analysis of these states, other determinations of the K** isotopic spin became available,[3,4] so that the results obtained from the two prongs assumed a confirmatory nature.

This chapter is devoted to a discussion of these reactions with special reference to the production and subsequent decay of the K**(1400) and K*(890).

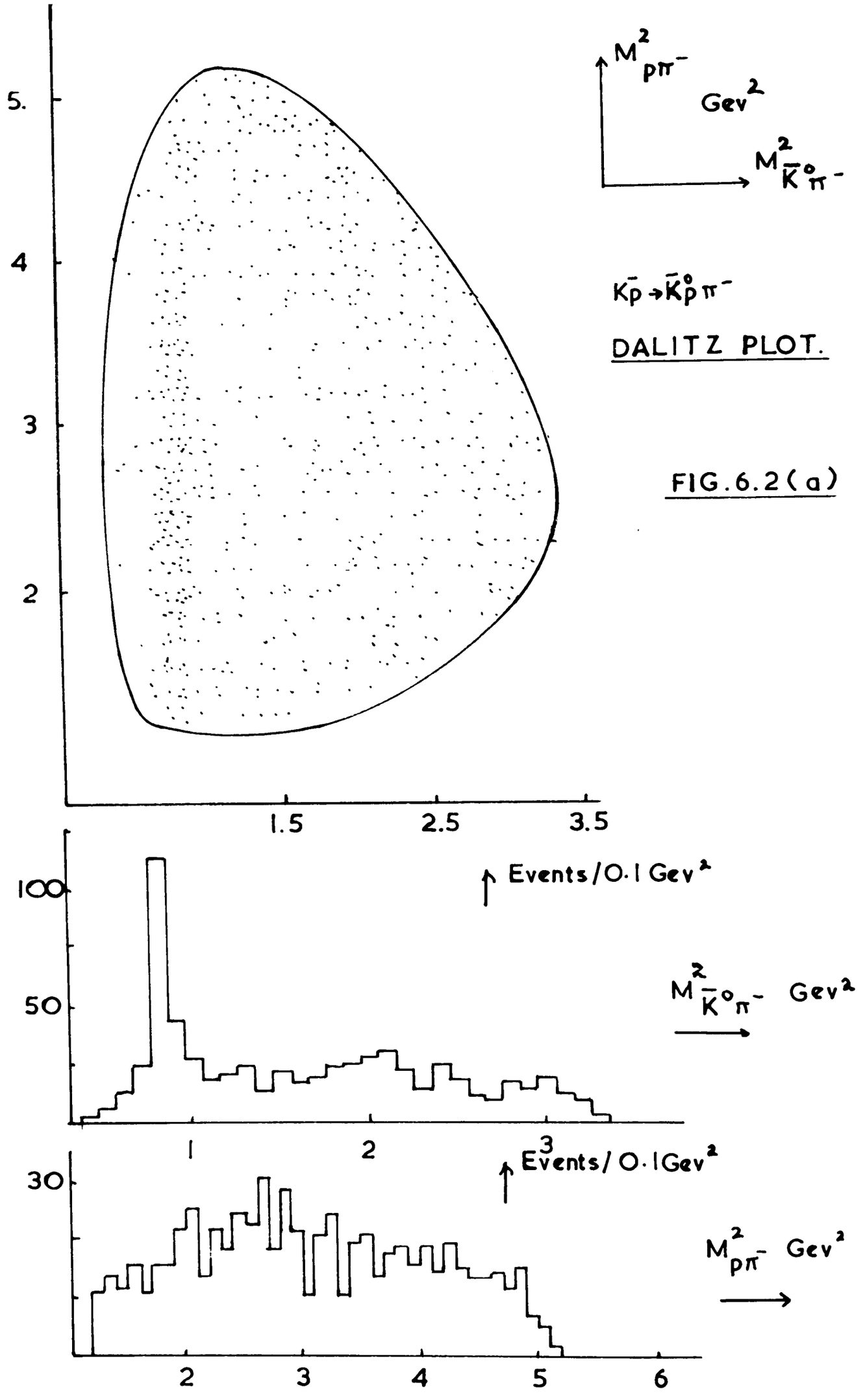
$M^2_{p\pi^-}$ Gev^2
$M^2_{\bar{K}^0\pi^-}$
$K^-p \to \bar{K}^0 p \pi^-$
DALITZ PLOT.
5.
4
3
2
1.5
2.5
3.5
100
50
Events/0·1 Gev^2
$M^2_{\bar{K}^0\pi^-}$ Gev^2
1
2
3
30
Events/0·1Gev^2
$M^2_{p\pi^-}$ Gev^2
2
3
4
5
6

FIG.6.2(a)

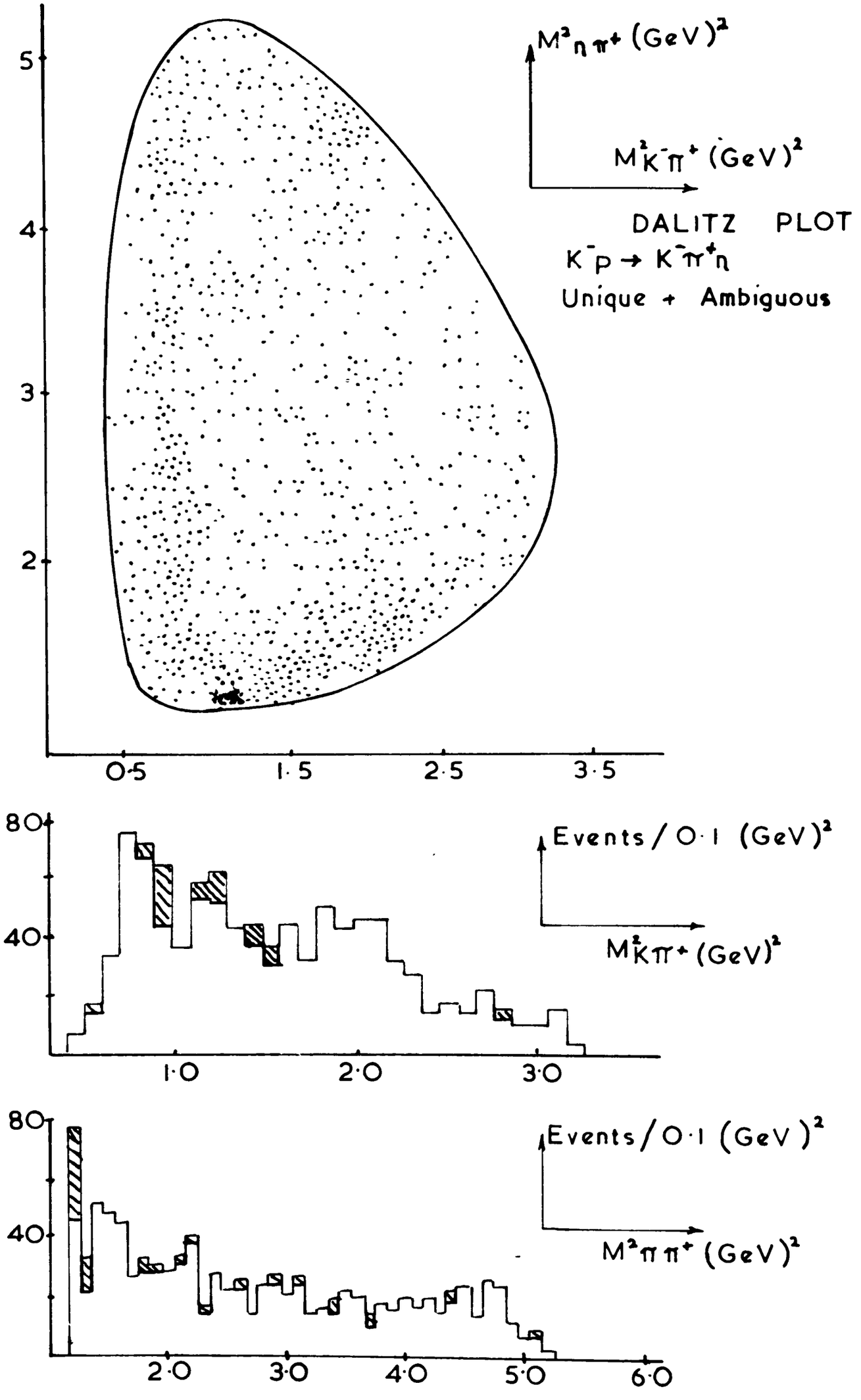
$M^2_{\eta\pi^+}$ (GeV)^2
$M^2_{K^-\pi^+}$ (GeV)^2
DALITZ PLOT
$K^-p \rightarrow K^-\pi^+\eta$
Unique + Ambiguous
5
4
3
2
0·5
1·5
2·5
3·5
80
40
Events / 0·1 (GeV)^2
$M^2_{K\pi^+}$ (GeV)^2
1·0
2·0
3·0
80
40
Events / 0·1 (GeV)^2
$M^2_{\pi\pi^+}$ (GeV)^2
2·0
3·0
4·0
5·0
6·0

FIG. 6.3

Mass Distributions

Figs.6.1-3(a) show the Dalitz plots and projections onto $M^2_{\bar{K}\eta}$ and $M^2_{N\pi}$ axes for reactions (2)-(4) respectively, whilst 1-3(b) show the $\bar{K}N$ invariant mass squared distributions for the same reactions.

As found previously in the 201s, no strong resonance production occurs in either the $\bar{K}^0 p$ or $p\eta^-$ systems, whilst the $\bar{K}\eta$ masses show marked peaks at the mass of the K*(890) and much weaker enhancements at about 1400 Mev, taken to correspond to the production and subsequent decay of the K**. The strikingly large number of events confined to lowest $n\pi^+$ mass values in reaction (4) is due to elastic events and is discussed below. Other minor features that are noticeable are the $Y^*_0(1520)$ in the K^-p spectrum of Fig.6.1(b) and $N^{*+}(1238) \rightarrow n\pi^+$ in reaction (4) Fig.6.3(c)). The corresponding decay of the N^{*+} into $p\pi^0$ in reaction (2) is somewhat less noticeable. This surprising result also is probably attributable to the elastic contamination present in the low mass $n\pi^+$ region.

Contamination from Elastic Events

The prolific nature of these events was underestimated in the adoption of the selection criteria discussed in the previous chapter. In order to carry out a sensible analysis, therefore, the following were undertaken:

(1) removal of all fits to the elastic hypothesis

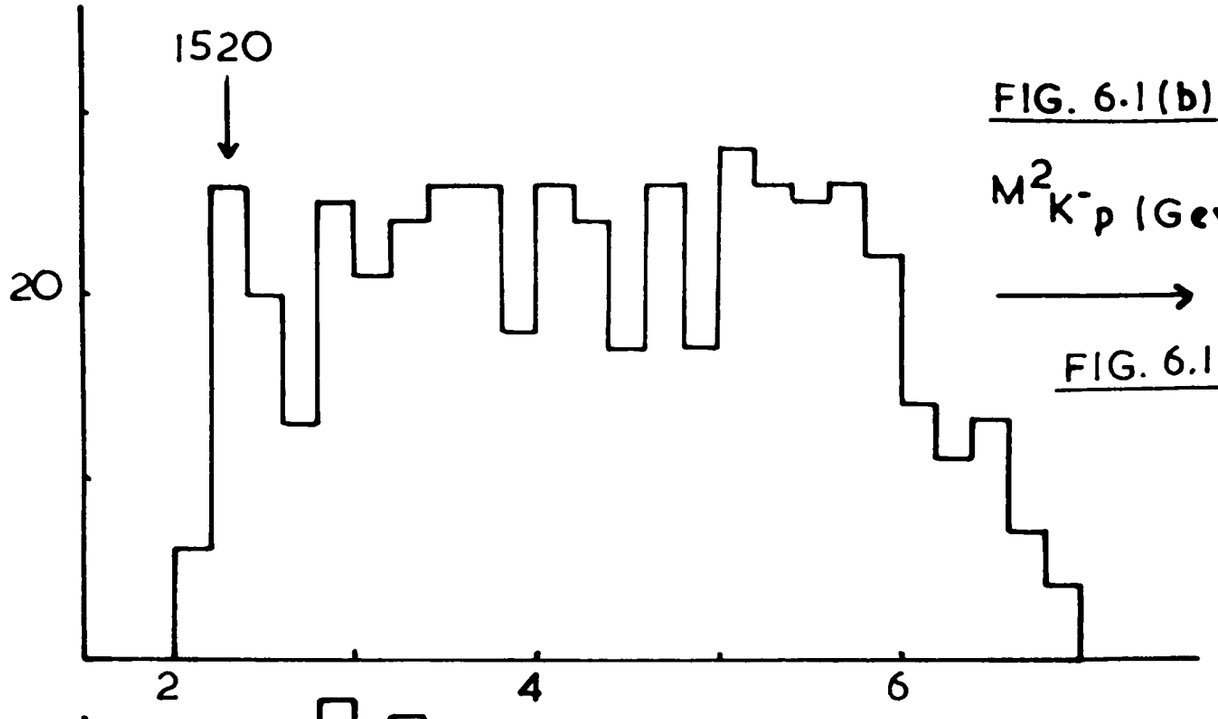

FIG. 6.1(b)

$M^2_{K^-p}$ (Gev)^2

FIG. 6.1(b)

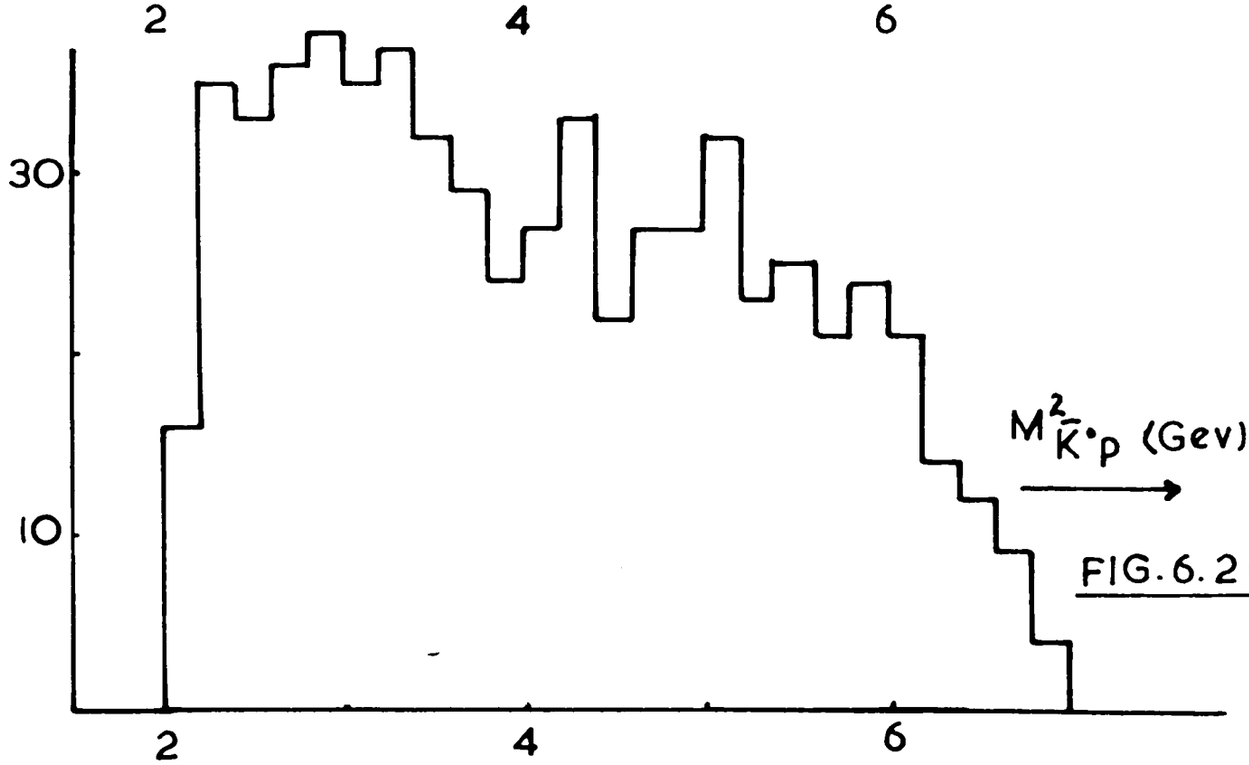

Events/
0.2 Gev^2

$M^2_{\bar{K}^0p}$ (Gev)^2

FIG. 6.2(b)

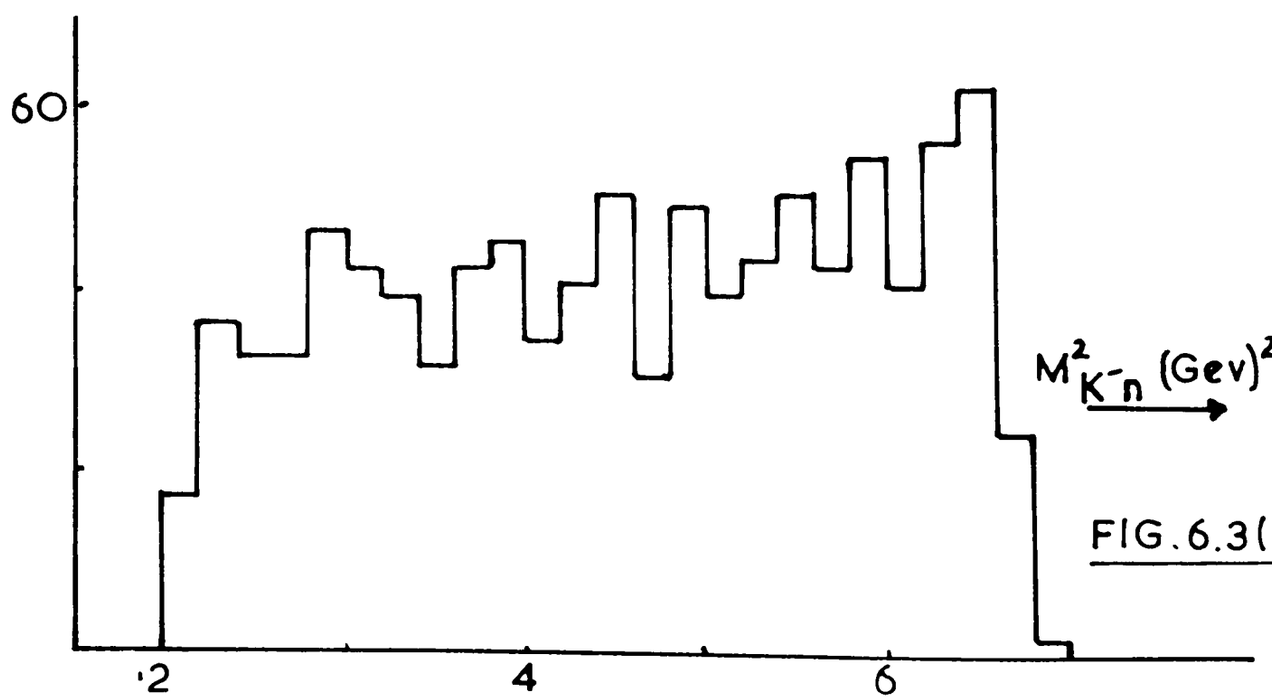

$M^2_{K^-n}$ (Gev)^2

FIG. 6.3(b)

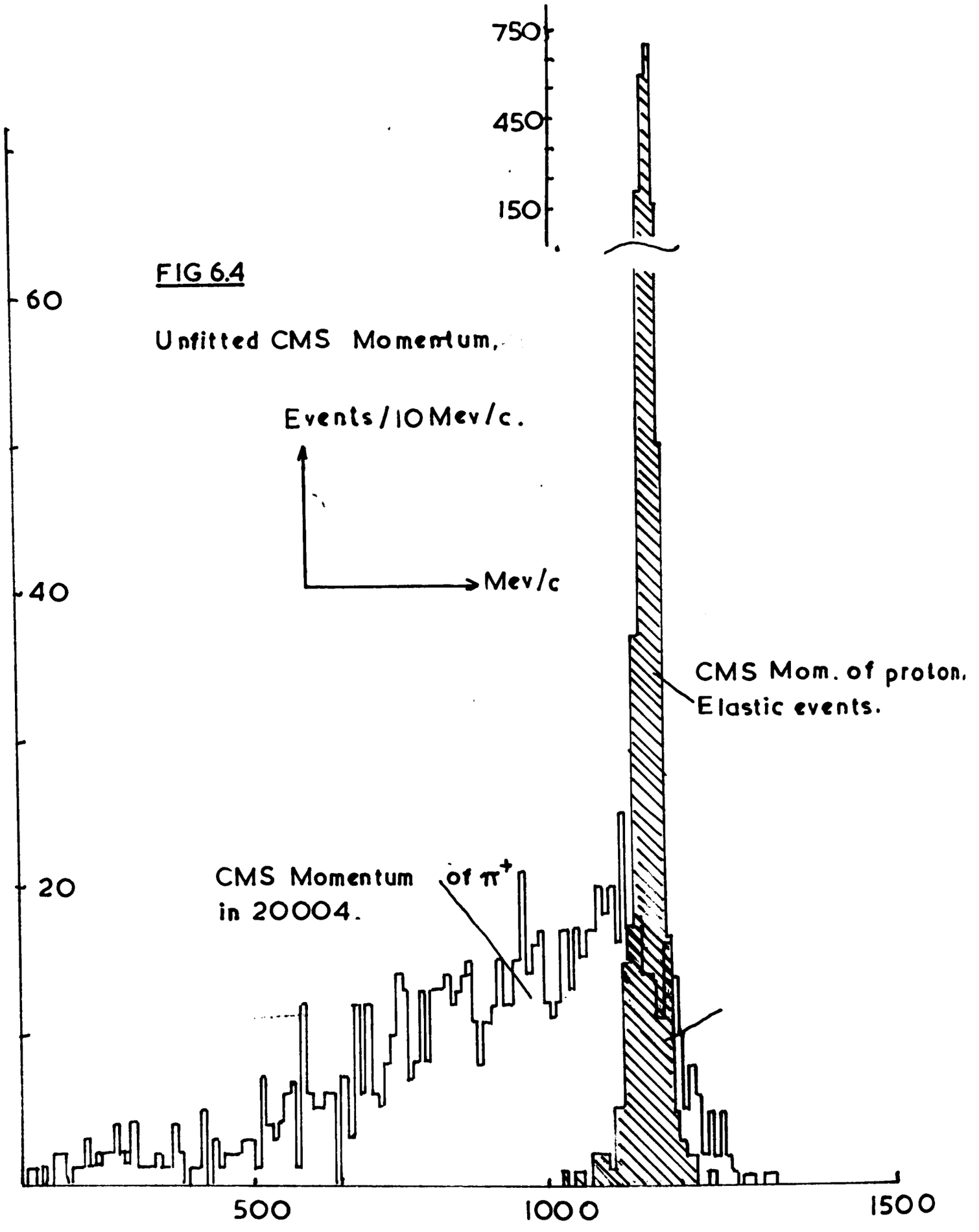
750
450
150
60
40
20
FIG 6.4
Unfitted CMS Momentum,
Events / 10 Mev/c.
Mev/c
CMS Mom. of proton,
Elastic events.
CMS Momentum of π^+
in 20004.
500
1000
1500

(i.e. probability $> 0.1\%$ or $\chi^2 < 18.4$)

(2) Investigation of the effect of any remaining contamination.

The events removed by (1) are shown shaded in the mass plots of Figs. 6.3, 4 where it is seen that the low mass peak in the $n\pi^+$ system remains, though to a much reduced extent. It is suggested from the numbers of these shaded events that the major contamination from any badly measured elastic events might occur in reaction (4). However, the main source of concern is the effect - if any - of such a contamination upon the decay angles (defined in Appendix E) of the K*'s.

One may understand the strong contamination of reaction (4) from the fact that in this case one needs to wrongly identify the proton track which is well measured. That this is so is seen from Fig.6.4(a) which shows the distribution of measured value for the centre of mass system (CMS) momentum of the particle, and it is seen to be a fairly narrow distribution about the expected value of 1.17 Gev/c. It was mentioned in Chapter II that three helices are fitted to the measurement of slower tracks - one for each of the masses of the p, K and π particles. Consequently the assumption of the pion mass for the positive, slow track of an elastic event would lead to a wrongly identified

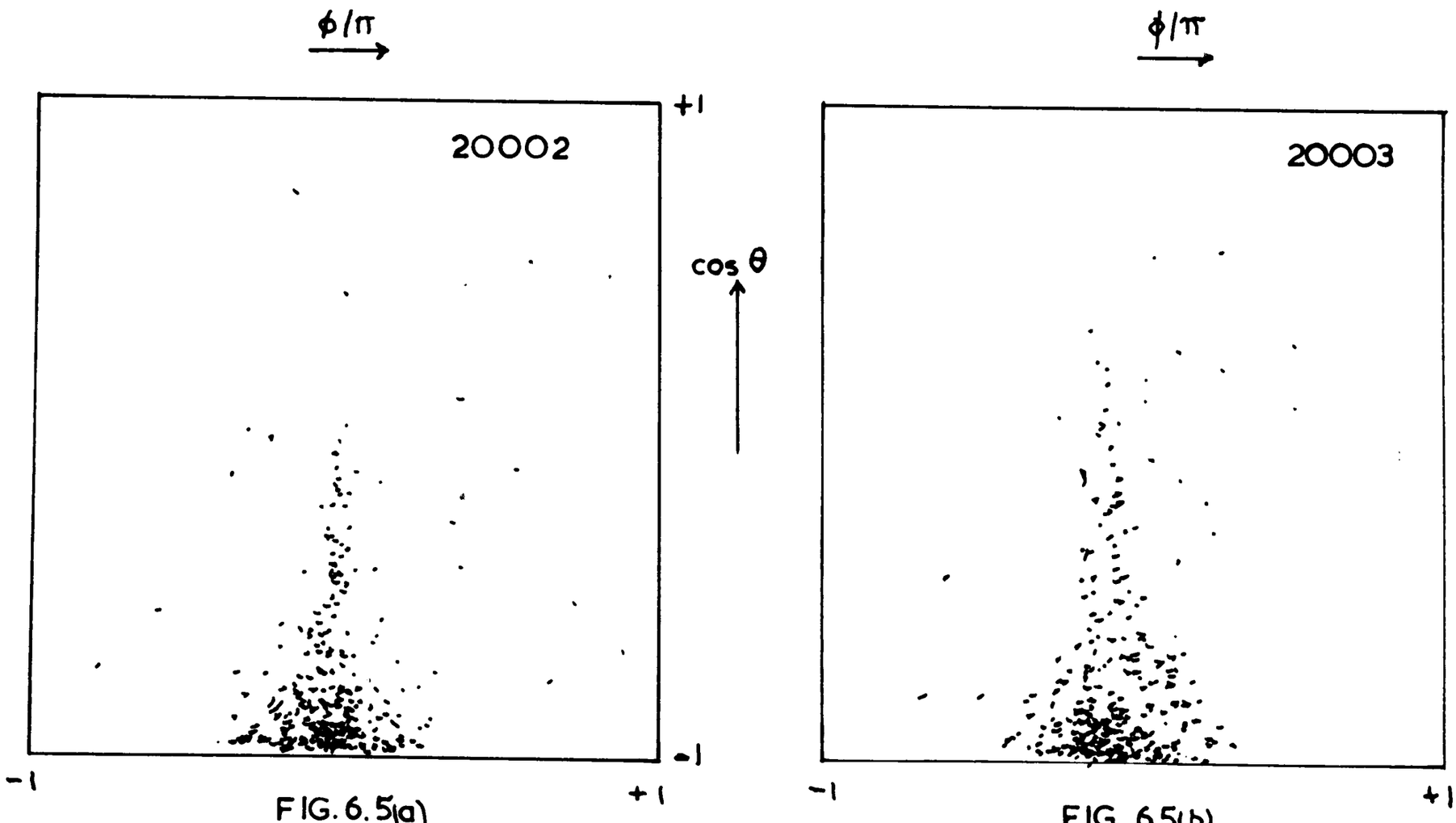

FIG. 6.5(a)

FIG. 6.5(b)

Faked Elastic Contamination

momentum, though usually in the correct direction. The missing momentum thus introduced allows the satisfaction of the kinematic constraints of energy and momentum balance by the introduction of a neutron having a direction almost coincident with the "π^+". Further, the small laboratory momentum of both these particles leads to a small relative momentum and low invariant mass. The effect upon the K* decay angles (see Appendix E) of such an event is obvious since not only do the three particles (K^-, n, π^+) have to be approximately coplanar, but the scattering angle (θ_{K^*}) is peaked at very low values (since this is really the K^- scattering angle of an elastic event). Consequently, one expects a clustering of points about the region $\cos\theta_{K\pi} = +1$ and $\phi_{K\pi} = 0$ (or $\pm\pi$). The corresponding effect of elastic contamination upon the other reactions is less obvious. An idea of its nature may be obtained from a faked sample of such events generated by taking the measured values for the tracks of events known to be elastic. The assignment of the required masses to the charged tracks, and to the missing momentum vector in order to simulate either reaction (2) or (3) led to the manufacture of events which satisfied momentum, though not necessarily energy, conservation. The ($\cos\theta_{K\pi}$, $\phi_{K\pi}$) scatter plots for these events (Fig.6.5(a)

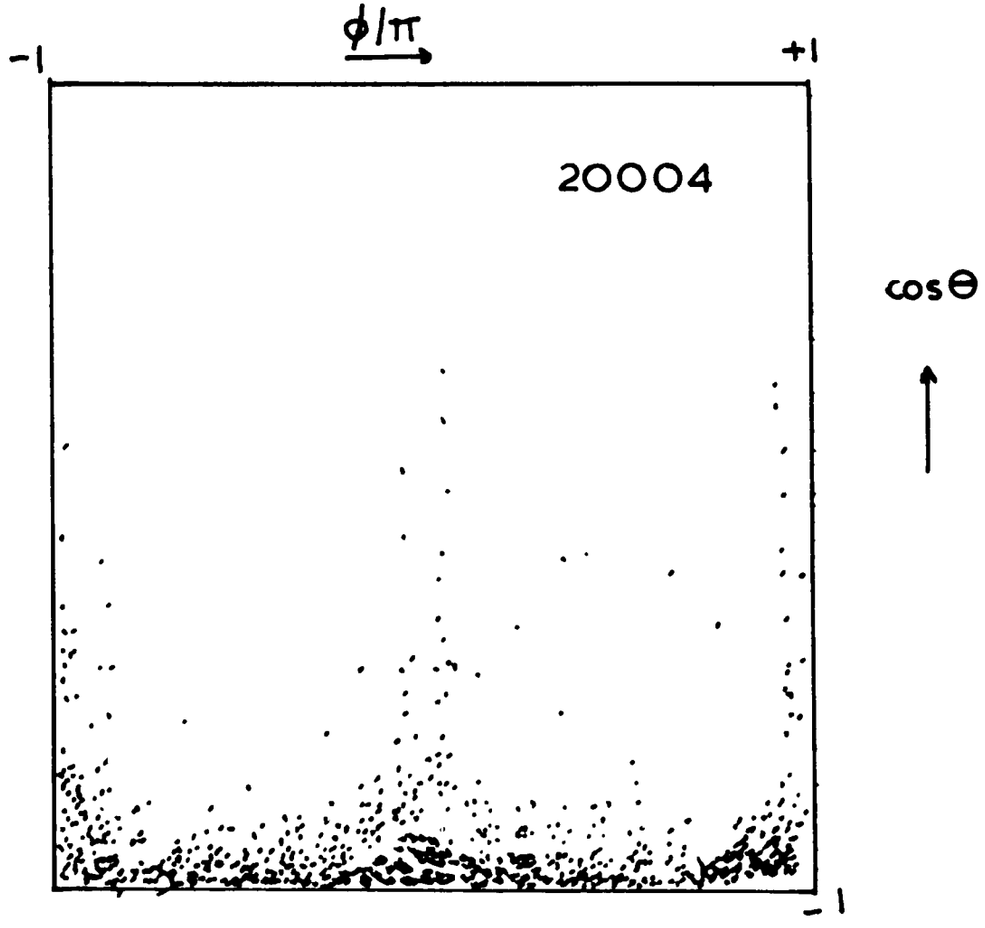

FIG 6.5(c)

Faked Elastic Contamination.

and (b)) show a marked assymmetry. That the failure of these events to satisfy energy conservation may have caused such a bias is uncertain. However, it is observed that a similarly faked sample of reaction (4) events exhibited the $(\cos\theta_{K-\pi^+}, \phi_{K-\pi^+})$ distribution shown in Fig. 6.5(c) which is just what one would have expected from the previous considerations.

Conclusions Regarding Elastic Contamination

It is clear that reaction (4) is most highly contaminated though any inclusion of elastic events in the other reactions would create a considerable bias in the decay angles. Consequently, some effort has been made to remove such a possibility by excluding events from the parts of the $(\cos\theta, \phi)$ plots most affected.

The Isotopic Spin of the K**(1400)

A direct comparison of the two reactions:

$$K^- p \rightarrow K^{**}(1400)^- p \quad \text{(reaction (2))} \quad \ldots\ldots (5)$$
$$\hookrightarrow K^- \pi^0$$

$$K^- p \rightarrow K^{**}(1400)^- p \quad \text{(reaction (3))} \quad \ldots\ldots (6)$$
$$\hookrightarrow \bar{K}^0 \pi^-$$

should yield a value for the K**(1400) isotopic spin.

The relative rates for these two decays $(\bar{K}^- \pi^0 : \bar{K}^0 \pi^-)$ should be either $\frac{1}{2}$ for isotopic spin $(T=\frac{1}{2})$ or 2 if the

other assignment (T = 3/2) applies.

Unfortunately, certain difficulties arose as pointed out in the previous chapter:

(a) considerable kinematic ambiguity exists in the identification of reactions (2) and (3) in particular with possible incoming pion hypotheses.

(b) some mutual ambiguity exists between the two reactions.

Consequently, the events were divided into the following classes:-

1. Unique reaction (2) or ambiguous with anything other than reaction (3) - 422 events

2. Unique reaction (3) or ambiguous with anything other than (3) - 490 events

3. Ambiguous between (2) and (3) - 143 events.

An attempt to remove the elastic events was made in the manner described in the previous section by removing those with certain values of $\cos\theta$ and ϕ. As pointed out in Appendix E, this should not bias the distribution of points on the Dalitz plot as the variables $M^2_{p\pi}$, $M^2_{N\pi}$, θ and ϕ should all be independent.

Determination of the Resonant Fractions

A method similar to that used by Ferro Luzzi et al[5] in the analysis of the reaction $K^+p \rightarrow K^0p\pi^+$ has been used

to determine the resonance production cross-sections. In this method one fits the density of points on the Dalitz plot for each reaction. In order to derive an expression for this density one assumes that the amplitude for production of a resonance can be written as:

$$T(M^2) = \frac{(\Gamma M_o)^{\frac{1}{2}}}{M^2 - M_o^2 - i M_o} \quad \ldots\ (7)$$

which, when its square modulus is taken, is the well-known relativistic Breit-Wigner distribution. It is thus assumed that the amplitude depends only upon the invariant mass M of the system forming the resonance, the resonant mass M_o and width Γ. The latter is connected with the resonance decay amplitude V by: $\Gamma = \frac{1}{32\pi^3} \frac{1}{2J+1} \int |V|^2 \, d\Omega$ integration being over the decay angles of the resonance. Expressions for Γ are given by Jackson[6] and relevant ones are:

$$N^*(1238) \rightarrow N\pi : \Gamma = \Gamma_o \left(\frac{p}{p_o}\right)^3 \cdot \frac{(M_{N\pi}+m_N)^2 - m_\pi^2}{M_{N\pi}^2} \cdot \frac{M_{N^*}^2}{(M_{N^*}+m_N)^2 - m_\pi^2}$$

$$\bar{K}^*(890) \rightarrow \bar{K}\pi : \Gamma = \Gamma_o \left(\frac{p}{p_o}\right)^3 \left(\frac{M_{K^*}}{M_{K\pi}}\right) \quad \ldots\ (8)$$

$$\bar{K}^*(1400) \rightarrow \bar{K}\pi : \Gamma = \Gamma_o \left(\frac{p}{p_o}\right)^5 \left(\frac{M_{K^*}}{M_{K\pi}}\right)^4$$

In these expressions the relative momentum of the 2 decay products in the resonance rest frame is p whilst m_N, m_π and m_K are, respectively, the nucleon, pion, and kaon

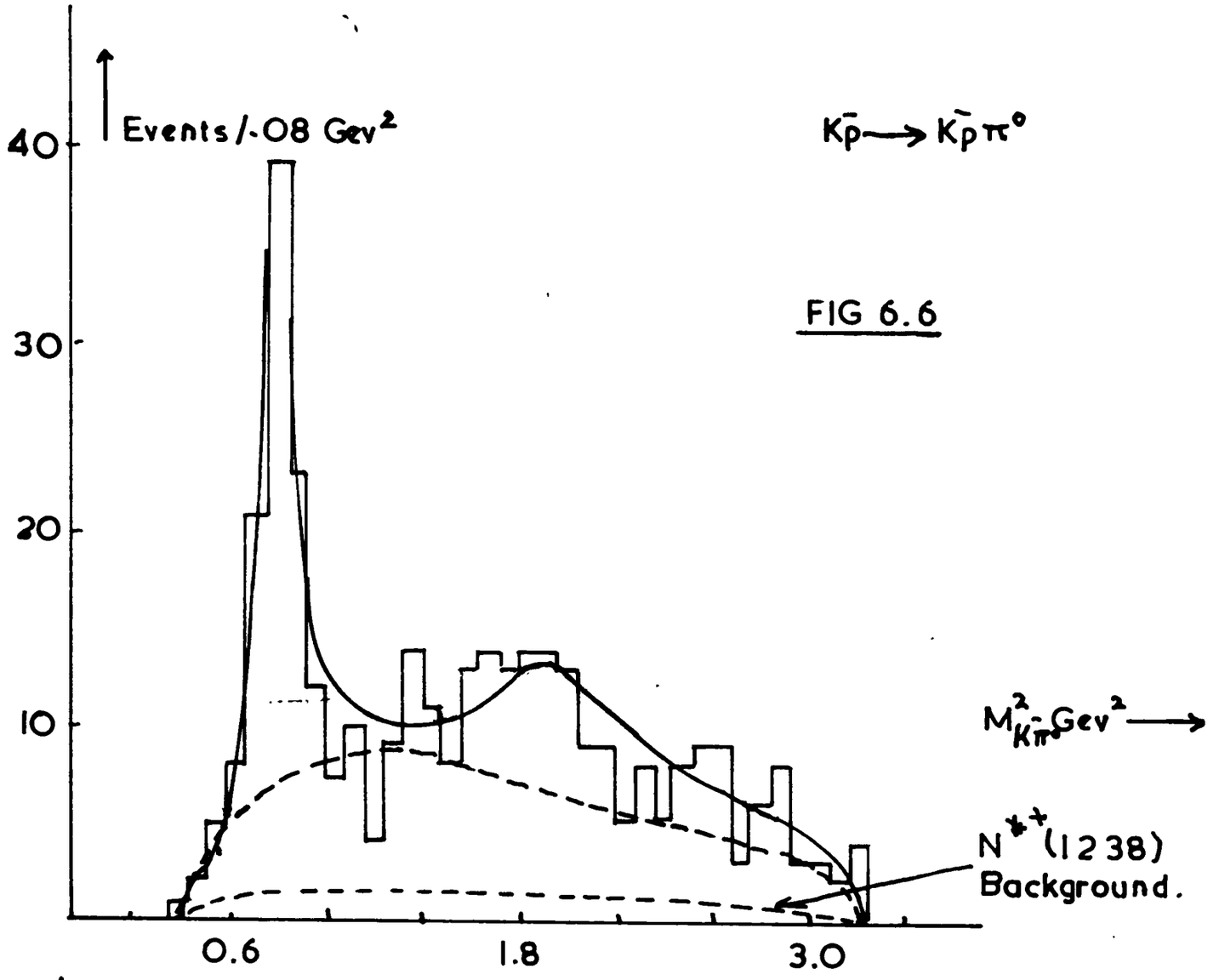
Events/.08 Gev²
$K^-p \rightarrow K^-p\pi^0$
40
30
20
10
$M^2_{K\pi^0}$ Gev² ⟶
$N^{*+}(1238)$
Background.
0.6
1.8
3.0

FIG 6.6

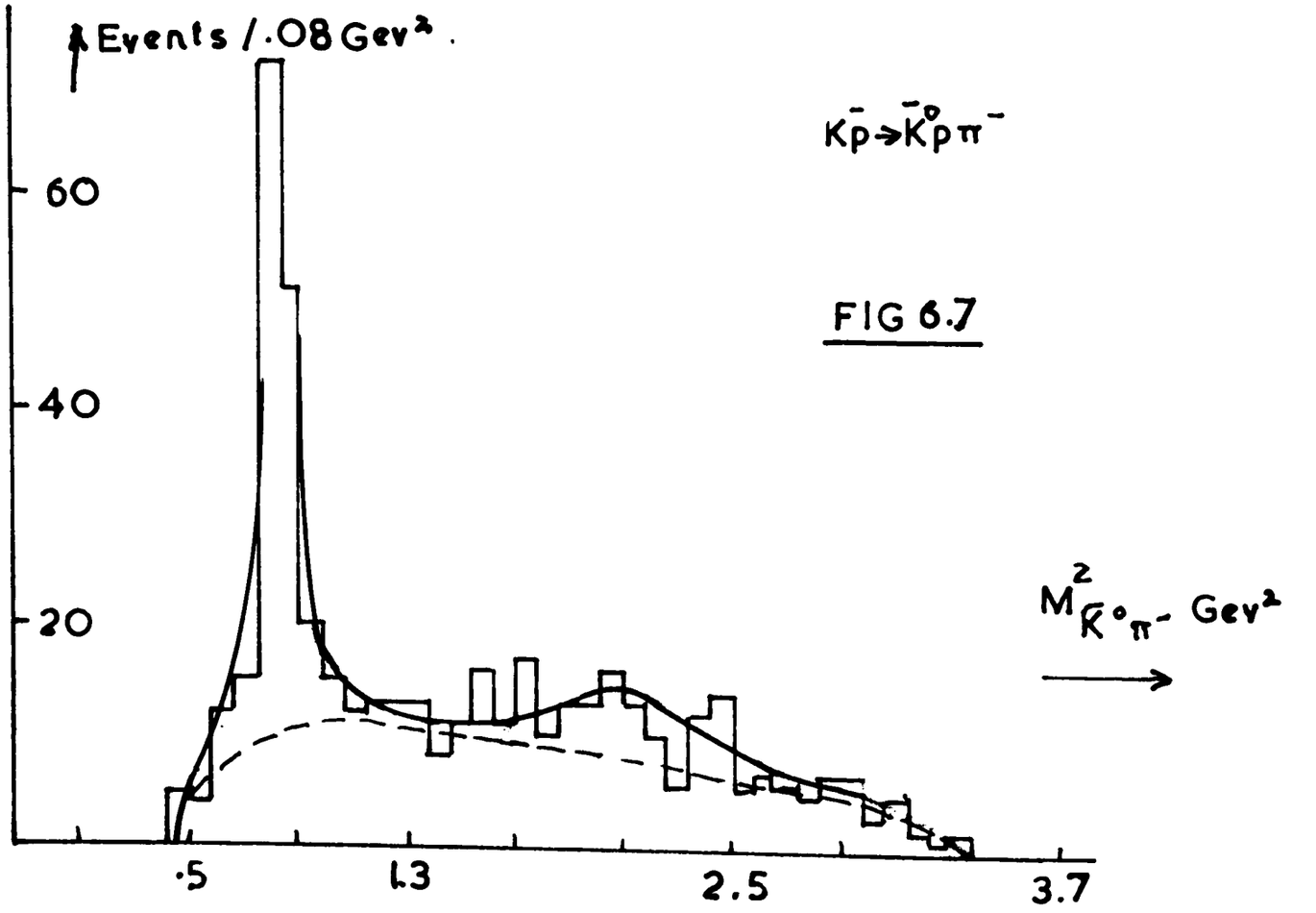
Events /.08 Gev²
$K^-p \rightarrow \bar{K}^0p\pi^-$
60
40
20
$M^2_{\bar{K}^0\pi^-}$ Gev²
⟶
.5
1.3
2.5
3.7

FIG 6.7

masses, and the expressions normalized such that $\Gamma = \Gamma_o$ at the resonant mass. p_o is the value of p at the resonant mass. As interest lay mainly in the cross-sections for the decays of the K** it was only necessary to fit the density of points on the Dalitz plot to obtain the best values for all resonant masses, widths and fractions. The method is discussed in more detail in the following chapter where the application to the many body final states is discussed but it is noted here that the density function may be written as:-

$$G(M_K^2, M_N^2) = \sum_{j=1}^{k} \left(\frac{f_j}{N_j} T_j \frac{2M_j}{q_j} - f_j\right)\phi + \phi \qquad \ldots\ (9)$$

where ϕ is the phase space density of points, f_j the fraction of the jth process (of which there are k) present, T_j its amplitude with the invariant mass M_j as argument as well as the resonant mass M_j^o and width $\Gamma(M_j)$. The denominator q_j is the relative momentum of the system j and the odd particle in the overall centre of mass.

The processes considered in the reactions (2) and (3) were:

$$K^- p \rightarrow \bar{K}^0 p \pi^0$$

$$\rightarrow \bar{K}^*(890)^- p$$

$$\rightarrow \bar{K}^{**}(1400)^- p$$

$$\rightarrow N^{*+}(1238)\, \bar{K}^0$$

TABLE 1

Results of Dalitz Plot Analysis

Reaction	Resonance	Mass (Mev)	Width (Mev)	% of Final State	No.of events	Cross-Section(μb)
$K^- p \rightarrow$ $\Lambda^- p \pi^0$	$K^{*-}(890)$	896 ± 4	52.5 ± 8.8	20.6 ± 2.5	87.0 ± 10.5	205 ± 25
	$N^{*+}(1238)$	1230 ± 20	170 ± 46	14.0 ± 2.6	59.1 ± 11.0	139 ± 26
	$K^{**-}(1400)$	1402 ± 20	160 ± 50	11.8 ± 2.8	49.8 ± 11.8	118 ± 28
$K^- p \rightarrow$ $\Lambda^0 p \pi^-$	$K^{*-}(890)$	898.7 ± 3.3	49.5 ± 8.6	30.4 ± 3.1	148.9 ± 15.2	527 ± 54
	$N^{*0}(1238)$	1238 fixed	125 fixed	1.7 ± 1.6	8.3 ± 7.8	29 ± 28
	$K^{**-}(1400)$	1440 ± 40	170 ± 72	9.8 ± 3.0	47.9 ± 14.7	170 ± 52
$K^- p \rightarrow$ $\Lambda^0 \pi^0 \pi^-$ ambig.with $\Lambda^0 p \pi^-$	$K^{*-}(890)$	898 fixed	50 fixed	11.0 ± 2.5	15.7 ± 3.6	
	$N^{*0}(1238)$	1238 fixed	125 fixed	-1.3 ± 2.0	-1.8 ± 2.9	
	$K^{**-}(1400)$	1420 fixed	160 fixed	7.6 ± 2.4	10.9 ± 3.4	
$K^- p \rightarrow$ $K^- p \pi^0$	$K^{*0}(890)$	900.5 ± 5.7	66.3 ± 18.0	25.3 ± 3.7	234.9 ± 34.4	555 ± 81
	$N^{*+}(1238)$	1226 ± 24	169 ± 47	15.0 ± 2.6	139.0 ± 24.1	328 ± 57
	$K^{**0}(1400)$	1420 ± 17	151 ± 30	14.3 ± 2.8	132.8 ± 26.0	312 ± 61

The effect of the $Y^{*0}(1520)$ was neglected as its production was relatively weak. The normalization integrals:

$$N_j = \frac{\iint |T_j|^2 \phi \frac{M_j}{q_j} \, dM_K^2 dM_N^2}{\iint \phi \, dM_K^2 \, dM_N^2}$$

are very simple in this case since we assume that:-

1. ϕ = constant

2. T is a function of only one mass .

Consequently, integration over one of the masses leads to the expression for N_A:

$$N_A = \frac{\int T_A^2 \, \frac{M_A}{q} \, \frac{pq}{M_A} \, dM_A^2}{\int \frac{pq}{M_A} \, dM_A^2} \qquad \ldots\ldots (10)$$

where p is the relative momentum of the particles forming system A in their own rest frame, M_A is their invariant mass, and q the relative momentum of system A and the third particle in the overall CMS. Equation (10) ensures that G is normalized such that: $\iint G \, dM_K^2 \, dM_N^2 = \phi$ = constant

The method employed to fit the data was that of maximum likelihood. The likelihood function was constructed from the values of G for each event and was L given by:

$$L = \sum_{i=1}^{N_T} \ln(G_i) \qquad \ldots\ldots (11)$$

where the summation was over the N_T events.

All variables (masses, widths and fractions) were

TABLE II

K**(1400) Mass, Width & Isospin

	Reaction	Beam Energy (Gev/c)	Mass	Width	Isospin
Reference 1	$K^- p \rightarrow \bar{K}^0 p \pi^-$	3.5	1400± 10	160	-
Reference 2	$\pi^- p \rightarrow \Lambda \pi^- K^+$ $\rightarrow \Sigma^0 \pi^- K^+$	3.9 & 4.2	1430±20	100±20	$\frac{1}{2}$ Preferred
Reference 3	$K^- p \rightarrow \bar{K}^0 p \pi^-$	3.0	1399±24 14	92±26	) $\frac{1}{2}$
	$\rightarrow K^- p \pi^0$		1417±11	86±9	)
	$\rightarrow K^0 \pi^+ n$		1400±12	92±12	
This Experiment	$K^- p \rightarrow \bar{K}^0 p \pi^-$	3.5	1440±40	170±72	) $\frac{1}{2}$
	$\rightarrow K^- p \pi^0$		1402±20	160±50	)
	$\rightarrow K^0 \pi^+ n$		1420±17	151±30	

allowed to vary and the method of maximization is described in Appendix D. The values obtained are shown in Tables I and II and are in good agreement with those of other workers.[1,4,2] Figs. 6.10 and 11 show the invariant masses with the fitted curves (solid lines) superimposed for reactions (2) and (3) respectively. The dotted lines illustrate the background (non-resonant) curves and indicate that the K*(890) is very pure in the mass region $0.83 < M_K < 0.95$ Mev whilst the K**(1400) has a considerable proportion of background events having $K\pi$ mass in its vicinity. This background includes genuine non-resonant K-induced processes, other resonant processes and some π-induced reactions which are assumed to contribute a uniform density of points on the Dalitz plot. The curves were estimated by generating Monte Carlo events having a production cross-section $\propto |T|^2$ for each process.

The effect of interference between any processes was ignored or, more precisely, the phase angle δ_{AB} which appears in the extra term necessary to equation (9) to account for interference between a pair of such processes A and B:

$$\frac{2\sqrt{f_A f_B \Gamma_A \Gamma_B T_A T_B}}{N_{AB}} \cdot \cos \delta_{AB}$$

was assumed to be 90^0. No noticeable enhancement or depopulation of events in the N*K* crossover region in the Dalitz plot of reaction (2) was noticed, for instance, and it appears unnecessary to assume any marked interference between any of the other processes.

The resulting resonance fractions are summarized in Table I. The significance of the method just described is that account is automatically taken of any background reactions contributing uniformly to the Dalitz plot. It appears reasonable, therefore, to accept the cross-sections in the last column of Table I as absolute, since it is unlikely that any events other than those corresponding to reactions (5) or (6) would contribute to enhancements in the invariant mass of the negative and neutral particles in the region of the K*s. Considering the "unique" events alone, one then sees that the ratio of K*(890) decays into $K^-\pi^0$ to those into $\bar{K}^0\pi^-$ is almost correct (1:2) within just a little more than one standard deviation, which encourages this point of view. Extending the argument to the K**(1400) it is seen that the observed decay rates into the two charge combinations are certainly (within error) in the same ratio and not the other way round(2:1) as required by an isospin of 3/2. It is seen that the ambiguous events

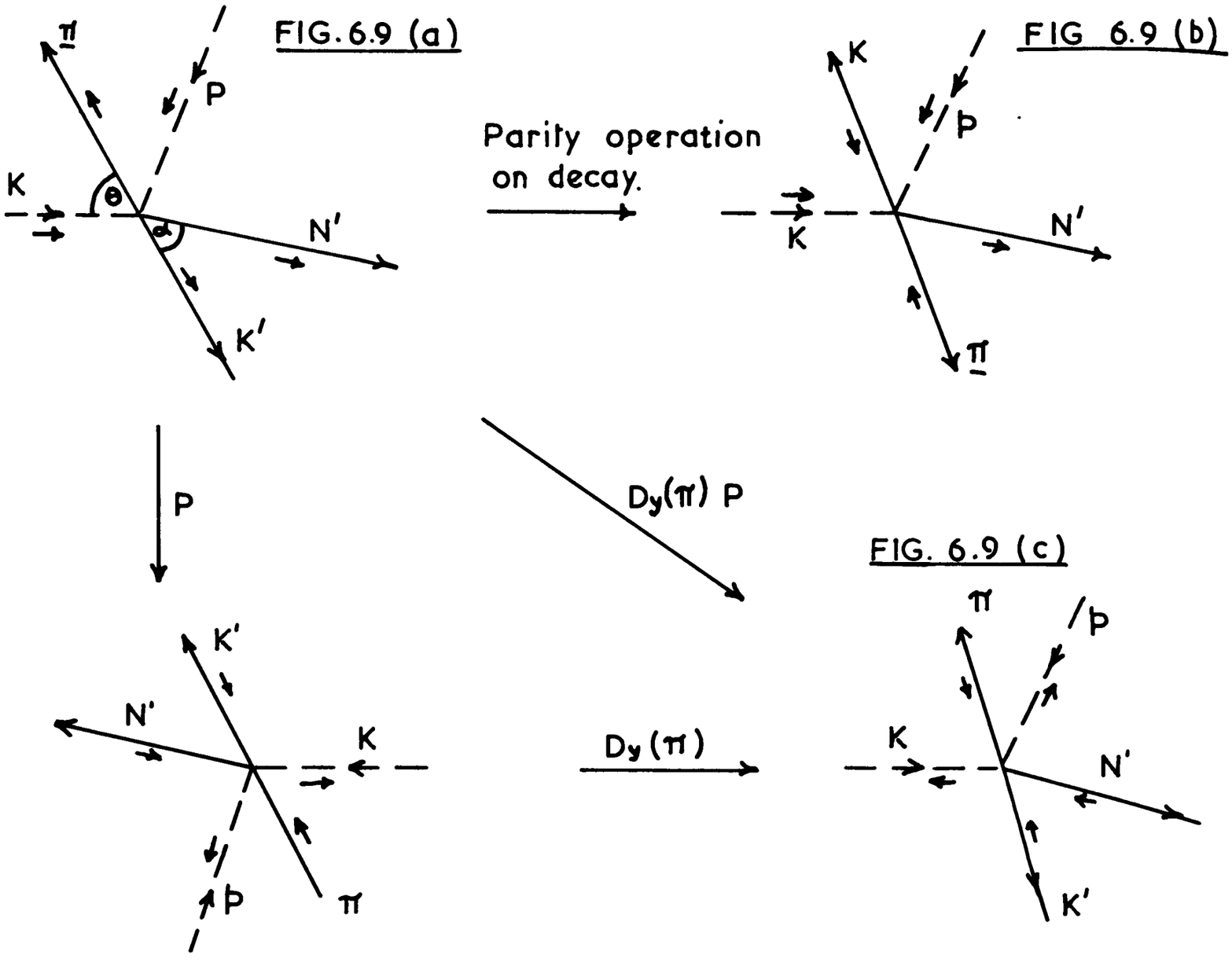

FIG. 6.9 Decay Symmetries. (Initial state particles drawn dotted.)

cannot significantly affect the conclusion that the isotopic spin of the K**(1400) is not 3/2 since, even if all of them were considered to belong to reaction (2), the maximum number of K**(1400)$\rightarrow \bar{K}\pi^0$ that could be collected would be (49.8 + 11.8) + (10.9 + 3.4) = 75;9 to be compared with the smallest number of K**(1400)$\rightarrow \bar{K}^0\pi^-$ of (71.8 - 22.1) = 49.7 giving a ratio of 1.52.

Decay of the K* Resonances

Symmetries in the Decay Distributions

Fig. 6.9. illustrates the three body final state in the $K\pi$ rest frame. The notation employed is the same as that used in the discussion of the kinematics. (Appendix E)

As a consequence of parity conservation, some simple results follow which have been used in the analysis. Applying the parity operation to the decay, one sees in Fig. 6.9(a) that the vectors $\vec{K}'$ and $\vec{\pi}$ change places. The resulting situation (Fig. 6.9(b)) is therefore expected to occur just as frequently as that in Fig. 6.9(a). Consequently the decay distribution is expected to be symmetric about $\alpha = \pi/2$. A similar result may be obtained by the simultaneous change of θ to $\pi - \theta$ and ϕ to $\phi + \pi$ so that symmetry with respect to such a change is also expected.

A further result follows from the fact that in a two body production process involving only strong interactions

if the initial state is one of random polarization, both initial and final states are symmetric under the operation $D_y(\pi)P$,[7] where P is the parity operator and $D_j(\gamma)$ causes a rotation through angle γ about the y-axis. Applying these two operations to Fig. 6.9(a) leads to 6.9(c) where the small arrows indicate the spins. It is observed that these have all changed sign whilst the momenta remain unchanged. Furthermore, the sign of ϕ has reversed. Thus, in such a process, one expects no polarization of the K* in the production plane and a further condition on the decay distribution is that it is symmetric about $\phi = 0$. If T denotes the decay distribution then we may summarize the results as follows:

$$T(\cos\theta, \phi, \cos\alpha) = T(-\cos\theta, \phi+\pi, -\cos\alpha)$$
$$= T(\cos\theta, -\phi, \cos\alpha) \quad \ldots\ (12)$$

The Density Matrix

ther The method employed to determine the spin of the K*[8] was to examine the decay distribution to test whether 1^- or 2^+ provided the better description for the observed $(\cos\theta, \phi)$ distributions. Higher spins were neglected and unnatural spin parities forbidden by the fact that the $K\pi$ decay is observed. It is usual to define the density matrix $\rho_{mm'}$ by:[7] $\langle Q \rangle = Tr(\rho Q)$ where Q is some physical

observable. Other properties of this spin-space matrix include:-

1. It is Hermitian $\rho_{mm'} = \rho_{m'm}^*$
2. $0 \leq \rho_{mm} \leq 1$ and ρ_{mm} is real
3. $Tr(\rho I) = Tr(\rho) = 1$ (I is the unit operator)
4. $\rho_{mm'} = (-1)^{m-m'} \rho_{-m,-m'}$ which follows from parity conservation.

In the magnetic quantum state representation, ρ for a particle of spin J requires $2(2J+1)^2$ real quantities in its complete specification. However, in view of some of the constraints imposed above, this number is somewhat reduced. (e.g. to 14 in the case of a spin 2 particle). For the decay of a state of definite spin-parity J^P into two spinless particles, the amplitude can be expanded in orbital angular momentum states $|J,m\rangle = Y_J^m$.

Using the definition of the density matrix it can therefore be shown that the distribution for such a state decaying into 2 spinless particles may be written as: [9]

$$W_J(\cos\theta, \phi) = \frac{\partial^2 \sigma}{\partial(\cos\theta)\partial\phi} = \sum_{mm'} Y_m^J(\vec{\alpha})\, Y_{m'}^{J*}(\vec{\alpha})\, \rho_{mm'} \quad \ldots\ldots (13)$$

where the Y's are spherical harmonics and the unit vector $\vec{\alpha}$ has the azimuthal and polar angles θ, ϕ defined above. Explicitly: for spin $1^- \rightarrow 0^-0^-$

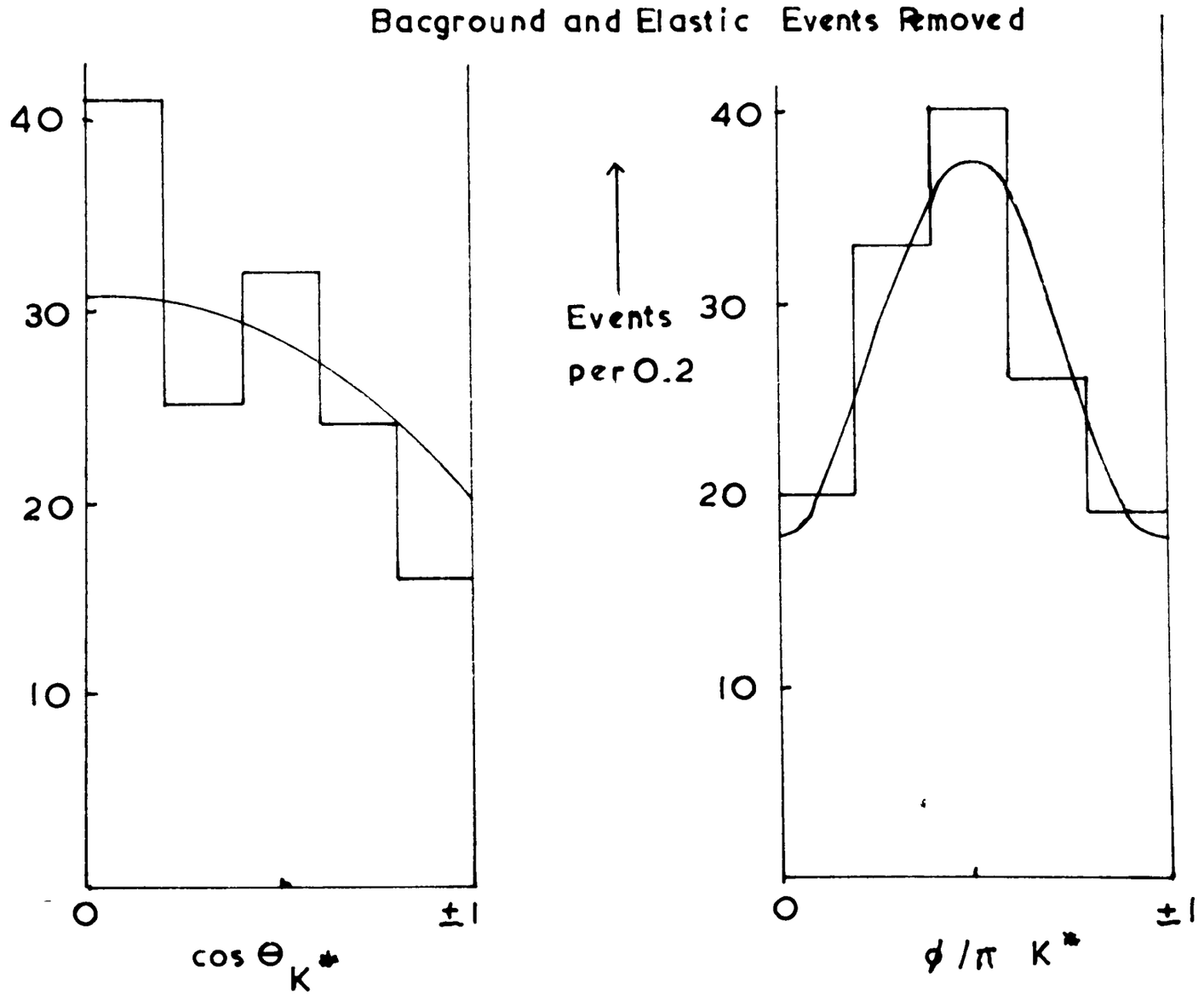

FIG 6.11 — Folded Angular Distributions With Fitted Curves For $\bar{K}^{*}(890)$.

$$W_1(\cos\theta, \phi) = \frac{\partial^2\sigma}{\partial(\cos\theta)\partial\phi} = \frac{3}{4\pi}(\rho_{00}\cos^2\theta + \rho_{11}\sin^2\theta - \rho_{1-1}\sin^2\theta\cos 2\phi - \sqrt{2}\,\mathrm{Re}\,\rho_{10}\sin 2\theta\cos\phi) \quad \ldots\ (14)$$

and for spin $2^+ \to 0^-0^-$

$$W_2(\cos\theta,\phi) = \frac{15}{16\pi}\Big[3\rho_{00}(\cos^2\theta-\tfrac{1}{3})^2 + 4\rho_{11}\sin^2\theta\cos^2\theta + \rho_{22}\sin^4\theta - 2\cos\phi\Big\{\sin 2\theta\,\mathrm{Re}\,\rho_{21}\sin^2\theta + \sqrt{6}\,\mathrm{Re}\,\rho_{10}(\cos^2\theta-\tfrac{1}{3})\Big\} + 2\mathrm{Re}\,\rho_{2-1}\cos 3\phi\sin^2\theta\sin 2\theta + \rho_{2-2}\cos 4\phi\sin^4\theta - 2\cos 2\phi\sin^2\theta\Big\{2\rho_{1-1}\cos^2\theta - \sqrt{6}\,\mathrm{Re}\,\rho_{20}(\cos^2\theta-\tfrac{1}{3})\Big\}\Big] \quad \ldots\ (15)$$

The factors $3/4\pi$ and $15/16\pi$ normalize the integration of the product $Y^J_m\, Y^{J*}_{m'}$ over θ and ϕ to unity.

<u>K*(890)⁻Decay</u>

Selecting all events in reactions (2) and (3) having a $\bar{K}\pi$ invariant mass between 830 and 950 Mev, we have chosen a sample containing 80% K*(890) with some background. Choosing, also a sample having $\bar{K}\pi$ masses between 770-830 Mev or 950-1010 Mev we have 50% K*(890) and 50% background. Using the method suggested, for instance, in reference [10] to determine the components of the density matrix by background subtraction, the former events were given a weight of one and the latter the weight of minusonein analysing the decay distribution. In this way it was

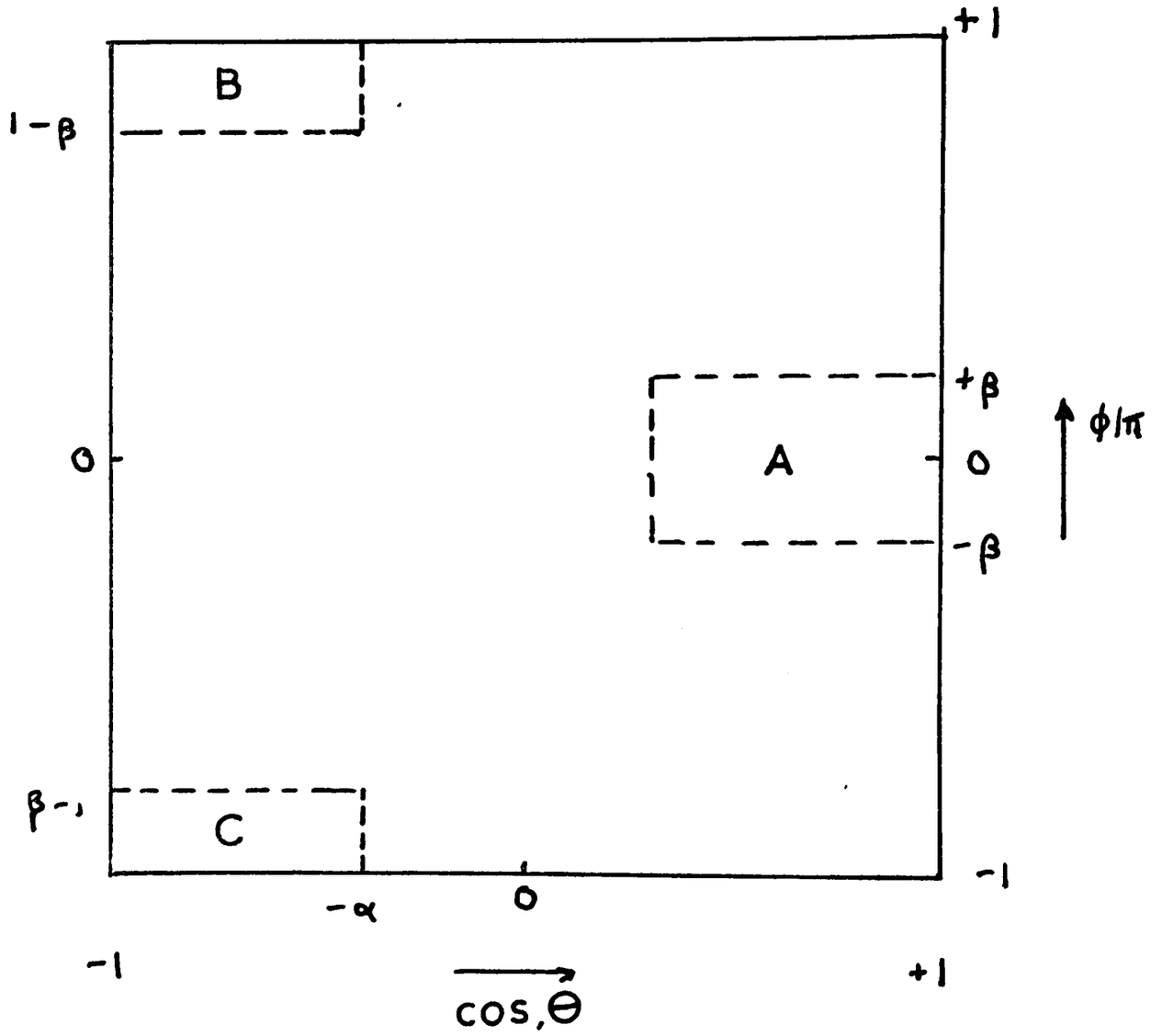

$\alpha = 0.3$

$\beta = 0.2$

FIG 6.10

hoped that the effect of incoherent background would have been removed. The method of maximum likelihood involves the construction of the likelihood function:

$$L(\rho) = \sum_{i=1}^{N} w_i \ln W_1(\cos\theta_i, \phi_i) \qquad \ldots\ (16)$$

where w_i is the weight of the ith event (of which there are N) and ρ the density matrix with $W_1(\cos\theta_i, \phi_i, \rho)$ being the value of the distribution (equation (14)) for the ith event. This method was adopted, and the simultaneous variation of the three parameters ρ_{00}, ρ_{1-1} and $Re\rho_{10}$ was carried out again by the procedure outlined in Appendix D in order to maximize L. It should be observed that W is already normalized to unity. However, removal of events from the $(\cos\theta, \phi)$ plot as suggested to remove elastic contamination invalidates this normalization since one must now ensure that

$$\int_{-1}^{+1}\int_{-\pi}^{+\pi} W(\cos\theta, \phi)\, d\cos\theta\, d\phi - \int_{\alpha}^{+1}\int_{-\beta}^{+\beta} W(\cos\theta, \phi)\, d\cos\theta\, d\phi$$

where α and β are defined in Fig. 6.10.

is unity. The normalization factor therefore depends upon the density matrix values. A way of overcoming this is illustrated in Fig.6.10. After removal of events from region A, the plot may be repopulated by events from regions B and C. This follows from the symmetry principles established earlier. Consequently, region A events were

TABLE III

The Reaction $K^- p \rightarrow RN$

Element	R	Experimental	Unadorned Peripheral Model		Absorption Model Best Fit
			Vector Exchange	Pseudo Scalar Exchange	
ρ_{00}	$\bar{K}^{*0}(890)$	0.45 ± 0.09	0	1	0.55
ρ_{1-1}		-0.04 ± 0.07	0.5	0	0.09
$Re\rho_{10}$		-0.04 ± 0.04	0	0	-0.09
ρ_{00}	$K^{*-}(890)$	0.24 ± 0.06	0	1	0.20
ρ_{1-1}		0.18 ± 0.06	0.5	0	0 29
$Re\rho_{10}$		0.05 ± 0 04	0	0	-0.04
ρ_{00}	$\bar{K}^{*0}(1400)$	0 65 ± 0.08	0	1	0.79
ρ_{1-1}		-0.18 ± 0 04	0.5	0	-0.02
$Re\rho_{10}$		0.09 ± 0.06	0	0	-
$Re\rho_{21}$		-	0	0	-
$Re\rho_{20}$		0.04 ± 0.01	0	0	-
ρ_{11}		-0.19 ± 0.05	0.5	0	-
$Re\rho_{2-1}$		-	0	0	-
ρ_{2-2}		-0.10 ± 0.10	0	0	-
ρ_{00}	K^{*0} (1400)	0.3 ± 0.07	0	1	0.45
ρ_{1-1}		0.30 ± 0.03	0.5	0	0.25
$Re\rho_{10}$		-0.02 ± 0.06	0	0	-
$Re\rho_{21}$		-	0	0	-
$Re\rho_{20}$		0.06 ± 0.09	0	0	-
ρ_{11}		0.33 ± 0.18	0.5	0	-
$Re\rho_{2-1}$		-	0	0	-
ρ_{2-2}		0.10 ± 0.11	0	0	-

TABLE III (Cont.)

Resonance	† Log-Likelihood Ratio (2^+ : 1^-)
$K^{*-}(1400)$	14.3 ± 18.4
$\bar{K}^{*0}(1400)$	22.1 ± 14.4

† A. Segar – Private Communication.

TABLE III a

$K^{*-}(1400)$ Density Matrix

Matrix Element	Spin 1	Spin 2
ρ_{00}	0.71 ± 0.14	
ρ_{1-1}	0.06 ± 0.09	See Table III
$\mathrm{Re}\,\rho_{10}$	0.09 ± 0.09	

rejected and those in B and C were counted twice.

The values found for the density matrix elements are summarized in Table III for future reference. Curves calculated from these values are superimposed upon the $\cos\theta$ and ϕ projections in Figs. 6.11(a) and (b).

Spin of the K**(1400)

As already noted, the possible spin-parities for a particle decaying into $\bar{K}\pi$ are limited to the natural values: $0^+, 1^-, 2^+, 3^-$, etc. However, the observed decays into $\bar{K}^*\pi$ [11,12] and $\bar{K}\pi\pi$ are prohibited to a 0^+ particle. Spins higher than 2 were neglected. Consequently, the only values considered were 1^- and 2^+.

The decay distributions expected for these two values have been quoted in equations (14) and (15) where it is noticed that for spin 1^- there are 3 and for spin 2^+ there are 8 unknown parameters. In order to compare the two cases, then, one must first determine these parameters for each case separately. In order to do this, the maximum likelihood method was used once more with the parameter variation being carried out in the manner discussed in Appendix D. The resulting values are summarized in Table IIIa for both cases and the two values for the likelihood function compared. Denoting these by L_I and L_{II} for 1^- and 2^+ respectively, the probability ratio R is given by:

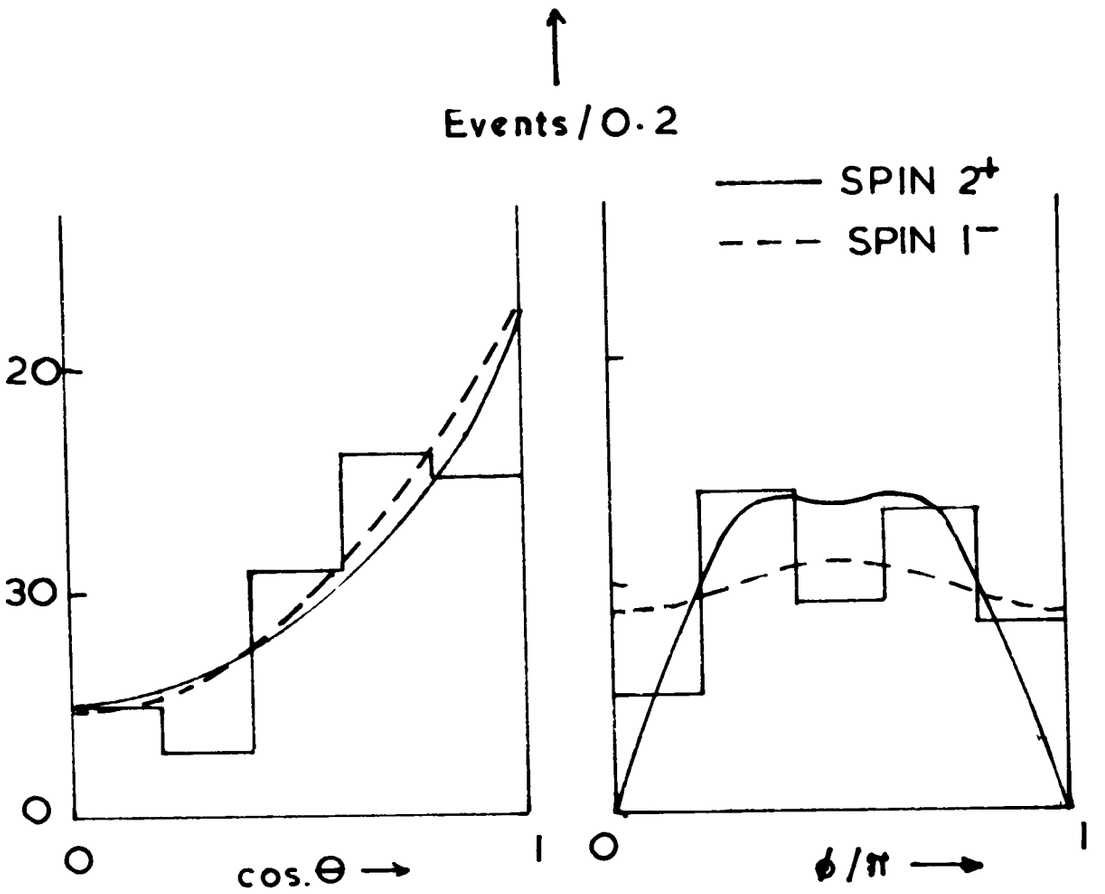

FIG 6.12 – $K^{*\pm}$(1400) Folded Decay Distributions

Plus Fitted Curves.

(Background and Elastic Events Removed.)

$$R = L_{II} - L_{I} = 14.3$$

where R is greater than unity if spin 2^+ is preferred.

Though this represents a large factor in probability the result is not so impressive when one considers the results presented in the form of Fig.6.12 where the $\cos\theta$ and ϕ distributions are shown separately, each with the fitted curves obtained by integration of W_2 (solid lines) and W_1 (dotted lines) over the other variable - superimposed. These plots also indicate the meagre nature of the data, for it is unfortunately true that the background in the K** region is considerable and subtraction by the method indicated in the previous section to give the distributions of Fig.6.12 leaves only few events. It is further noted that the 2^+ case is allowed 5 more degrees of freedom than the 1^- so consequently more chance to provide a better description of the data.

It is possible to estimate an error for this likelihood ratio,[13] and this has been done as follows. The expectation value for the likelihood ratio is:

$$\langle R \rangle_2 = N \iint \ln\left(\frac{W_2}{W_1}\right) W_2(\cos\theta, \phi)\, d\cos\theta\, d\phi$$

for N events assuming that the spin is two. The corresponding expectation value if spin 1^- is true is:

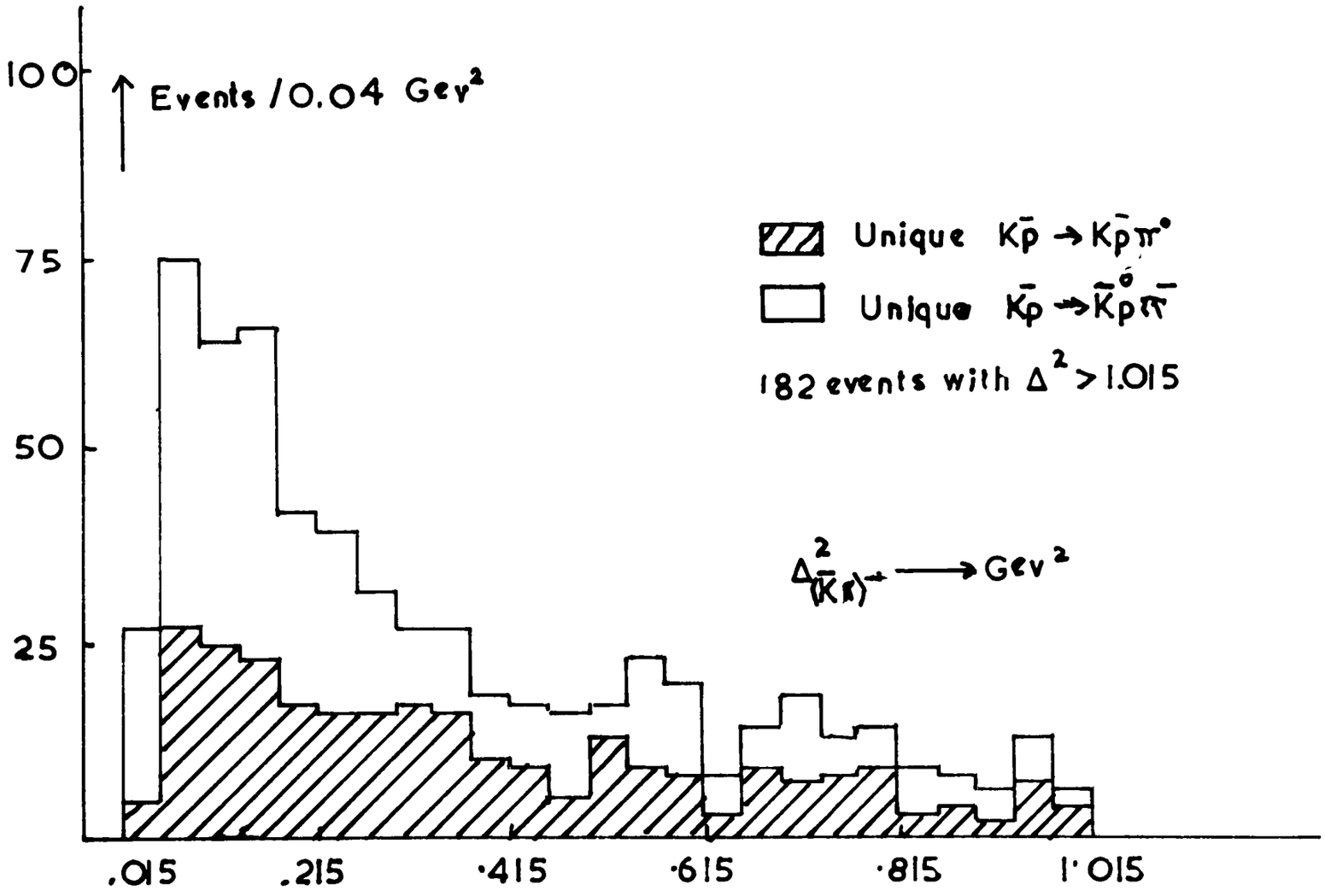

FIG 6.13 – Illustrating the peripheral nature of the reactions mentioned.

$$\langle R \rangle_1 = N \iint \ln\left(\frac{W_2}{W_1}\right) W_1(\cos\theta, \phi) \, d\cos\theta \, d\phi$$

The error on the ratio may be calculated from:

$$\sigma^2(R)_2 = N(\langle R^2 \rangle_2 - \langle R \rangle_2^2)$$

where the suffix 2 refers to the spin two case, and the first term in brackets is the second moment of the likelihood ratio. A similar expression may be calculated for spin 1 and the results are summarized in Table III. It is apparent that spin 2 is preferred.

The Peripheral Model

So far, attention has been concentrated upon the four variables $M_N^2, M_K^2, \theta_{K\pi}$ and $\phi_{K\pi}$ which are necessary to the specification of an event. However, a slightly different aspect of the data is revealed by an investigation of the distribution in t_N (defined in Appendix E). Fig. 6.13 shows the t_N distribution for all events $K^- p \rightarrow \bar{K} N \pi$ constituting reactions (2), (3) and (4) and indicate that the majority of interactions occur within the meson cloud surrounding the target proton. Chew and Low [14] suggested the peripheral model description of such interactions as a possible means of investigating scattering reactions where both of the participants are unstable. For instance, neutron-neutron scattering could be studied by the investigation of neutron-deuteron reactions. They pointed

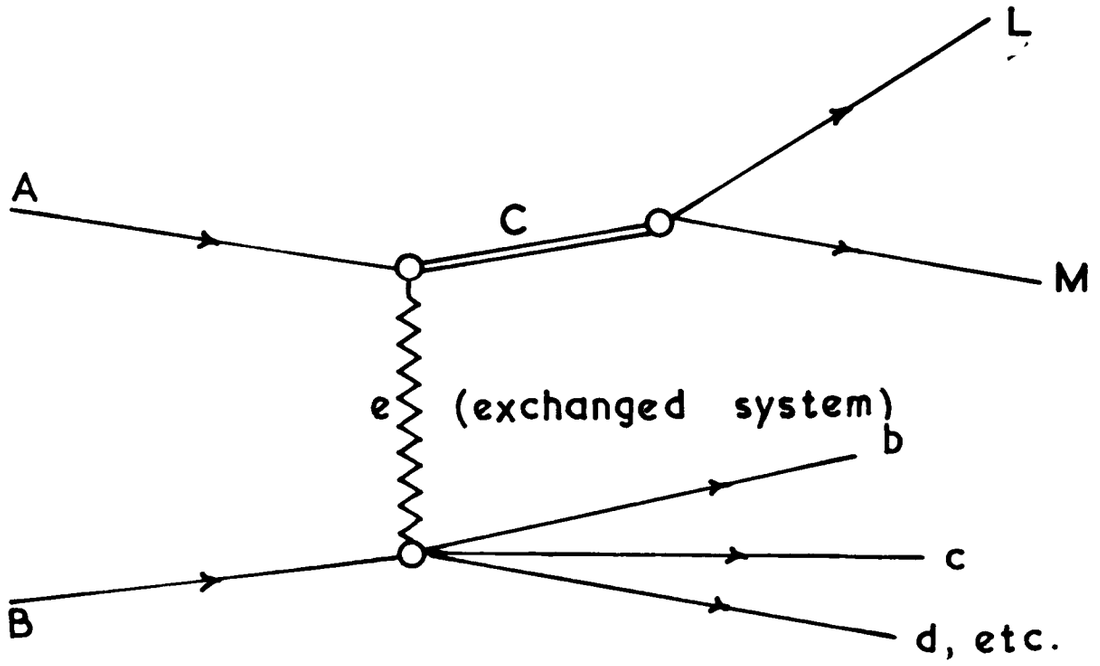

FIG . 6 .14

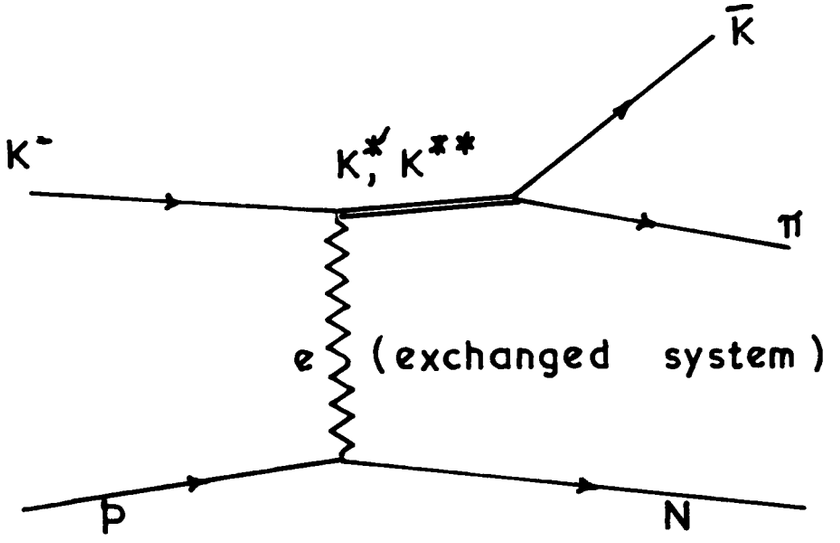

FIG. 6 .15. (a) Production of K^*

$C = |J, M\rangle$

$A = K^- (J^P = 0^-)$ $\qquad$ $e\ (Je\ Pe)$

$C\ K^*_{or}\ K^{**} (J^{(-1)^J})$

FIG. 6 . 15 (b)

out that reactions such as (see Fig.6.14)

$$A + B \rightarrow (C + b + c + \ldots) \rightarrow (l + m + b + c + \ldots)$$

involve a term:[15] $V_I(A+e \rightarrow C \rightarrow l+m)\frac{1}{t-m_e^2}V_{II}(B+e \rightarrow b+c+\ldots)$

.... (17)

in the matrix element where e is the exchanged system indicated in Fig.6.14 and m_e its mass. In this, t is the momentum transfer to the resonance C and V_I and V_{II} are the amplitudes for the two vertices I and II including spin factors. In the limit that e is a real particle, these become the actual cross-sections for the real processes indicated within the brackets. However, the expression for t: $t = (m_A^2+m_C^2) - 2E_AE_C + 2p_Ap_C\cos\theta^*$ where m,E,p refer, respectively, to the mass, energy and 3-momentum of the particle denoted by the subscript, is bounded by the physical restriction on $\cos\theta^*$ (where θ^* = the centre of mass scattering angle) - that it lies between ± 1. Consequently, the lower and upper values of t are given by:-

$$4E^2t^{max}_{min} = \left[(m_C^2-m_A^2)-(m_B^2-m_B^2)\right]^2 - \left\{(E^2+m_C^2-m_D^2)-4E^2m_C^2\right\}^{\frac{1}{2}} \pm \left\{(E^2+m_A^2-m_B^2)^2-m_A^2\right\}^{\frac{1}{2}}\Big]^2$$

where E is the total CMS energy and D is the particle system b + c +... as indicated in Fig.6.14. The corresponding diagram for the reactions:

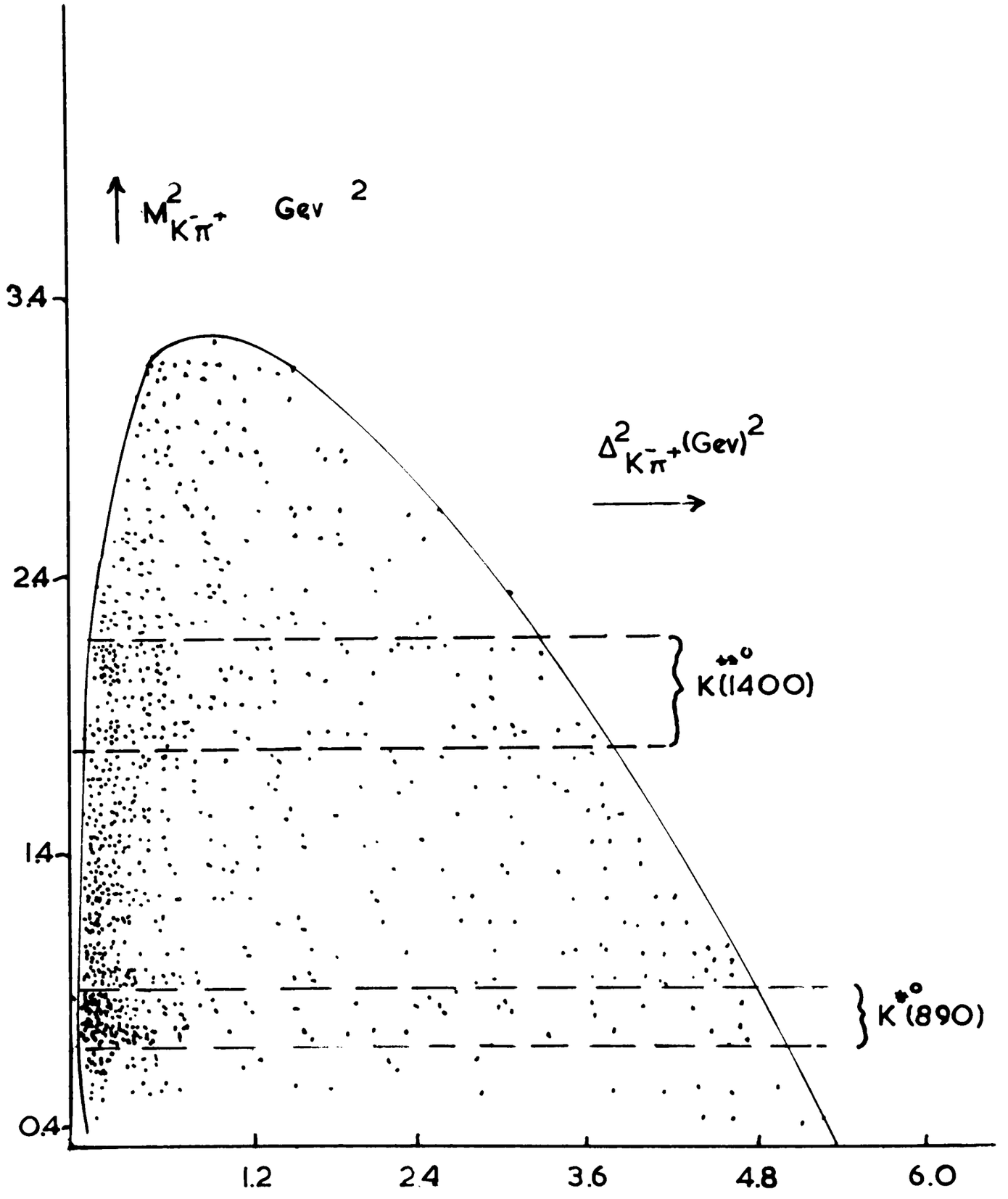

FIG 6.16 CHEW-LOW PLOT

$$K^- p \rightarrow K^{**} N$$

$$\rightarrow K^{*} N$$

has $m_A = 0.494$; $m_B = 0.938$; $m_C = M_K$ and $m_D \doteq m_B$ and is shown in Fig. 6.15(a). The Chew-Low plot of Fig.6.16 demonstrates the physical bounds on t_N (momentum transfer to the proton) as a function of $m_C (= M_{K\pi})$ and illustrates the fact that it is never allowed to go positive. (The plot actually shows $\Delta_N^2 = -t_N$ as ordinate). However, the distribution does show a marked tendency towards low t_N values especially in the regions of the K* resonances, and leads us to accept that the single particle exchange term might well dominate their production amplitude.

The assumption that this is so leads to considerable simplifications, under certain conditions, to the form of W_1 and W_2 (equations (15) and (16)), since the nature of the particle exchanged imposes restrictions upon the allowed magnetic quantum states m of the produced resonance.

The Exchanged System

The only restriction upon the spin parity of the exchanged system is that it cannot be 0^+ for production of either K*(890) or K**(1400) since they both have natural parity. This can be seen by referring to Fig.6.15(b) which shows the incoming beam (K^-) and exchanged system e in

the resonance rest frame. We now classify the spin-parities of the exchanged particle (denoted by J_e^{Pe} with similar notation for other particles) in order to estimate the effect on the decay distributions in the following three cases:

(a) pseudo-scalar exchange $J_e^{Pe} = 0^-$

(b) natural parity exchange $P_e = (-1)^{Je}$

(c) unnatural parity exchange $P_e = (-1)^{J_e \pm 1}$

(a) If one considers Fig.6.15(b) it is apparent that whatever the spin (J) of the resonance C, the orbital angular momentum of A and e will be J with $J_z = 0$ (z is the direction of A and e in this frame). Consequently, the z-component of the resonance spin is zero and the density matrix is all zero except for ρ_{oo} (required to be unity by the trace condition).

(b) Natural parity exchange leads to a coupling between L and J_e such that the resultant has angular momentum J. Consequently, the allowed values of L are $J_{e-}J \leqslant L \leqslant J_{e+}J$ Conservation of parity requires that $P_A \cdot (-1)^{Je}(-1)^{L} = (-1)^{J}$

.... (18)

(for resonance of natural parity) As $P_A = -1$ for an incoming K meson, this means that $J_e + L$ must be odd if J is even and vice versa. Now consider the amplitude contribut-

ing to zero z-component of the resonance-M. This will be proportional to the vector coupling coefficient $\langle J_e\, M_e 0 | JM \rangle$ since the z-component of L must be zero with $M_e = M = 0$. This is zero unless J_e+L+J is even. But this has already been shown to be not possible if parity is to be conserved. Consequently, we expect a depopulation of the $M = 0$ states and the density matrix elements $\rho_{mo} = 0$ in both (15) and (16).

(c) Unnatural parity exchange allows, by exactly similar argument with an extra (-1) in equation (18), only even values for J_e+L+J. Consequently, no restrictions on the ρ-values arise from this source.

Possible candidates for exchange are $\pi, \eta, X^0, \omega, \rho, f_o, \phi, A_2$ amongst the known mesons, and since all but the pseudo scalars are of natural parity, the only component of the density matrix having one index zero is expected to be ρ_{oo}. This is in qualitative agreement with the results in Table III. Further, the consistency of the ρ_{m2} values with zero in the case of the K* (1400) can be taken as evidence for the lack of any spin 2 exchange, since $M = \pm 2$ for the resonance can only arise from $J_c = 2$ as $L_z = 0$. This lack can be appreciated when one considers the masses of the possible candidates for spin 2 exchange (f_o, A_2). In both cases the physical region is very distant from the pole,

and their pole contributions to the scattering cross-section are not expected to be large.

The absorption Model [16,17,18]

The peripheral model enables one to calculate physically interesting quantities (decay distributions and momentum transfer distributions) for reactions of the form $a + b \rightarrow c + d$. In what follows, the exchanged particle is denoted by e. Expressions for the t distribution predicted by the peripheral model are [19] for pseudo-scalar exchange.

$$\frac{d\sigma}{dt} = \frac{G^2}{4\pi}\cdot\frac{g^2}{4\pi}\cdot\frac{\pi}{sq^2}\cdot\frac{a_c^2\left[(m_b-m_d)^2-t\right]}{(m_e^2-t)^2}\left|F(t)\right|^2$$

for production of a 1^- particle. For the exchange of a vector particle the corresponding expression is:-

$$\frac{d\sigma}{dt} = \frac{g^2}{4\pi}\cdot\frac{\pi}{2m_c^2sq^2}\left|\frac{F_v(t)}{m_e^2-t}\right|^2\left\{\frac{(G^V+G^T)^2}{4}m_c^2a_c^2\left[(m_b-m_d)^2-t\right]\right.$$
$$\left. + 2S\left[\frac{G^{V2}}{4\pi}-\frac{G^{T2}}{4\pi}\cdot\frac{t}{(m_b+m_d)^2}\right]\right\}$$

for 1^- production.

In these expressions

G = coupling constant at the baryon vertex

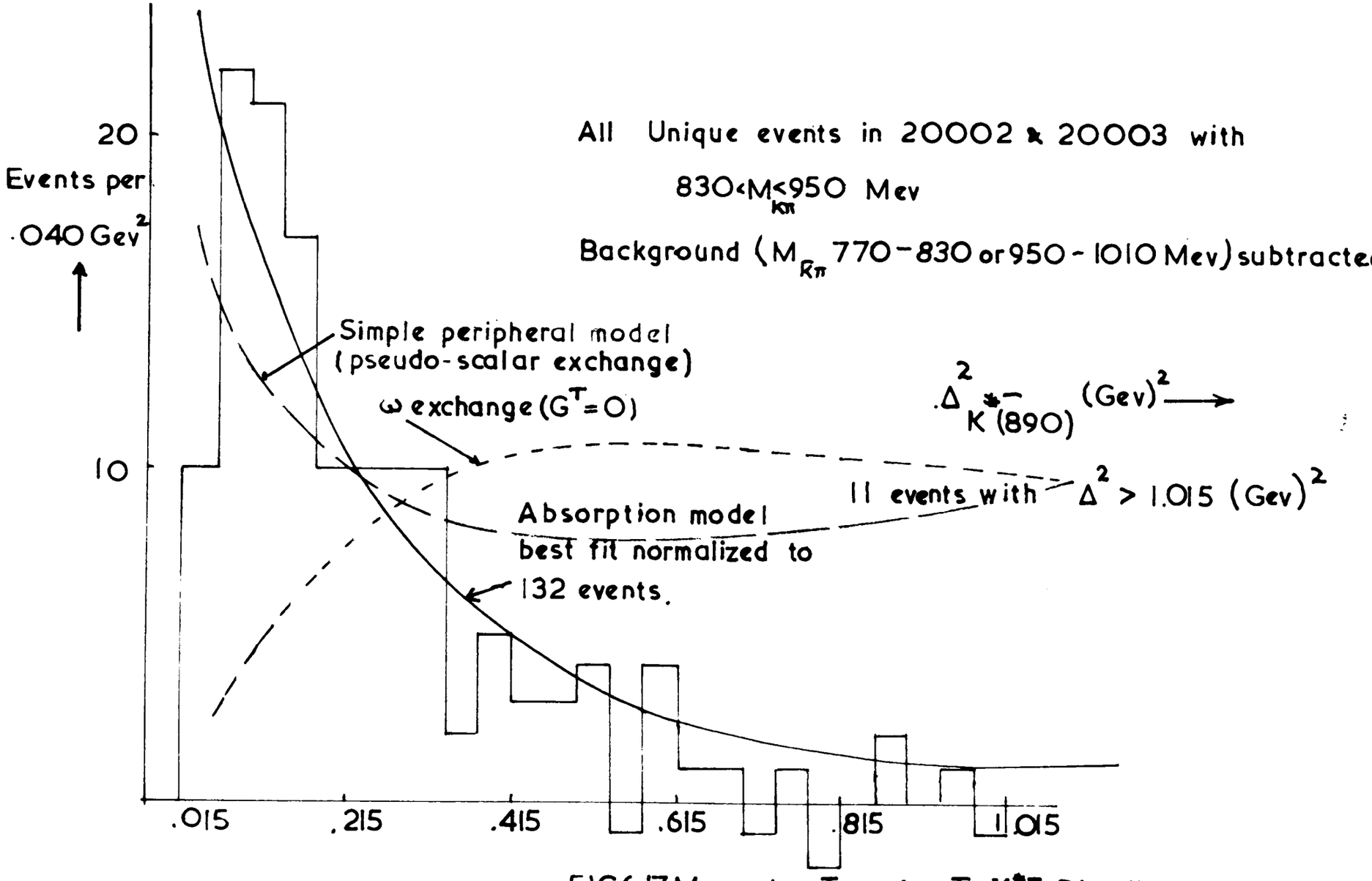

FIG 6.17-Momentum Transfer To K^{*-} Distribution

(All curves normalized to 132 events in Δ^2 range .015-1.015 Gev^2)

g = coupling constant at the vertex involving the mesons

s = total centre of mass energy

q = centre of mass momentum

$$a_c^2 = \frac{1}{4m_c^2}\left[t-(m_c+m_a)^2\right].\left[t-(m_c-m_a)^2\right]$$

$$\Delta = sq^2q'^2\sin^2\theta$$

where θ = centre of mass production angle and

q' = final centre of mass momentum.

$$y = \frac{2G^T}{G^V+G^T}$$

$$v = 2-y$$

These curves are drawn on the experimental $K^*(890)$ t-distributions of Fig.6.17 and illustrate one of the fundamental difficulties of the peripheral model - that the calculated slope of this distribution is not nearly sharp enough. Various attempts have been made to modify the calculations to overcome this.[20,21,22] However, the most popular modification appears to have been the absorption model. In this the effect of elastic scattering in the initial and final states was calculated such that competing processes which were not considered to contribute to the cross section were taken into account. It was, therefore, assumed that in region A of the diagram Fig.6.18 only elastic scattering contributes to the peripheral (one

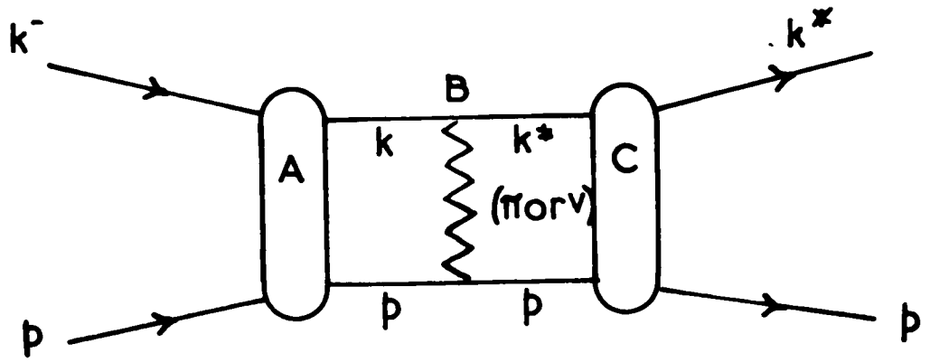

FIG. 6.18 The absorption model for K* production.

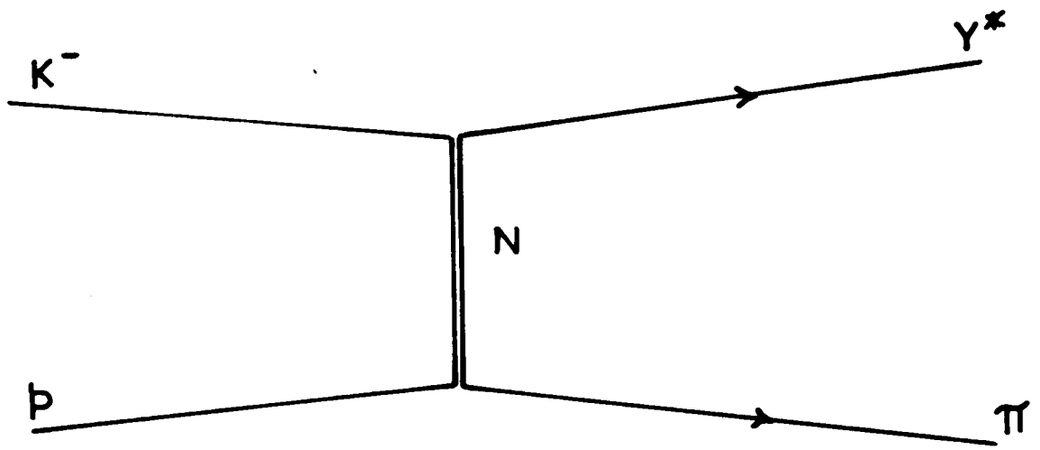

FIG. 6.21 (a) Y* production by baryon exchange.

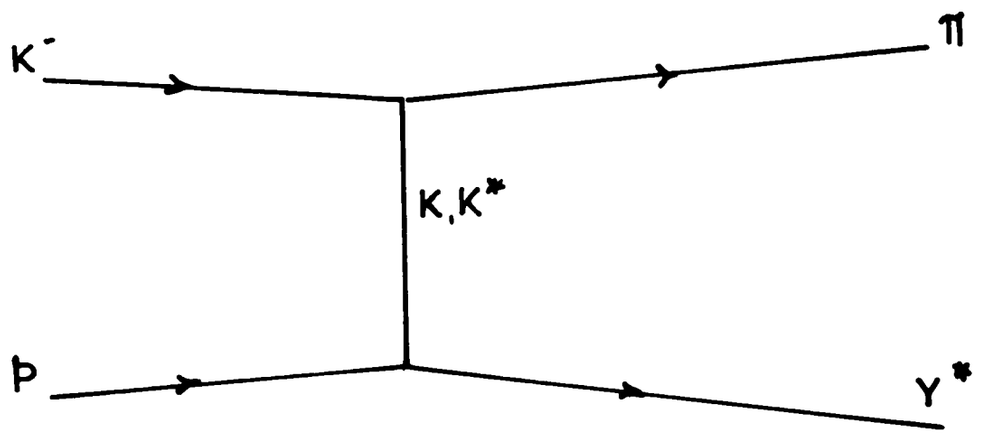

FIG. 6.21 (b) Y* production by strange partical exchange.

particle exchange) and that, further, only elastic scattering in part C contributes to the required final state. The fact that inelastic processes have smaller cross sections than elastic ones is the justification for the neglect of the contribution from inelastic processes in the initial and final states which nevertheless contribute to the same initial and final states. It is, furthermore, to be expected that the lower partial waves will be more depleted by inelastic processes than the higher ones with subsequent sharpening of the t distribution.

The absorption model calculations for 1^- and 2^+ production have been tested against the 2 prong data by Dr. A. Segar of the Rutherford Laboratory and variations of the parameters ξ and η were carried out to provide the best agreement possible with both production and decay angular distributions. The values of ξ and η are:

$$\xi = \frac{f_{KK^*V}(G^V_{V p\bar{p}} + G^T_{V\bar{p}p})}{2g_{K\pi K^*} G_{\pi \bar{p}p}}$$

$$\eta = \frac{f_{KK^*V} G^T_{V\bar{p}p}}{g_{K\pi K^*} G_{\pi \bar{p}p}}$$

where V denotes the vector particle exchanged, K* refers to either of the K*s and f, g and G are coupling constants for the vertices indicated by subscripts. Superscripts V

TABLE IV

Reaction	ξ †	η †
$K^-p \rightarrow K^{*-}(890)p$	0.8 ± 0.2	0.6 ± 0.2
$\rightarrow K^{**-}(1400)p$	0.5 ± 0.3	-1.5 ± 0.5
$\rightarrow \bar{K}^{*o}(890)n$	0.10	0.04
$\rightarrow \bar{K}^{**o}(1400)n$	0.9	1.9

† The errors on these quantities have little meaning as they are strongly correlated. In particular the values for $K^{*o}(1400)$ production are consistent with pseudo-scalar exchange ($\xi = \eta = 0$) through the fact that the likelihhod contours in the $\xi - \eta$ plane indicate a constraint of the form $\eta = 2\xi$.

and T refer respectively to vector and tensor coupling.

The method of fitting was one of maximum likelihood. The calculated distribution of t and of the angles θ and ϕ were compared with experiment to form a likelihood function which was a product of the t distribution and that of the θ and ϕ values. In this way, the effect of t upon the density matrix which is a consequence of the absorption was neglected. The calculated production angular distributions which result are shown in Figs 6.19 where they are compared with experiment, and the predicted density matrix values are included in Table III. The best values of ξ and η are summarized in Table IV.

Production and Decay of the zero Charged K*s

A similar analysis has been carried out on reaction (4). The decay density matrices and production cross-sections for the two K*s have been found in a manner identical to that used on the negative K*s.

In this final state, one might think to eliminate the elastic contamination by omitting the events from the

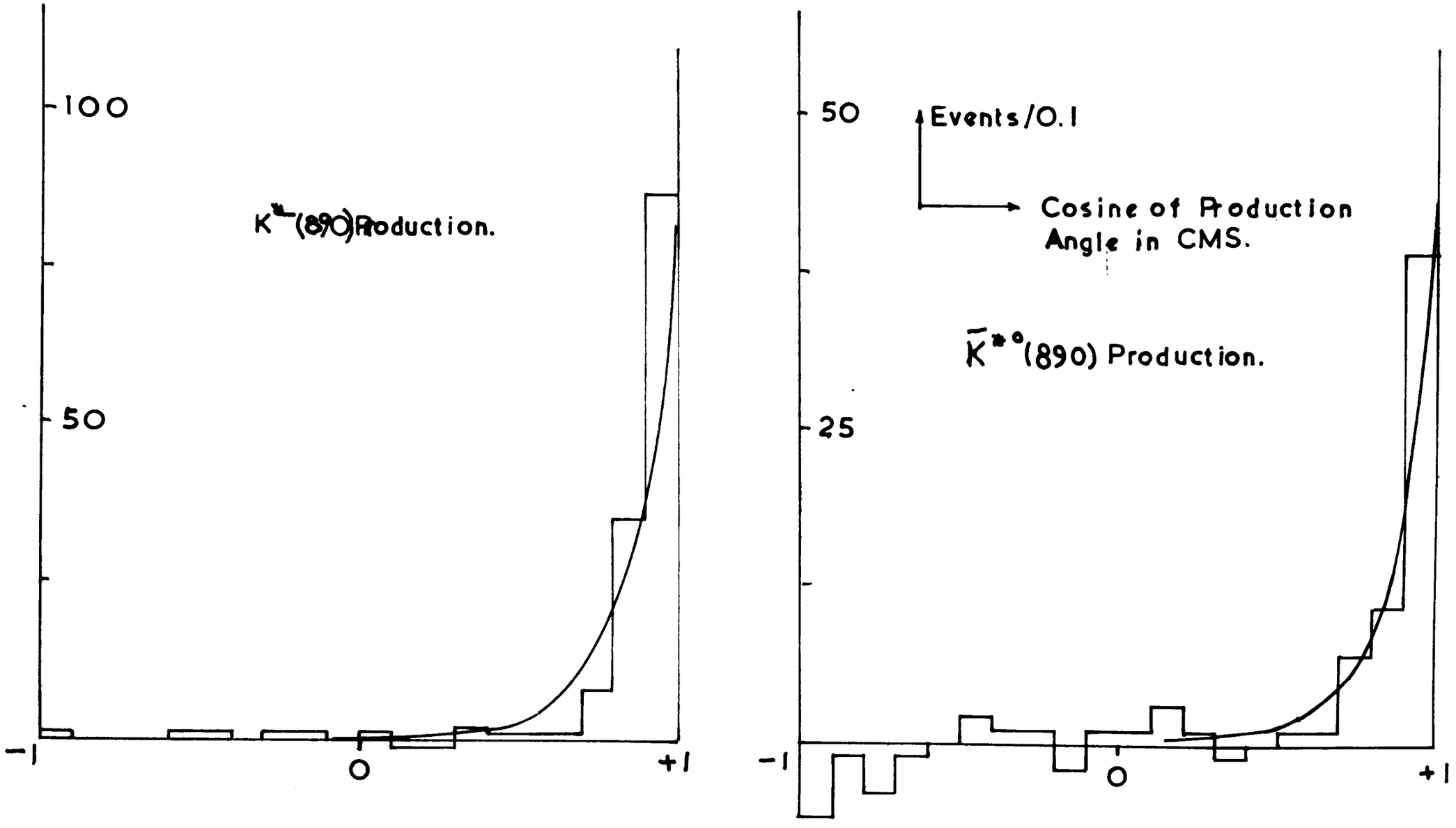

FIG 6.9 – Examples of Absorption Model Fits to Two Prong Data
(Curves Normalized.)

lower half of the Dalitz plot (corresponding to low $n\pi^+$ mass values). However, some difficulty would have arisen by doing this as the angle θ would suffer some bias. That this should be so is not obvious since θ only depends upon the $n\pi^+$ invariant mass because the momentum transfer t_N is preferentially small. This makes θ and α (the "decay" angle) not very different. However, as a consequence of the symmetry implied by equation (12) one might remove events from the Dalitz plot having $\cos\alpha$ such that the $n\pi^+$ mass is small, and repopulate with events having the opposite sign of $\cos\alpha$. Unfortunately, however, this would make the density of points on the plot somewhat complicated unless one removed the whole N*. Consequently, the θ, ϕ selection was chosen as a filter for elastic events since this was anyway a more direct means of removing any bias in the decay distribution of the K^{*o}s.

The first stage consisted of the determination of the masses, widths and fractions for each of the processes included:

TABLE V

Production Process	Cross Section (μb)
$K^- p \rightarrow K^*(890)^- p$	750 $\pm$ 79
$\rightarrow K^{**}(1400)^- p$	289 $\pm$ 80
$\rightarrow \bar{K}^{*o}(890) n$	553 $\pm$ 94
$\rightarrow \bar{K}^{*o}(1400) n$	315 $\pm$ 61

$$K^- p \rightarrow K^- \pi^+ n$$

$$\rightarrow K^{*o}(890) n$$

$$\rightarrow K^{**o}(1400) n$$

$$\rightarrow N^{*+}(1238) K^-$$

in reaction (4). The resulting values for masses, widths and cross-sections are included in Table I.

In the decay analysis, the method of maximum likelihood was used as before, and the density matrix elements are included in Table III. A striking difference is observed in this case. The negative K*'s appear to be produced by almost pure vector exchange (more precisely-natural parity exchange). The zero charged K*'s, however, seem to prefer a pseudo-scalar exchange production mechanism. This tends to indicate that ω exchange is an important part of the production of the K* since its isospin is zero. It further indicates that the $\rho K^* K$; coupling is weak.

The relative rates of K^{*-} and K^{*o} production in the cases of both the 890 and 1400 resonances yield information on the isotopic spin of the exchanged system. The ratio of 4:1 expected for $\bar{K}^{*o}$:K^{*-} for simple isovector exchange follows if we assume a value of $\frac{1}{2}$ for either K* isospin. The observed rates are summarized in Table V where it is clear that pure isovector exchange does not account for the

whole cross-section. Instead, an admixture of some 30% of isosinglet exchange is required in the case of K*(890) and 72% in the K**(1400) production. The decay of the K*(890) into either ω K or η K is energetically impossible, but it appears that we might expect to see K**(1400) decaying into these systems.

Y* Production in the Two Prongs

The presence of Y*(1520) in reaction (2) has been previously acknowledged and has an estimated production cross-section in the reaction $K^- p \rightarrow Y^{*0}(1520)\pi^0$ of $162 \pm 30\ \mu b$ after correcting for the unobserved $\bar{K}^0 n$ decays. The lack of any other noticeable Y* enhancement can be understood from a simple interpretation of the peripheral model. Figs. 6.21 indicate the simplest single particle exchange diagrams which indicate that either a baryon (Fig.21(a)) or a strange particle (Fig.21(b)) must be exchanged. It appears that either such mechanisms are forbidden or at least highly damped, or that the prolific K* productions swamp any such effects. Baryon exchange was noticed in the reaction:

$$K^- p \rightarrow Y^{*}_{0}(1815)^0 \pi^0 (3.5\ \text{Gev/c}) \qquad \ldots\ (22)$$
$$\hookrightarrow \Sigma^- \pi^+$$

where the Y* was observed to have a forward production

angle. The corresponding process should be observed in the two prongs in reaction (2)

$$K^- p \rightarrow Y_o^*(1815)\pi^o$$
$$\hookrightarrow K^- p$$

No noticeable enhancement appears in the K^-p mass spectrum Fig.6.1(b) at this position nor any structure in the K^-p production angle as a function of mass in this vicinity. The statistics are limited but the expected number of events is 71 if the branching ratio

$$\frac{Y_o^*(1815 \rightarrow \Sigma\pi}{Y_o^*(1815) \rightarrow \bar{K}N} = 0.12$$

is assumed as the isotopic spin of the Y_o^* is zero and the cross section for reaction (22) is $40 \pm 10 \mu b$.[23]

This figures is inconsistent with the observed rate and the production angle of the K^-p system, though not obviously biased in the backward direction, certainly shows no forward peaking. The lack of $Y_o^*(1815)$ in reaction (2) perhaps indicates the presence of final state interaction in the reaction $K^-p \rightarrow Y_o^{*o}\pi^o$ when the $\bar{K}N$ decay mode occurs.

REFERENCES TO CHAPTER VI

1. N. Hque et al - Physics Letters, 14,338(1965)
2. L. M. Hardy et al - PRL 14,401(1965)
3. S. Focardi et al - Physics Letters 16,351(1965)
4. J. Badier et al - Physics Letters 19,612(1965)
5. M. Ferro-Luzzi et al - Nuovo Cimento, 36,1101(1964)
6. J.D.Jackson - Nuovo Cimento, 34,1644(1964)
7. W. Kock - Proceedings of the 1964 Easter School for Physicists, Hereeg-Novi, Volume II, CERN 64-14
8. P.M.D.Gray - D.Phil Tesis,Oxford,P.70(1965)
9. H. Pilkuhn - Proceedings of the 1965 Easter School for Physicists, Bad Kreuznach, Volume I,CERN 65-24
10. N. Schmitz - Proceedings of the 1965 Easter School for Physicists, Bad Kreuznach, Volume I,CERN 65-24
11. See Reference 4
12. Ibid - Chapter VIII (Table I)
13. P.M.D.Gray - D. Phil Thesis, Oxford P.92 (1965)
14. G. F. Chew & F. E. Low - Phys.Rev.113,1640(1958)
15. R. H. Dalitz - Annual Review of Nuclear Science,13,339(1963)
16. K.Gottfried & J.D.Jackson, Nuovo Cimento,33,309(1964)
17. Gottfried, Jackson, Donohue, Keyser & Svensson - Phys Rev. 139,B428(1965)
18. J.D.Jackson - Rev. Mod. Phys., 37,484 (1965)
19. J.D.Jackson & H. Pilkuhn - Nuovo Cimento,33,906(1964)

20. Durand & Chiu - PRL 12,399(1964)

21. N. Sopkovitch - Nuovo Cimento, 26,186(1962)

22. Dar, Kugler, Dothan, Nussinov, PRL, 12,82(1964)

23. N. Haque et al - to be published.

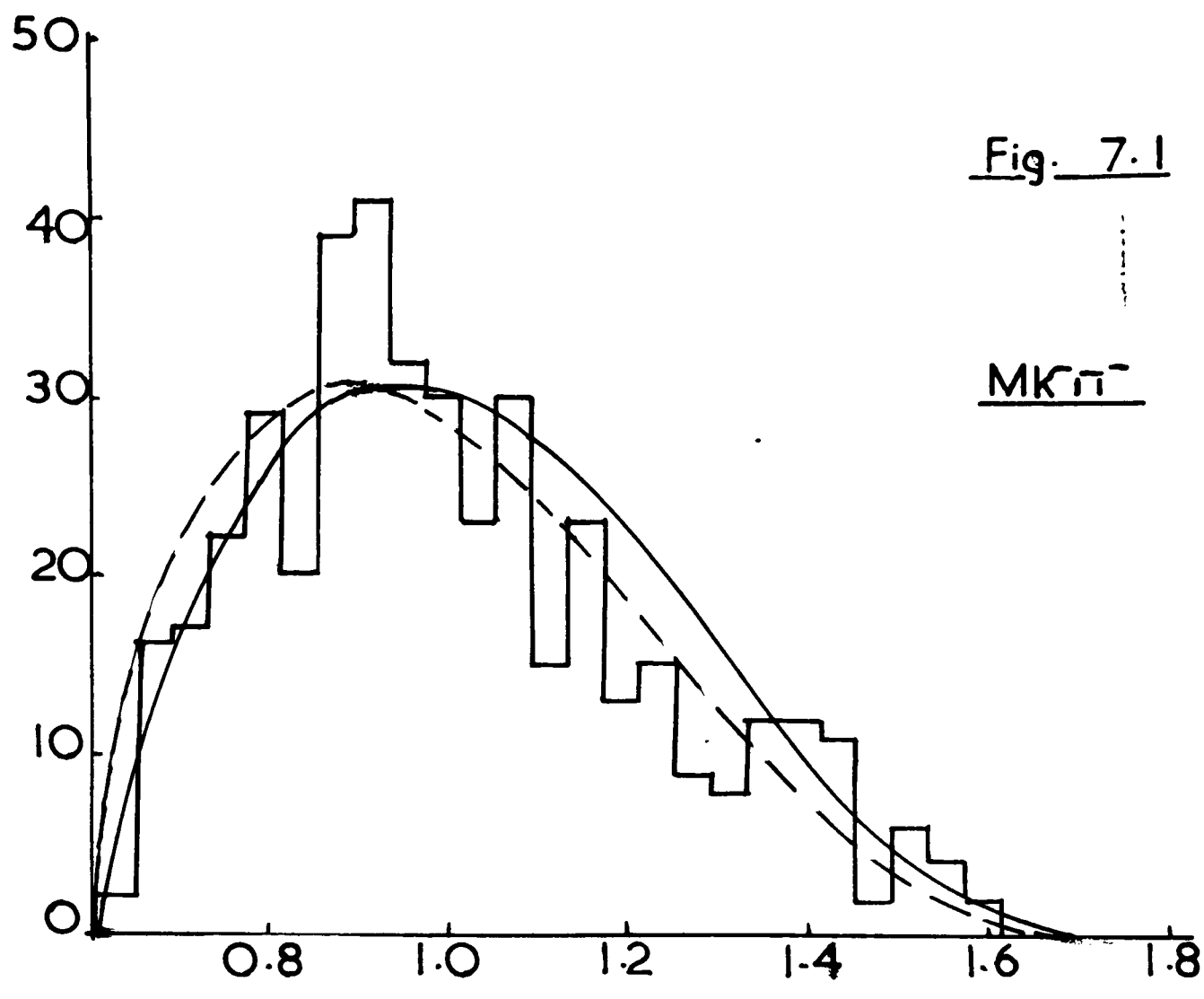
50
40
30
20
10
0
0.8
1.0
1.2
1.4
1.6
1.8
MK π⁻

Fig. 7.1

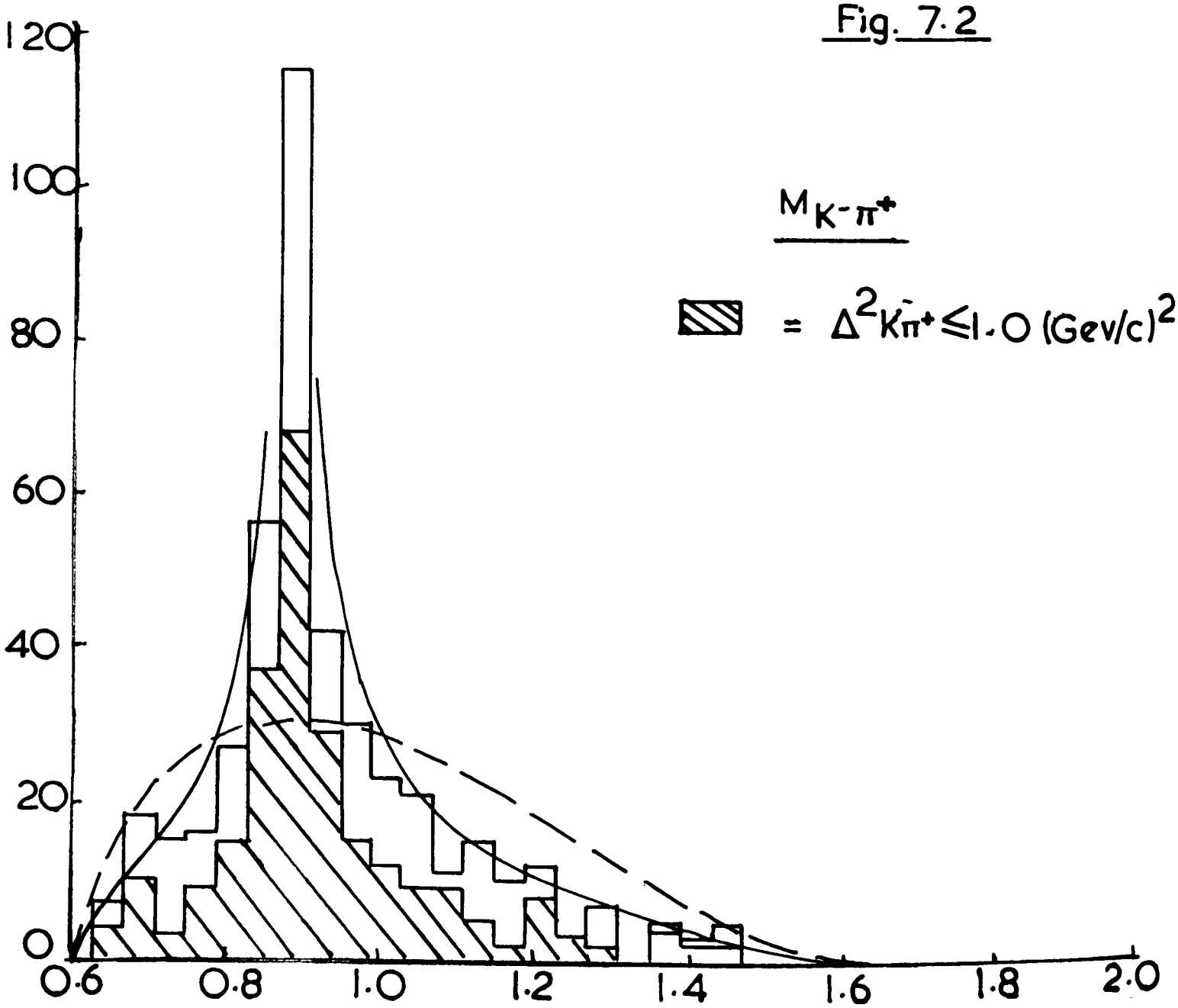
120
100
80
60
40
20
0
0.6
0.8
1.0
1.2
1.4
1.6
1.8
2.0
$M_{K^-\pi^+}$
= $\Delta^2 K\pi^+ \leq 1.0$ (Gev/c)^2

Fig. 7.2

CHAPTER VII

Analysis of the Four Prong Events

The reactions under study in this chapter are:

$$K^- p \rightarrow K^- p \pi^+ \pi^- \quad \ldots\ldots (1)$$

$$K^- p \pi^+ \pi^- \pi^o \quad \ldots\ldots (2)$$

$$K^- \pi^+ \pi^+ \pi^- n \quad \ldots\ldots (3)$$

though a comparison of reaction (1) with the reactions:

$$K^- p \rightarrow \bar{K}^o \pi^- p \pi^- \quad \ldots\ldots (1)a$$

$$\bar{K}^o n \pi^- \pi^+ \quad \ldots\ldots (1)b$$

is also made when relevant. It is proposed to deal with reaction (1) first.

Two Body Invariant Mass Distributions

These are shown in Figs.7.1-6 where it is apparent that enhancements in all but the $K^-\pi^-$ spectrum are observed. The dotted curves are Lorentz invariant phase space calculated on the assumption that no resonances occur and that all angular distributions are consistent with a statistical non-interacting system of particles. It is clear that the following single resonance production processes are present:-

$$K^- p \quad K^*_{(890)}{}^o p \pi^- \quad \ldots\ldots (4)$$

$$N^*_{(1238)}{}^{++} K^- \pi^- \quad \ldots\ldots (5)$$

$$N^*_{(1238)}{}^o K^- \pi^+ \quad \ldots\ldots (6)$$

$$Y^*_{(1520)}{}^o \pi^- \pi^+ \quad \ldots\ldots (7)$$

$$K^- p \rho^o_{(750)} \quad \ldots\ldots (8)$$

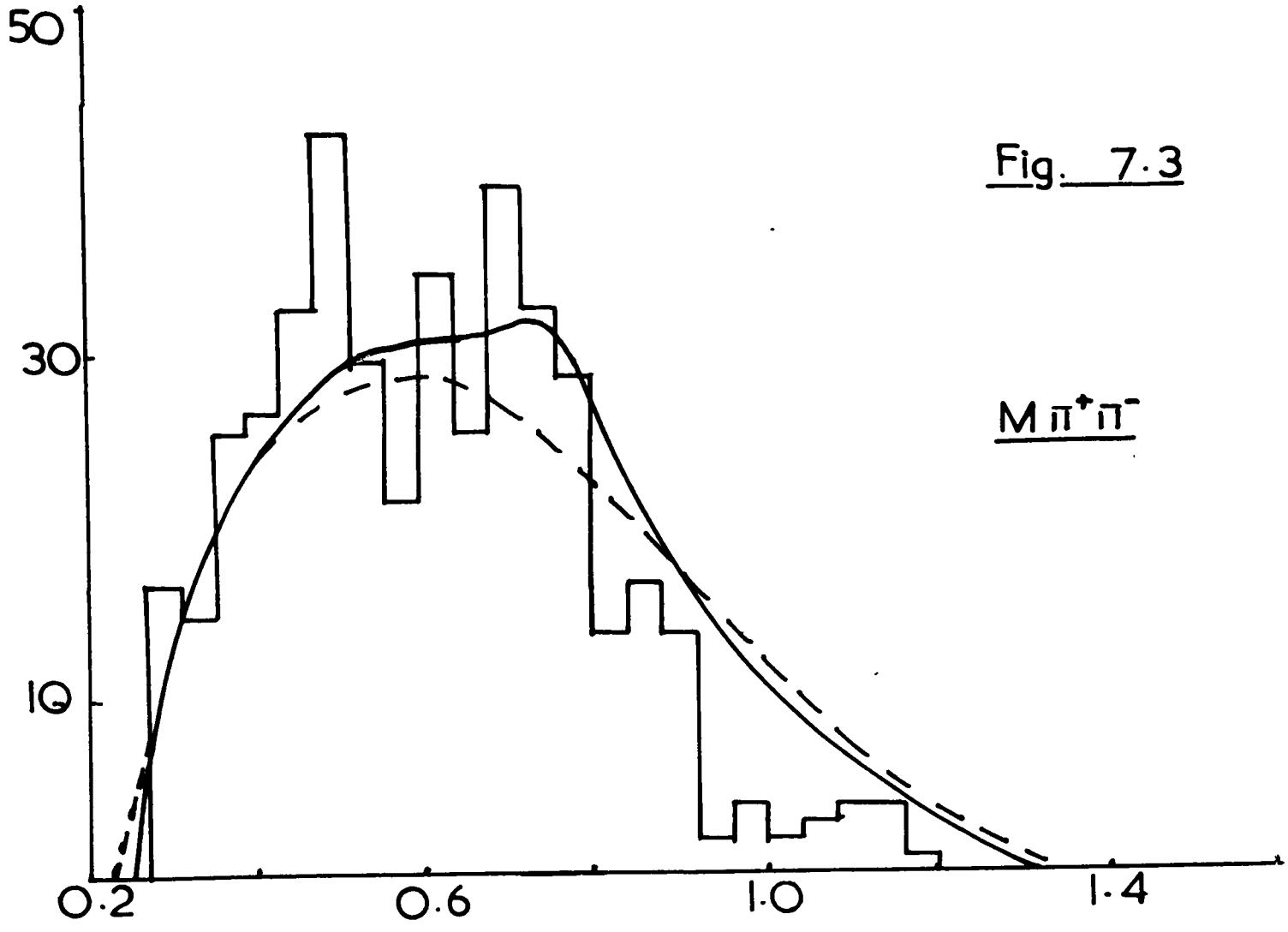

Fig. 7·3

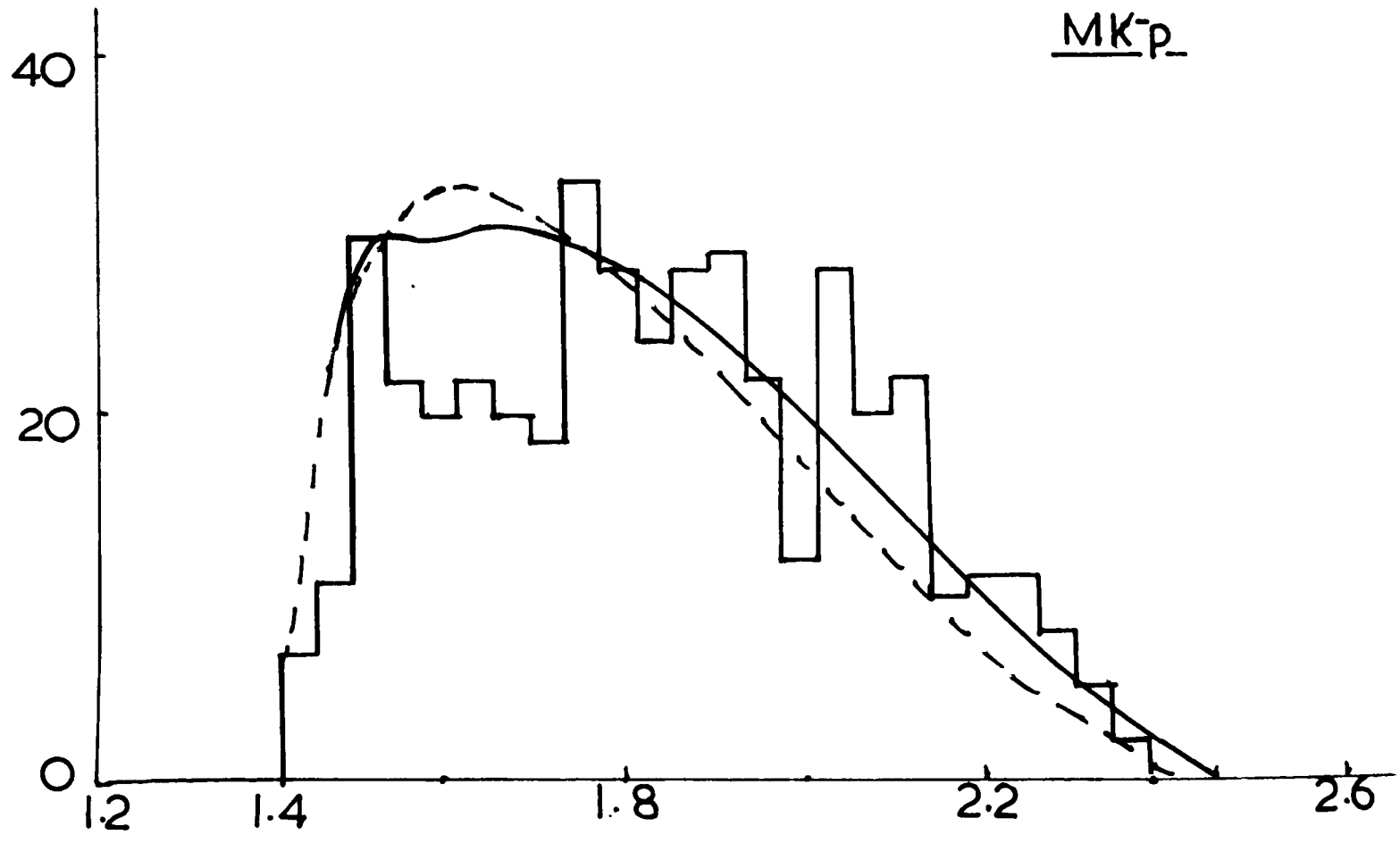

Fig. 7·4

and that the presence of $Y_1^*(1765)$ or $Y_0^*(1815)$ in the K^-p spectrum is doubt significant.

A notable exception from the two body resonances is the $K^{**0}(1400)$ whose observed decay into $K^-\pi^+$ might have been expected since it has isotopic spin $\frac{1}{2}$. However, a similar absence was noted in the other four body reactions at this energy[1]

$$K^-p \rightarrow \bar{K}^0\pi^0 p\pi^-$$

$$\rightarrow \bar{K}^0 n \pi^+\pi^-$$

and in the corresponding $K^\pm$ reactions at similar energies.[2,3] The suggestion of Goldhaber et al[4] from their K^+p data at 4.6 Gev/c that a strong $K^{**}(1400)$ $N^*(1238)$ production mechanism is favoured is possibly an explanation for this as the threshold for this reaction is only just exceeded at 3.5 Gev/c. However, the absence of events (See Fig. 7.2.) with $M_{K^-\pi^+}$ above 1320 Mev except for a brief reappearance at 1360 - 1480 Mev may be regarded as significant.

Possibility of Interference

The strong production of both $K^{*0}(890)$ and $N^{*++}(1238)$ each of which requires the only π^+ in the reaction leads one to expect interference between the two resonances. In order to demonstrate the lack of this to a serious extent, one may inspect the Dalitz plots of Fig.7.7. In these, the $K^-\pi^+$ invariant mass squared is plotted against that of the $p\pi^+$, for various $K^-p\pi^+$

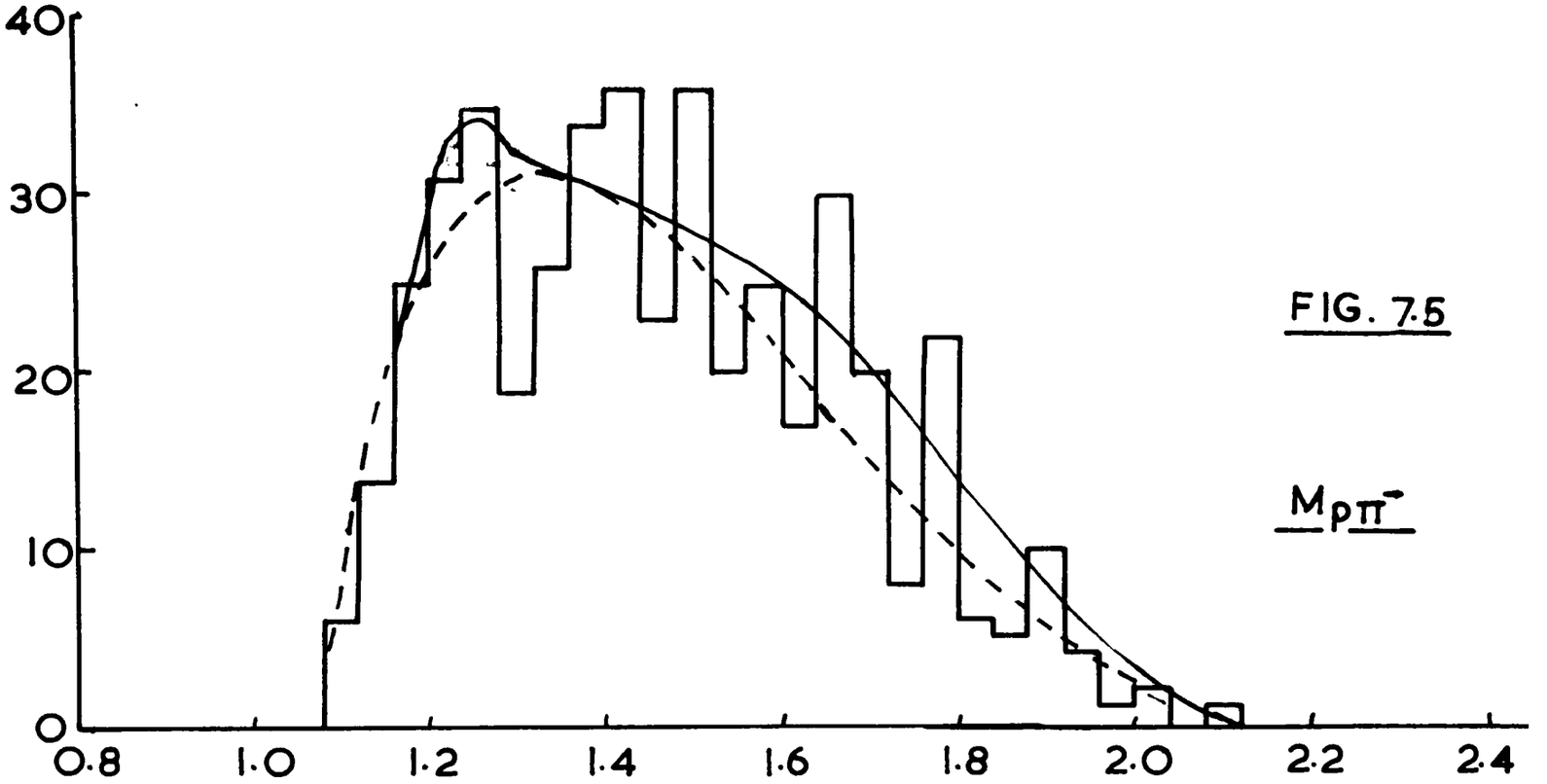

FIG. 7.5

$M_{p\pi^-}$

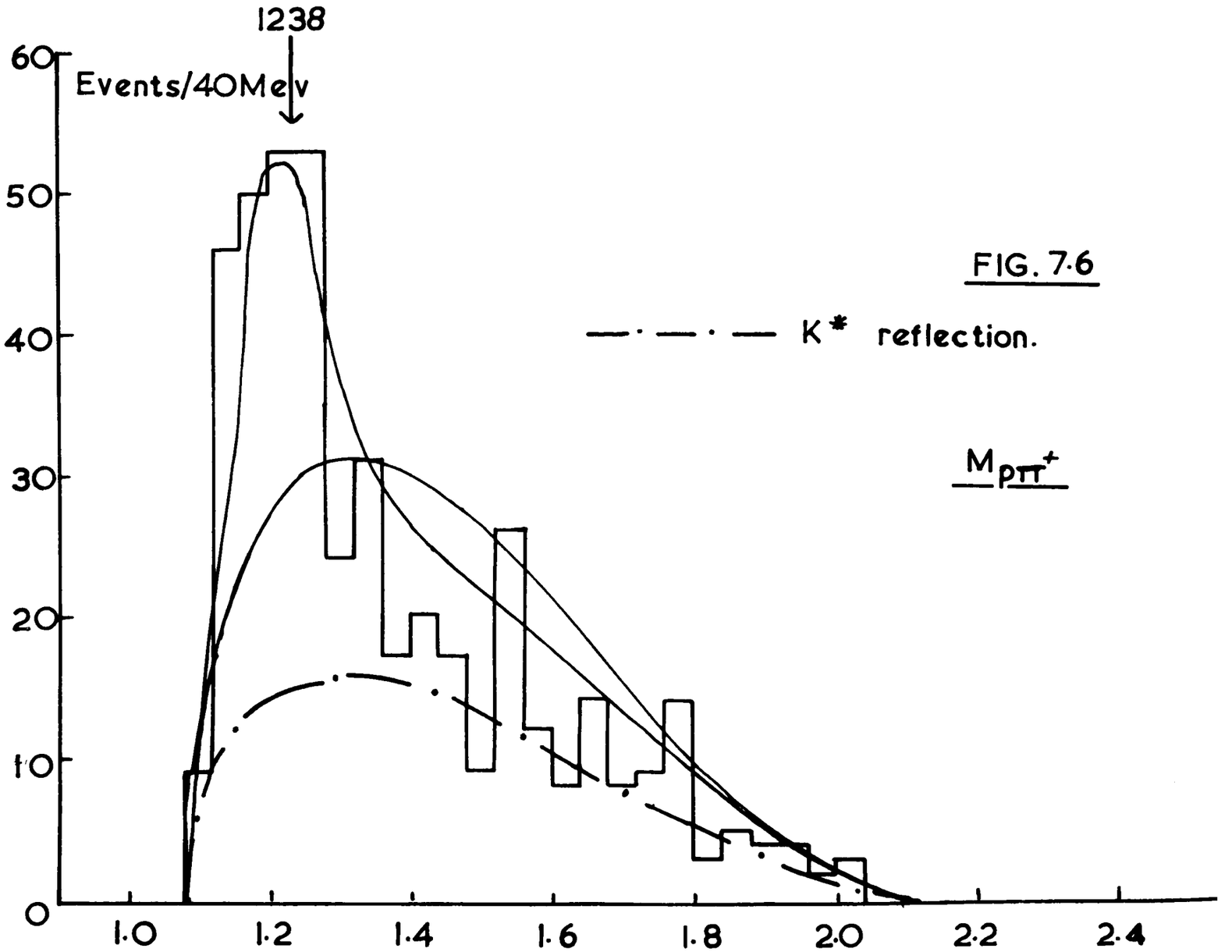

FIG. 7.6

—·—·— K* reflection.

$M_{p\pi^+}$

mass selections. In all cases the K^{*o} and N^{*++} bands are clearly defined, though the intensity of points within the crossover regions is not vastly different from that expected from an incoherent sum of the intensities elsewhere within the bands. The background density of points on these plots is difficult to calculate, however, owing to the spread in π^- momentum (which alters the boundary of the plot) and is not likely to be uniform except perhaps at the highest $K^-p\pi^+$ mass selection (Fig.7.7b) where such a spread is least significant. In this case the absence of either strong constructive or marked destructive interference between the K^{*o} and the N^{*++} is apparent.

Three Body Invariant Masses

These four distributions are illustrated in Figs.7.8-11. The $K^-p\pi^+$ and $K^-p\pi^-$ spectra are interestingly different, though the more peaked appearance of the latter can be explained in terms of N^{*++} production. Selecting the events having $p\pi^+$ mass between 1190 and 1290 Mev yields the shaded distribution illustrated in Fig.7.9. It is clear that for low backward $p\pi^+$ masses the $K^-\pi^-$ system travels fast in the forward direction in the overall centre of mass giving the observed high $K^-p\pi^-$ mass enhancement. Apart from this, however, the only noticeable anomaly in these spectra is the broad hump centred at about 1400 Mev in the $K^-\pi^+\pi^-$ system. Evidence that this corresponds to the process

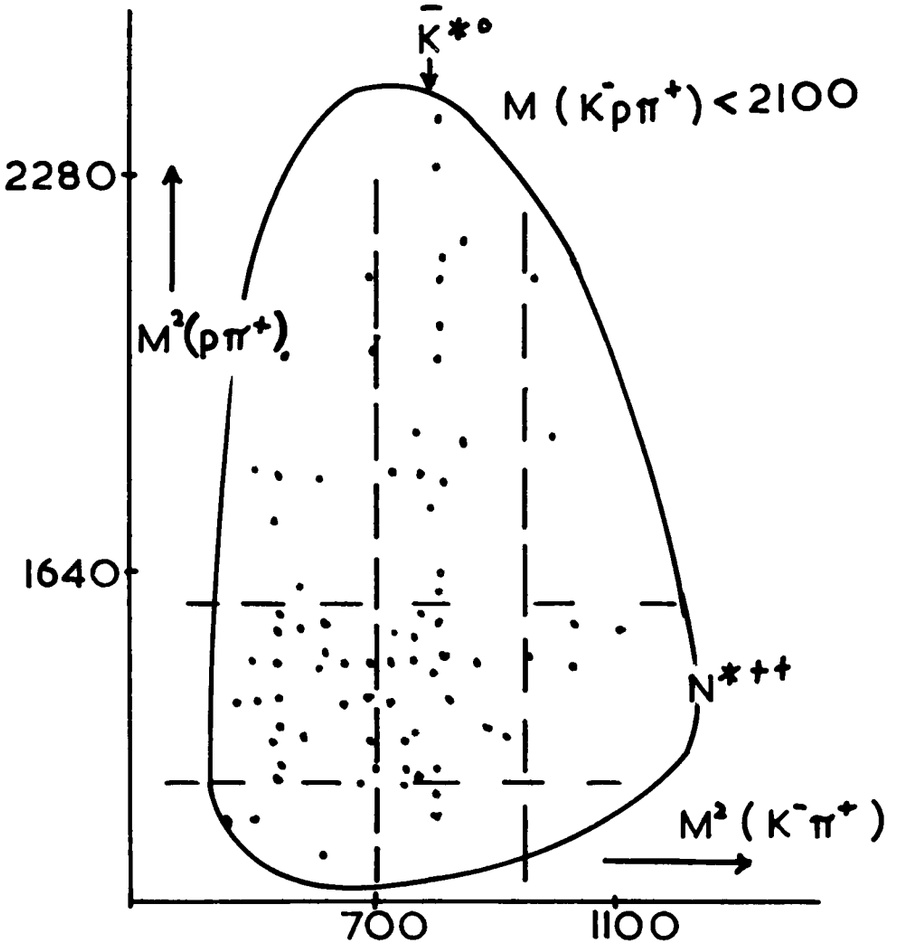

FIG. 7.7 (a)

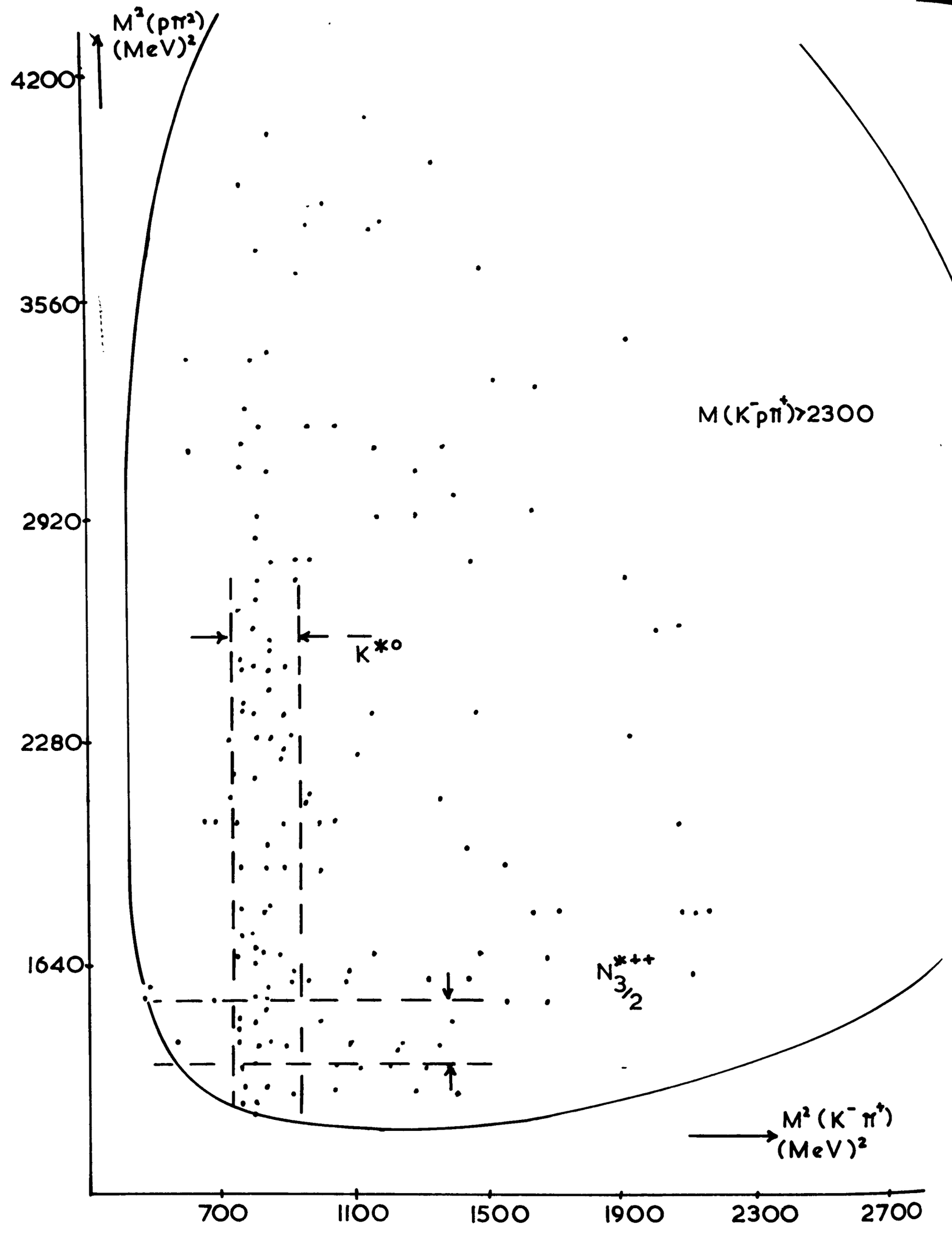
M²(pπ²)
(MeV)²
4200
3560
2920
2280
1640
M(K⁻pπ⁺)>2300
K*o
N*++ 3/2
M²(K⁻π⁺)
(MeV)²
700
1100
1500
1900
2300
2700

FIG. 7.7 (b)

$$K^-p \Rightarrow K^{**}(1400)^-p$$
$$\hookrightarrow K^-\pi^+\pi^-$$

is offered later, but the suggestion is taken for granted in the following section.

Estimation of Resonance Production Cross-sections

It is apparent that this final state is somewhat complex as resonance production clearly accounts for a large part of it. The previously discussed 3 body states could be quite well represented on the Dalitz plot where at least one could simultaneously observe all invariant mass combinations. The corresponding plot for the present state would require a further 3 dimensions (owing to the presence of one further particle) and it is clear that the resulting multi-dimensional representation would be interlaced by resonance bands in a very complicated way. In order to determine the fraction of each resonant process contributing to the overall final state, therefore, one may project this distribution onto any one invariant mass axis by integrating over all the other masses and determine the best mixture of background + resonant (Breit-Wigner) curves describing its shape. An alternative way is actually to find the best set of resonant masses, widths and fractions describing the density of points within the multi-dimensional phase space. Such a method was first used by Friedman & Ross [5] in the analysis

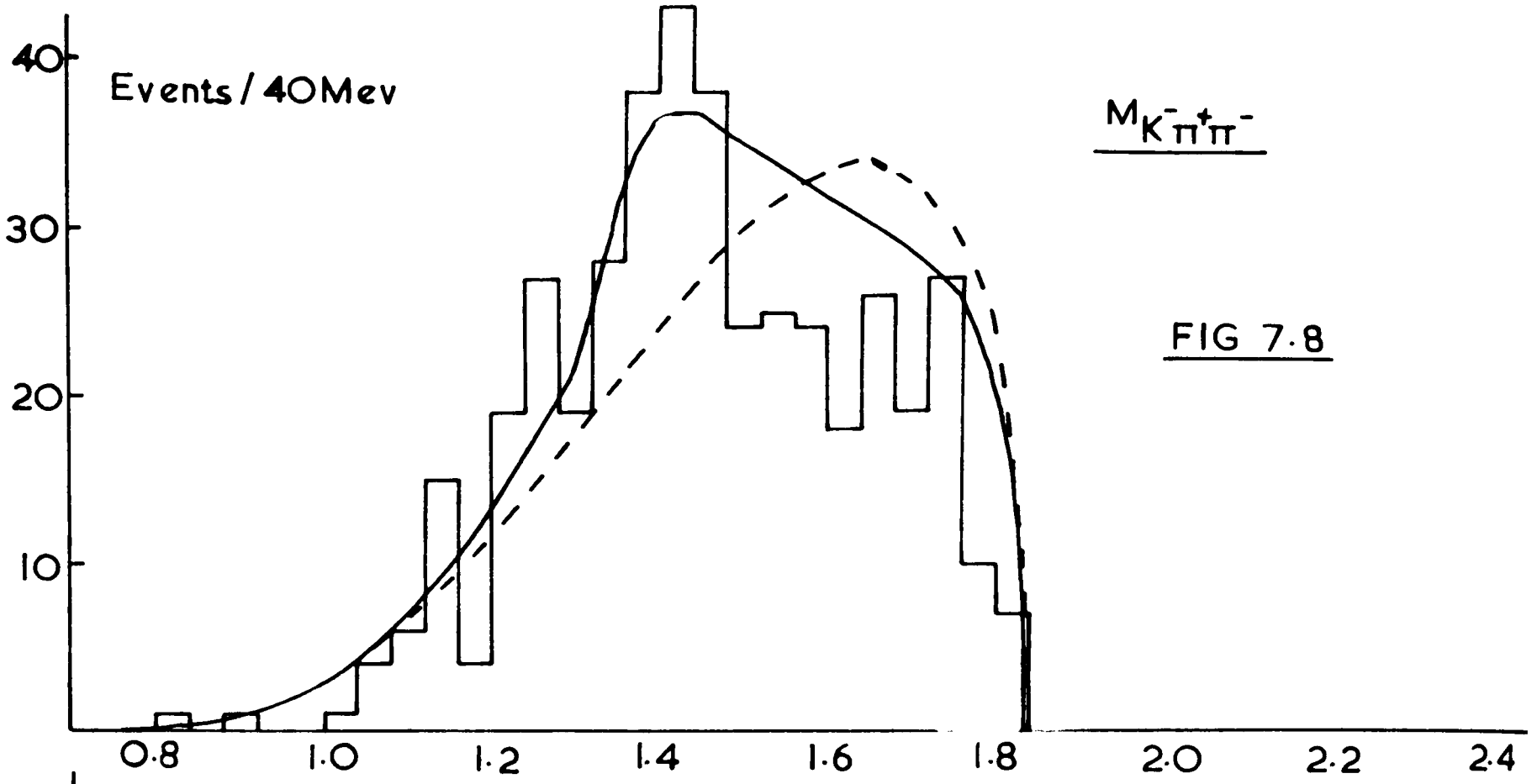
Events / 40Mev
40
30
20
10
0.8
1.0
1.2
1.4
1.6
1.8
2.0
2.2
2.4
$M_{K^-\pi^+\pi^-}$

FIG 7.8

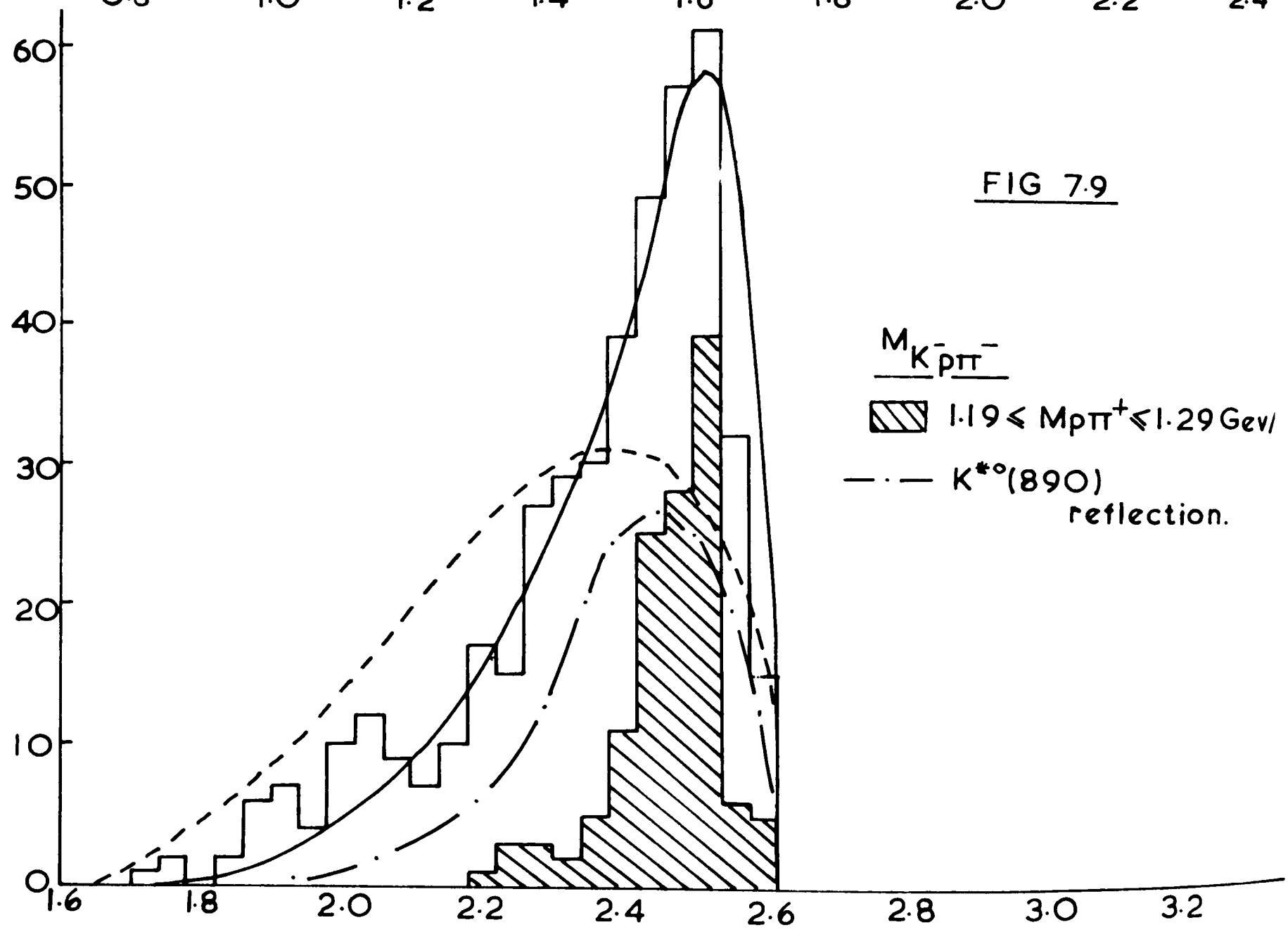
60
50
40
30
20
10
0
1.6
1.8
2.0
2.2
2.4
2.6
2.8
3.0
3.2
$M_{K^-p\pi^-}$
$1.19 \leq M p\pi^+ \leq 1.29$ Gev/
$K^{*0}(890)$ reflection.

FIG 7.9

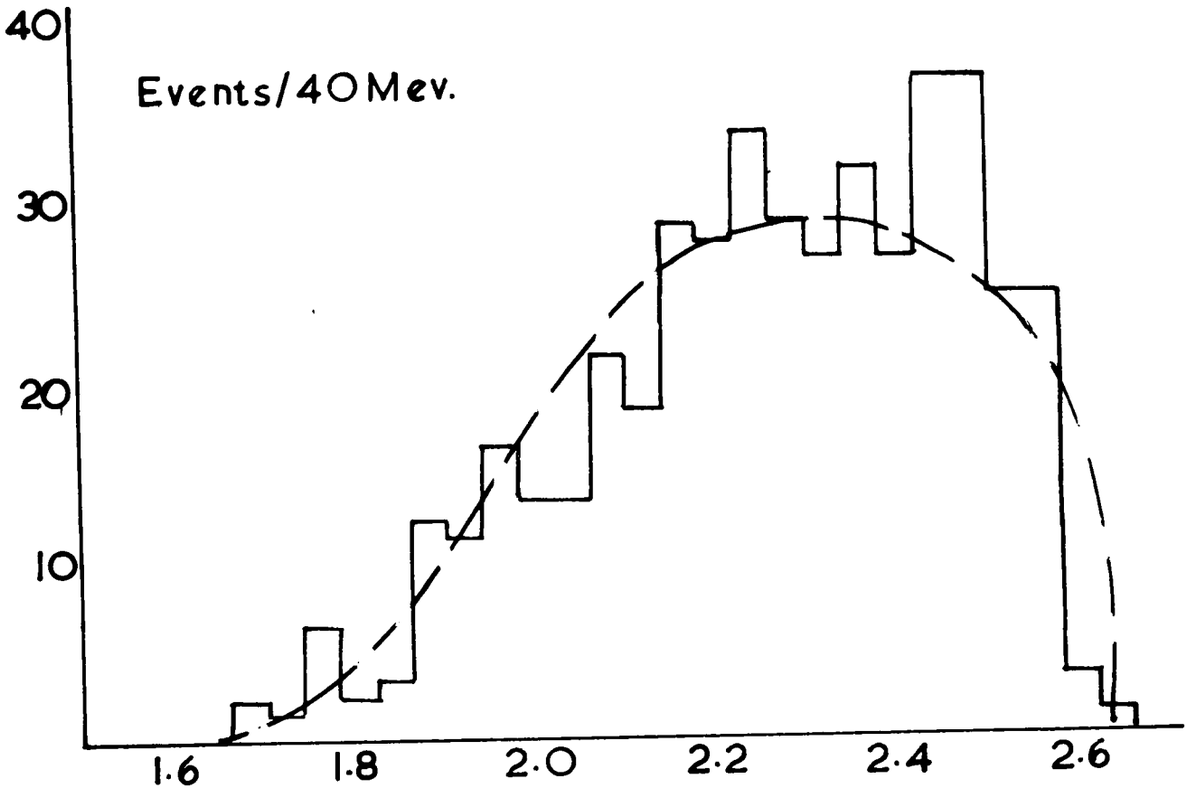

FIG. 7.10

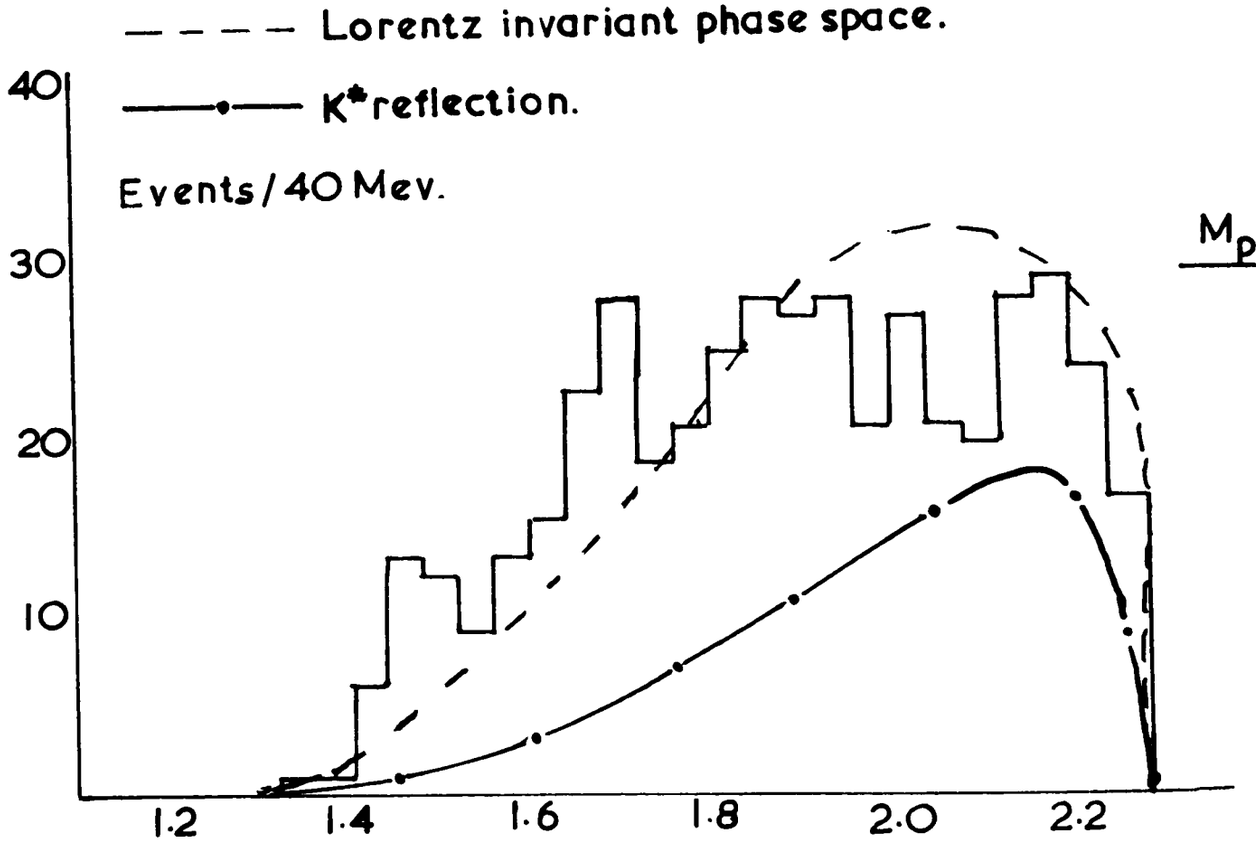

FIG. 7.11

of the $\Lambda 3\pi$ final state produced by the K^-p interaction at 2.45 GeV/c incident momentum, and is now described.

Consider an n-body final state produced by the scattering of a K^-p system, and let R_n be the total phase space available for such a reaction. If this is Lorentz invariant it may be written as [6]

$$R_n(E) = \int \frac{dp_1}{2E_1} \quad \frac{dp_2}{2E_2} \quad \ldots\ldots \frac{dp_n}{2E_n} \quad \times \delta^3\left(\sum_{i=1}^{n} p_i - P\right) \times \delta\left(\sum_{i=1}^{n} E_i - E\right)$$

where P is the CMS momentum and E the total energy. If one then considers the production of a single resonance between a system of K particles in this state as in Fig. 7.12 one may write the cross section (σ) as a function of the invariant mass of that system (M_K) as [7]

$$\frac{\partial \sigma}{\partial M_K^2} = \frac{1}{\pi} \frac{M_o \Gamma(M_K)}{(M_o^2 - M_K^2)^2 + M_o^2 \Gamma^2(M_K)} \quad R_{n-K+1}(E) \quad \ldots. \quad (8)$$

where M_o is the resonant central mass and Γ the mass dependent width. This is the familiar relativistic Breit-Wigner function. The factor $R_{n-K+1}(E)$ is the total phase space available to the n-K+1 particles in the final state one of which is the resonance having mass M_K.

It is possible to show that the differential mass spectrum of the system M_K in the absence of a resonance can be written

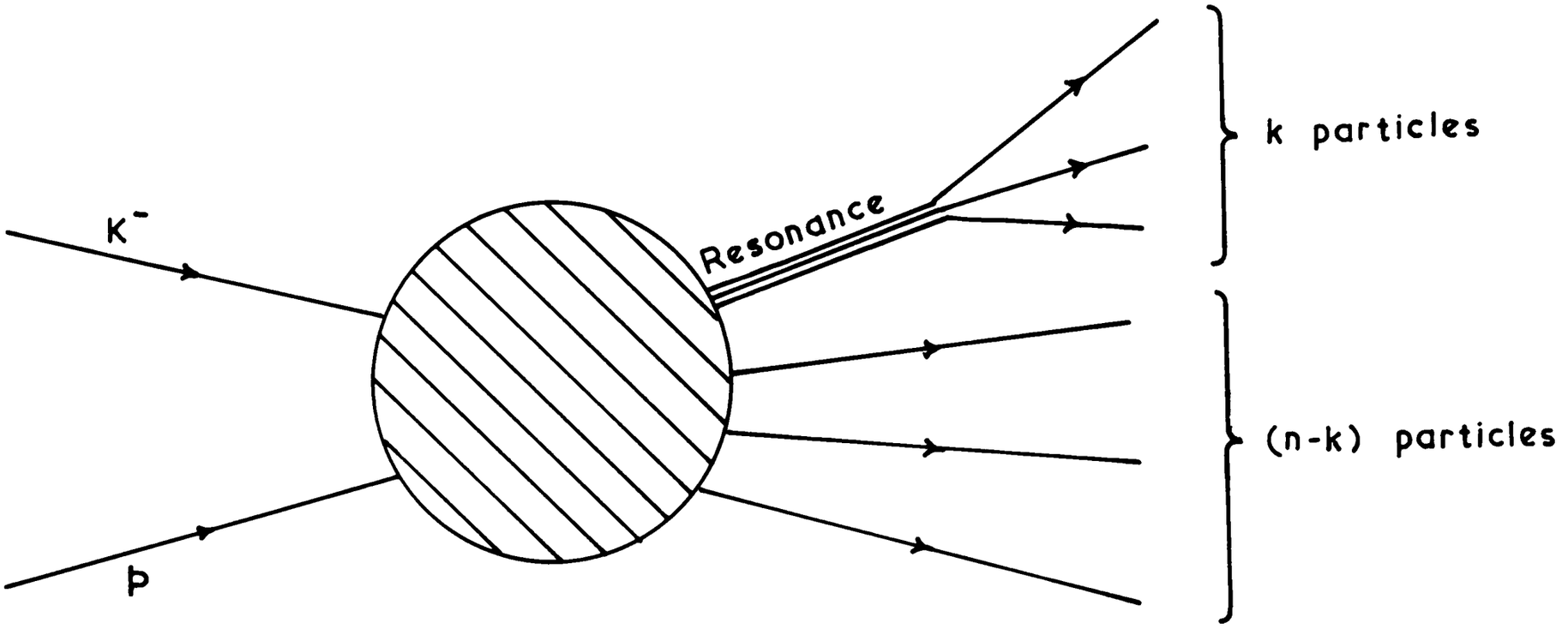

FIG. 7.12 Single resonance production.

as: $$\frac{\partial R_n}{\partial M_K^2} = R_K(M_K) \times R_{n-K+1}(E) \qquad \ldots\ (8)a$$

where R_{n-K+1} is the factor referred to above, and $R_K(M_K)$ is the total phase space available to the K particles in their own centre of mass system. In the case K = 2 this is proportional to p/M_K where p is the relative momentum of the two particles in their own CMS.

Therefore, for a two body resonance (8) may be written as:

$$\frac{\partial \sigma}{\partial M_K^2} = \left[\frac{1}{\pi} \frac{M_o \Gamma(M_K)}{(M_o^2 - M_K^2)^2 + M_o^2 \Gamma^2(M_K)} \cdot \frac{M_K}{p} \right] \frac{\partial R_n}{\partial M_K^2} \qquad \ldots\ (8)b$$

One may differentiate this cross-section with respect to as many further independent invariant masses as desired to yield the factor:

$$\rho = \frac{\partial^s R_n}{\partial M_1^2 \partial M_2^2 \ldots \partial M_s^2}$$

multiplying the term in square brackets above. If s is the maximum number of degrees of freedom allowed (depending upon n) then ρ is a simple product of momenta and is illustrated in Fig. 7.13. for a four body state. One keeps subdividing the particles into pairs for each of which there is a relative momentum p_i (for the ith pair) in their centre of mass of the pair. Then the cross section for one process may be written as $|T|^2\rho$, say. Making the assumption that all processes are independent, the cross-section as a function of the invariant masses (M_i) for the ith event can be expressed as a sum of the

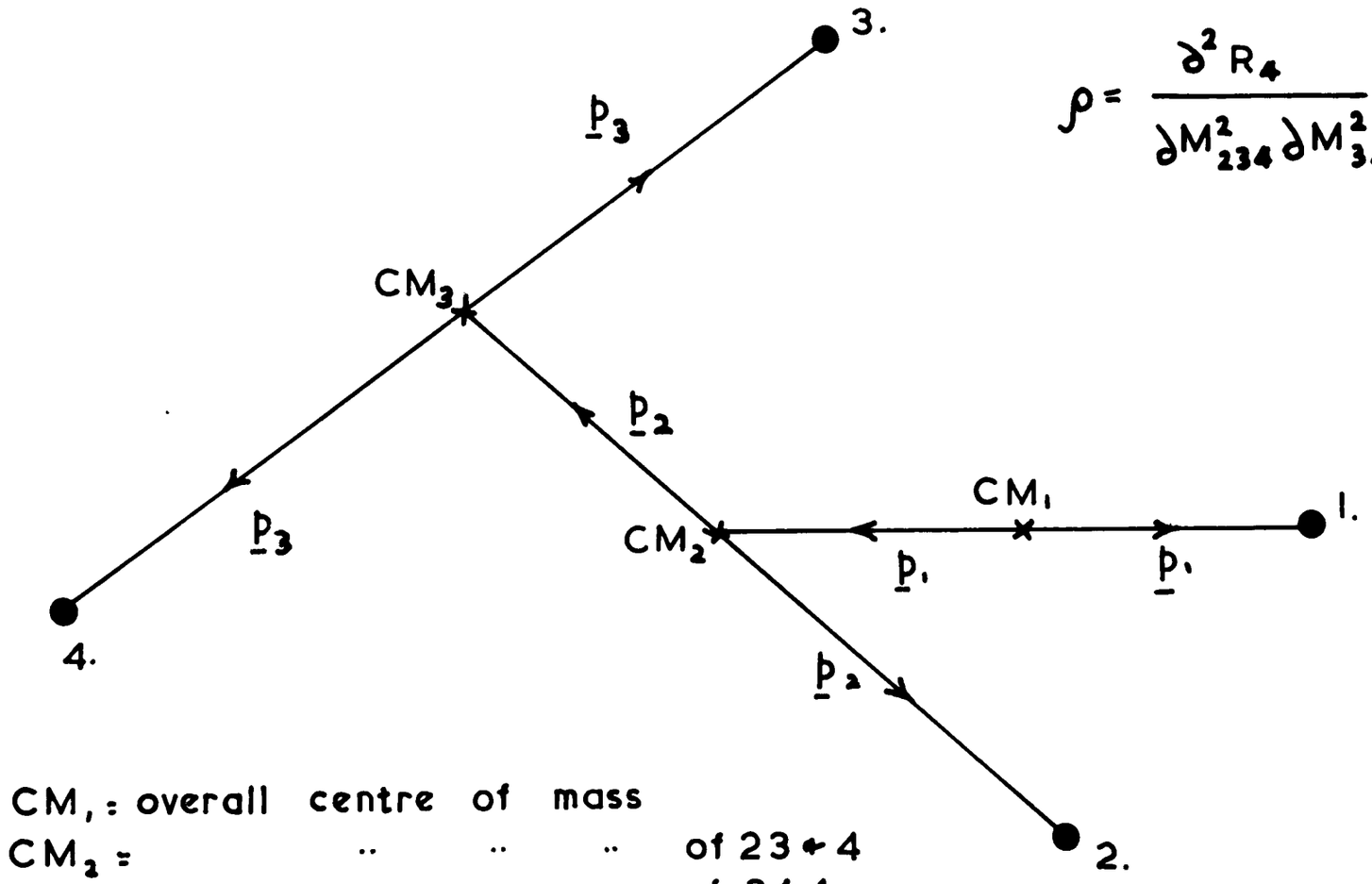

$$\rho = \frac{\partial^2 R_4}{\partial M_{234}^2 \partial M_{34}^2} \propto \frac{p_1 p_2 p_3}{M_{234} M_{34}}$$

CM_1 : overall centre of mass
CM_2 = " " " of 23+4
CM_3 = " " " of 3+4

FIG. 7·13

partial cross-sections as follows:-

$$\sigma(M_i^2) = \sum_j \frac{f_j |T_j|^2 \rho_i}{N_j} + (\text{non-resonant term}) \quad \ldots\ (9)$$

The subscript (i) on ρ indicates the dependence of this quantity upon the total centre of mass energy which in turn depends upon the beam momentum. This is assumed to be the same for all events in the present analysis so that i may be dropped. Subscript (j) specifies the process under consideration which is assumed to contribute a fraction f_j to the final state, and the normalization N_j is given by:

$$N_j = \int |T_j|^2 \rho \, dM_i^2$$

where integration is over all invariant masses. It is therefore the single integral

$$N_j = \int |T_j|^2 \frac{\partial R_n}{\partial M_j^2} dM_j^2 \quad \ldots\ (10)$$

if M_j is the invariant mass used in the amplitude T_j.

The application of this simple model to the events under study involved the construction of the log-likelihood function

$$L = \sum_i \ln \left\{ \sum_j f_j \frac{|T_j|^2}{N_j} \rho + (\text{non-resonant term}) \right\} \quad \ldots\ (11)$$

and we see that the factor ρ was unimportant as it was a constant. The non-resonant process has amplitude $|T_o|^2 = 1$ and contributes a fraction $f_o = 1 - \sum_j f_j$ to the final state, and the normalization (10) is seen to ensure that $\int \sigma(M_i^2) dM_i^2$ over all masses was equal to unity. The expressions used for the resonant widths were:[7]

for and $K^{*o}(890)$: $\Gamma = \Gamma_o \left(\frac{M_o}{M}\right)\left(\frac{p}{p_o}\right)^3$

for $N^{*++}(1238)$ & $N^{*o}(1238)$:

$$\Gamma = \Gamma_o \left[\frac{(M_{p\pi} + m_p)^2 - m_\pi^2}{M_{p\pi}^2} \right] \left[\frac{M_{N^*}^2}{(M_{N^*} + m_p)^2 - m_\pi^2} \right] \left(\frac{p}{p_o} \right)^3$$

and for $Y_o^*(1520)$ & $K^{**}(1400)$: $\Gamma = \Gamma_o$

where p was the momentum of the particles in the (2-body) resonant centre of mass and subscripts zero referred to quantities at the resonant masses. For the 3-body decay ($K^{**} \rightarrow K^-\pi^+\pi^-$) the overall factor $1/R_3(M_{K\pi\pi})$ replaced the M/p factors used in the 2-body resonances. This was calculated from:[6]

$$R_3(M_{K\pi\pi}) = \int_o^{p_{max}} \frac{p_K^2 dp_K}{2E_K} \times$$

$$\left\{ \left[M_{K\pi\pi}^2 + m_K^2 - 2M_{K\pi\pi}E_K - (m_{\pi^+} + m_{\pi^-})^2 \right] \left[M_{K\pi\pi}^2 + M_K^2 - 2M_{K\pi\pi}E_K - (m_{\pi^+} + m_{\pi^-})^2 \right] \right\}^{\frac{1}{2}}$$

$$2(M_{K\pi\pi}^2 + m_K^2 - 2M_{K\pi\pi}E_K)$$

where E = total energy and m = mass of the particle whose subscript is used, and

$$p_{max} = \frac{\left\{ \left[M_{K\pi\pi}^2 - (m_{\pi^+} + m_{\pi^-} - M_K)^2 \right] \left[M_{K\pi\pi}^2 - (m_{\pi^+} + m_{\pi^-} + m_K)^2 \right] \right\}^{\frac{1}{2}}}{2M_{K\pi\pi}}$$

The method used to perform the maximization of L (equation (11)) has already been referred to and is described in Appendix D. It is clear that the alteration of a resonant mass or width requires the re-calculation of the relevant normalization N_j (equation (10)) so that the resulting maximization process was very time consuming. In order to fit masses, widths and fractions to each resonant process, sixteen parameters were varied (the N^{*o}

TABLE I

Maximum Likelihood Resonance Parameters

	Maximum Likelihood		Accepted Values [8]	
Resonance	Mass	Width	Mass	Width
$\bar{K}^{*o}(890)$	896.9±3	49.0±2	891±1	50±2
† $N^{*++}(1238)$)				
)	1209.9±8	167.4±7	1236±0.4	120±1.5
$N^{*o}(1238)$)				
$K^{**-}(1400)$	1428.3±18	135.1±11	1410±10	100±20
$\rho^{o}(750)$	722.7±24	131.1±12	769±3	112±4
$Y^{*o}(1520)$	1519.8±11	27.3±14	1518.9±1.5	16±2

† Constrained to have same values

and N^{*++} were constrained to have the same mass and width). Variation of the masses was therefore carried out first and the widths and percentages allowed to vary subsequently (keeping the masses fixed). Overall variation was not feasible for the reason pointed out in Appendix D and the final values for resonant parameters are summarized in Table I where they are also compared with the accepted values.[8]

Monte Carlo Events

One would like to check the solutions presented in Tables I-II with experiment in order to investigate the presence of any minor resonant channels. One possible way of obtaining the shape of a particular invariant mass combination would have been to integrate the density function (equation (9)) over all but the required mass. This would have been somewhat tedious as the evaluation of the limits of each integration would have been difficult and the many-fold integration very time consuming. A more convenient way was the use of an existing computer programme to generate some Monte Carlo events corresponding to each resonance production process in turn. The resulting smooth curves are shown as solid lines on the invariant masses of Figs. 7. 1-6 and 8-11 and suggest that all the major resonant channels have probably been included.

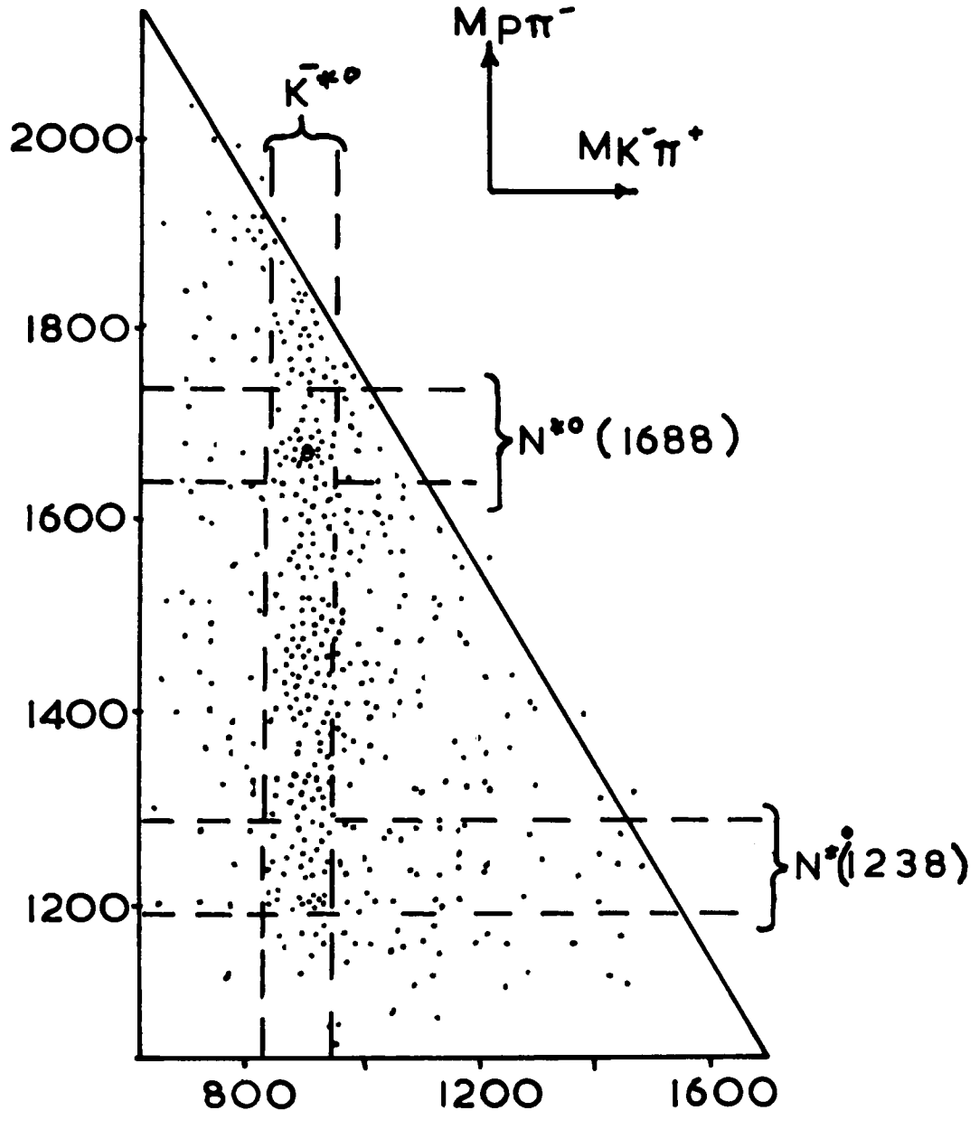

FIG 7.14 (a)

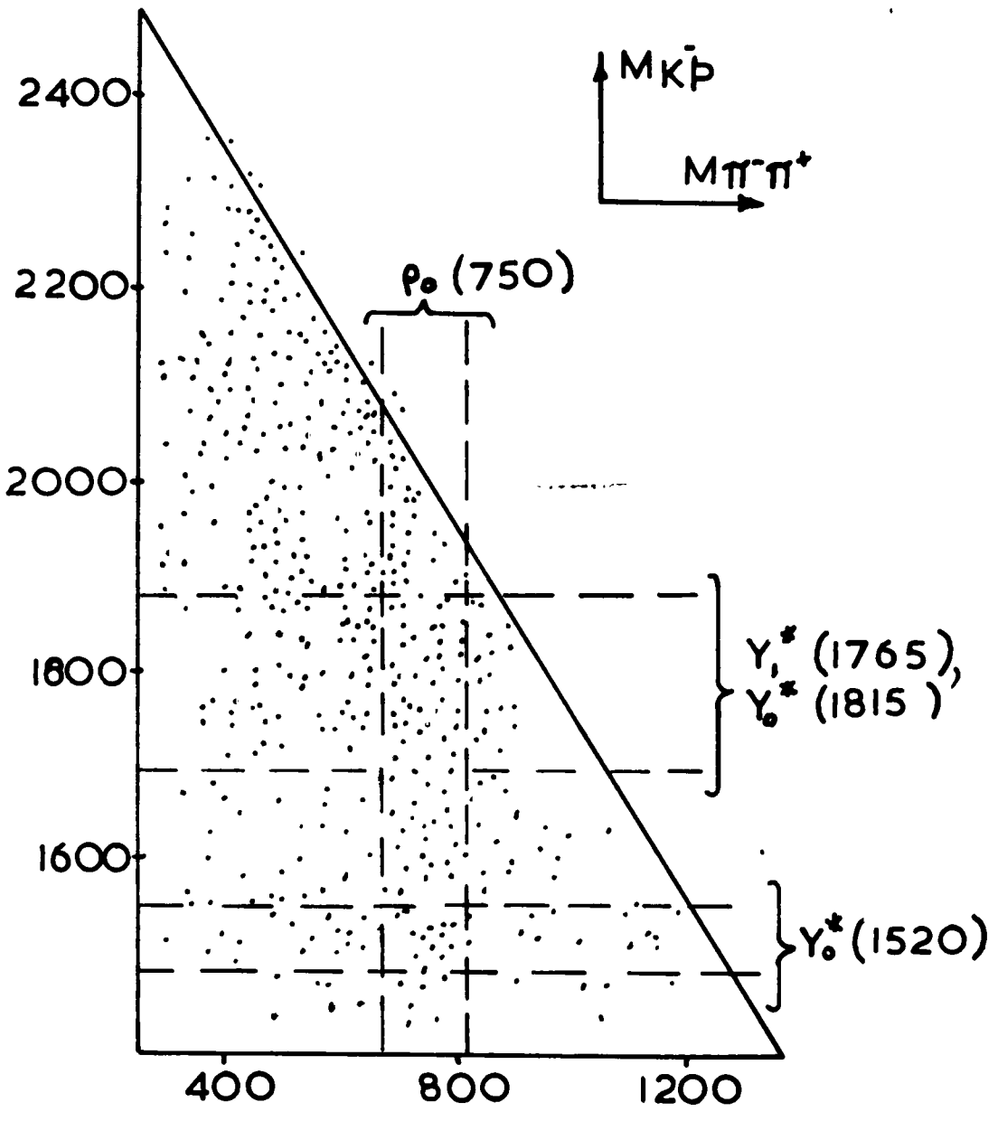

FIG. 7.15 (a)

Associated Productions

It is of interest to consider the possibility of double resonance production among the two body resonances. This may be conveniently investigated by an inspection of the triangle plots which show the scatter of events when the invariant mass of one pair of particles is plotted against the invariant mass of the remaining pair. As is demonstrated subsequently, the distribution of points is expected to be fairly uniform over the central portion of such a plot, but to vanish at the edges. As no $K^-\pi^-$ resonance is observed, it is only of interest to consider the (2-body) triangle plot with $M_{p\pi^-}$ and $M_{K^-\pi^+}$ forming rectangular axes (Fig. 7.14) and that having $M_{\pi^-\pi^+}$ and M_{K^-p} as axes (Fig. 7.15). The kinematic boundary (drawn in these figures) is simple to understand since, for fixed $p\pi^-$ mass, for instance, the $K^-\pi^+$ system is allowed to take any value from $K\pi$ threshold ($=m_K + m_\pi$) up to $E - M_{p\pi^-}$ (where E is the total centre of mass energy).

$K^-p \rightarrow K^{*0}(890) + N^{*0}(1238)$

From Fig. 7.14 it is observed that little, if any, $N^{*0}(p_{\pi^-})$ band at 1238 Mev is noticeable, whereas the selection of events lying in the very pronounced K^{*0} band tends to enhance the peak in the projected $M_{p\pi^-}$ distribution (Fig. 7.14(b)). The further selection of events having low momentum transfer to the (p_{π^-})

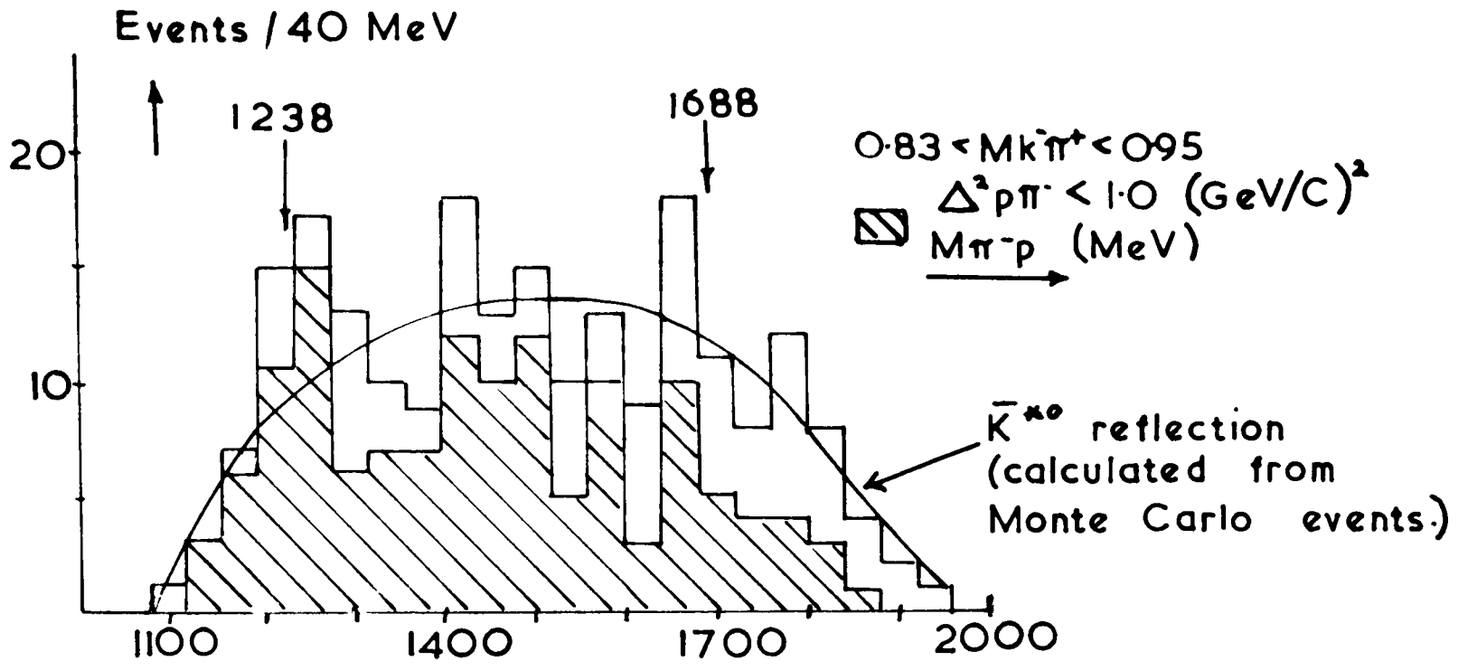

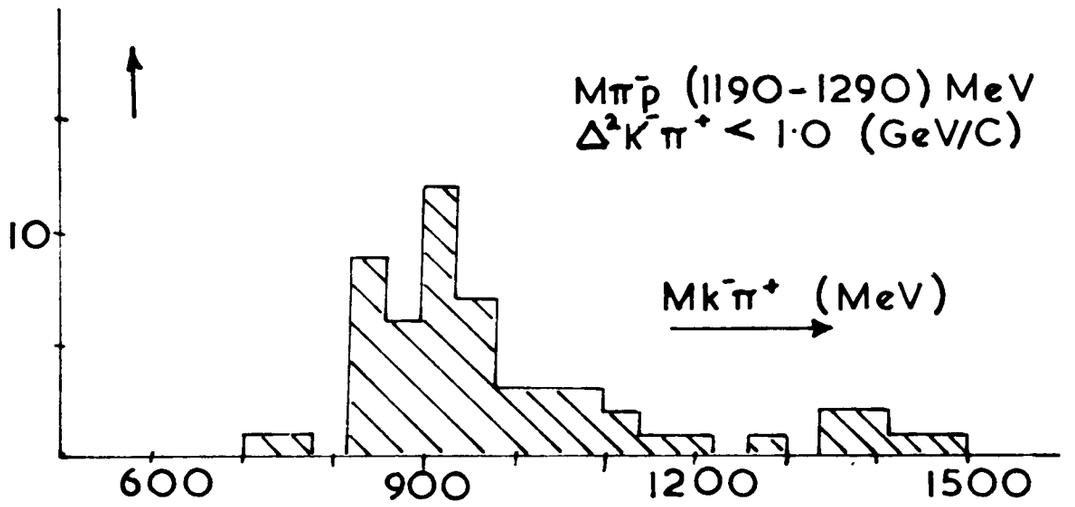

FIG 7 14 (b)

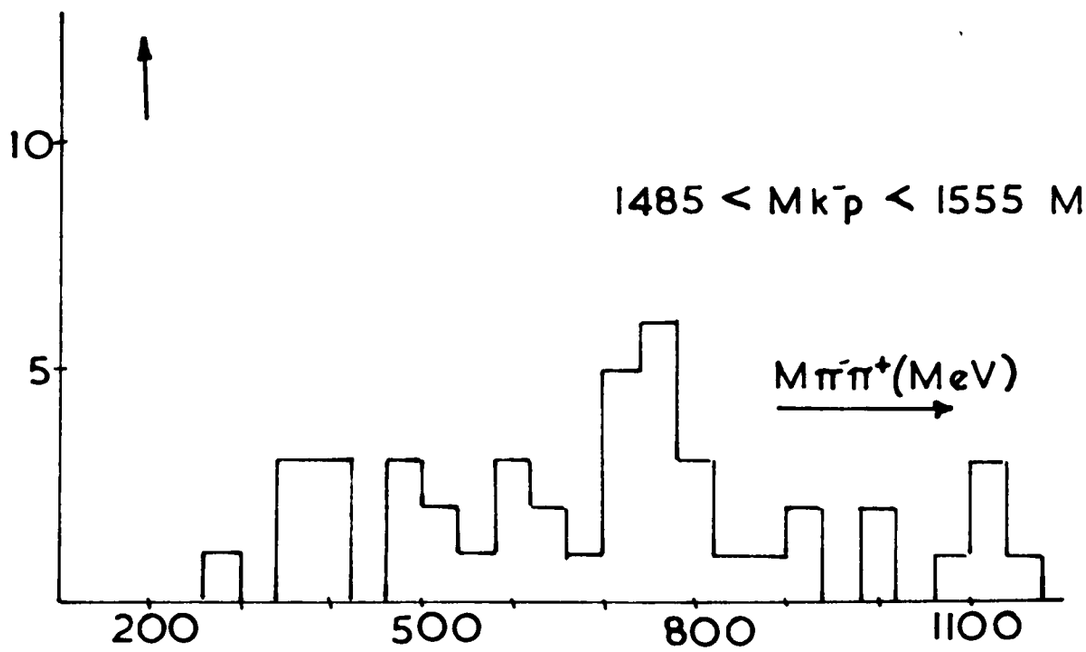

FIG 7 15 (b)

system ($<1.0(\text{Gev/c})^2$) does not lessen the effect. The peripheral production process $K^-p \rightarrow K^*(890)N^*(1238)$ has been noticed previously at 3.5 Gev/c[9] and found to be consistent with single pion exchange in the application of both the unadorned[9] and the absorption modified[10] one meson exchange models. One may estimate the number of events corresponding to the associated production of K^{*o} and N^{*o} from Fig. 7.16(a) in the following way:- In A we expect events representing the associated production process as well as the following reactions:

$$K^-p \rightarrow K^{*o}p\pi^- \quad \ldots\ldots (a)$$

$$\rightarrow N^{*o}K^-\pi^+ \quad \ldots\ldots (b)$$

$$\rightarrow \text{other processes} \quad \ldots\ldots (c)$$

We may use regions B and C to estimate the number of such events since B contains examples of reactions (a) and (c), whilst C contains (b) and (c). However, if one were to subtract the number of events contained within these areas the background events (c) would have been subtracted twice. Consequently, one needs also to consider the regions D. If each of these has an area of one quarter of A, the total number of events in D must be added. Performing this crude calculation one obtains the total number of $K^{*o}N^{*o}$ events of 14. Allowance need also be made for the tails of the resonances which have been neglected and may be estimated from the Monte Carlo events to amount to an

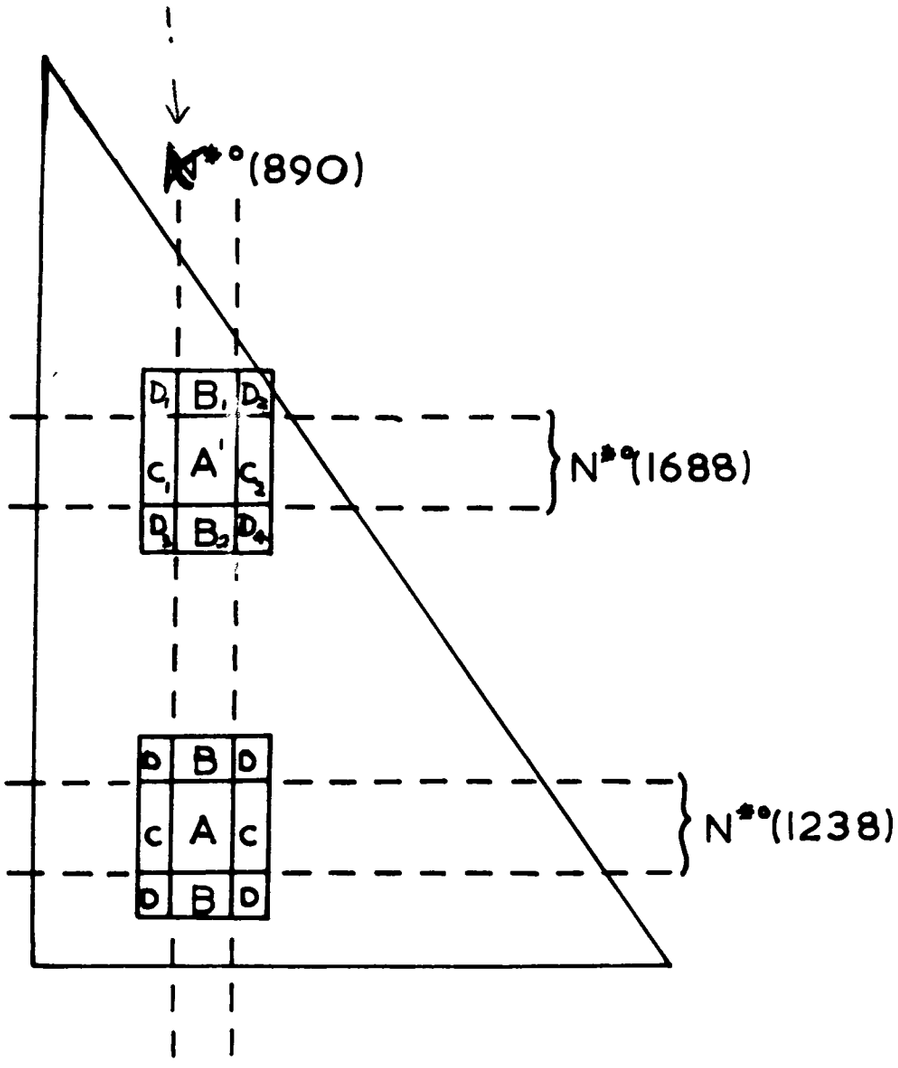

FIG 7.16(a)

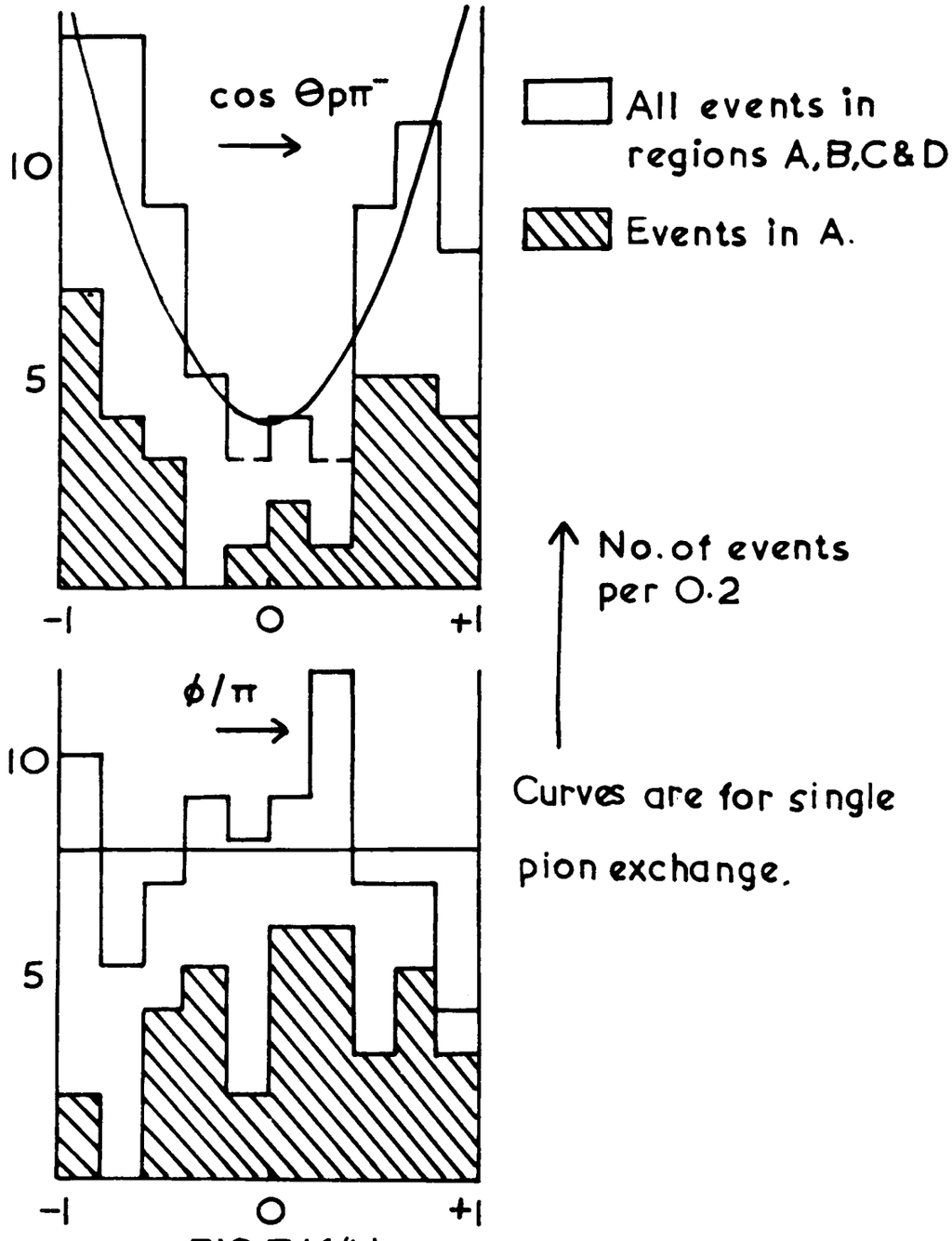

FIG 7.16(b)
$N^{*0}(1238)$ decay angles.

additional 40% to give a total of 19.6 events.This small number of events makes the analysis of the decay distribution of these resonances somewhat meaningless.However,the Cosθ^* and ϕ distributions (where these variables are similar to those defined in the previous chapter) are shown in Fig.7.16(b) and are not inconsistent with the expectation of pion exchange.

$K^-p \rightarrow K^{*o}N^{*o}(1688)$

Fig.7.14(b) illustrates the $p\pi^-$ mass spectrum for events lying in the K* band.The curve superimposed is that calculated from the Monte Carlo events representing the process $K^-p \rightarrow K^{*o}p\pi^-$ which forms 80% of the final state in this region and is normalized to the number of events in the plot.The $N^{*o}(1238)$ is evident as a two standard deviation enhancement.The small peak at about 1688 Mev is,however,far less significant (little more than one standard deviation). One might have expected to find stronger production of $N^{*o}(1688)$ in this state as it was observed (at this energy)[9] to be produced with a positive charge in association with K*.This is interesting from the point of view of the production mechanism.The distribution of the four momentum transfer to the $p\pi^-$ shows a somewhat enhanced N*(1238),though no bump at 1688 at all (see Fig.7.5). The plot of momentum transfer to the $p\pi^-$ vs the $p\pi^-$ mass (Fig.7.17) also demonstrates this.If the latter resonance were produced by one pion exchange - in analogy with the lower N* - one might expect to observe a preference for low

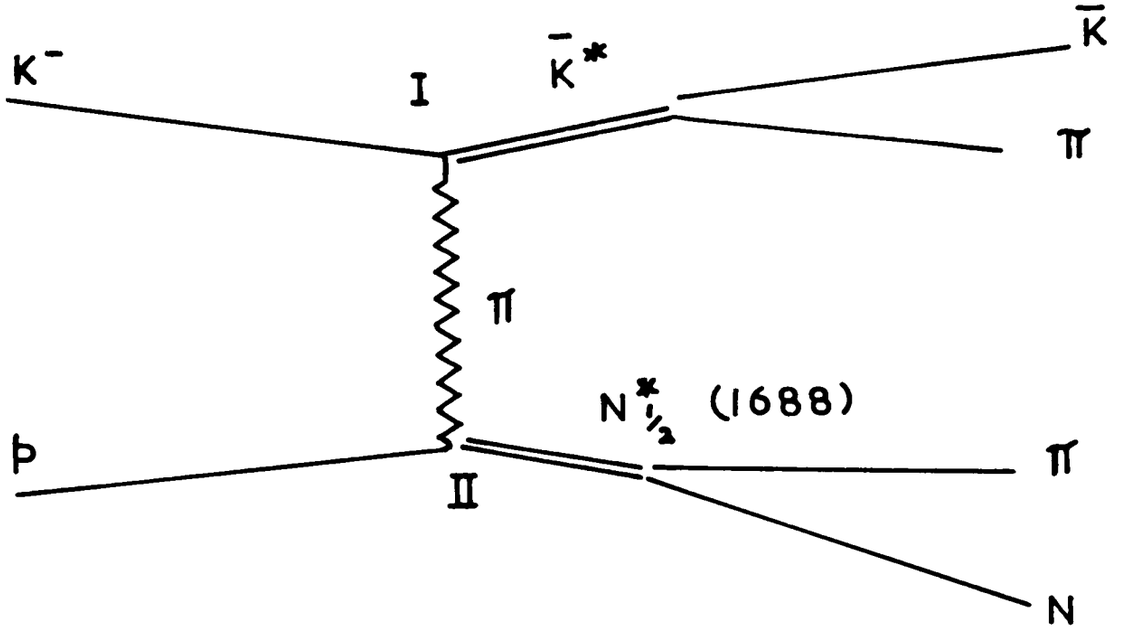

At vertex I:

$$|K^-\rangle = -\sqrt{\frac{2}{3}}|\bar{K}^{*0}\rangle|\pi^-\rangle + \sqrt{\frac{1}{3}}|K^{*-}\rangle|\pi^0\rangle$$

At vertex II:

$$|p\rangle = -\sqrt{\frac{1}{3}}|N^{*+}\rangle|\pi^0\rangle + \sqrt{\frac{2}{3}}|N^{*0}\rangle|\pi^+\rangle$$

FIG. 7.17 (a)

momentum transfer. Further, the diagrams illustrating this process in Fig. 7.17 (a) and (b) indicates - by charge independence at the strongly interacting vertices I and II - that the production of $N^*(1688)^0K^*(890)^0$ might occur four times as often as $N^*(1688)^+K^*(890)^-$. However, preferred exchange of an isosinglet (η, ω, etc) might account for the lack of this process in the four prongs.

An upper limit to the cross-section might be obtained in a similar way to the estimation of the $K^{*\Theta}(890)N^{*\circ}(1238)$ rate. In this case, however, region D_4 (see Fig. 7.16) occurs off the edge of the triangle plot. Consequently, D_2 is used twice in order to estimate the background contribution. The resulting number of events (8 ± 3) indicates an upper limit of about 0.16 mb, after correcting for the other possible decay modes of the $N^{\circ}_{\frac{1}{2}}$ and the $\bar{K}^{*\circ}_{\frac{1}{2}}$ and for the Breit-Wigner tails, to be compared with the figure of 0.29 ± 0.09 mb which can be inferred from the $N^{*+}(1688)$ production.[9]

Associated Production of $Y^{*\circ}$ and ρ°

Turning to Fig. 7.15 which is the triangle plot having the $\pi^+\pi^-$ and K^-p masses as x- & y-axes respectively, the presence of the ρ° is apparent. The only band in the perpendicular direction corresponding to a known resonance is at the mass of about 1520 Mev, and this is seen to be rather weak (see Table II).

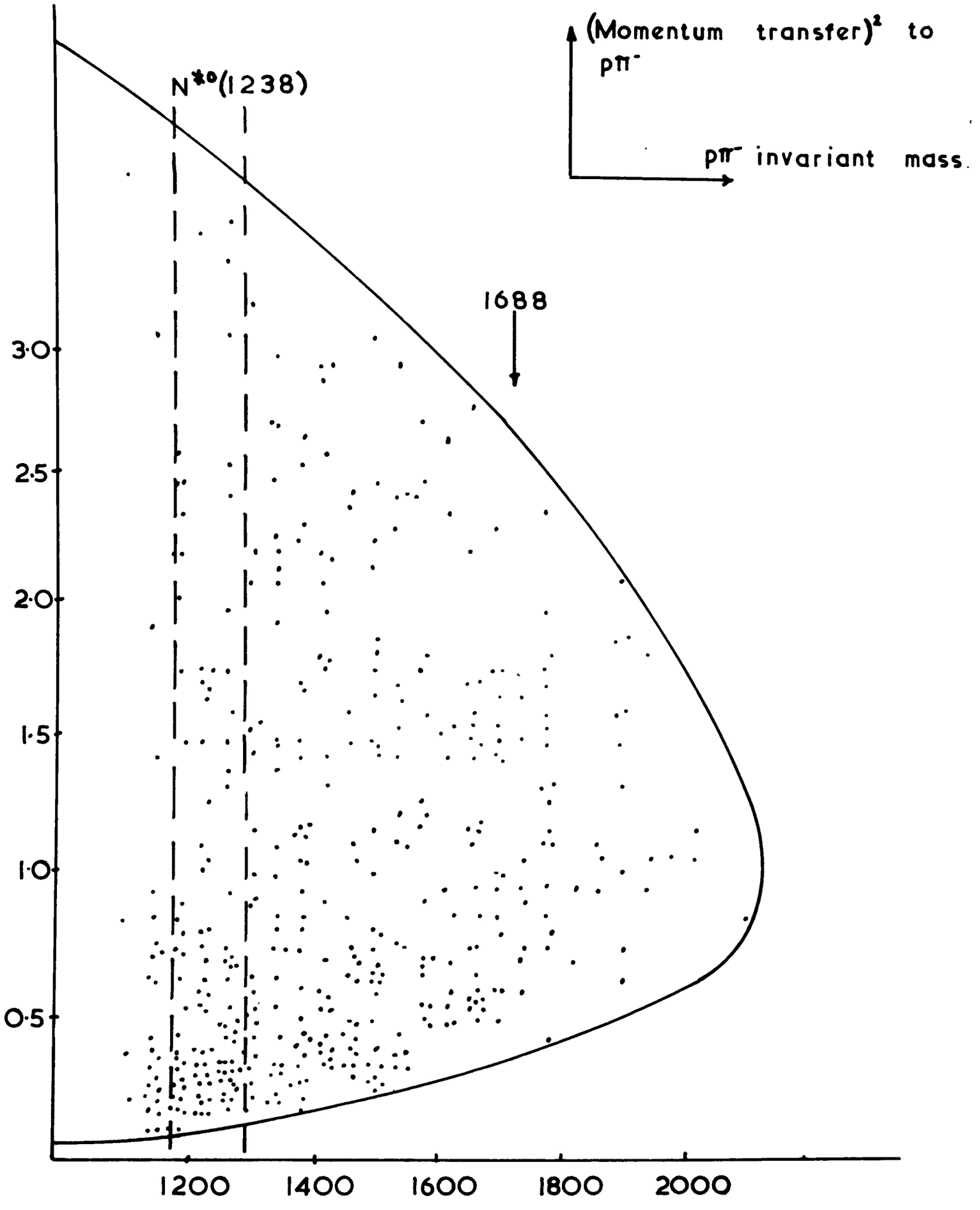
(Momentum transfer)² to pπ⁻
pπ⁻ invariant mass.
N*⁰(1238)
1688
3·0
2·5
2·0
1·5
1·0
0·5
1200
1400
1600
1800
2000

FIG. 7.17 (b)

No clear evidence for the production of Y*(1765) or Y*(1815) is offered by Fig. 7.15, and the association of $Y^{*o}(1520)$ and ρ^o is also certainly not strong. Though Fig.7.15(b) indicates the presence of ρ^o in the $\pi^+\pi^-$ mass spectrum when the latter Y* is selected, the counting of events in the manner just indicated yields a result of a possible four events consistent with $Y^*_o(1520)\rho^o$ associated production. A similar crude analysis provides a negative result for the number of Y*(1765)ρ or Y*(1815) events. No improvement in those numbers results from a selection on low momentum transfer, though the removal of K* from the sample tends to enhance the mass peak associated with the Y*(1520) as shown in Fig. 7.4.

Quantitative Analysis of Associated Production

The method used to estimate the associated production cross-sections was certainly very crude, and made no allowance, for instance, for the expected density of points on the triangle plot mentioned previously. Further, the triangle plot itself is just a projection of the whole phase space for the final state onto a plane and the actual distribution of points on it must anyway be affected by the presence of other processes (for instance the production of N^{*++}). A more consistent analysis can be achieved by including these double resonant processes in the maximum likelihood function already described.

Reverting to equation (8) it is apparent that the production cross-section for a pair of resonances will be given by

$$\frac{\partial^2 \sigma}{\partial (M^1)^2 \partial (M^2)^2} = \left[\frac{1}{\pi} \frac{M_o^1 \Gamma^1 (M_{K1}^1)}{\left\{ (M_o^1)^2 - (M_{K2}^1)^2 \right\}^2 + (M_o^1)^2 (\Gamma^1)^2} \right] \times \left[\frac{1}{\pi} \frac{M_o^2 \Gamma^2 (M_{K2}^2)}{\left\{ (M_o^2)^2 - (M_{K2}^2)^2 \right\}^2 + (M_o^2)^2 (\Gamma^2)^2} \right] \times R_{(n-K1-K2+2)}$$

(where the superscripts refer to the first and second resonances) since it is only necessary to replace $R_{n-K+1}(E)$ in equation (8) by the whole of the expression for $\partial\sigma / \partial M_1^2$.

The factor $R_{n-K_1-K_2+2}$ represents the available phase space for the remaining $(n-K_1-K_2+2)$ particles which include the resonances which decay respectively into K_1 and K_2 particles, and may be calculated from the equation 8(a) since:

$$\frac{\partial^2 R_n}{\partial (M^2)^2 \partial (M^1)^2} = \frac{\partial}{(M^2)^2} \left[R_{K_1}(M^1) \times R_{n-K1+1}(E) \right]$$

$$= R_{K_2}(M^2) \times R_{K_1}(M^1) \times R_{n-K_2-K_1+1}(E)$$

Substituting this into the above expression for the double resonant cross-section we obtain:-

$$\frac{\partial^2 \sigma}{\partial (M^1)^2 \partial (M^2)^2} = F(M^1) F(M^2) \frac{1}{R_{K_2}(M^2) R_{K_1}(M^1)} \frac{\partial^2 R_n}{\partial (M^1)^2 \partial (M^2)^2} \quad \ldots\ldots (8)c$$

where the Fs replace the square brackets.

We may once more differentiate with respect to as many masses as possible in order to obtain the factor ρ multiplying the intensity function $|T_{ij}|^2$ which describes the production of ith and jth resonances. In this case, therefore, the $|T_{ij}|^2$ is just a product of two single resonant amplitudes:

$$|T_{ij}|^2 = |T_i|^2 \, |T_j|^2$$

The normalization integral N_{ij} is given by:

$$N_{ij} = \int |T_i|^2 \, |T_j|^2 \, \rho \, dM^2 = \iint |T_i|^2 \, |T_j|^2 \, \frac{\partial^2 R_n}{\partial M_i^2 \partial M_j^2} \, dM_i^2 dM_j^2$$

In the present case of two particle resonances, the differential factor is simple to evaluate as it is:

$$\frac{\partial^2 R_4}{\partial M_i^2 \partial M_j} = \frac{\partial}{\partial M_i^2}\left[\frac{p_j}{M_j} \times R_3\right] = \frac{p_j}{M'_j} \times \frac{p_i}{M_i} \times \frac{P}{E} \qquad \ldots\ (12)$$

where p_i is the relative momentum in their CMS of the particles of resonance i, M_i is their invariant mass and P is the relative momentum of the two resonances in the overall centre of mass. It is seen that at the boundaries of the triangle plot, one of the momenta will vanish, and so account for the zero density of points ($\frac{\partial^2 R_4}{\partial M_i \partial M_j}$) expected in this region. The integration of N_{ij} extends over the relevant triangle plot and the addition of the term:

$$f_{ij} \frac{|T_i|^2 \, |T_j|^2}{N_{ij}}$$

into the likelihood function can be seen to have the effect of

TABLE II

Resonance Fractions in the Reaction

$K^- p \rightarrow K^- p \pi^+ \pi^-$

Production Process	Beam Energy (Gev/c)	% Of Final State	Cross-Section (μb)	Ref.
$K^- p \rightarrow \bar{K}^{*o} p \pi^-$	2.0 2.24 3.5	3±2 20 47±4	21±11 89±22 637±50	27 26e Ibid
$\rightarrow N^{*++} K^- \pi^-$	2.0 2.24 3.5	44±2 20 31±4	275±15 89±22 418±54	
$\rightarrow N^{*o} K^- \pi^+$	2.0 3.5	6±2 7±3	36±11 93±38	
$\rightarrow Y^{*o}(1520) \pi^+ \pi^-$	2.0 2.24 3.5	13±2 8 2±1	82±13 38±5 26±17	
$\rightarrow \rho^o K^- p$	3.5	7±3	90±37	
$\rightarrow K^{*-}(1400) p$	3.5	14.±4	193±50	
$\rightarrow \bar{K}^{*o} N^{*o}(1238)$	2.0 2.24 3.5	20±2 < 3 1±1	125±11 - 14±12	
$\rightarrow \bar{K}^{*o} N^{*o}(1688)$	3.5	< 2.4	< 32	
$\rightarrow Y^{*o}(1520) \rho^o$	3.5	2±3	33±40	
$\rightarrow N^{*o}(1688) K^-$	2.0	10±3	63±19	
$\rightarrow K^- p \pi^+ \pi^-$	2.0 2.24 3.5	< 4 52 10±12	< 25 248±30 136±163	
TOTAL	2.0 2.24 3.5		630±30 476±58 1359±136	

giving events within region A of the plot (See Fig. 7.16) a large weight. In this way, the estimation of the fraction of the final state (f_{ij}) that corresponds to associated production automatically takes account of the tails of the Breit-Wigner curves ($|T_i|^2$ and $|T_j|^2$), as well as the reflection from other processes. The big assumption is, however, that all processes are incoherent.

Bearing in mind that the adjustment of either resonant mass or width in an associated production process requires the re-calculation of the double integral, N_{ij}, the fitting to these processes consisted only of the variation of the fractions f_{ij}. The two processes considered were:

$$K^-p \rightarrow K^{*o}(890)N^{*o}(1238)$$

$$\rightarrow Y^{*o}(1520) \quad {}^{o}(750)$$

as these are the only two not completely absent from the triangle plots. The resulting fractions for all processes are given in Table II. The masses and widths of the resonances used were those previously calculated for the single resonance productions.

The results are not inconsistent with those previously estimated by counting events, and the $K^{*o}N^{*o}$ cross-section may be compared with those found for other charge states at 3.5 Gev/c,[9] for the production of K*N* requires the initial K^-p system to be in the pure isotopic spin state T = 1. Starting from this fact,

TABLE III — $\bar{K}^* N^*$ production.

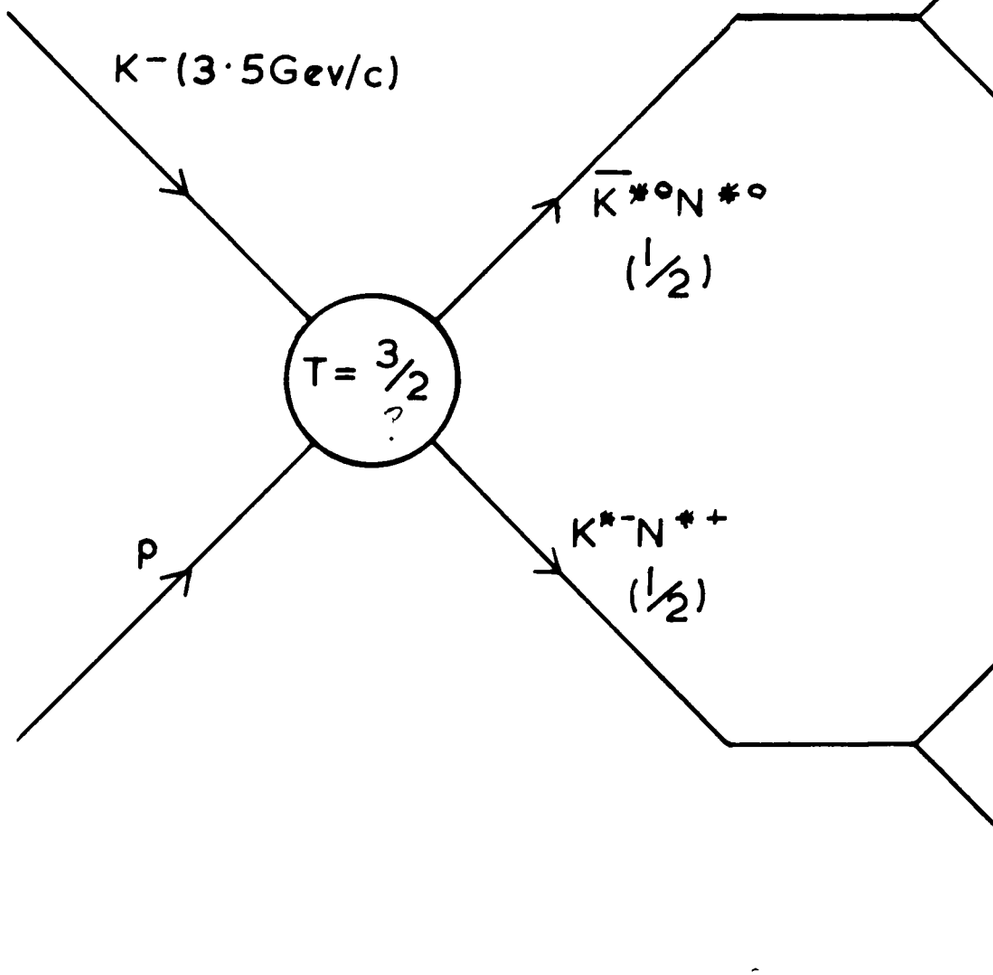

Final State.	Expected Rate.	Observed Rate. (μb)
$K^-\pi^+p\pi^-$	$(\frac{1}{2}\times\frac{2}{3}\times\frac{1}{3})=\frac{1}{9}$	14 ± 12
$K^-\pi^+n\pi^0$	$(\frac{1}{2}\times\frac{2}{3}\times\frac{2}{3})=\frac{2}{9}$	——
$\bar{K}^0\pi^0p\pi^-$	$(\frac{1}{2}\times\frac{1}{3}\times\frac{1}{3})=\frac{1}{18}$	Very little.
$\bar{K}^0\pi^0n\pi^0$	$(\frac{1}{2}\times\frac{1}{3}\times\frac{2}{3})=\frac{1}{9}$	——
$K^-\pi^0p\pi^0$	$(\frac{1}{2}\times\frac{1}{3}\times\frac{2}{3})=\frac{1}{9}$	——
$K^-\pi^0n\pi^+$	$(\frac{1}{2}\times\frac{1}{3}\times\frac{1}{3})=\frac{1}{18}$	——
$\bar{K}^0\pi^-p\pi^0$	$(\frac{1}{2}\times\frac{2}{3}\times\frac{2}{3})=\frac{2}{9}$	50 ± 20
$\bar{K}^0\pi^-n\pi^+$	$(\frac{1}{2}\times\frac{2}{3}\times\frac{1}{3})=\frac{1}{9}$	Very little.

all possible K*N* modes may be calculated from charge independence as in Table III. The other 3.5 Gev/c cross-sections are included in this and seen to be compatible with the result just obtained. A contrast may be made between the production from an incoming K^- of K*N* in four prong events with the corresponding production with incoming K^+. In the latter case, the whole initial state is pure T=1 and the production of K*N* dominates the whole four body reaction:[11]

$$K^+p \rightarrow K^+N\pi\pi$$

at all energies from threshold to at least 4.6 Gev/c.[4,11] In fact, the most favourable observation of this quasi two body state is in the four prong events. In the K^- case, however, K*N* in four prongs is a relatively unimportant channel.

It is clear, therefore, that the present state is dominated by production of K^{*o} and N^{*++}, but that each of these resonances has a weak partner (π^- and K^-) for formation of an associated resonance. The reaction therefore proceeds almost entirely via the quasi three body states some of which are discussed in the next sections.

<u>$K^-p \rightarrow K^{*o}p\pi^-$</u>

Selecting events with an invariant mass $0.83 < M_{K^-} < 0.95$ Gev. yields a sample containing approximately 80% $K^{*o}p\pi^-$ (estimated from the Monte Carlo events). It also contains approximately 7% $N^{*++}K^-\pi^-$. It is reasonable to estimate the

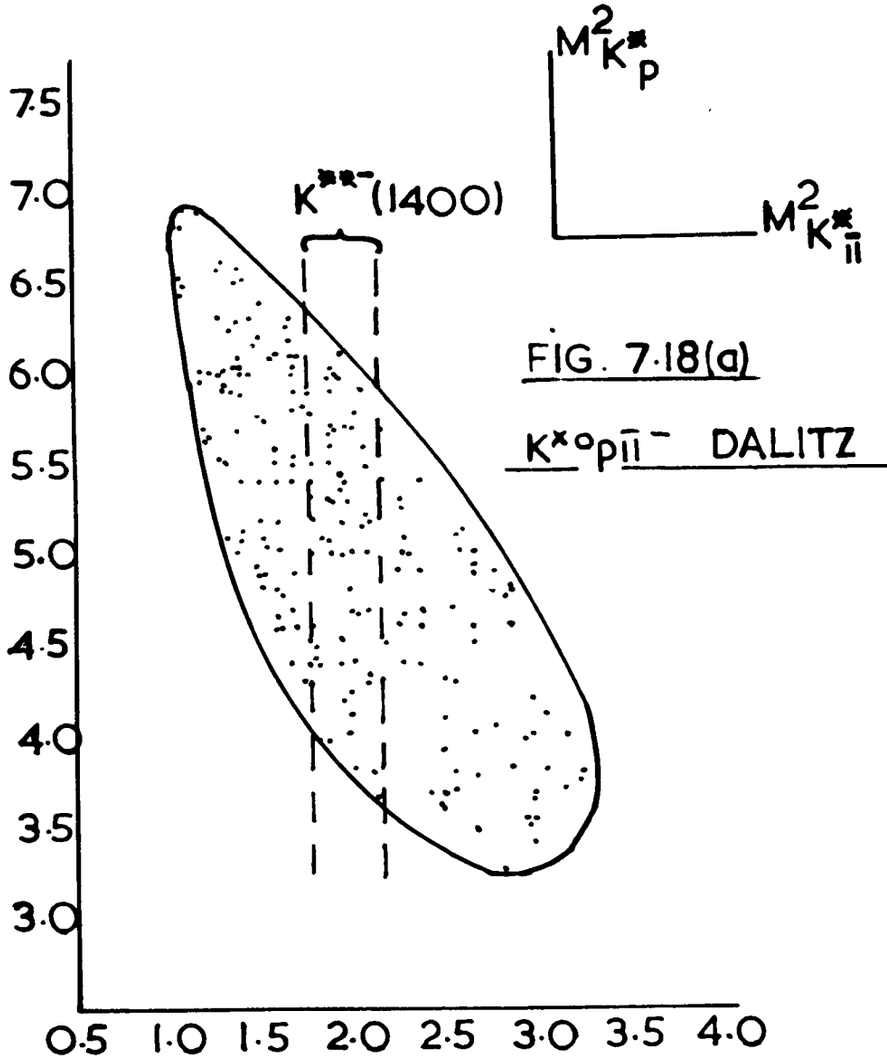

FIG. 7·18(a)

$K^{*0}p\pi^-$ DALITZ PLOT.

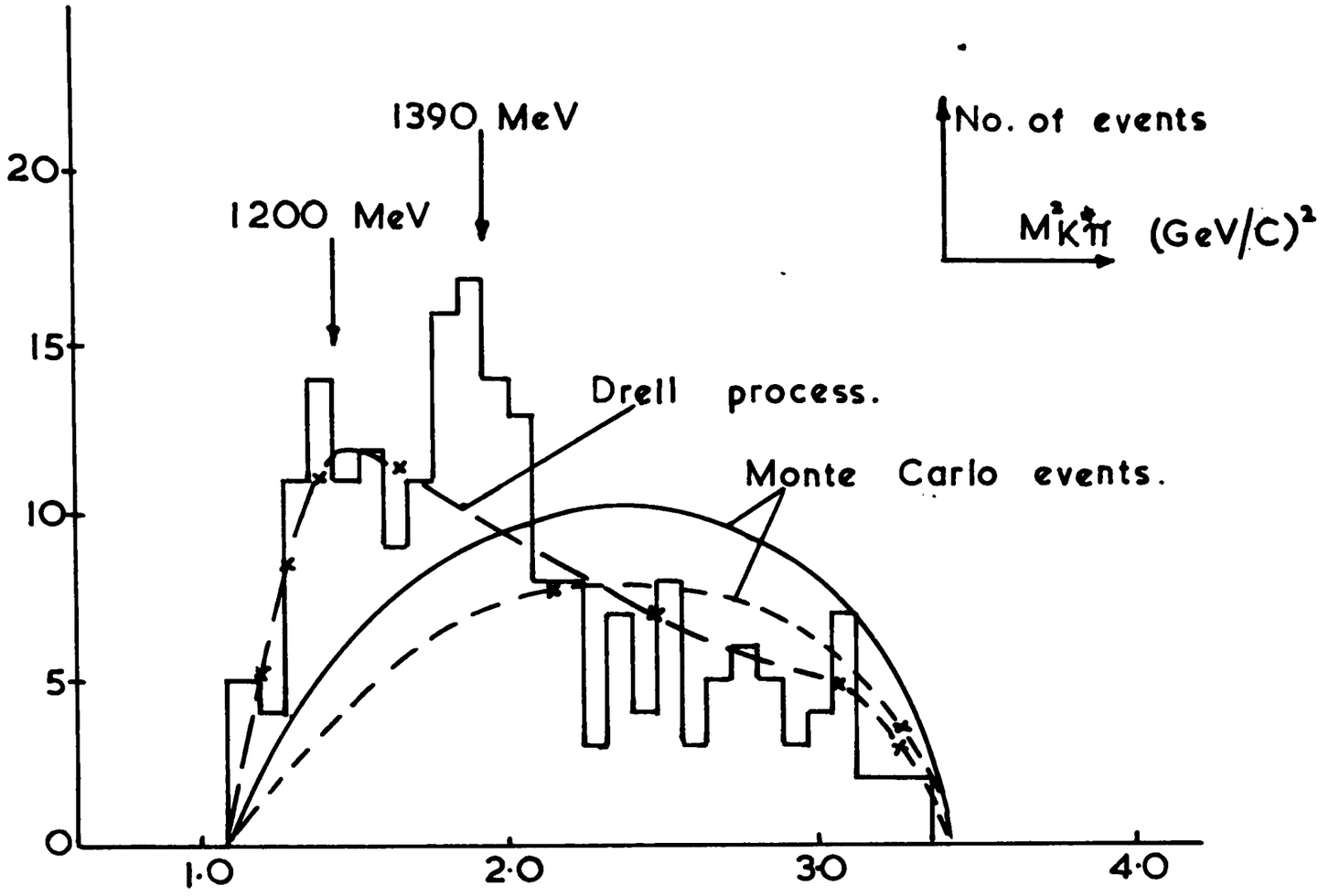

FIG. 7.18 (b)

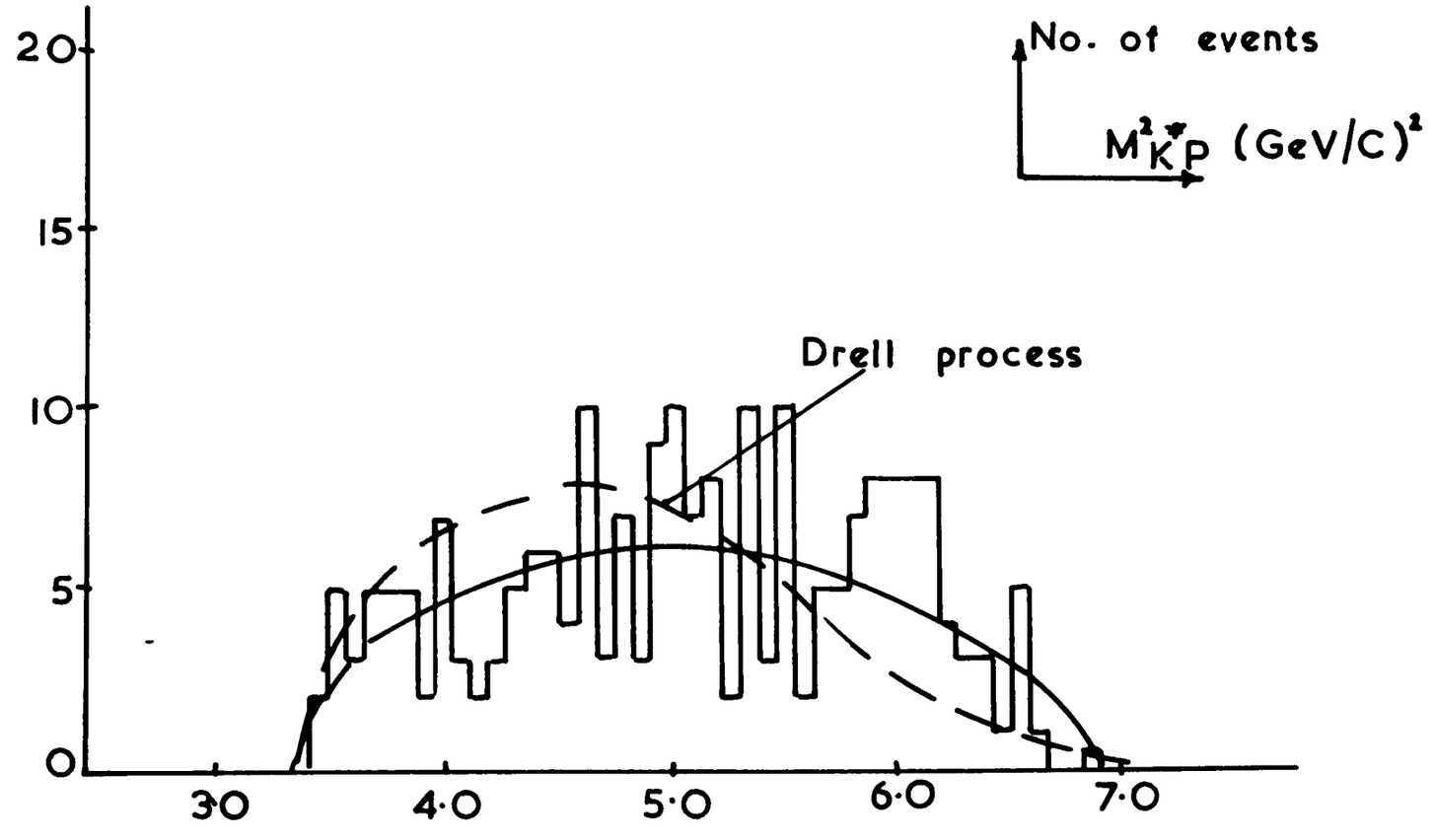

FIG. 7.18 (c)

expected invariant mass distributions from the Monte Carlo events for those two processes alone, normalizing the curves to the observed number of events. Fig. 7.18(a) shows the $K^{*o}p\pi^-$ Dalitz plot with a boundary calculated corresponding to a K^{*o} mass of 892 Mev. Figs.7.18 (b) and (c) show the projections onto $K^*\pi$ and K^*p axes, respectively. The experimental distribution of the $K^*\pi$ system is markedly different from the Monte Carlo prediction and shows two apparently distinct, broad enhancements centred approximately at 1200 Mev. and 1390 Mev. respectively. A simple count of events above and below the curve indicates that these represent a 3.4 and a 3.$\frac{1}{2}$ standard deviation effect, respectively. When the distribution is normalized to the events under the solid curve the dotted line results.

The $K\pi\pi$ invariant mass spectrum has recently been of considerable interest to high energy physicists. A number of resonances have been reported in this spectrum over the last two years, the first of which was that with mass centred at 1170 Mev.[12,13] Several others have been reported with various masses - 1215 Mev,[14] 1275 Mev[15] and 1320 Mev[16] - though the only one that appears to be definitely established is the K**(1400). The present results tend to confirm this latter point as is shown in the next sections.

FIG. 7.19

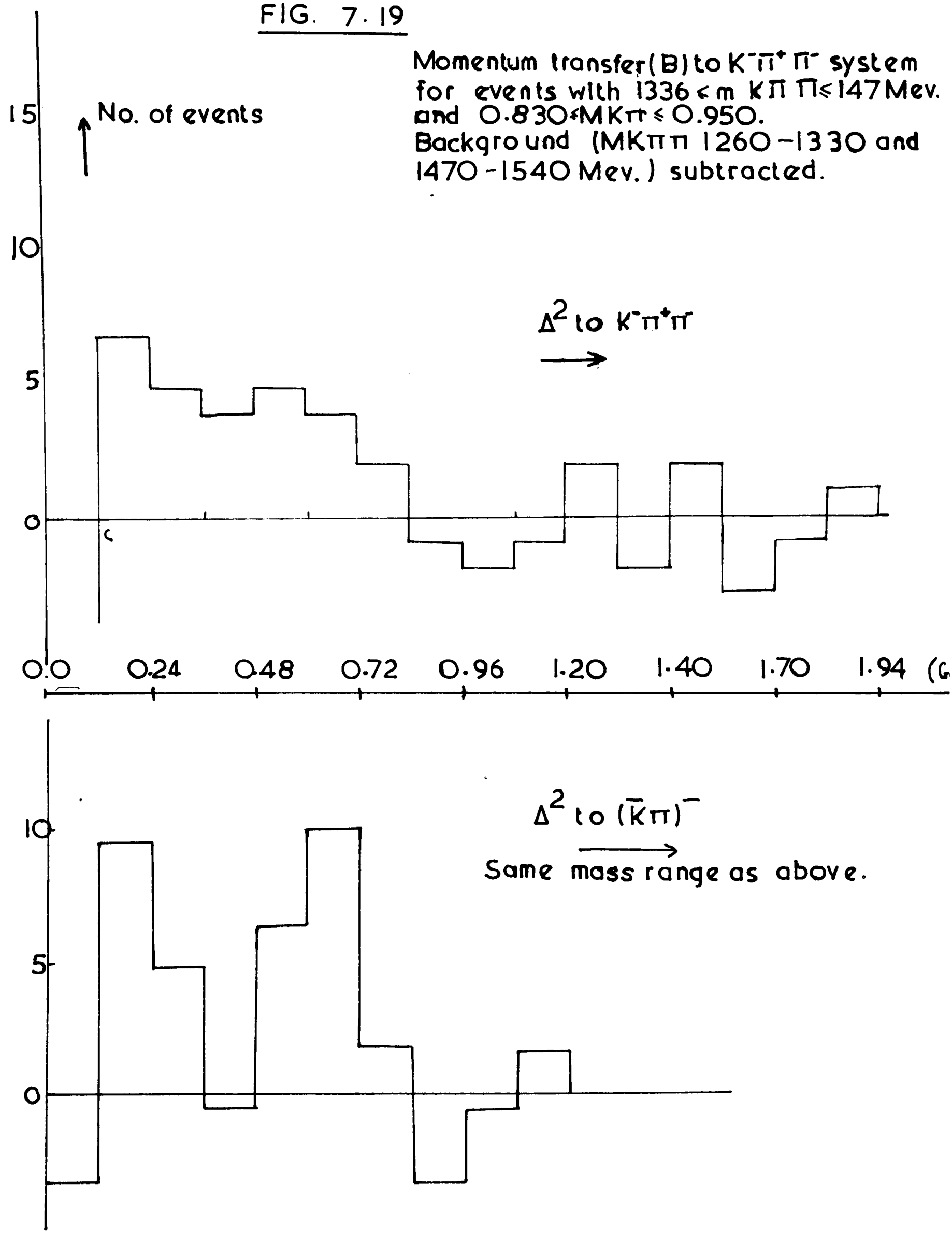
Momentum transfer (B) to $K^-\pi^+\pi^-$ system for events with $1336 < m\,K\pi\pi \leq 147$ Mev. and $0.830 < MK\pi\pi \leq 0.950$.
Background ($MK\pi\pi$ 1260 – 1330 and 1470 – 1540 Mev.) subtracted.
No. of events
15
10
5
0
Δ^2 to $K^-\pi^+\pi^-$
0.0
0.24
0.48
0.72
0.96
1.20
1.40
1.70
1.94
Δ^2 to $(\bar{K}\pi)^-$
10
5
0
Same mass range as above.

Production of K**(1400)

If we interpret the higher mass enhancement in Fig.7.18(b) as due to K**(1400) we expect to find similarities with the corresponding two prong reaction:-

$$K^- p \rightarrow K^{**}(1400)^- p$$
$$\hookrightarrow \bar{K}\pi$$

except that we here observe the decay into $\bar{K}^*\pi$. Fig.7.19 shows the square four-momentum transfer distribution to the system with background subtracted.The corresponding two prong plot is also shown for comparison.Within the limited statistics a similarity is seen.Fig.7.20 illustrates the variation in the squared four-momentum transfer with the $K^-\pi^+\pi^-$ mass,and the greater peaking at the 1400 mass is noticeable - supporting the view that this represents peripheral resonance production. The distribution of this quantity is of interest in a consideration of the commonly known "Deck Effect" about to be discussed.

Deck Mechanism

It is interesting to investigate the mechanism of this quasi three body production process in view of the recent interest in the Deck process.The introduction of this model into the problems of resonance identification obtained prominence in connection with the observation of the A_1"phenomenon".[17,18]

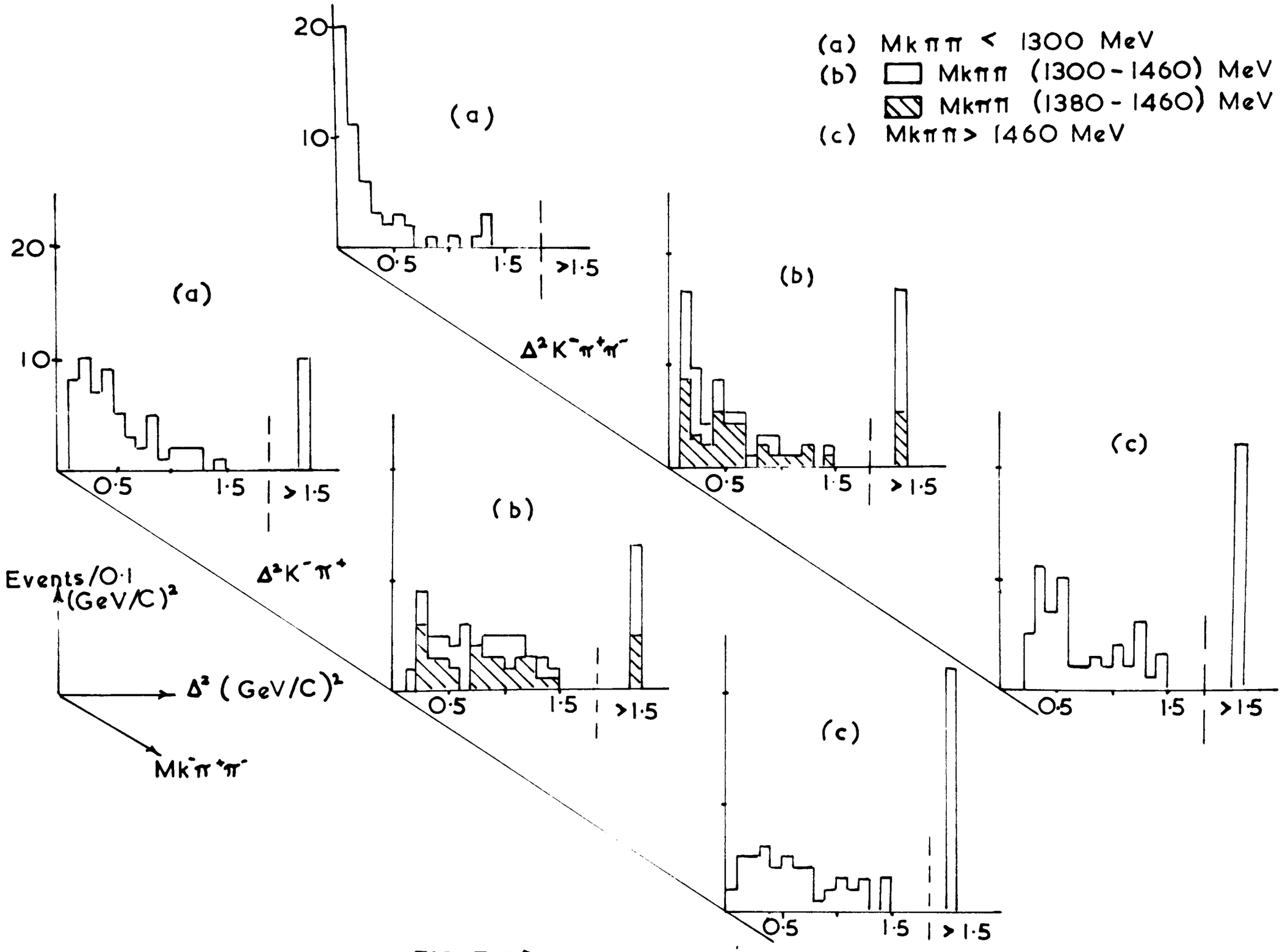
(a) Mkππ < 1300 MeV
(b) Mkππ (1300 - 1460) MeV
Mkππ (1380 - 1460) MeV
(c) Mkππ > 1460 MeV
(a)
(b)
(c)
20
10
0·5
1·5
>1·5
Δ² K⁻π⁺π⁻
Δ² K⁻π⁺
Events/0·1 (GeV/C)²
Δ² (GeV/C)²
Mk⁻π⁺π⁻

FIG. 7.20

The Drell process[19] was invoked by Deck[20] and later by Maor and O'Halloran[21] as a possible means of explaining the A_1 as a kinematic enhancement in the $\pi\rho$ mass spectrum. The opinions on the significance of the model in this respect are varied[17,18] but it appears to be generally agreed that the mechanism exists in practice and at least contributes to a high background under the A_1. The details of the calculations performed to estimate the effect on the $\pi\rho$ spectrum appear to make significant differences to the predicted positions and widths of the kinematic enhancement[17] and it appears that the best calculation performed by Wolf[22] fails to account for the whole peak in the CERN data at least. The relevance of this to the $K\pi$ system is apparent, as an analogous process with the ρ replaced by the K*(890) is thought by some[17] to be a possible explanation for the K**(1320). In the data of Fig. 7.18(b) the 1400 peak extends down to below 1320 Mev. and the possible indication of the presence of this resonance cannot be ruled out. An attempt has therefore been made to ascertain the relative importance and the role played by the Drell process in this final state.

The Feynman diagrams of Fig. 7.21 sum up the uncertainty that exists as to whether the K*(1320) is a genuine resonance or not. The Deck mechanism (Fig. 7.21(a)) uses the fact that the virtual exchanged pion is travelling preferentially forward

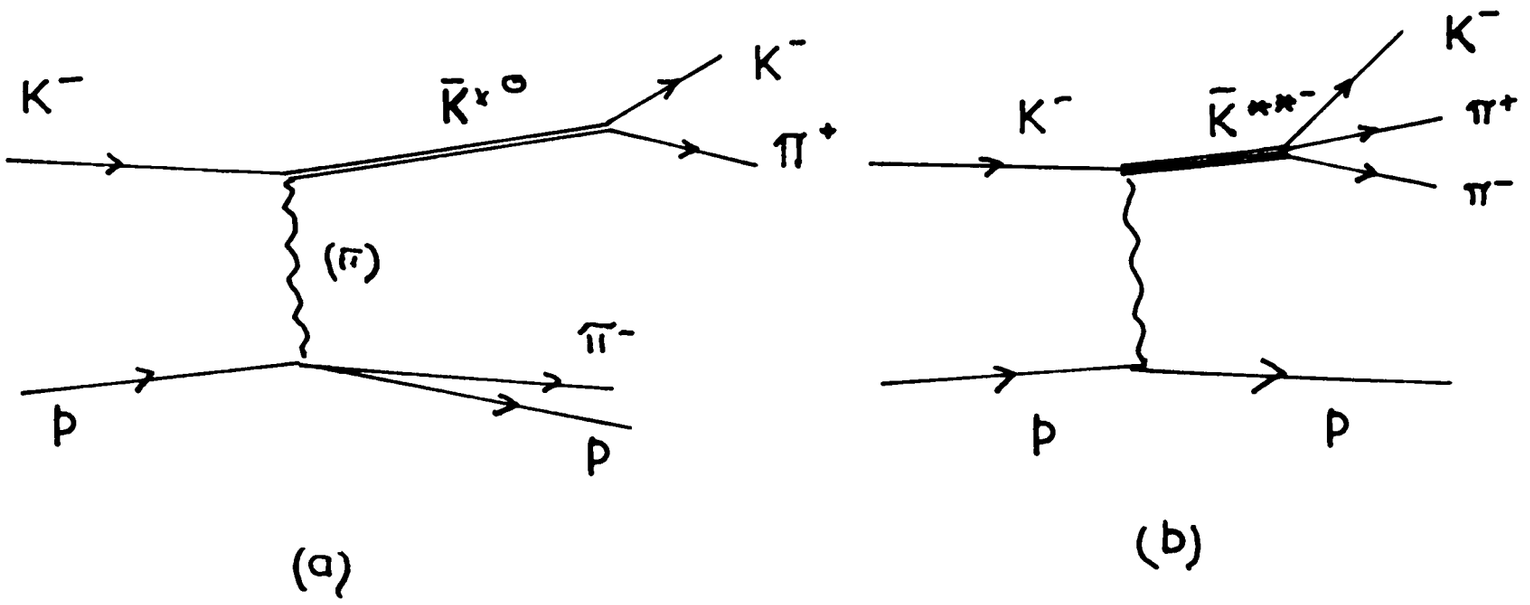

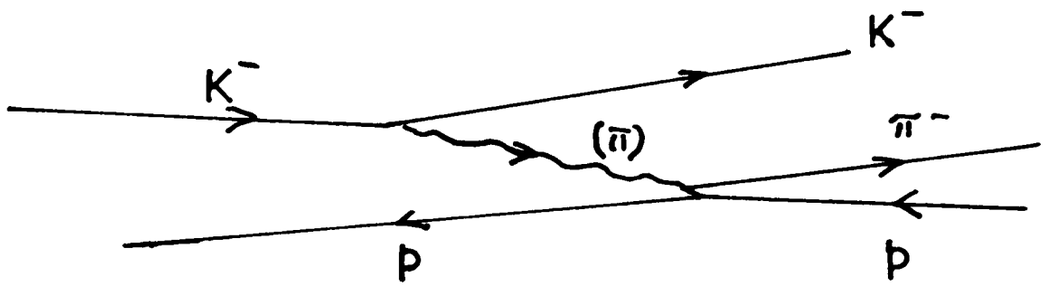

(c) – Mechanism (a) viewed from overall CMS.

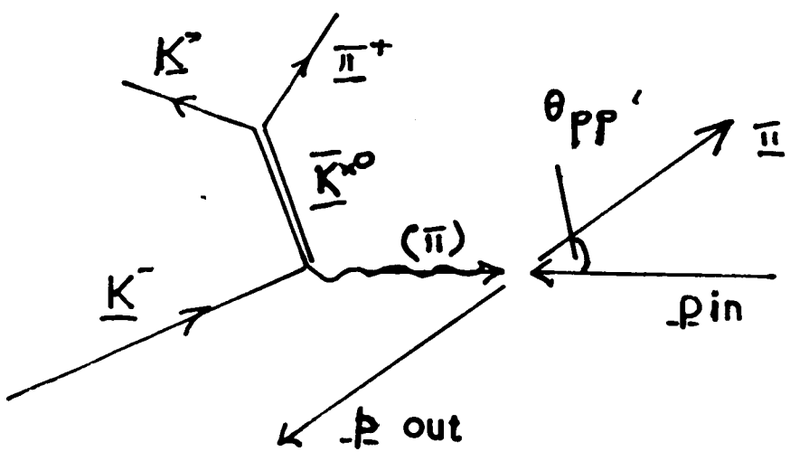

(d) Mechanism (a) viewed from pπ⁻ rest frame.

FIG. 7.21

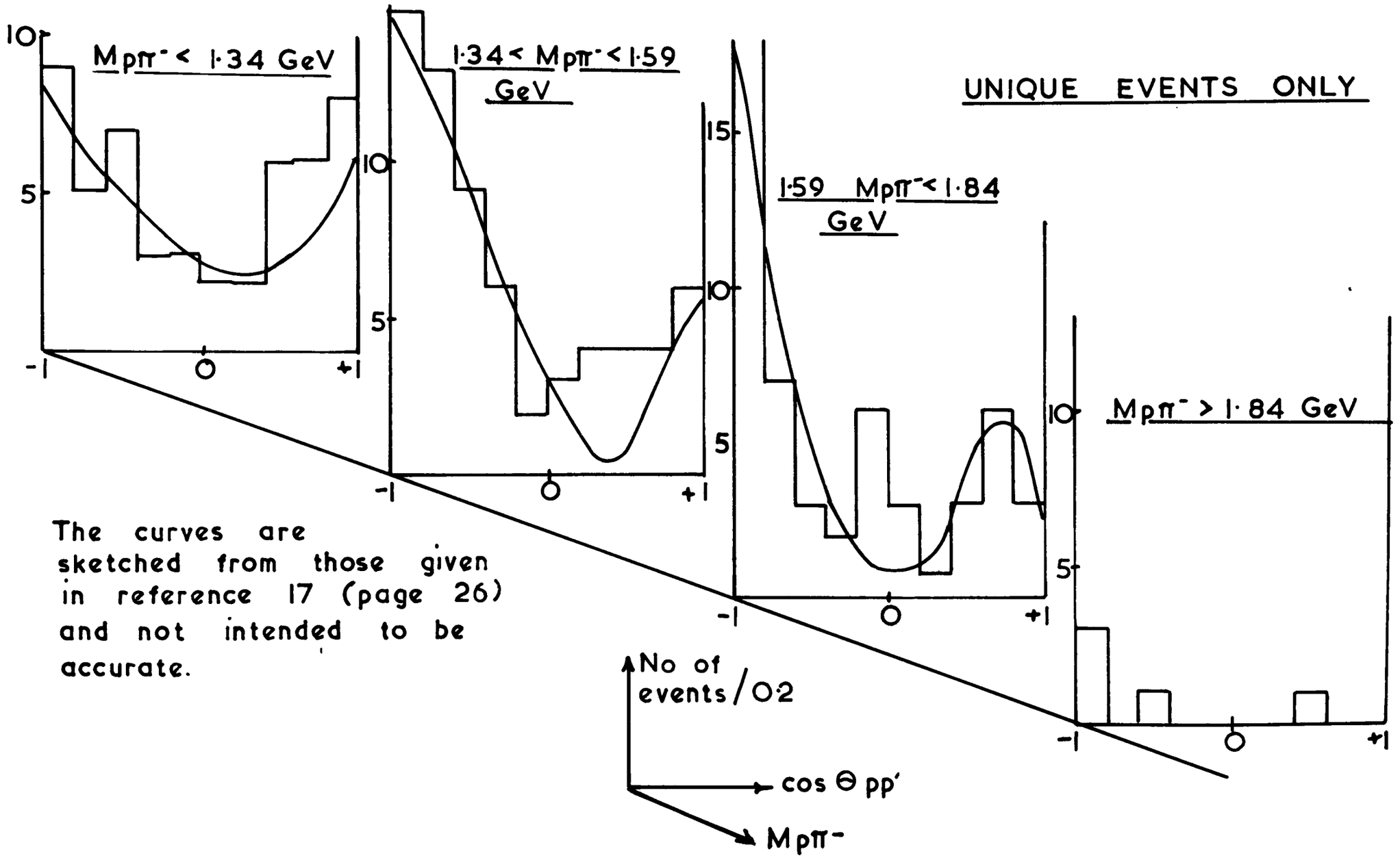
UNIQUE EVENTS ONLY
Mpπ⁻ < 1·34 GeV
1·34 < Mpπ⁻ < 1·59 GeV
1·59 Mpπ⁻ < 1·84 GeV
Mpπ⁻ > 1·84 GeV
10
5
15
-1
0
+1
The curves are sketched from those given in reference 17 (page 26) and not intended to be accurate.
No of events / 02
cos Θ pp'
Mpπ⁻

FIG. 7·22

in the overall centre of mass system with the K*, and has a high cross-section for scattering elastically off the proton which is travelling in the opposite direction. The resulting K*π system has small relative momentum and therefore preferentially low invariant mass. The situation is represented more realistically in Fig. 7.21(c). The model is amenable to several tests as follows:-

1. In the $p\pi^-$ centre of mass system, one expects the scattering angle $\theta_{pp'}$ (defined by $\cos\theta_{pp'} = \underline{p}_{in} \cdot \underline{p}_{out}$ where these vectors are shown in Fig. 7.21(d)) to be consistent with elastic scattering. In Fig. 7.22 the cosine of this angle is plotted as a function of $p\pi^-$ mass, and it is interesting to see that the $1 + 3\cos^2\theta_{pp'}$ distribution is a reasonable description for masses between 1190 - 1290 Mev. corresponding to single pion exchange to produce an N^{*0} which subsequently decays into $p\pi^-$. As the mass increases, however, the expected peaking toward $\cos\theta_{pp'} = +1$ corresponding to diffraction scattering is noticeable. The curves drawn on these distributions are taken from ref. 17 and are normalized to the numbers of events in the plots. They represent elastic π^-p scattering on the mass shell.

It is interesting to investigate the variation of the $\cos\theta_{pp'}$ distribution with $K\pi\pi$ mass also, since we expect to find

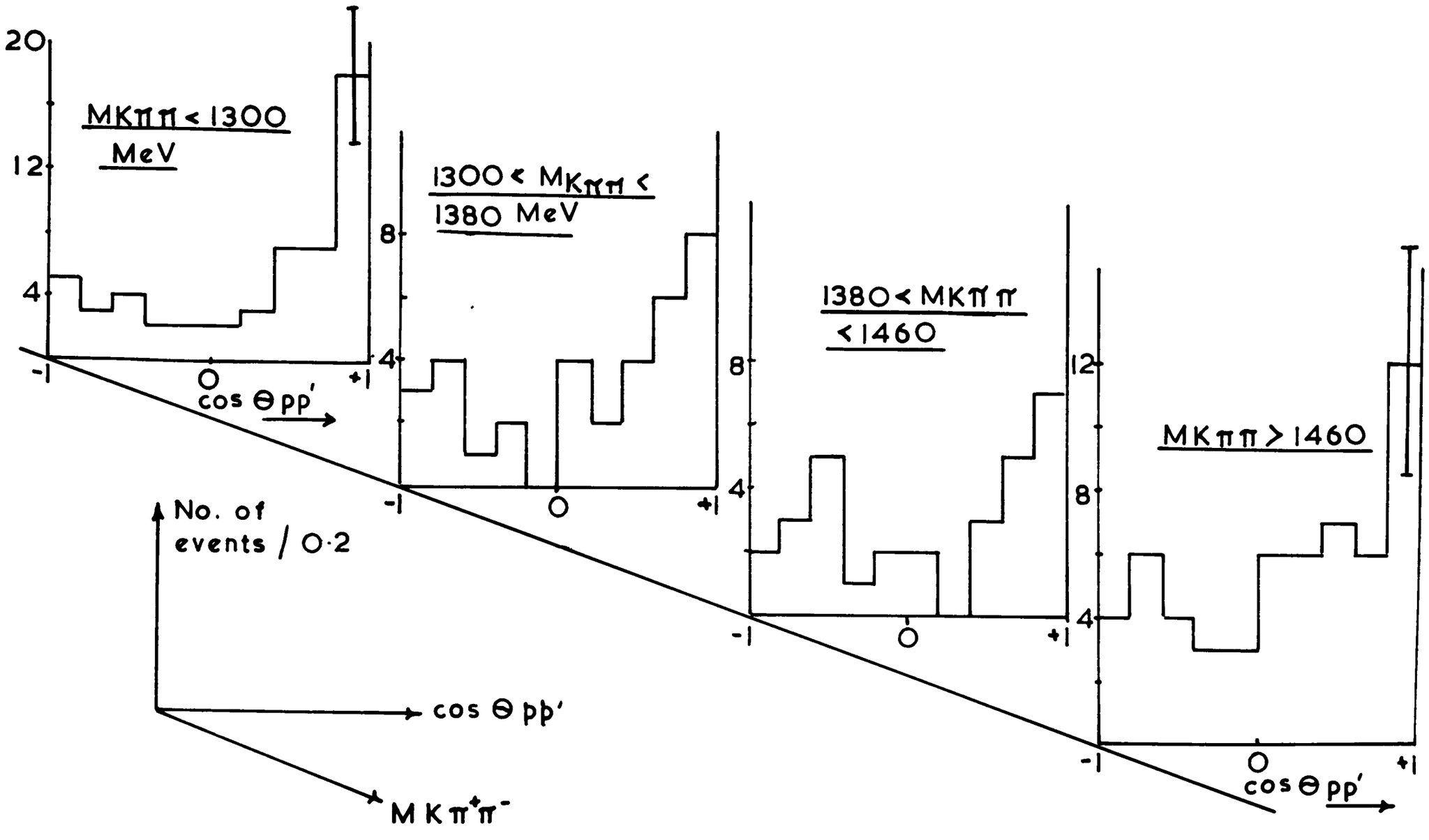
20
12
4
MKππ < 1300
MeV
-1
0
cos Θ pp'
+1
8
4
1300 < MKππ <
1380 MeV
-1
0
+1
8
4
1380 < MKππ
< 1460
-1
0
+1
12
8
4
MKππ > 1460
-1
0
+1
cos Θ pp'
No. of
events / 0·2
cos Θ pp'
MKπ+π-

FIG. 7·23

the most strongly peaked diffraction type of scattering for the lowest $M_{K\pi\pi}$ if the diagram of Fig.7.21(b) is an important part of the reaction mechanism. The plots shown in Fig.7.23 illustrate this variation, and it is certainly found that $\cos\theta$ is quite strongly peaked in the lowest $M_{K\pi\pi}$ ($<$ 1300Mev.) range whilst having a fairly isotropic background at the higher mass end. An interesting comparison may be made between the two middle mass regions since they correspond to the "K**(1320)" and K**(1400) regions. The difference between the two is, perhaps, not statistically significant, though we notice that the $K^*\pi$ spectrum is modified by the selection of $\cos\theta_{pp}, < 0$ (corresponding to the removal of all diffraction scattering) in such a way that the K**(1400) peak remains (see Fig.7.24) and now appears at a slightly higher mass.

2. The scattering angle θ_{pp}, is almost equivalent to the squared four-momentum transfer to the $K\pi\pi$ system as may be realized from Fig. 7.21(c), therefore the tests involving this angle do not really differentiate between the two mechanisms (Figs.7.21(a) and (b)) in a very sensible way since one might expect a small proton scattering angle in either case. However, a direct comparison between the four-momentum transfer to the $K\pi\pi$ and $K\pi$ systems might be more informative. This is made in Fig.7.20 where the distributions of these quantities are shown for a

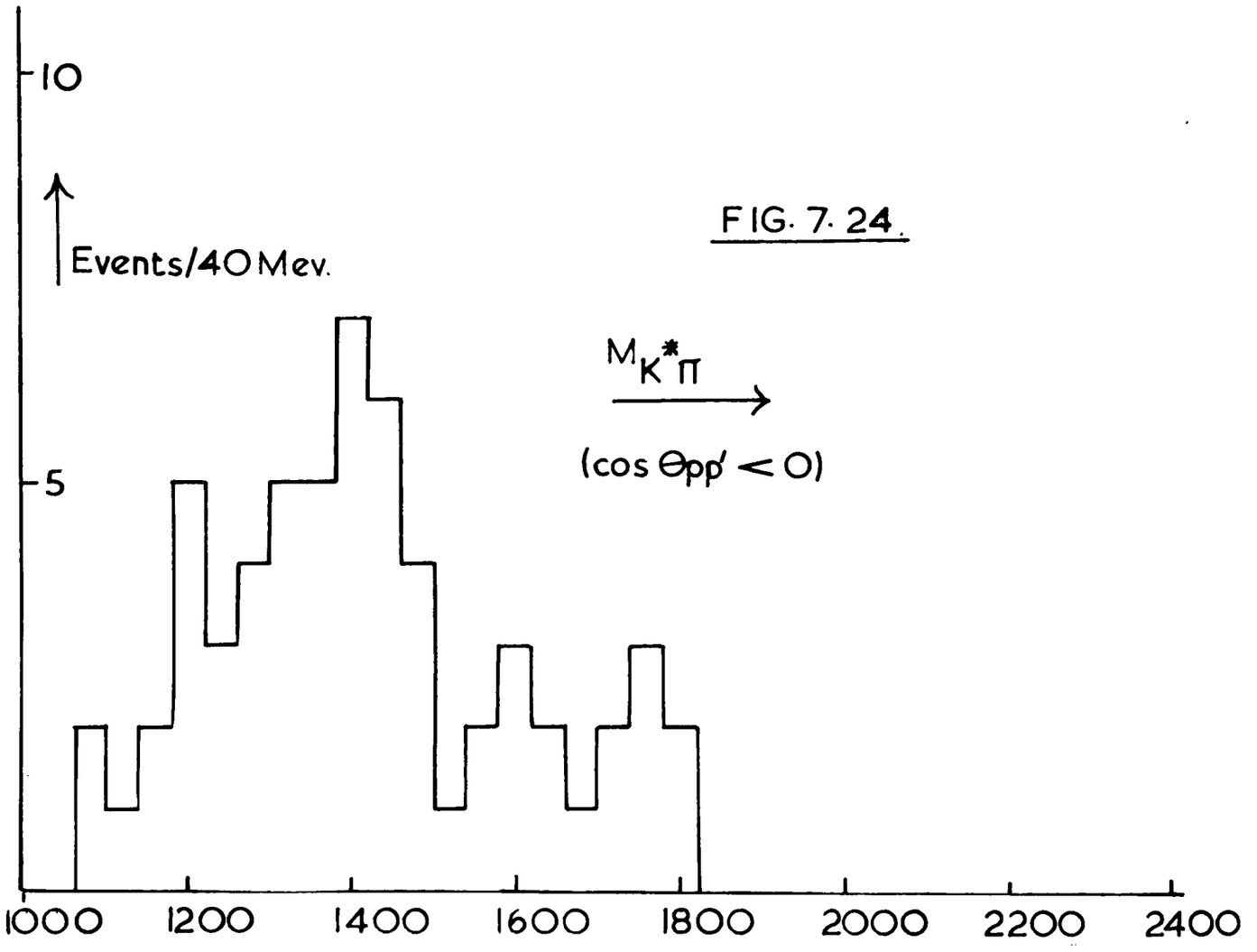
10
5
Events/40 Mev.
$M_{K^*\pi}$
(cos Θpp' < 0)
1000
1200
1400
1600
1800
2000
2200
2400

FIG. 7.24.

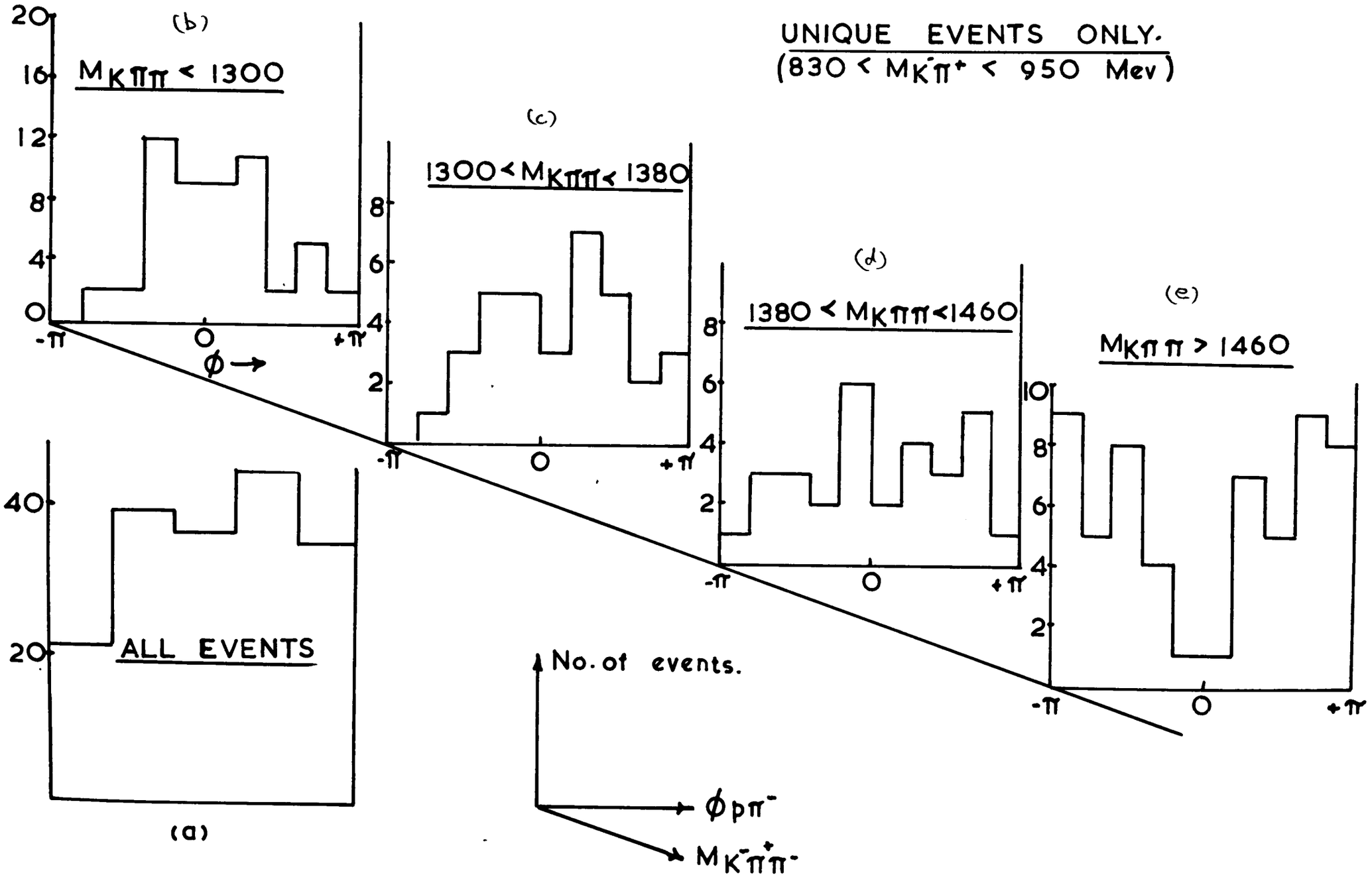
UNIQUE EVENTS ONLY.
(830 < MK⁻π⁺ < 950 Mev)
(a)
ALL EVENTS
(b)
MKππ < 1300
(c)
1300 < MKππ < 1380
(d)
1380 < MKππ < 1460
(e)
MKππ > 1460
-π
0
+π
φ →
No. of events.
φpπ⁻
MK⁻π⁺π⁻

FIG. 7·25

variety of $K\pi\pi$ masses. It is clear that the $K^{*0}(890)$ is formed peripherally at all such masses, but the $K\pi\pi$ system appears to be more peripheral in the region of K**(1400).

3. The azimuthal angle ϕ (defined analogously with that in the previous chapter) in the $p\pi^-$ system is expected to be distributed isotropically if events corresponding to the diagram of Fig. 7.21(b) are present. Any lack of isotropy might be regarded as a consequence of the decay of the $K\pi\pi$ resonance of Fig. 7.21(a) or of some other process. The distribution of ϕ is shown in Fig.7.25(a) for all $K^{*0}p\pi^-$ events, and appears to be nearly isotropic. If, however, one enquires more closely into the distribution as a function of $K\pi\pi$ invariant mass, in order to test, for instance, the relative merits of K**(1320) as a kinematic enhancement or as a resonance by making a comparison with K**(1400), a complication arises as illustrated by Figs.7.25(b) - (e). The lowest and highest $K\pi\pi$ invariant masses appear to involve events in which the Drell mechanism cannot possibly apply as the angle ϕ has a distribution which markedly violates parity conservation at the supposed $p\pi^-$ vertex, by peaking respectively, at angles of 0 and $\pm\pi$.

One may possibly understand this, however, as the result of a kinematic constraint as suggested by the appearance of

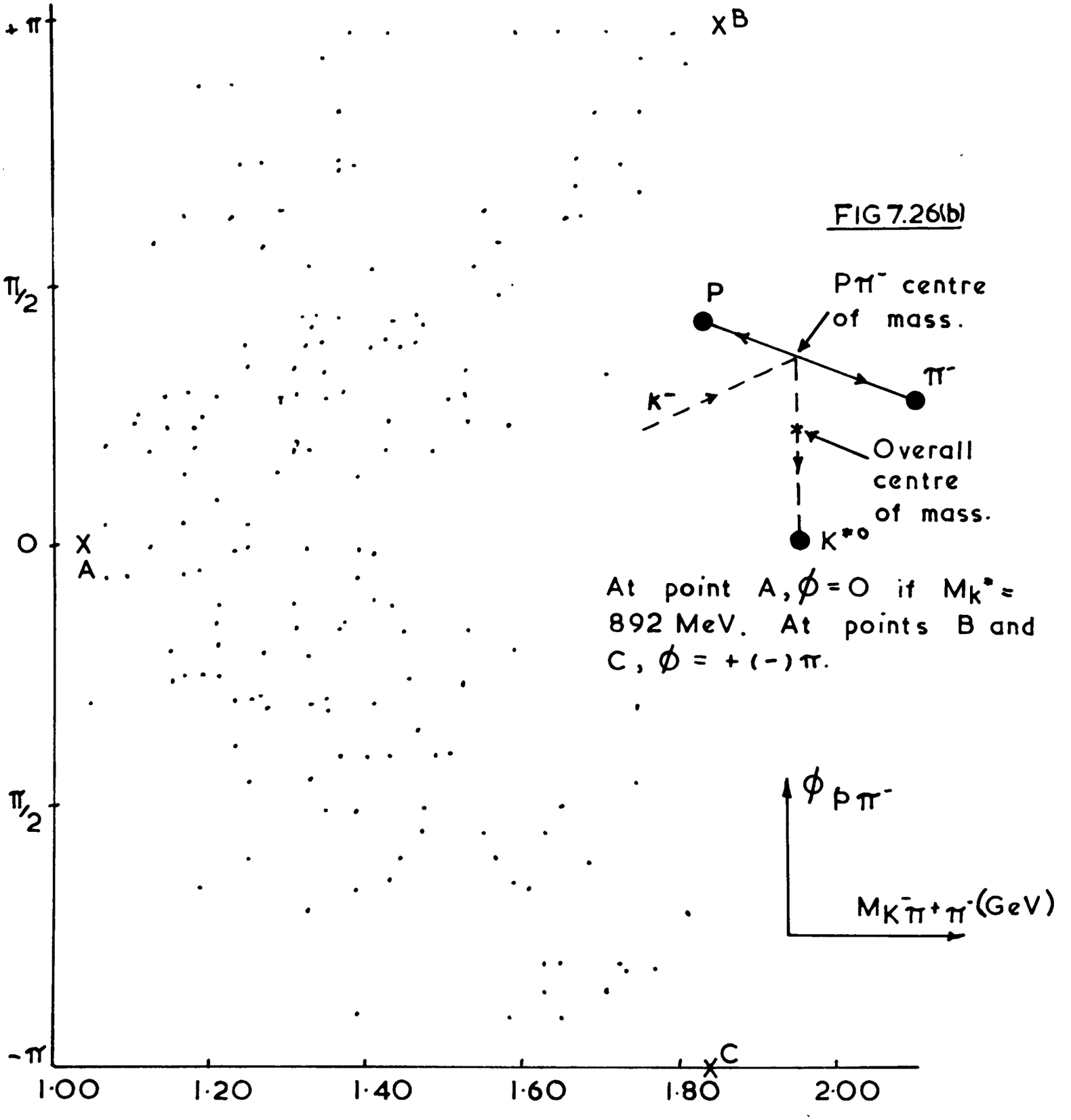

FIG 7.26(b)

At point A, $\phi = 0$ if $M_{K^*} = 892$ MeV. At points B and C, $\phi = +(-)\pi$.

FIG. 7.26 (a)

Fig.7.26(a) which is a scatter plot of ϕ against $M_{K^*\pi^-}$. Fig.7.26(b) shows the three body system viewed from the centre of mass of the $p\pi^-$ particles. The angle ϕ is defined as that between the plane formed by the incoming and outgoing proton, and that formed by the K^- and the K^{*o}. The $K^*\pi$ mass is determined by the angle θ (between the K^* and the π) and the $p\pi^-$ invariant mass. The selection of a fixed value for the former quantity may well, therefore, impose limits upon the value of ϕ. Three special cases are of interest:-

(a) at the lowest $K^*\pi$ masses the three particles are aligned and it is clear that the angle ϕ is zero. This situation extends over a range of masses corresponding to the finite width of the K^{*o}.

(b) at the upper end of the $K^*\pi$ spectrum the value of ϕ is restricted to $\pm\pi$

(c) the selection of events in the "diffraction peak" of the $p\pi^-$ scattering is equivalent to the choice of those events aligned in the direction of the incident K^-. In such a case, the angle ϕ is no longer defined. One might, therefore, expect an isotropic distribution of ϕ for events close to this limiting case.

One way to test that the anisotropic ϕ distributions are a

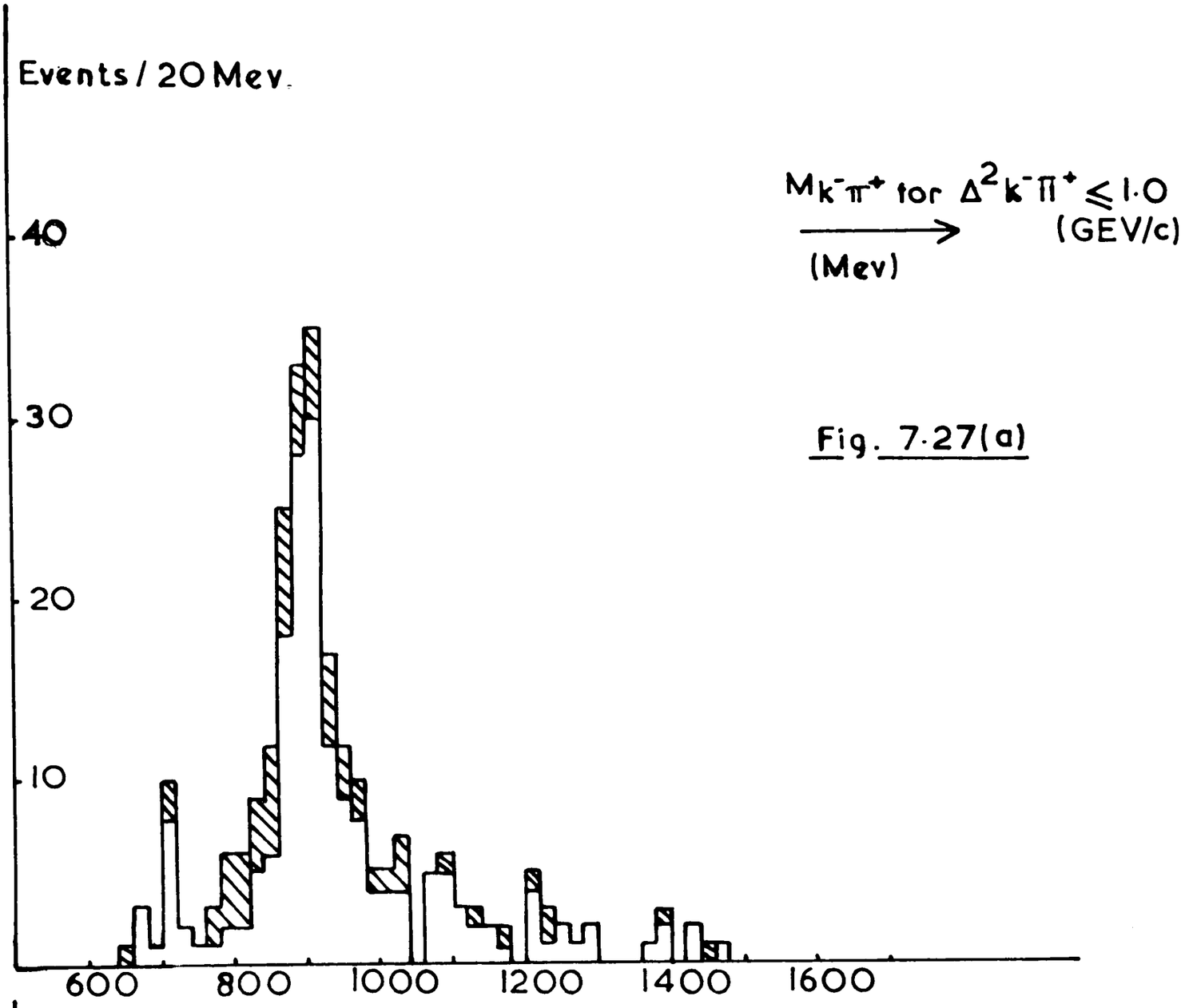

Fig. 7·27(a)

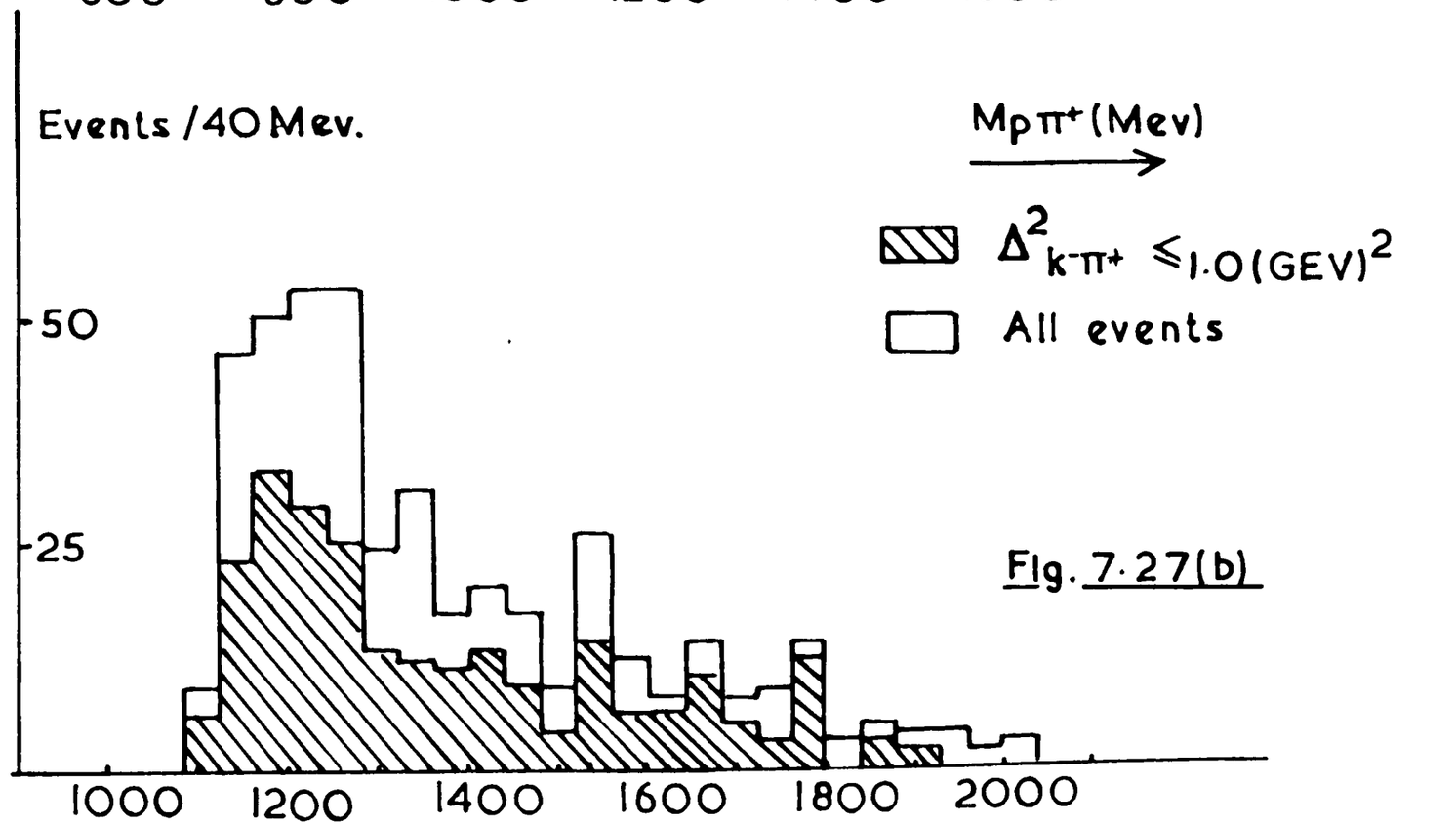

Fig. 7·27(b)

result of a genuine kinematic effect would be to examine the effect of $K^{*}\pi$ mass selection upon the $K^{*o}N^{*o}$ events which should form a particular part of the Drell mechanism where the $p\pi^{-}$ scattering corresponds to N^{*o} formation. Unfortunately, the weakness of this channel in the present case does not permit a sensible investigation of this kind.

4. The existence of the Drell process in the $K^{*o}p\pi^{-}$ events implies the presence of pion exchange in the production of the $K^{*o}(890)$. A direct check upon this is available from an analysis of the decay of this particle. The method used assumed that the resonance was produced and that it decayed as a free particle. In order to remove arbitrariness in the selection of the $K^{*}(890)$ mass band and in estimating the background effect upon the decay distributions, no mass cuts were employed at all. It is evident from Fig.7.27(a) that the selection of small 4-momentum transfer ($\Delta^2 \leq 1.0(\mathrm{Gev/c})^2$) to the $K^{-}\pi^{+}$ system yields a very highly purified sample of $K^{*o}(890)$, and that the contamination from $N^{*++}(1238)$ is greatly reduced (as seen in Fig.7.27(b) which shows the $p\pi^{+}$ mass distribution). In the estimation of resonance fractions the quantities:

$$A = (1 - \sum_{j \neq K^{*o}} f_j) + \sum_{j \neq K^{*o}} \frac{f_j |T_j|^2}{N_j}$$

TABLE IV

Decay Density Matrix for $\bar{K}^{*o}(890)$

Events Having $\Delta^2 K^-\pi^+ \leq 1.0$ (Gev/c)^2

Element	Assumed Fraction of $\bar{K}^{*o}$ in Final State			Expected Value	
				Pseudo Scalar Exchange	Vector Exchange
	47%	57%	80%		
ρ_{oo}	0.862 ±0.073	0.837 ±0.068	0.792 ±0.060	1.0	0.0
ρ_{1-1}	-0.011 ±0.055	-0.004 ±0.049	0.004 ±0.044	0.0	0.5
$Re\rho_{10}$	-0.192 ±0.208	-0.131 ±0.200	-0.171 ±0.195	0.0	0.0

All Events

Element	Assumed Fraction of $\bar{K}^{*o}$ in Final State			Pseudo Scalar Exchange	Vector Exchange
	47%	57%	81%		
ρ_{oo}	0.672 ±0.078	0.642 ±0.073	0.605 ±0.059	1.0	0.0
ρ_{1-1}	-0.032 ±0.055	-0.021 ±0.050	-0.007 ±0.042	0.0	0.5
$Re\rho_{10}$	-0.090 ±0.150	-0.082 ±0.095	-0.074 ±0.090	0.0	0.0

and $B = \dfrac{f_{K^*}|T_{K^*}|^2}{N_{K^*}}$

were computed for each event. A represents the part of the density function (equation (9)) corresponding to all processes other than K* production which is represented by B. We may therefore, write the K* decay likelihood function as:

$$L = \sum_i \ln\left[A_i + 4\pi B_i W(\cos\theta_i, \phi_i)\right] \qquad \ldots\ (13)$$

where i refers to the ith event, and (θ, ϕ) are the usual K^{*o} decay angles. The function W is that corresponding to the decay of a pseudo-vector particle into two pseudo-scalers and is given by equation (14) of the previous chapter. On the assumption that all non-K* events contribute an isotropic background to the θ, ϕ distributions, the effect of (13) is apparent since an event near to the K* mass has a large value of B and so its influence upon W is large. If, however, it also has a $p\pi^+$ mass close to that of the N^{*++}, for instance, then a large isotropic background term (A) will tend to swamp its effect upon W. Further, the integration of the function which forms the argument of the log in equation (13) over all invariant masses and all values of θ and ϕ is unity, (provided one includes the factor 4π), so that normalization is ensured. The maximization of L lead to the values for the K*(890) density matrix which are listed in Table IV and appear to be consistent with a large contribution from pseudo-scaler exchange. One should, perhaps,

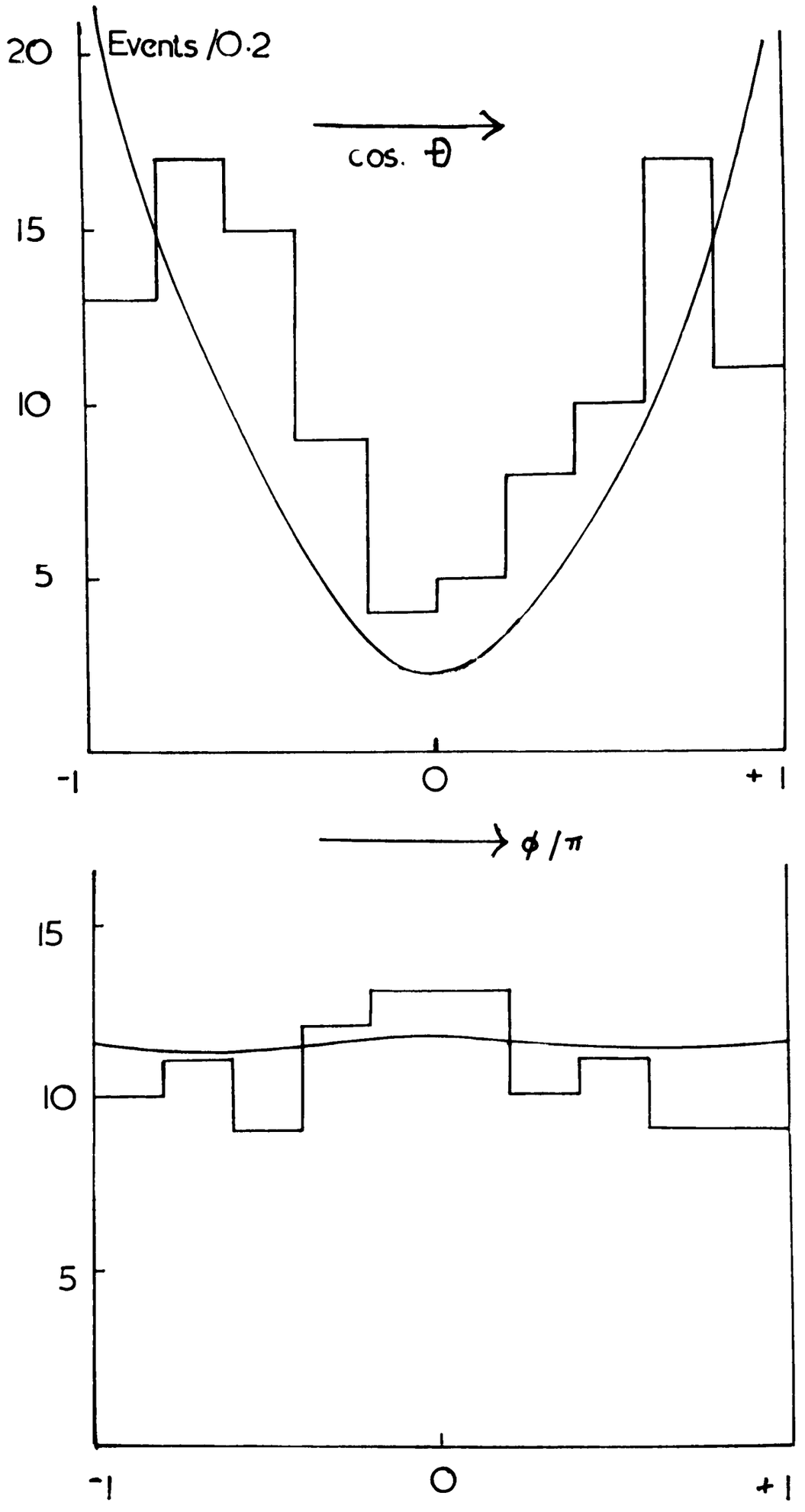

FIG. 7.28 $\bar{K}^{*0}$ Decay angles

have determined the resonant fractions separately for this sub-set of events ($\Delta^2_{p\pi^-} < 1.0$ (Gev/c)^2) in order to obtain correct values for A and B. The effect of varying the K*^{o} fraction, however, has been investigated, and the values of the density matrix elements summarized in Table IV indicate that such a variation does not significantly alter the conclusion that pseudo-scalgr exchange is important. The further requirements that the exchanged particle must have strangeness zero and isospin ≥ 1 lead to the interpretation of single pion exchange. The cos θ and ϕ distributions are shown in Fig. 7.28 for events with $\Delta^2 \leq 1.0$ (Gev/c)^2) and $M_{K^-\pi^+}$ from 830 - 950 Mev.

5. A calculation of the Drell process for the reaction $K^-p \rightarrow K^{*o}p\pi^-$(3.5 Gev/c) has been carried out by Drs.P.M.D.Gray[28] and J.H.Field and has yielded a prediction for the $K^*\pi$ invariant mass distribution for events with $M_{p\pi^-} > 1290$ Mev. The curve is shown superimposed on the experimental distribution of Fig.7.18(b) where the effect of the $p\pi^-$ mass selection has been ignored. The reason for this is that the N*^{o} is comparatively weak and forms a relatively small part of the total $N\pi$ scattering cross-section in this channel. It has already been shown that the presence of diffraction scattering (which forms the basis of the calculation) does not appear until the higher $p\pi^-$ masses, but the calculation serves a purpose here in qualitatively

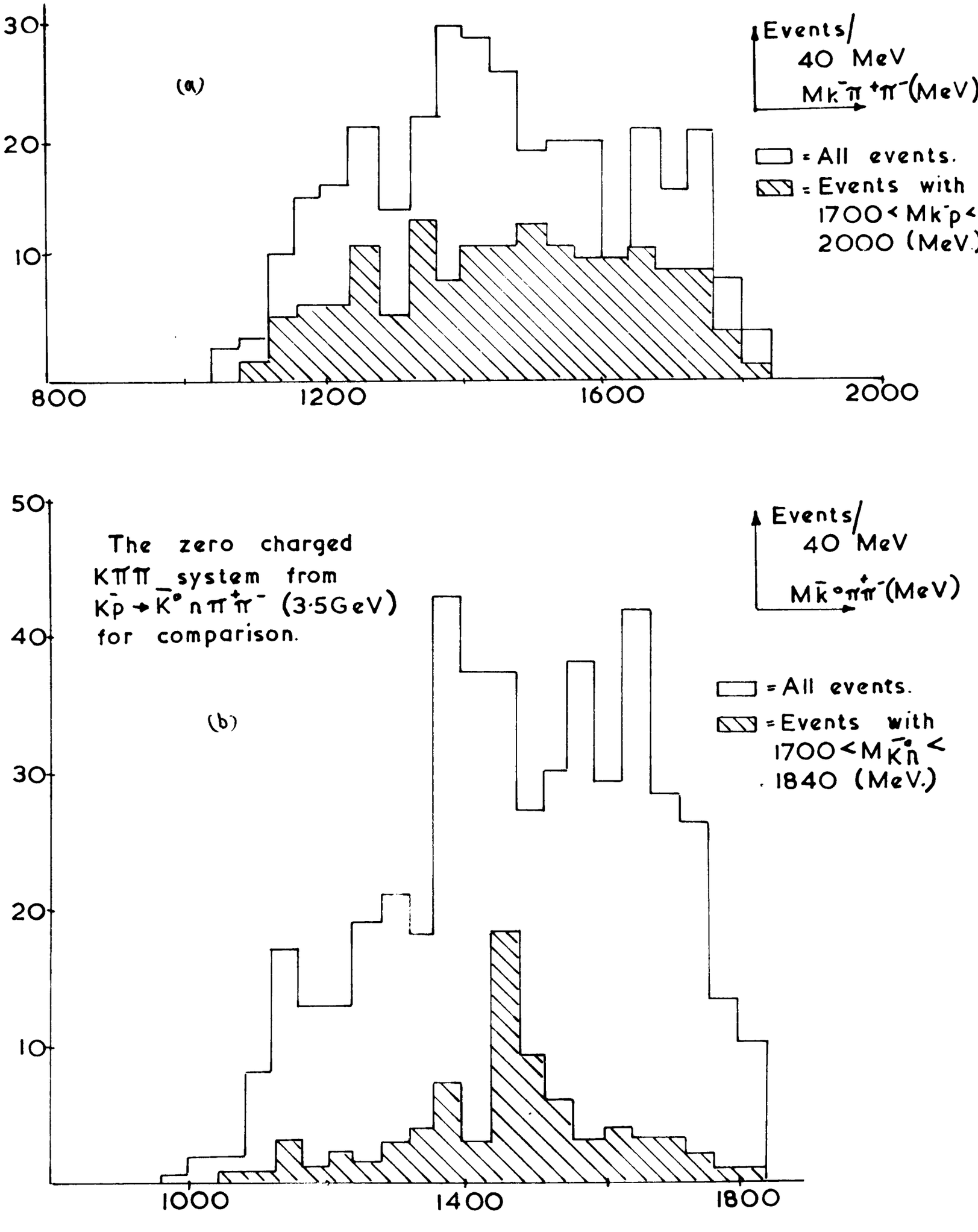
30
20
10
(a)
Events/
40 MeV
$Mk^-\pi^+\pi^-$(MeV)
= All events.
= Events with
1700 < Mk^-p <
2000 (MeV.)
800
1200
1600
2000
50
40
30
20
10
The zero charged
$K\pi\pi$ system from
$K^-p \to \bar{K}^0 n\pi^+\pi^-$ (3·5GeV)
for comparison.
(b)
Events/
40 MeV
$M\bar{k}^0\pi^+\pi^-$(MeV)
= All events.
= Events with
1700 < $M\bar{K}^0n$ <
1840 (MeV.)
1000
1400
1800

FIG. 7. 29

accounting for the general shape of the mass distribution. In particular, it appears, the enhancement at 1200 Mev., loses its significance entirely, and the K**(1400) remains as the only significant peak.

It appears, therefore, that the data show no marked inconsistencies with the Drell process, and that it may form an important part of the production mechanism. This is not unlikely when one considers that the two factors - strong $K^*K\pi$ coupling and large $p\pi^-$ elastic scattering cross-section - which largely determine the relative rate of the process. It further appears that production of K**(1400) is important, though the presence of a state at 1320 Mev. cannot be ruled out.

Decay of K**(1400)

If the above assumptions regarding the presence of K**(1400) are correct, a further comparison with the two prong reaction

$$K^-p \Rightarrow K^{**}(1400)^-p$$
$$\hookrightarrow \bar{K}\pi$$

may be made - the density matrix values should be similar in both cases.

Before analysing the decay into $K^*\pi$, it is well to check one point.

In one other four-body reaction cited previously (reaction 1(b)) this resonance was observed and it appeared to be correlated with the presence of not only K*(890), but also with

TABLE V

$\bar{K}^{**-}(1400) \rightarrow \bar{K}\pi\pi$ Decay

Mode	Cross-Section (μb)	Density Matrix
$\rho^0 K^-$	20	
$\bar{K}^{*0}\pi^-$	61±43	$\rho_{00} = -0.09\pm0.24$ $\rho_{1-1} = 0.17\pm0.11$
$K^-\pi^+\pi^-$	189±59	†(0.39±0.07) †(0.30±0.03)

† Values obtained from $\bar{K}\pi$ decay

$Y^*(1765)$ or $Y^*(1815)$. We note that these resonances do not appear to be important in the present final state (reaction (1)). Further, selection of K^-p invariant mass between (1700-2000Mev) is shown in Fig.7.29(b) where it is apparent that there is no significant association with the enhancement at 1400 Mev.

The decay of a 2^+ meson into a 0^- and 1^- pair of particles leads to a distribution [24]

$$W(\cos\theta, \phi) =$$

$$\rho_{22}\sin^2\theta(1+\cos^2\theta)+\rho_{11}\left[1+\cos^2\theta(1-4\sin^2\theta)\right]+3\rho_{oo}\sin^2\theta\cos^2\theta$$
$$-\rho_{2,-2}\sin^4\theta\cos 4\phi-\rho_{1,-1}\sin^2\theta(1-4\cos^2\theta)\cos 2\phi-4R_e\rho_{2,1}\cos^3\theta\sin\theta\cos\phi$$
$$-4R_e\rho_{2,-1}\sin^3\theta\cos\theta\cos 3\phi-2\sqrt{6}R_e\rho_{2,0}\cos^2\theta\sin^2\theta\cos 2\phi$$
$$-\sqrt{6}R_e\rho_{1,0}\sin 2\theta(1-2\cos^2\theta)\cos\phi \qquad \ldots.(14)$$

In the application of equation (14) the only non-zero elements of the density matrix were taken to be ρ_{oo} and ρ_{1-1} corresponding to the peripheral productions by exchange of either pseudo-scaler particles or ones of natural parity. Then ρ_{11} was given by the trace condition (with $\rho_{22} = 0$)

$$\rho_{11} = \tfrac{1}{2}(1-\rho_{oo})$$

The background subtracted was from events in the side bands ($M_{K^*\pi}$ from 1260 - 1330 or 1470 - 1540 Mev) of the $K^*\pi$ resonance. The maximum likelihood values for ρ_{oo} and $\rho_{1,-1}$ are given in Table V together with the values found for the corresponding $K^{**}(1400)$ decay into $K\pi$ for comparison.

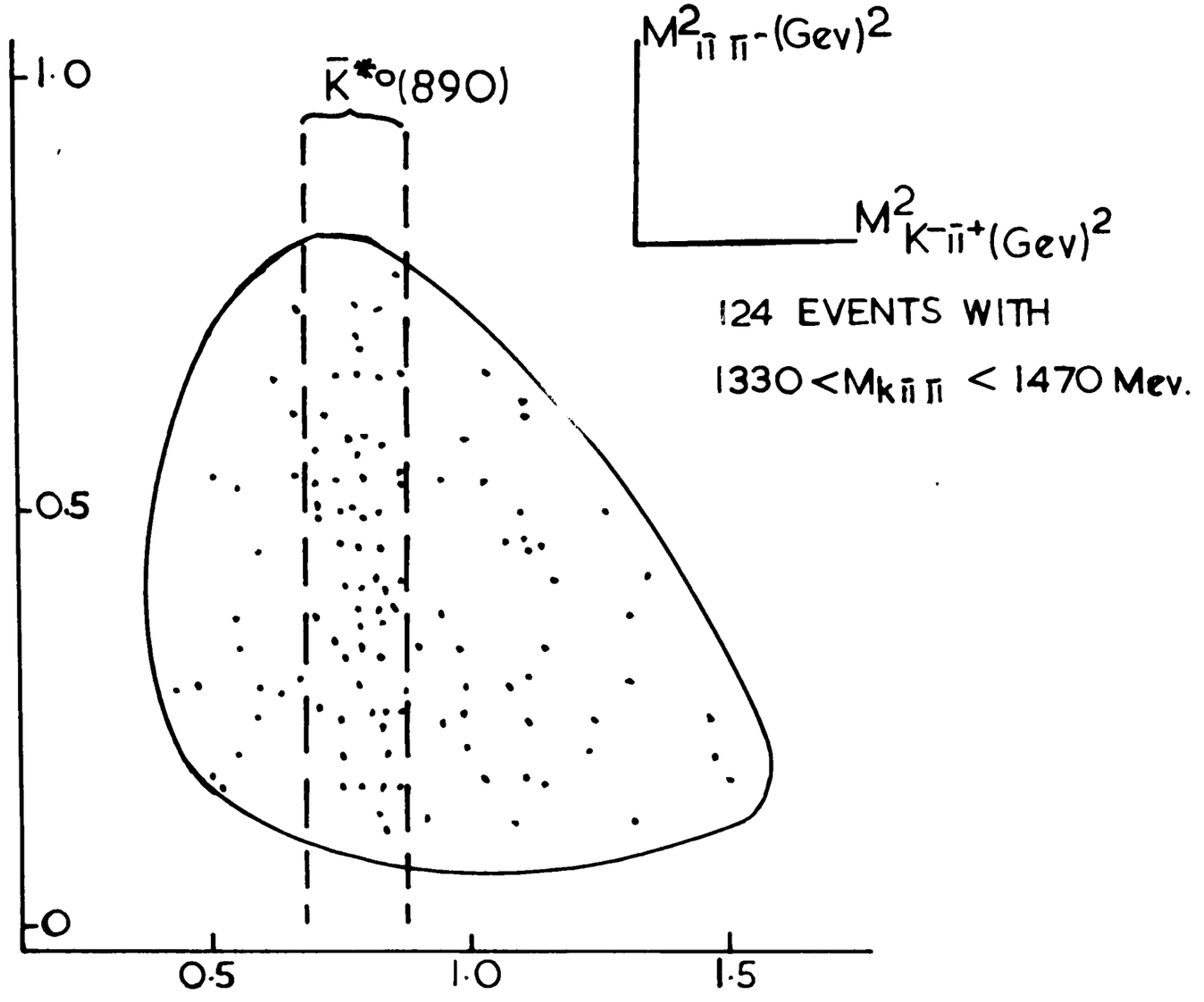

FIG. 7.29(c) K^{**} (1400) DALITZ PLOT

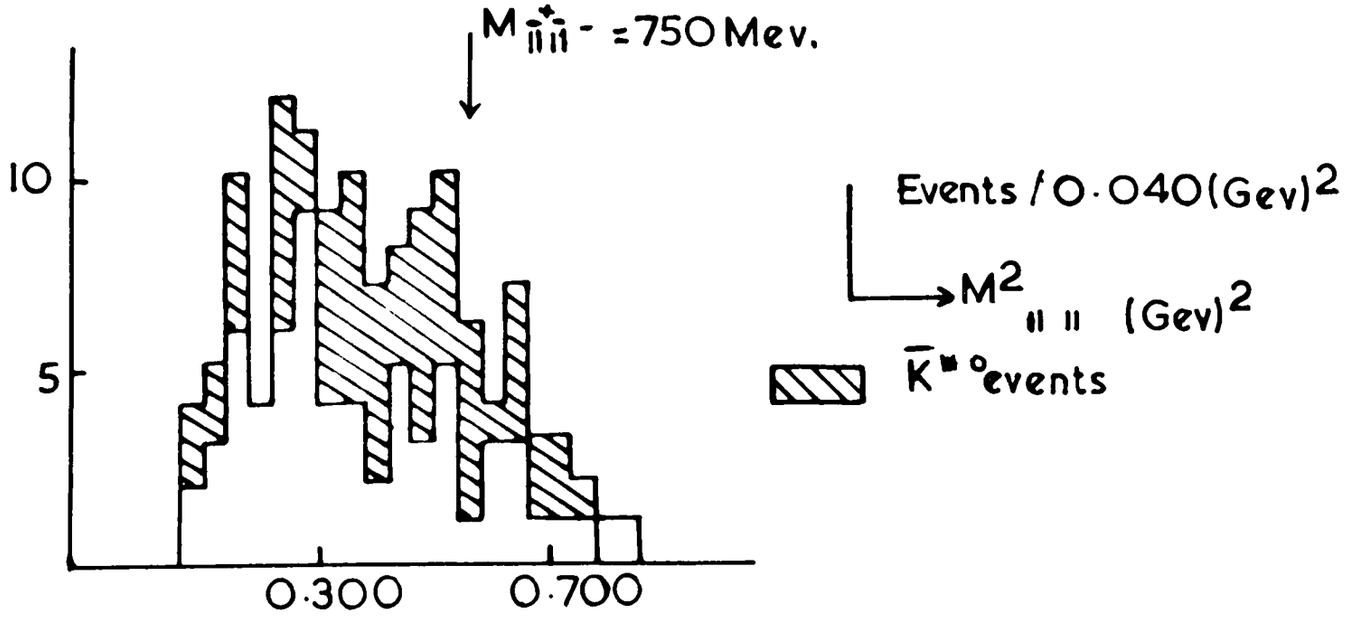

It is also of interest to look for the decay of this resonance into either $K\pi\pi$ or $K\rho$. The Dalitz plot of Fig.7.29 (c) shows the invariant mass squared of the $K^-\pi^+$ versus that of the $\pi^-\pi^+$ for events having $1330 < M_{K\pi\pi} < 1470$ Mev. The projection onto the latter axis with removal of the K*(890) shows no noticeable preference for ρ masses (700 - 800 Mev). A slight background is, however, observable and could correspond to the former $(K^-\pi^+\pi^-)$ decay. In order to test this, it is worth inspecting the triangle plot of Fig.7.30. The $K^{*0}(890)$ band is clearly visible, though the presence of such a band in the $K\pi\pi$ mass is not distinct. A considerable accumulation of points within the cross-over region is, however, observed, and probably corresponds to the decay

$$K^{**}(1400)^- \Rightarrow K^{*0}(890)\pi^-$$

A quantitative estimate of the ratio of this decay to that into $K^-\pi^+\pi^-$ may be made in the following way.

Consider the three body decay of the resonance in the centre of mass of the $K^-\pi^+$ system. If the relative momentum of these two particles in this frame is $\vec{p}$; their relative orbital angular momentum is 1; their overall momentum relative to the π^- is $\vec{q}$; and the relative orbital angular momentum of the π^- in the $K\pi\pi$ rest system is L, then the amplitude for the decay $K^{**} \Rightarrow K\pi\pi$ is proportional to the product

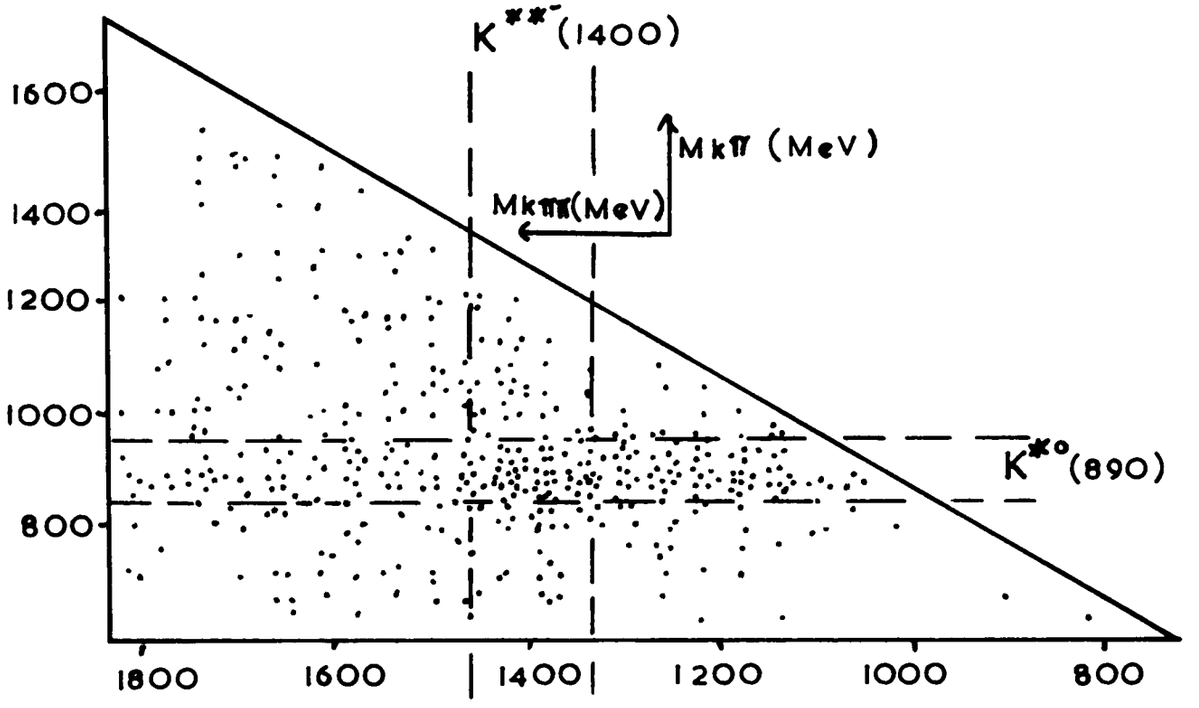
K**-(1400)
1600
1400
1200
1000
800
Mkπ (MeV)
Mkππ(MeV)
K*0(890)
1800
1600
1400
1200
1000
800

FIG. 7.30

of the solid harmonics of p^3 is already

$$p^l Y_l^m\left(\frac{\vec{p}}{|\vec{p}|}\right) q^L Y_L^{m'}\left(\frac{\vec{q}}{|\vec{q}|}\right) \qquad \ldots\ (15)$$

If we restrict the discussion to the decay into $K^*\pi$, then $l = 1$ and $L = 2$. The summation over m and m' (which must add to give M - restricted to the values $\pm 2, \pm 1, 0$) and subsequent integration over both the spaces implied by $\vec{p}$ and $\vec{q}$ gives a term proportional to $p^l q^L$. The fact that the $K^-\pi^+$ form a resonance in the $l = 1$ state may be described by a Breit-Wigner(B.W.) amplitude. The partial amplitude for decay into $K^*\pi$ is therefore given by:

$$T \propto \frac{\sqrt{\Gamma_{K^*}}}{M_K^2 - M_{K^*}^2 - i\sqrt{\Gamma_{K^*}} M_{K^*}}\, pq^2$$

Using $|T|^2$ as the partial width for this decay to be put in the denominator[7] of the Breit-Wigner term describing the $K^{**}(1400)$ decay and including the phase space factors p and q, the density of points on the $K\pi\pi/K\pi$ triangle plot may be written as

$$\frac{\partial^2\sigma}{\partial M_{K\pi}\partial M_{K\pi\pi}} = \left[B.W._{K^*} \times B.W._{K^{**}}\right] \times (p^3q^5) \times (pqQ) \qquad \ldots\ (16)$$

where Q is the relative momentum of the K and proton in the overall centre of mass system. The last term describes the phase space expectation of points on the plot $\left(\frac{\partial^2 R_4}{\partial M_{K\pi\pi}\partial M_{K\pi}}\right)$ whilst p^3q^5 is included for the reasons stated above. In fact, if BW_{K^*} is the $K^*(890) \rightarrow K^-\pi^+$ Breit-Wigner distribution used

before, the factor of p^3 is already included in the expression for its total width. It is strictly necessary to take a coherent sum of amplitudes such as (15) over different values of L and l subject to the condition that the $K\pi\pi\pi$ system have spin-parity 2^+. Restricting the discussion to values for L and l less than or equal to 3, the following combinations (l,L) are possible:-

(1,2), (2,1), (2,3), (3,2)

The complex mixing parameters necessary to make a coherent sum of these partial modes would thus lead to the introduction of six unknown numbers. The assumption that the $K^*\pi$ and $K\pi\pi$ decay modes are independent leads to a simplification since we then only require two numbers - the fraction of decay into $K\pi\pi$ and that into $K^*\pi\left[(l,L) = (1,2)\right]$. The latter course was adopted.

The inclusion of (16) into the likelihood function (equation (11)) required the replacement of $(pq)^2$ by ρ^2 (see equation (11)). In this way, the effect of other processes was automatically taken account of and the decay was treated in a manner similar to the associated productions apart from the inclusion of the p^5 term in the matrix element. The normalization factor in this case was the double integral of (16) over all $K\pi$ and $K\pi\pi\pi$ masses with limits as indicated by the triangle plot (Fig.7.30). Variations of the

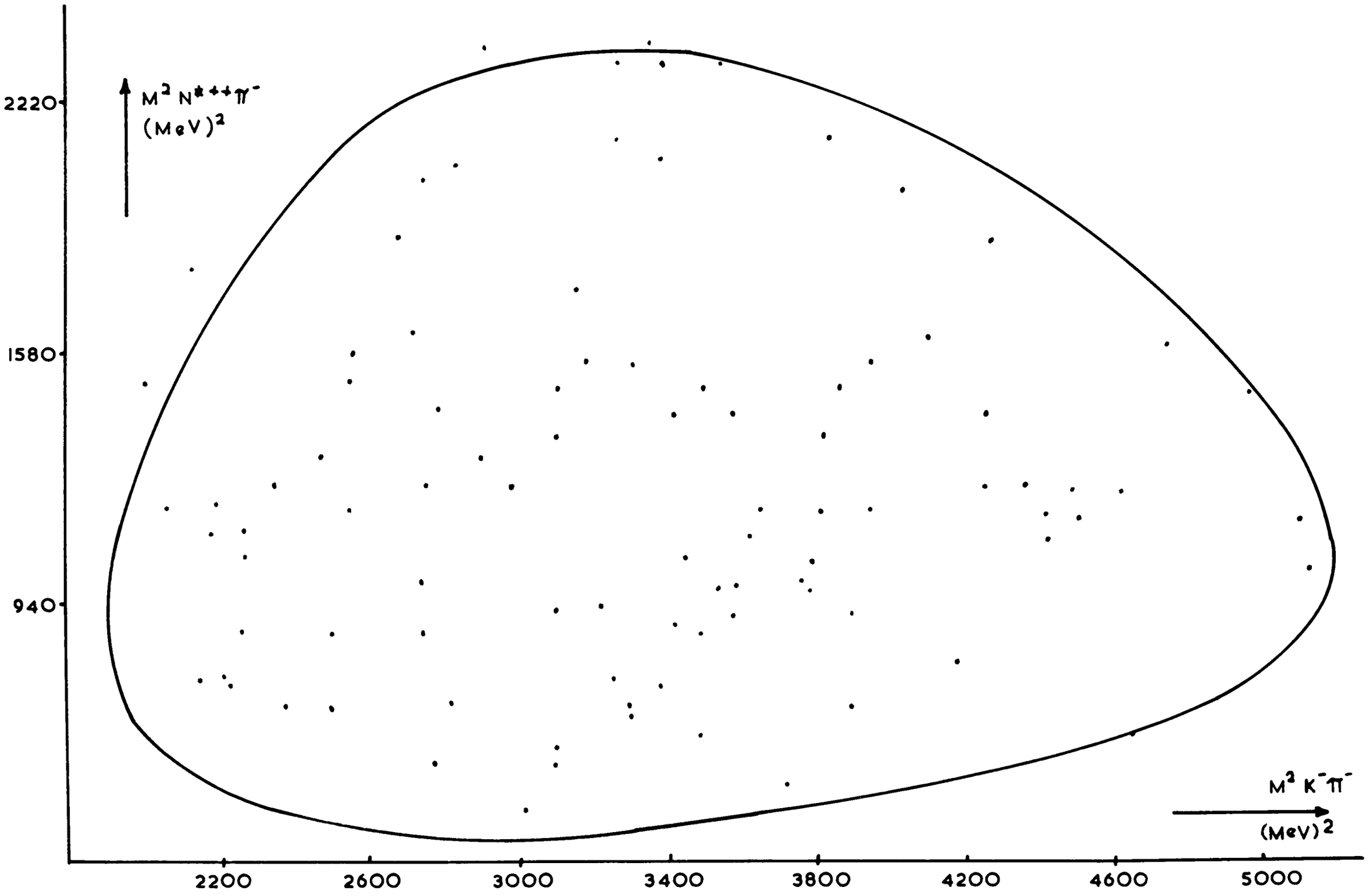

FIG.7·31 $N^{*++}K^-\pi^-$ DALITZ PLOT

fractions of $K^{**} \rightarrow K\pi\pi$ and that of $K^{**} \rightarrow K^{*}\pi$ contributing to the whole of reaction (1) were allowed and gave the results listed in Table V. It appears from this that the $K\pi\pi$ decay mode is at least as important as that involving K^{*}. The figures would probably have been subject to some adjustment if the mass and width of the $K^{**}(1400)$ were allowed to vary. As pointed out in connection with the associated productions, however, such a variation would have required the subsequent re-calculation of the normalization factor - a time consuming process - so that no such variation was undertaken. We notice that the number of events in the region A of Fig.7.30 in excess of the expectation from the population of the regions adjacent is 11 (i.e. 3.25% of final state if an additional 30% of $K^{**} \rightarrow K^{*}\pi$ events lie in the tails of the resonances). The estimate in Table V does not, therefore, appear to be too badly in error.

The Reaction $K^{-}p \rightarrow N^{*++}K^{-}\pi^{-}$

Fig.7.31 shows a Dalitz plot of events having $p\pi^{+}$ invariant mass between 1190 and 1200 Mev.This sample includes 73% of events of the above reaction and 24% of $K^{-}p \rightarrow K^{*0}p\pi^{-}$ as estimated from the Monte Carlo events. The plot is evenly populated within statistical accuracy and there appears to be no reason to suspect the presence of any resonances which would have shown up as bands.

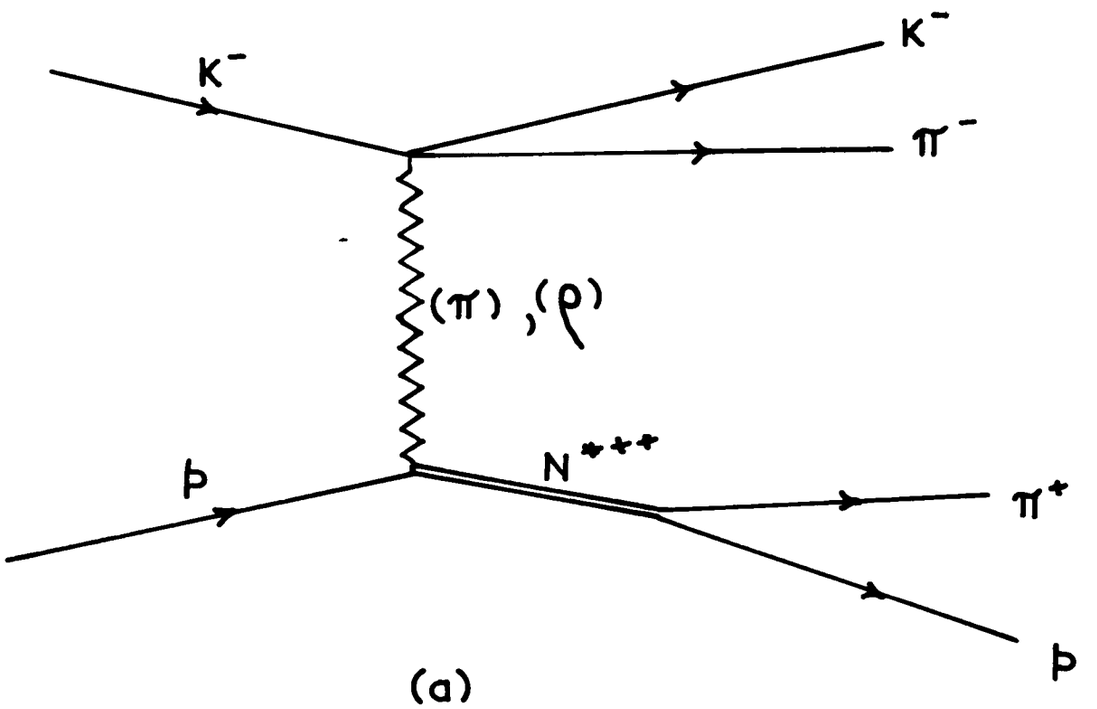

(a)

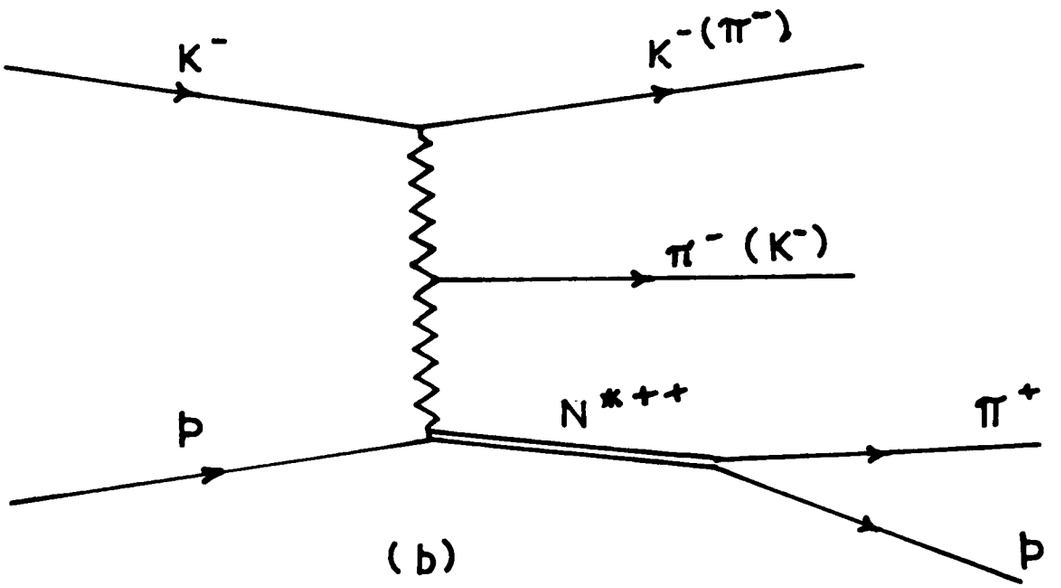

(b)

FIG 7·32 N^{*++} Production

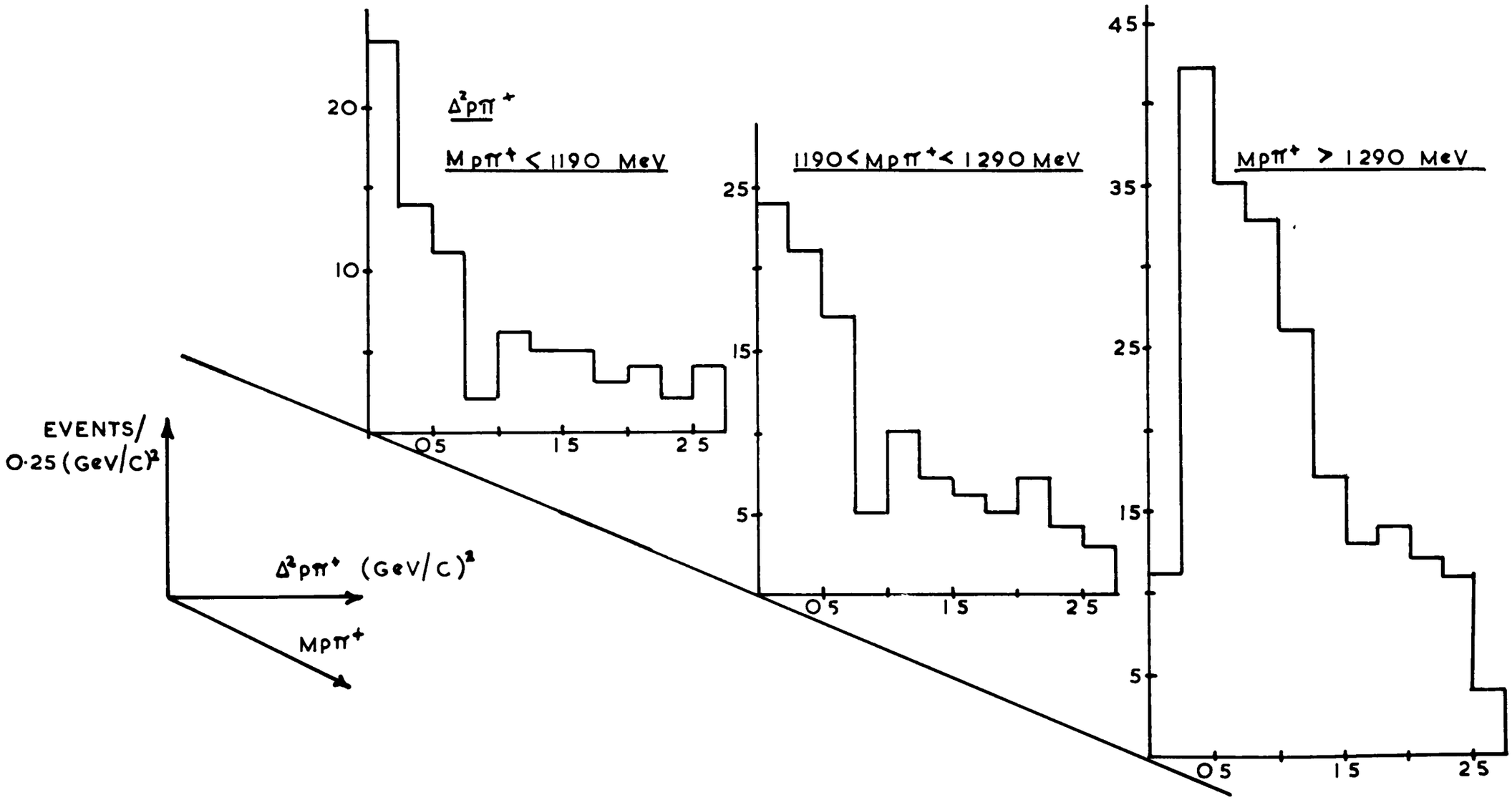

FIG. 7·33 Squared 4-Momentum transfer to $p\pi^+$.

It is of interest to investigate the reaction mechanism contributing to this final state.Some simple diagrams are illustrated in Figs.7.32(a) and (b) where it is observed that baryon exchange is forbidden as this requires the existence of a baryon with charge +3.The tendency in the 4-momentum transfer distribution (Fig.7.33) to the $p\pi^+$ system to assume low values in the region of the resonance is apparent, and consistent with this notion.Analysis of the decay of the N^{*++} is,however, not so straightforward as Fig.7.34(a) suggests.This shows the distribution in Cosθ (with the usual definition) for the resonance plus background.It is highly asymmetric as is the background itself (shaded events in Fig.7.34(a)).This appears to violate the conservation of parity at the strongly interacting N* vertex in any of the diagrams of Fig.7.32.However, it is likely that the peaking towards cosθ = -1 is the result of the decay of the K^{*o}.The peak corresponds to the forward motion of the π^+ in the overall centre of mass (assuming that the N^{*++} is produced in the backward direction),and could well come from the K*.Removal of this by subtraction of events having $830 < M_{K-\pi+} < 950$ Mev results in a somewhat purified $N^{*++}K\pi^-$ sample (92%).The cosθ distribution of the N* appears, nevertheless,to be somewhat uninteresting and not characteristic of either pion exchange which would predict a distribution of the form $(1+2\cos^2\theta)$ or M_1 vector $(\rho)^{25}$ exchange which would result in a distribution of the form $(1-3/5\cos^2\theta)$.

It appears,therefore,that N^{*++} production does not take

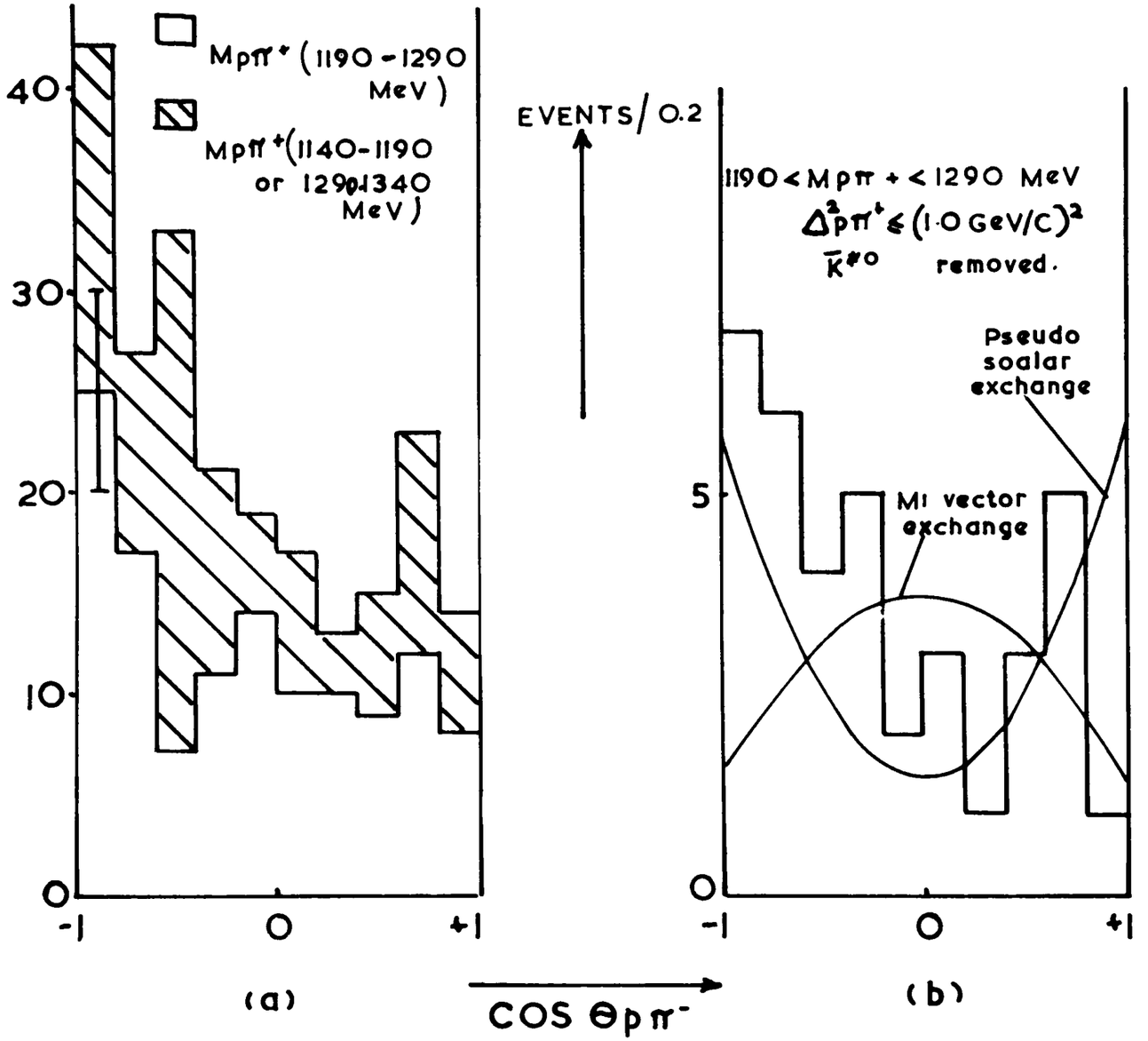

FIG. 7.34 N^{*++} DECAY ANGLES.

place in a simple way as far as one can tell from present statistics. We are therefore unfortunately unable to analyse the data in terms of pure isospin (T = 3/2) $K\pi$ scattering of a virtual exchanged pion at the K^- vertex nor of the Stodolsky-Sakurai isobar production model.

The Kappa Meson - K*(725)

The existence of this particle is in considerable doubt owing to its appearance in few reactions.[26] The distribution shown in Fig.7.2 shows a slight departure from the Monte Carlo expectation in the region of the accepted mass for this particle. The further selection of low momentum trasfer to the $K^-\pi^+$ ($\lesssim 1.0(\mathrm{Gev/c})^2$) is shown in Fig.7.27(a) and tends to enhance the effect. One may wonder whether this is caused by the ambiguous events in the sample, but their removal tends merely to make the effect even more noticeable - the shaded events in Fig. 7.27(d) are the unique ones. Various mechanisms have been proposed to explain away the presence of this "particle" as a triangle singularity.[27,28] Of the 10 events in the K "peak" in this experiment, 7 have a p_{π^+} mass consistant with N^{*++}. This is surprising if the rescattering mechanism such as that of Fig. 7.35 really takes place since the re-scattering of the pion would tend to redistribute the p_{π^+} mass out of the N* region. The fact is also surprising in a different way if the

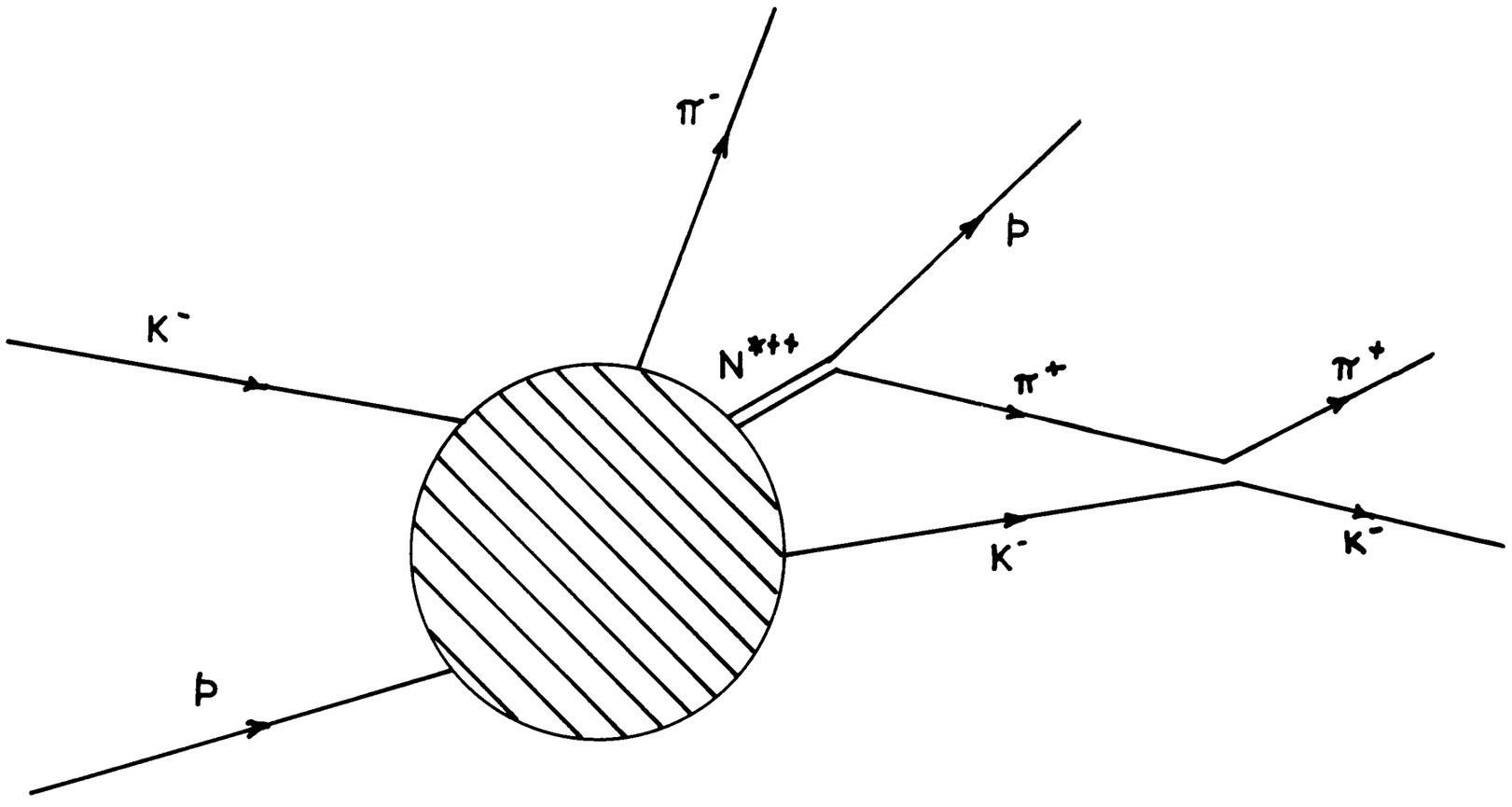

FIG. 7.35

TABEL VI

Evidence for K(725)

Reaction	Beam Momentum	Charge State	Cross-Section (μb)	Mass (Mev)	Width (Mev)	Reference
$\pi^- p \rightarrow Y K \pi$	1.5	0	> 0	735 ± 5	< 20	26d
	1.8	0	> 0			
	1.9, 2.05	+	6 ± 2			
	2.17, 2.25 2.36	+	3 ± 1	726 ± 3	< 20	26a
$K^- p \rightarrow \bar{K}^0 p \pi^-$	1.08	-	82 ± 40			
	1.22	-	30 ± 20			
	1.33	-	25 ± 15	723 ± 3	< 12	26c
	1.43	-	8 ± 15			
	1.51	-	12 ± 5			
	1.71	-	10 ± 10			
$K^- p \rightarrow K N \pi$	2.24	$\pm, 0$	> 0	730	≤ 15	26e
$K^+ p \rightarrow K N 3\pi$	3.0	+, 0	85, 65	725 ± 5	< 30	26b
	3.5	-	Not Observed	-	-	31
$K^- p \rightarrow K N 3 \pi$	3.5	0	> 0 (Not Obser'd in other charge States)	-	-	Ibid
$K^- p \rightarrow K^- p \pi^+ \pi$	1.80, 1.95	0	> 0			26f
	3.0	0	~ 10 (Unexplained Enhancement)	690-710	-	27
	3.5	0	0-33	710 ± 10	≤ 20	Ibid
$K^- p \rightarrow K^0 \pi^0 p \pi^-$	3.5	0	0-10	~ 730	-	9

majority of events consisting of a supposed resonance are to have another invariant mass within another resonance. The situation regarding this particle is certainly very obscure at the moment and Table VI gives a summary of some of the reactions in which it has been seen.[31] The chief source of K^0_s appears to have been in the $KN3\pi$ final states produced by 3.0 Gev/c K^+ mesons. It is, therefore, interesting to observe the $K\pi$ spectra in the corresponding final states initiated by 3.5 Gev/c K^- particles. These are shown for the two reactions (2) and (3) in Figs.7.36(a),(b) and (c), and, except in the case of the zero charge state of reaction (2), no effect is noticed. In the former case, however, a slight enhancement appears, though somewhat broad. It has a width camparable with the K*(890) which is also visible. Upper limits for the production cross-section of this particle - if it exists - may be estimated by counting events and are given in Table VI.

Other Rare Decay Modes of the K**(1400)

In reaction (3), the most noticeable resonance productions are that of the $N^{*++}(\rightarrow p\pi^+)$ and $\omega^0(\pi^+\pi^-\pi^0)$. The three pion invariant mass distribution is shown in Fig.7.37. The three events occurring at the η mass may be taken as indicative of its production owing to the combination of factors - small phase space expectation and the accumulation of events within

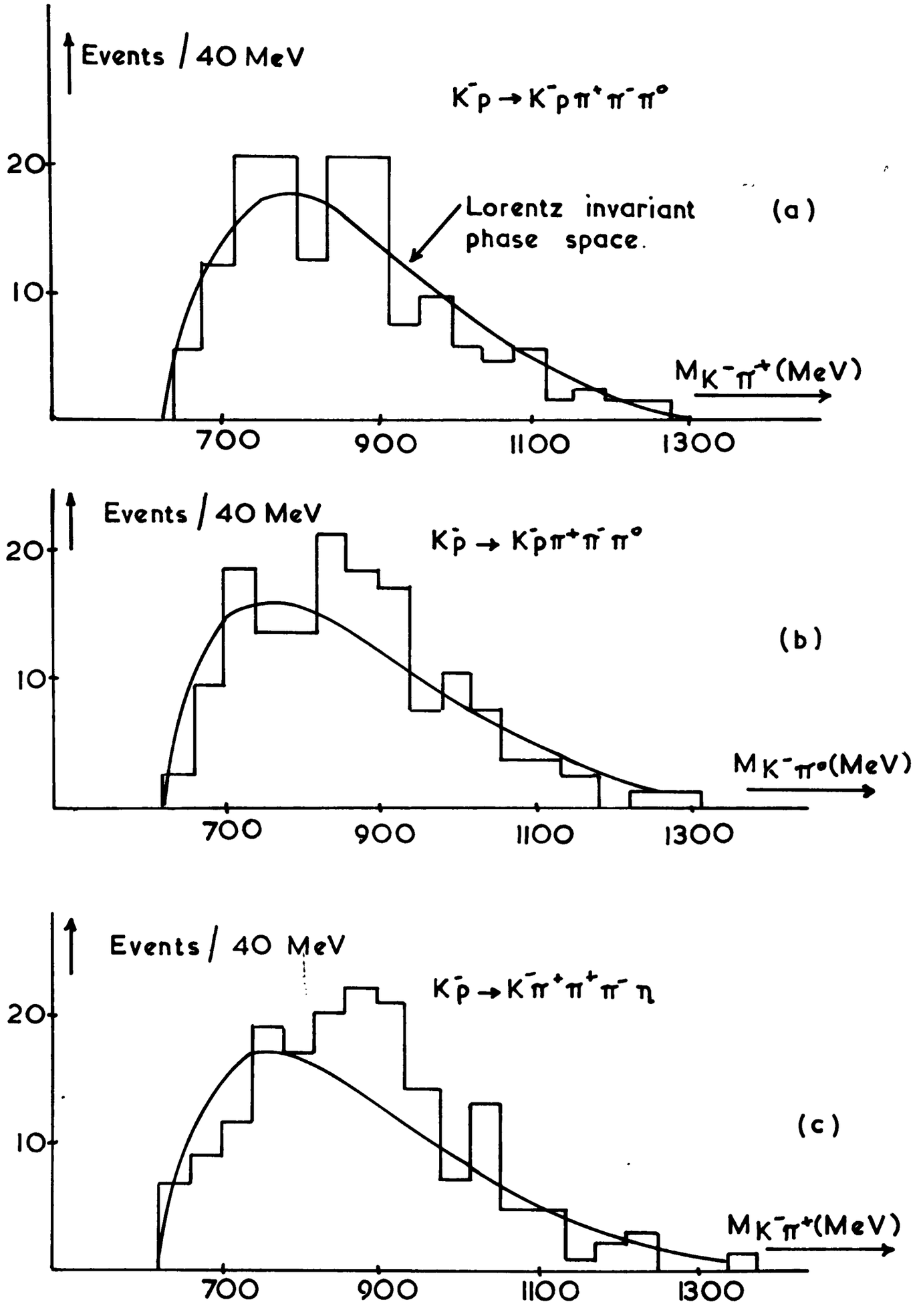
Events / 40 MeV
$K^-p \to K^-p\pi^+\pi^-\pi^0$
20
10
Lorentz invariant phase space.
(a)
$M_{K^-\pi^+}$(MeV)
700
900
1100
1300
Events / 40 MeV
$K^-p \to K^-p\pi^+\pi^-\pi^0$
20
10
(b)
$M_{K^-\pi^0}$(MeV)
700
900
1100
1300
Events / 40 MeV
$K^-p \to K^-\pi^+\pi^+\pi^-\eta$
20
10
(c)
$M_{K^-\pi^+}$(MeV)
700
900
1100
1300

FIG 7.36

one 40 Mev bin. Branching ratios for decay of the K**(1400) into $\bar{K}\omega$ and $\bar{K}\eta$ have been theoretically predicted[29] by Gloshow and Socolow using SU(3) and a search for these modes has been made using these events. Not one of the η events has a $\bar{K}\eta$ invariant mass anywhere near to 1400 Mev so that only an upper limit has been determined for this decay. The $K\bar{\omega}$ spectrum is illustrated in Fig.7.38. The presence of K**(1400) is not expected to be very significant as only 32 events exist in the whole mass region. However, the peak in the vicinity of the K**(1400) mass is a little more than a one standard deviation effect. The cross-section for decay of this resonance:

$$K^-p \rightarrow K^{**-}p$$
$$\hookrightarrow K^-\omega$$

was determined by fitting a curve to the $\omega\bar{K}$ mass spectrum consisting of a sum of the Lorentz invariant phase space and a simple Breit-Wigner form multiplied by the phase space factor. The fraction of resonance with fixed mass of 1430 Mev and fixed width of 100 Mev was adjusted to give a cross-section of $36 \pm 29 \mu$b for this decay.

K** Resonances with Isospin (T = 3/2)

The absence of any noticeable enhancements in the $K^-\pi^-$ spectrum of reaction (1) has already been noted. A similar situation is found in the corresponding distributions for the

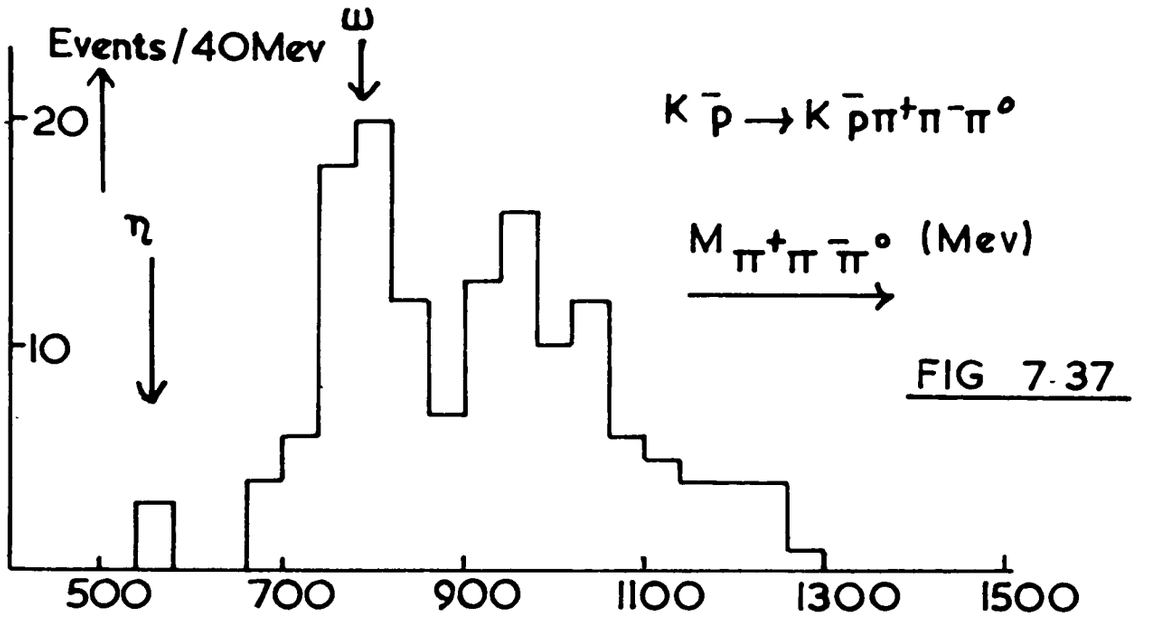

FIG 7·37

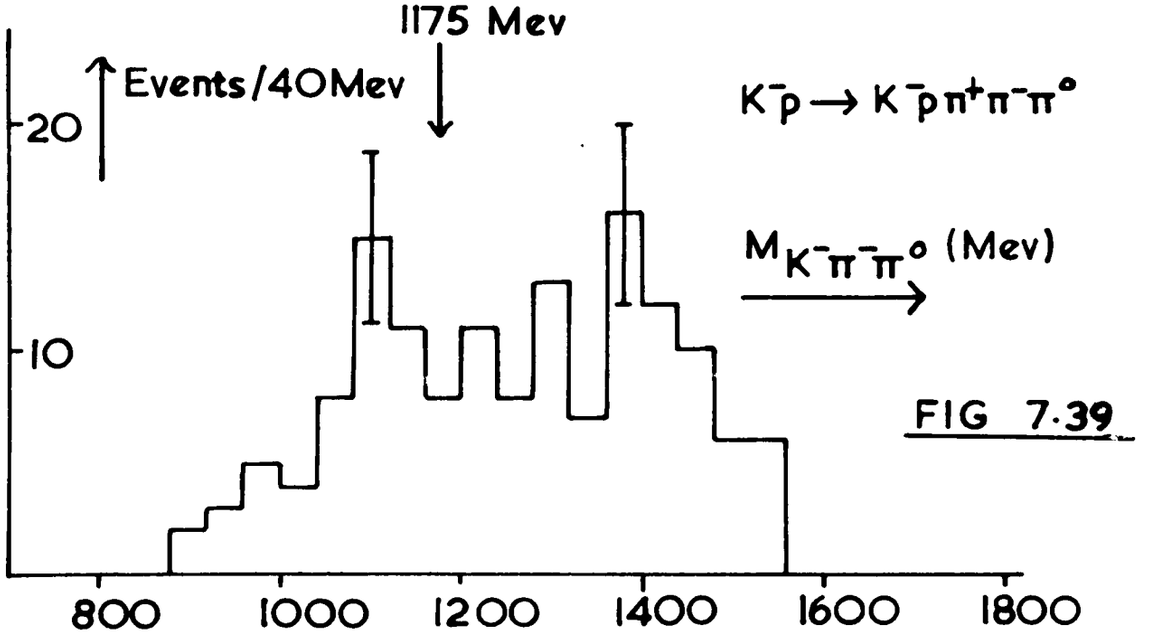

FIG 7·39

five body final states. The report of a resonance in the ($T = 3/2$) doubly charged $K\pi\pi$ spectrum from the reaction $\pi^- + p \rightarrow K + Y + 2\pi$ by Wangler et al[12] followed by other reports from Miller et al[13] and Walker et al leads us to inspect the $K^-\pi^-\pi^0$ mass spectrum of reaction (2). This is shown in Fig.7.39 where it is seen that no noticeable enhancement in the region of 1175 Mev is found.

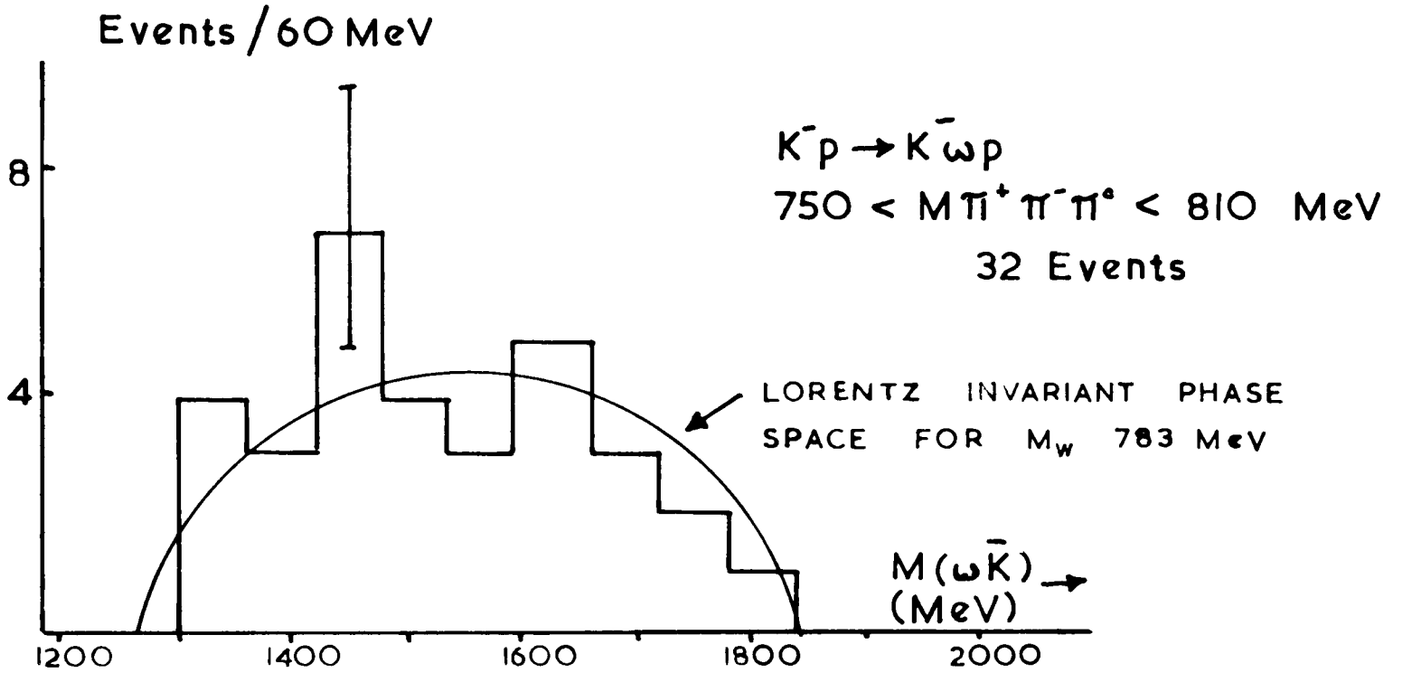
Events / 60 MeV
8
4
1200
1400
1600
1800
2000
$K^- p \to K^- \omega p$
$750 < M\pi^+\pi^-\pi^0 < 810$ MeV
32 Events
LORENTZ INVARIANT PHASE SPACE FOR M_w 783 MeV
$M(\omega K^-)$ (MeV)

FIG. 7.38

REFERENCES TO CHAPTER VII

1. N. Haque et al - Physics Letts. 14,338(1965)

2. J. Badier et al - Physics Letts. 19,612(1965)

3. S. Focardi et al - Physics Letts. 16,351(1965)

4. S. Goldhaber et al - UCRL 16332 - Revision of a paper presented at the Oxford International Conference on Elementary Particle Physics, September 1965.

5. J. Friedman & R. Ross, "Maximum Likelihood Estimation of Resonant State Prediction in Multiparticle Final States", LRL Report P.102

6. O. Skjeggestad. Proceedings of the 1964 Easter School for Physicists. Herceg Novi, Vol.II.

7. J. D. Jackson - Nuovo Cimento 34,1644(1964)

8. A. H. Rosenfeld et al - UCRL 8030

9. P.M.D.Gray - D.Phil.Tesis, Oxford (1965)

10. A. M. Segar - Private Communication

11. G. Goldhaber et al - Physics Letts. 6,62(1963)

    M. Ferro - Luzzi et al, "The reaction KN at 3 Gev/c and the Production Mechanism of K*N*,"CERN TC/PHYS 65-6 (1965)

    See Reference 4

12. Wangler et al - Physics Letts. 9,71(1964)

13. Miller et al - Physics Letts. 15,74(1965)

14. R. Armenteros et al - Physics Letts. 9,207(1964)

15. R. Boch et al - Physics Letts. 12,65(1964)

16. S. P. Almeida et al - Physics Letts. 16,184(1965)

17. G. Goldhaber & S. Goldhaber - Proceedings 4th Anniv. Symposium. Inst. Math. Sci. Madras, India (Jan.1966) Also UCRL 16744

18. D. R. O. Morrison - Physics Letts. 22,226(1966)

19. S.D. Drell - PRL 5, 342(1960)

20. R. T. Deck - PRL 13,169(1964)

21. U. Maor & T. A. O'Halloran,Jr., Physics Letts.15,281(1965)

22. G. Wolf - Determination of the $\pi\pi$ scattering phase Shifts up to 1.3 Gev CMS Energy - Hamburg DESY 65/13(1965)

23. P.D.Gray, J. H. Field - Oxford Bubble Chamber Group Programme Library (June 1966)

24. H. Hogaasen, J. Hognasen, R. Keyser and B.E.T.Svensson - CERN TH.584(1965)

25. L. Stodolsky & J. J. Sakurai, PRL 11,90(1963)

26. A.D. H. Miller et al - Physics Letts 5,299(1963)
B.M. Ferro-Luzzi et al - Physics Letts. 12,255(1964)

C.S. Wojcicki et al - Physics Letts. 5,283(1963)

D.Y.S.Kim et al - Physics Letts. 19,350 (1965)

E. G. W. London et al - Phys.Rev. 143,1o34(1966)

F.L. T. Smith, Resonance Production in K⁻p Interactions at 1.80 to 1.95 Gev/c. Ph.D. Thesis, UCLA,1965 (Unpublished)

27. P. M. Dauber - Ph.D. Thesis, UCLA,1966(Unpublished)

28. M. Month - Physics Letts. 18,357(1965)

29. S. L. Glashow & R. H. Socolow - PRL 15,329(1965)

30. J. Bishop et al - University of Wisconsin rept.53706(1965)

31. Graham et al - Physics. Letts. 22,348(1966)

PART III

CHAPTER VIII

Conclusions

Ionization Measurements in Hydrogen Bubble Chambers

As a result of an investigation of the use of ionization measurements on film derived from an exposure of the Saclay 81cm Hydrogen Bubble Chamber at CERN to a beam of separated K^- mesons, the following conclusions may be drawn:-

(i) The gap-length distribution is exponential down to a certain minimum length. It is likely - judging from the results of Morrison et al (Ref.7 Chapter III) that the mean gap length is a reasonable estimator of the particle velocity β. The measurements carried out by the author using a microscope appear to favour the view that the first moment of the blob length distribution is also representative of the same quantity, since the minimum gap length cut off (α in the text of Chapter III) appears to match both the value that can be inferred from the mean blob length

$$\bar{b} = \frac{e^{\alpha g} - 1}{g} \qquad \ldots\ (1)$$

(g =ionization)

or from the gap length distribution itself. This tends to indicate that both mean blob length and mean gap

length are what might be expected from a truly exponential distribution of bubble nucleation centres, though it has also been seen that counting bubbles gives an answer lower than might otherwise be inferred, so that bubble counting is an unreliable measurement.

(ii) Though, from the statistical point of view, the lacunarity method of ionization estimation is a good one, the dependence of the measurements made by a device as simple as the one described in this thesis upon bubble diameter precludes its use. Perhaps the incorporation of a separate scanning system to measure the average track width over a finite length of track would increase the meaning of the readings. An attempt to perform such a measurement using the one scanning aperture which covered only a short track length (less than a bubble diameter) met with little success largely owing to the fact that the device was driven along the track at variable speed.

(iii) The measurement of mean gap length was found possible. However, detailed investigation indicated that the device appeared to have a response to the gaps to which it assigned a length of (typically) about one bubble diameter, which was somewhat variable. The shadow

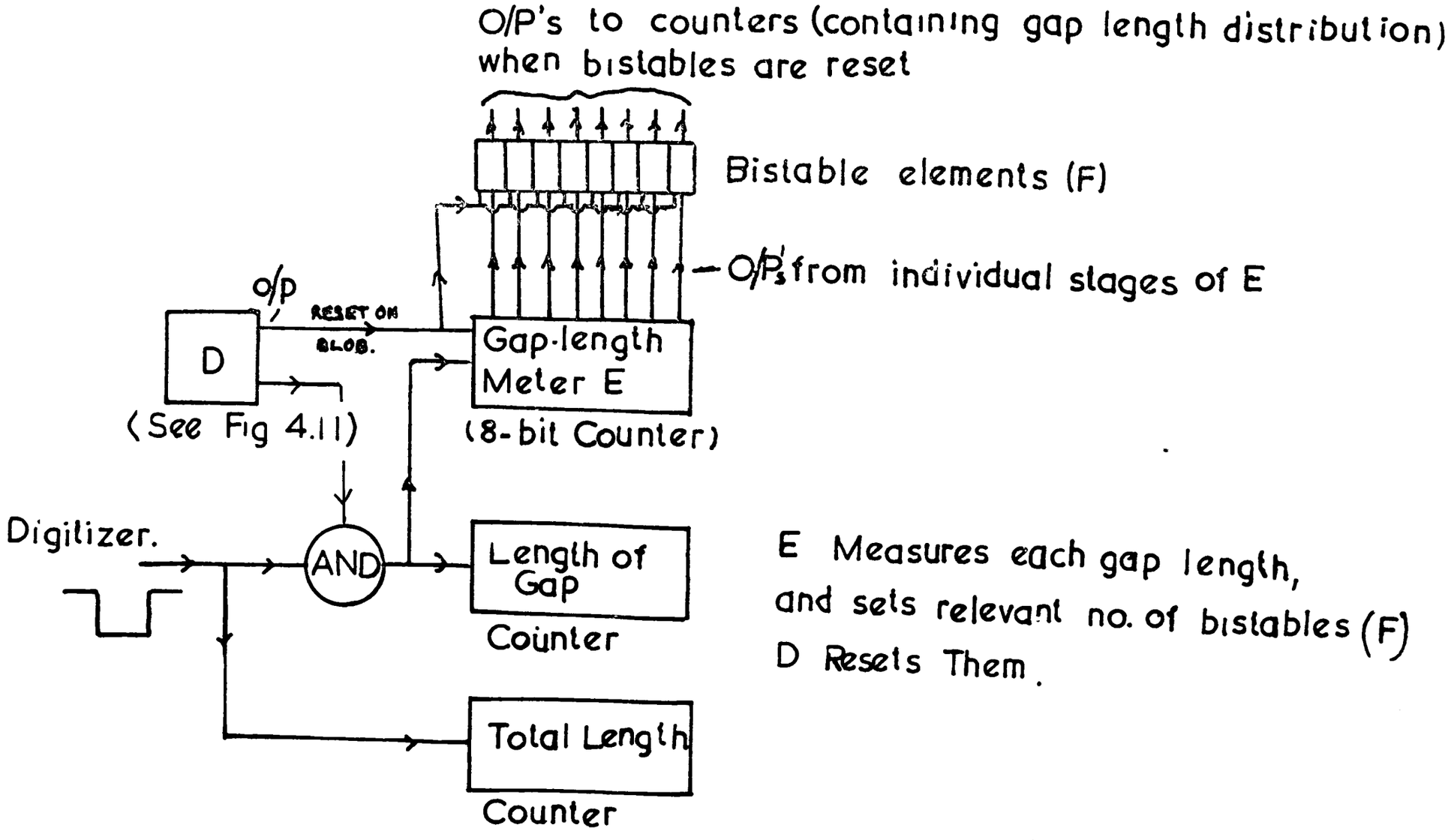
O/P's to counters (containing gap length distribution) when bistables are reset
Bistable elements (F)
O/P's from individual stages of E
o/p
RESET ON BLOB.
D
(See Fig 4.11)
Gap-length Meter E
(8-bit Counter)
Digitizer.
AND
Length of Gap
Counter
Total Length
Counter
E Measures each gap length, and sets relevant no. of bistables (F)
D Resets Them.

FIG 8.1

(often found in such gaps) is a likely explanation for this. It was not found possible to reduce the sensitivity of the measurements to this effect without the necessity of readjusting the "blob-gap detection threshold" to suit each measured track section. The only safe way of overcoming the effects of the smaller gaps would be to completely ignore them. In order to estimate the lowest value of gap length to accept, it would be desirable to measure the distribution in order to detect at which point it ceased to be exponential.

(iv) After deciding the gap length cut off in the way suggested in (iii), it would be possible to use the method of Appendix B to extract the maximum information from a track by measuring the quantities:-

(a) Total Gap Length;

(b) Gap-Length Distribution;

also (c) Total length of track measured.

The necessary modifications to the present device to do this have been designed and built from SGS Fairchild micro-logic (solid state) elements and only require testing. The system is represented in Fig.8.1

(v) It would appear that the minimum gap length visible to a simple scanning system like the present one is

approximately two bubble diameters (bubble centre to centre). It is not unreasonable to suppose that this is so for any bubble diameter, so that the smaller this quantity (consistent with having a good film contrast) the better. The statistical accuracy of ionization measurements depends upon:=

(a) the number of bubbles;

(b) the number of visible gaps (i.e. track "cells").

The latter quantity is a maximum when the mean gap length is equal to the minimum gap visible (for a fixed ionization). In the medium energy experiments such as the present one where the resolution of lower relative ionizations (e.g. $\leq$ 1.6 relative to minimum) is often sought, it would therefore be reasonable to aim at a bubble diameter of about 160μm in the chamber (comparable with that used by Morrisson et al) and a primary mean gap length of about 300μm (representing an average vertex measurement error). This would provide relativistic tracks with lacunarity 0.6 - quite easy to scan.

Production of $\bar{K}^*(890)$

In all reactions discussed in this thesis, strong evidence for this resonance has been found. When made in

TABLE I

Decay Mode †	Cross-Section[7] (μb)	Reference			SU_3 Prediction
		3	4	5	
$K\pi$	289±80	1.0±0.28	1.0±0.5	1	1
$K^*\pi$	61±43	0.48±0.33	1.10±0.35	$\frac{1}{3}\pm\frac{1}{3}$	0.62
$K\rho$	20	0.3	0.36±0.11	1/12	0.19
$K\omega$	36±29	0.12±0.10	0.18±0.10	$\frac{1}{3}$	0.06
$K\eta$	11	0.15	0.05±0.05	$\frac{1}{2}$	0.03
$K^-\pi^+\pi^-$	189±59	0.65±0.20	-	-	

† All rates are relative to $K\pi$ and corrected for unobservable decays.

association with a nucleon, the following features appear evident:-

(a) Negative $\bar{K}^*(890)$ is made in a manner characteristic of single particle (Natural Parity) exchange. This is in agreement with the findings from 3.0 Bev/c K^+p or K^-p reactions.[1,2]

(b) Zero charged $\bar{K}^{*o}(890)$ appears to be made largely by single pion exchange.

Production of $\bar{K}^*(890)$ in the three body reaction:

$$K^-p \rightarrow \bar{K}^{*o}p\pi^-$$

also appears to proceed by single pion exchange. Qualitatively the reaction seems to occur in a manner characteristic of the Drell process.

$\bar{K}^{**}(1400)$

An isotopic spin assignment of $\frac{1}{2}$ for this resonance appears to be confirmed. The spin and parity 2^+ are also confirmed. Similar conclusions regarding the production mechanism for this particle in association with a single nucleon appear to hold as for the $\bar{K}^*(890)$.

It has been found possible to observe a variety of decay modes for the negatively charged resonance produced in the reaction: $K^-p \rightarrow K^{**-}(1400)p$

In Table I are collected the branching ratios for these decays. They are also compared with the findings of other workers, and with the predictions of SU_3.[6]

REFERENCES TO CHAPTER VIII

1. M. Ferro-Luzzi et al - Physics Letts. 9, 359(1964

2. J. D. Jackson et al - Phys.Rev. 139, B425(1965)

3. Ibid

4. J. Badier et al - Physics Letts., 19, 612(1965)

5. M. Hardy et al - PRL, 15, 325(1965)

6. S. Glashow & R. Socolow - PRL 15, 329(1965)

7. Cross-Section refers to $K^-p \rightarrow K^{*-}(1400)p$ observed in 2 and 4 prong events at 3.5 Gev/c

APPENDIX A

Gap Geometry of Ideal Tracks

We define an ideal bubble track to consist of identical, spherical bubbles of diameter α, and to have an exponential distribution of distances (x) between bubble centres. Thus, although the bubbles have finite size, there is no restriction upon the distance between their centres.

The distribution law may be written as:

$$dn(x) = Ae^{-kx}dx$$

giving the number of gaps from x to x + dx, where A and k are constants, and may be used to connect physically measurable track quantities with the bubble density (number of bubble centres/unit track length).

If this quantity is g/unit length:

$$g = \frac{\int_{x=0}^{\infty} dn}{\int_{x=0}^{\infty} x\,dn} = k \qquad \ldots\ A1$$

The first moment (or mean) of gaps $> \alpha$ in length is:

$$\langle x_{>\alpha} \rangle = \frac{\int_{x=\alpha}^{\infty} x\,dn}{\int_{x=\alpha}^{\infty} dn} = \alpha + \frac{1}{g}$$

Therefore, the average length of gap between bubble

circumferences ($y=x-\alpha$) is $\langle y \rangle = 1/g$ A2

and is independent of α.

$$L(\alpha) = \frac{\text{total gap length of gaps between bubble circumferences}}{\text{total track length}}$$

$$= \frac{\int_{x=\alpha}^{\infty} (x-\alpha)\,dn}{\int_{x=0}^{\infty} x\,dn} = e^{-g\alpha} \quad \text{.... A3}$$

It follows from the distribution law that the relationship between the logarithm of the number of gaps $\rangle$ d (some distance) and d itself is a linear one. The slope of the line connecting the two is g. In other words:

$$g = \frac{\ln H(d_1) - \ln H(d_2)}{d_2 - d_1} \quad \text{.... A4}$$

where H(d) is the density of gaps $\rangle$ d.

The first moment of the blob length distribution is

$$\langle b \rangle = \frac{1-L(\alpha)}{H(\alpha)} = \frac{e^{\alpha g} - 1}{g} \quad \text{.... A5}$$

Theoretical Variances of Some Quantities

The number of bubbles (m) in a unit track length obeys a Poisson distribution law. The probability of m being the number of bubbles found when n are expected is: $P(m) = \frac{n^m e^{-n}}{m!}$

Consequently, the variance of m is = m A6

The evaluation of the second moment of the gap length (y) distribution leads to an estimate of the variance of a single gap length from:

$$\sigma^2(y) = \langle y^2 \rangle - \langle y \rangle^2 = 1/g^2 \text{ (independent of } \alpha) \quad \text{.... A7}$$

Consequently, the quantity f(L) - see equation (3) of Chapter III - for the estimate of g obtained from the mean gap length is:

$$f(L) = \frac{\sigma^2(g)}{g} = \frac{g}{n} = \frac{1}{L} \qquad \ldots\ldots A8$$

(where n = number of gaps $> \alpha$ in unit length = $g e^{-g\alpha} = gL$)

The second moment of the blob length distribution may be calculated as follows:-

Suppose a blob consists of "gap lengths" (i.e. distances between bubble centres) of lengths $x_1, x_2, \ldots\ldots x_n$. Then the blob length is $(\alpha + x_1 + \ldots\ldots + x_n)$.

Using the fact that the probability for a gap to be $< \alpha$ is $(1-e^{-g\alpha})$ the required moment is:

$$\langle b^2 \rangle = e^{-g\alpha} \sum_{n=0}^{\infty} \left\langle \left(\alpha + \sum_{k=1}^{n} x_k\right)^2 \right\rangle (1-e^{-\alpha g})^n$$

since there is no restriction on the number (n) of bubbles in the blob.

$$\langle b^2 \rangle = \alpha^2 + (2\alpha\langle x \rangle + \sigma^2(x)) e^{-g\alpha} \sum_{n=0}^{\infty} n(1-e^{-\alpha g})^n + \langle x \rangle^2 e^{-g\alpha} \sum_{n=0}^{\infty} n^2 (1-e^{-\alpha g})^n$$

where the x's are all $\leq \alpha$ and $\sigma^2(x) = \langle x^2 \rangle - \langle x \rangle^2$.

The moments of x are:

$$\langle x \rangle = \frac{1}{g}\left(1 - \frac{\alpha g e^{-\alpha g}}{1-e^{-\alpha g}}\right)$$

and $\langle x^2 \rangle = \dfrac{2(1-e^{-\alpha g} - \alpha g e^{-\alpha g}) - \alpha^2 g^2 e^{-\alpha g}}{g^2(1-e^{-\alpha g})}$

so that $\sigma^2(b) = \langle b^2 \rangle - \langle b \rangle^2$

$$\frac{\sigma^2(b)}{\alpha^2} = \frac{1-L^2 + 2L \ln L}{(L \ln L)^2} \qquad \text{.... A9}$$

(using $L = e^{-g\alpha}$)

Armed with the variances of the mean gap length (gaps α) and the mean blob length, all other variances are obtainable. For instance the lacunarity: $L = \dfrac{\langle y \rangle}{\langle y \rangle + \langle b \rangle}$

$$\gamma^2(L) = \left(1 + \frac{\langle b \rangle}{\langle y \rangle}\right)^{-4} \left(\frac{\sigma^2(b)}{\langle y \rangle^2} + \frac{\langle b \rangle^2}{\langle y \rangle^2} \frac{\sigma^2(y)}{\langle y \rangle^2}\right)$$

for the lacunarity estimated from a single track cell (one blob and one gap).

For a unit length of track (containing gL cells)

$$\gamma^2(L) = \frac{L}{g}\left((1-L)(2-L) + 2L \ln L + \frac{(L \ln L)^2}{1-L} \right)$$

Consequently, the function f(L) for the value of g estimated from lacunarity is:

$$f(L) = \frac{\sigma^2(g)}{g} = \frac{L}{(1-L)} + \frac{2}{\ln L} + \frac{(1-L)(2-L)}{L(\ln L)^2} \qquad \text{....A10}$$

APPENDIX B

The Combination of Blobs and Gaps

An important fact was pointed out by Barkas[1,3] concerning the estimation of ionization - g. It is that as much information resides in the blobs as in the gaps in a track and that the two sets of information are clearly independent. Thus, measuring the mean length of either blobs or gaps separately, one can completely ignore the other. If both are measured, therefore, the two estimates g_1 and g_4 (see equations A.2 and A.5 of Chapter III) may be linearly combined to form an average which will be defined as g_6 where $g_6 \doteq wg_1 + (1-w)g_4$ where w is a function of lacunarity. That this is so is clear when one considers that the relative information content in blobs and gaps varies with L.

In order to calculate the form of w, Barkas used the method of maximum likelihood. The result obtained was:-

$$\frac{w}{(1-w)} = \frac{(L\ln L)^2}{(1-L+\ln L)} 2\left(\frac{\sigma_b}{\lambda}\right)^2 \qquad \ldots\ldots(1)$$

where σ_b = standard deviation of blob length.

Further, the width of the likelihood function can be estimated from its second derivatives in the usual way,[2] and the result is that $f_6(L) = w/L$ (see equation (3)). The function $f_6^{\frac{1}{2}}$ is plotted with those corresponding to the other ionization estimates in Fig. 3.1. (Chapter III). It will be

noticed that it is more uniform over the whole range of L than the others. This is because g_6 is an estimate that combines the information from blobs and gaps in a way which automatically gives the most significance to the most informative. All other estimates described so far are very dependent upon the type of track considered, in particular, on its value of L.

Maximum Likelihood Estimation of Ionization

The fundamental difficulty with the Barkas' method of obtaining g_6 is that the value of g_4 may be made as close to g_2 as desired simply by making slight alterations to λ. On a typical beam track, a variation in λ of 10% gives a 40% change in g for fixed mean blob length. The best way to determine α in the use of the emulsion technique is by observing the blob density along a track. As the particle causing the track slows down, the mean gap length decreases until it is equal to λ. At this point, the blob density is at a maximum. No equivalent method is available in bubble chamber analysis since the slowing down is more gradual, and the lack of statistics completely prohibitive. Unless one can find a better way to determine this quantity, therefore, the Barkas' estimation is reduced to a good procedure wasted on a bad measurement, and measuring mean blob length at all is futile.

Though, as pointed out by Barkas, the mean gap length is

a sufficient estimator for the distribution of gaps, it is here observed that more information, in the form of a value for λ, is actually obtained from measuring the distribution. As already shown (Chapter III), the gap lengths greater than a bubble diameter do show an approximately exponential character in their distribution, and an extrapolation to zero gap is quite well constrained for instance, in the tracks illustrated in Fig. 3.2. as in most others measured by the author. The method suggested, therefore, consists of measuring the distribution of gap lengths - subject to the normalization condition that the total number of gaps greater than zero in length will be equal to the bubble density multiplied by the track length - in order to obtain α. Its value can then be used to obtain g_4 from the mean blob length which is an independent determination of g. In fact, the procedure suggested is to perform both parts simultaneously by maximizing the likelihood function:-

$$F(g,\lambda) = \left[\frac{N!}{(N-m)\prod_{i=1}^{k} N_i!}\right](1-e^{-g\lambda})^{N-m} \times e^{-N_0 g(\lambda+\lambda_R)}$$

$$\times \prod_{i=1}^{k} e^{-g\lambda}(e^{-g\lambda_{i-1}} - e^{-g\lambda_i})^{N_i} \qquad \ldots.(2)$$

$$\times \left[\frac{1}{\sigma_b^2} \exp\left\{-\frac{(\bar{b} - \langle b \rangle)^2}{2\sigma_b^2}\right\}\right]$$

with respect to g and λ. In equation (2):

N = total number of bubbles in track length ($= gL_{TOT}$)

m = total number of gaps observed

N_i = number of gaps of visible length λ_{i-1} to λ_i

k = number of such intervals

$\bar{b}$ = mean blob length (independent of the gaps)

and σ_b = standard deviation of $\bar{b}$

and for consistency, we replace g by g_7.

The expression may be divided into three parts. The last of these is the Gaussian term:

$$\frac{1}{\sigma_b^2} \exp\left[- \frac{(\bar{b} - \langle b \rangle)^2}{2\sigma_b^2} \right]$$

and describes the probability for obtaining the value $\bar{b}$ for mean blob length when the expectation value is:

$$\langle b \rangle = \frac{e^{\lambda g} - 1}{g}$$

In order to avoid having to measure the variance on this quantity, the expectation value $\langle \sigma_b^2 \rangle$ derived in Appendix A is used.

The second part of expression (2) describes the probability for having the observed distribution of gap lengths. N_o is the number greater than $\lambda + \lambda_k$ for instance, whilst there are supposedly N-m less than λ.

The multinomial expression simply allows for the permutations possible amongst the gaps.

The measured quantities may be obtained with a microscope by writing down the length (in eyepiece divisions, say) of each

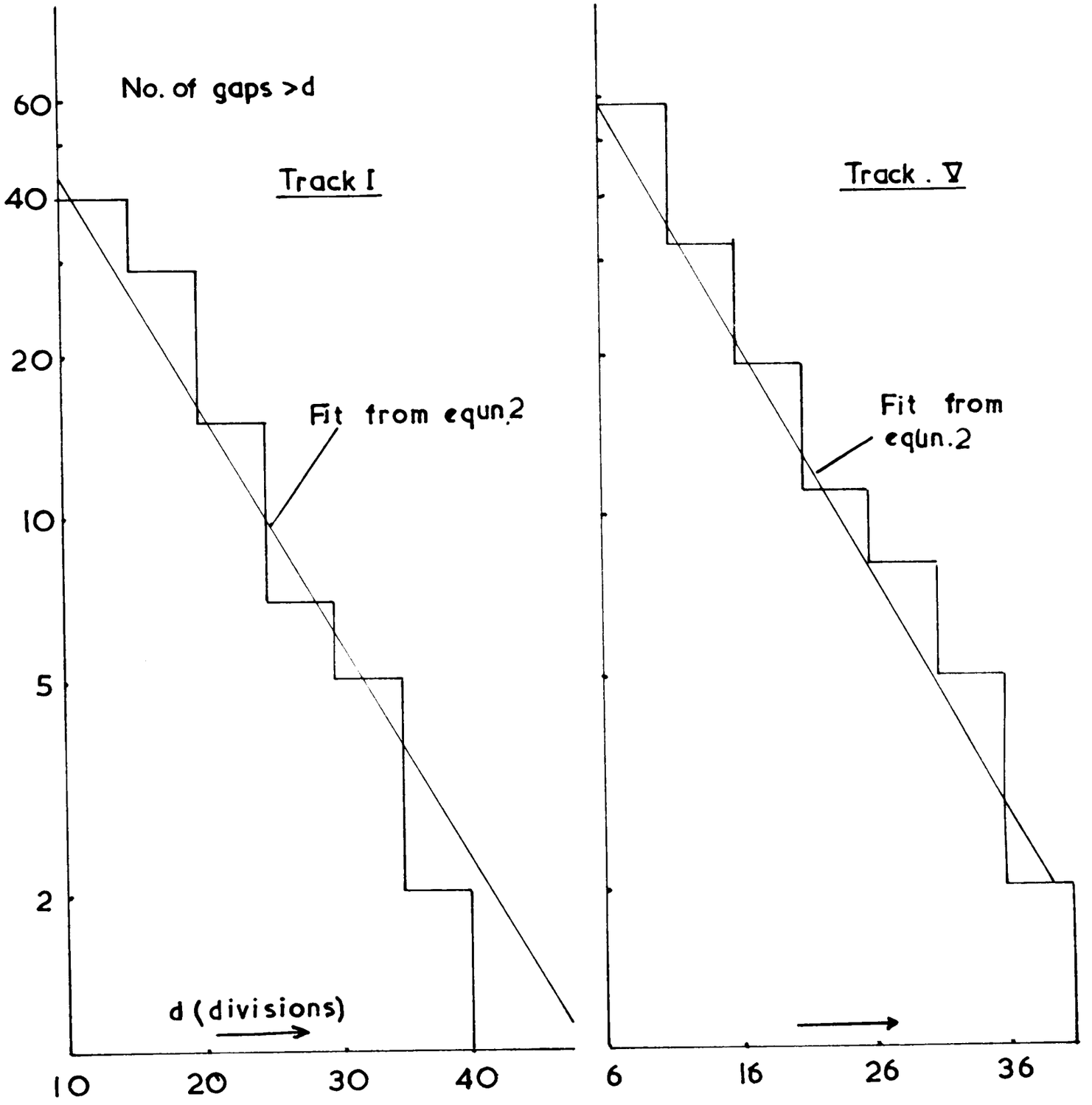

FIG B.1. - Maximum Likelihood Fits.

TABLE I

Track No. See Fig. 3.2	α (μm)		g (cm^{-1} on film)			Mean Blob Length (μm)	
	By Direct Measurement	Equation (2)	Equation (2)	(Mean Gap Length)$^{-1}$	$-\ln(L)/\delta$	By Direct Measurement	Equation (2)
I	$\sim$ 45	47.0	279.5	284.7	283.6		
		+4 -3	+45 -64		+25 -20	98.1	97.4
III	$\sim$ 59	60.8	252.0	252.1	253.8		
		+6 -5	+40 -51		+25 -20	145.9	143.9
V	$\sim$ 45	48.6	278.7	282.5	282.2		
		+4 -5	+40 -51		+25 -21	108.1	107.1
VII	$\sim$ 45	48.7	325.7	340.3	334.8	120.8	119.4
		+4 -3	+45 -58		+29 -24		

visible gap and also the total length of track measured. A computer programme for the Oxford KDF9 has been written by the author to perform the maximization which has been carried out on seven measured beam tracks.

The results of the fits to the measured tracks are given in Table I and the distribution fit in Fig. B.1 and appear satisfactory. The errors are calculated from the width and second derivatives of W = ln.F at the maximum and agree quite well with the observed spread of values. It should be pointed out that all the tracks were on the same frame, so had the same expectation value for g (but not necessarily α).

The same procedure, omitting the mean blob length information (by leaving out the Gaussian term) provides a maximum likelihood fit to the gap length distribution alone. This was again performed on the measurements to estimate the accuracy of α determined in this way. The results indicated an error of about 6% to be compared with up to 15% by direct measurement. The result of fitting the slope in this manner has already been shown in Fig. 3.2. of Chapter III.

Monte Carlo Investigation

Ideally, in order to test the various ways of estimating g, one would like to make measurements of a large number of tracks and observe the spreads of the quantities $g_0 - g_7$ (see

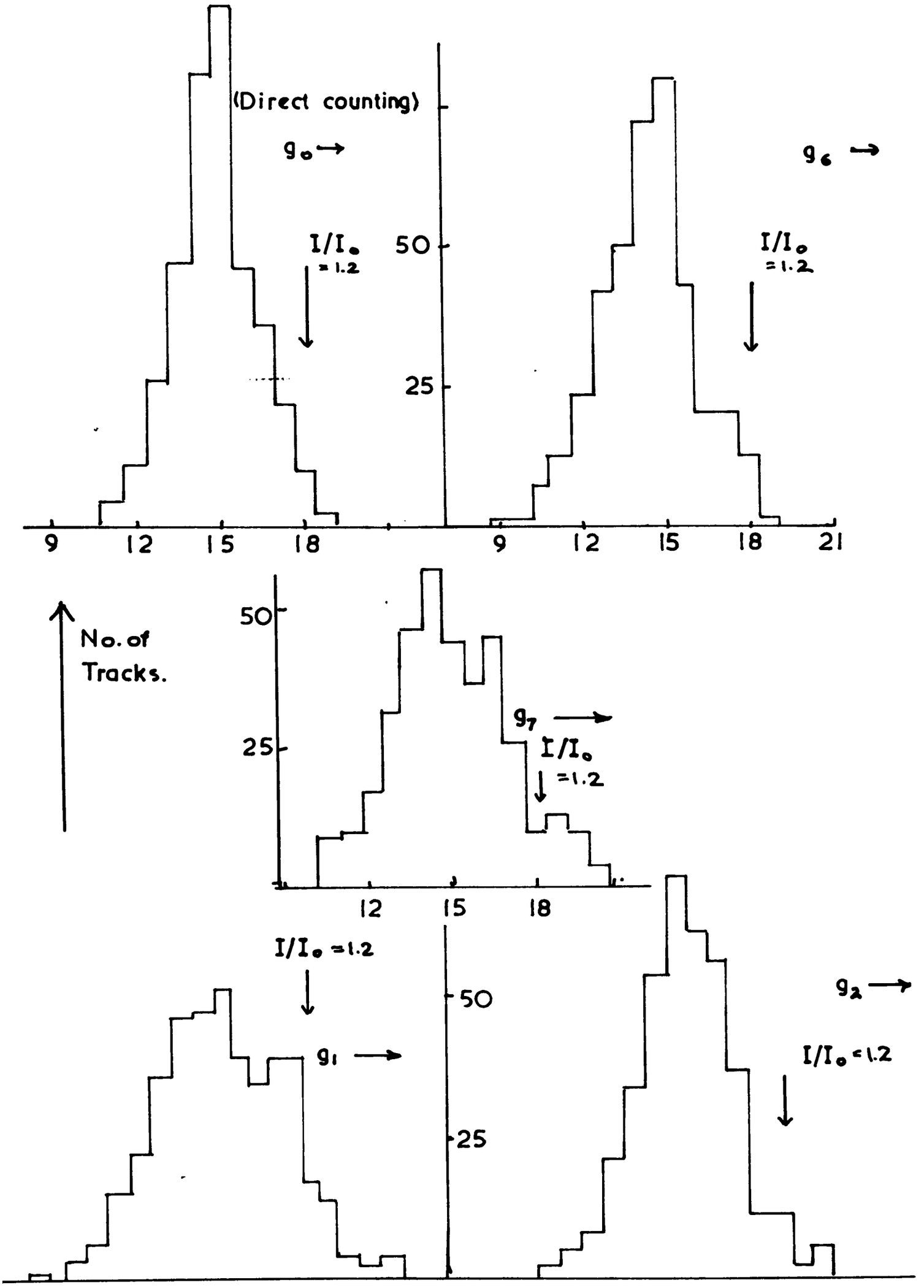

FIG B2 Monte Carlo Tracks with $\langle g \rangle = 15\,cm^{-1}$

Chapter III). The practical difficulty of obtaining a large number of tracks with the same expectation value of g, however, and the tedium of making the measurements are inhibitive. Consequently, a Monte Carlo technique has been used to generate some ideal tracks (essentially generating a large number of gaps whose distribution followed the form of equation (1)) which had a fixed length comparable with that measured by the machine. To illustrate the usefulness of ionization measurements from the statistical point of view, tracks with values of λ and g typical of actual beam tracks (= 0.030 cms; g = 20 cm^{-1}) were generated. The resulting spreads are illustrated in Fig.B.2. where the ability for g_{1-7} to distinguish relative ionizations of 1.0 and 1.2 for instance, may be assessed. Experimental spreads would be greater owing to systematic effects already described (Chapter III), but it is usually possible (on the Saclay 81cm chamber film) to measure at least 2 or 3, and usually 4, sections as large as those illustrated. On this basis, it would appear that the mean gap length method for instance, would be capable of distinguishing 1.0 from 1.2 in about 50% of cases.

In conclusion it appears that, could one obtain an accurate measurement of λ, the Barkas method of estimating g would be most satisfactory. A possible way of doing this involving only a few measurements (gap length distribution, etc.)

is suggested and shown to provide reasonable results. Monte Carlo analysis shows that one might hope to obtain a separation of 1.0 and 1.2 in relative ionization (i.e. Ks from π s up to about 1.25 Gev/c) in favourable cases.

REFERENCES TO APPENDIX B

1. W. Barkas: Phys. Rev., 124, 897 (1961)

2. D. J. Hudson: C.E.R.N. Statistics Lectures II, 64-18

3. R. L. Gluckstern: Determination of Bubble Density, M.I.T. Internal Report

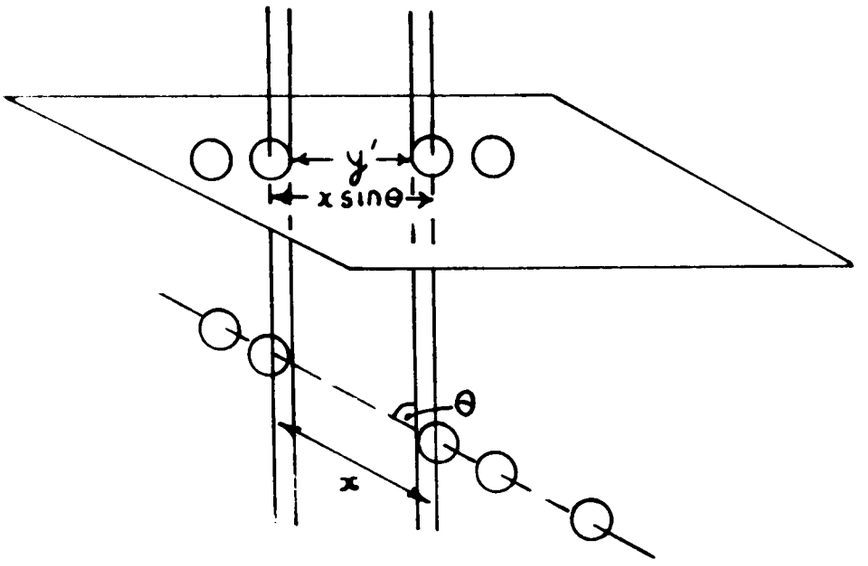

FIG C.1

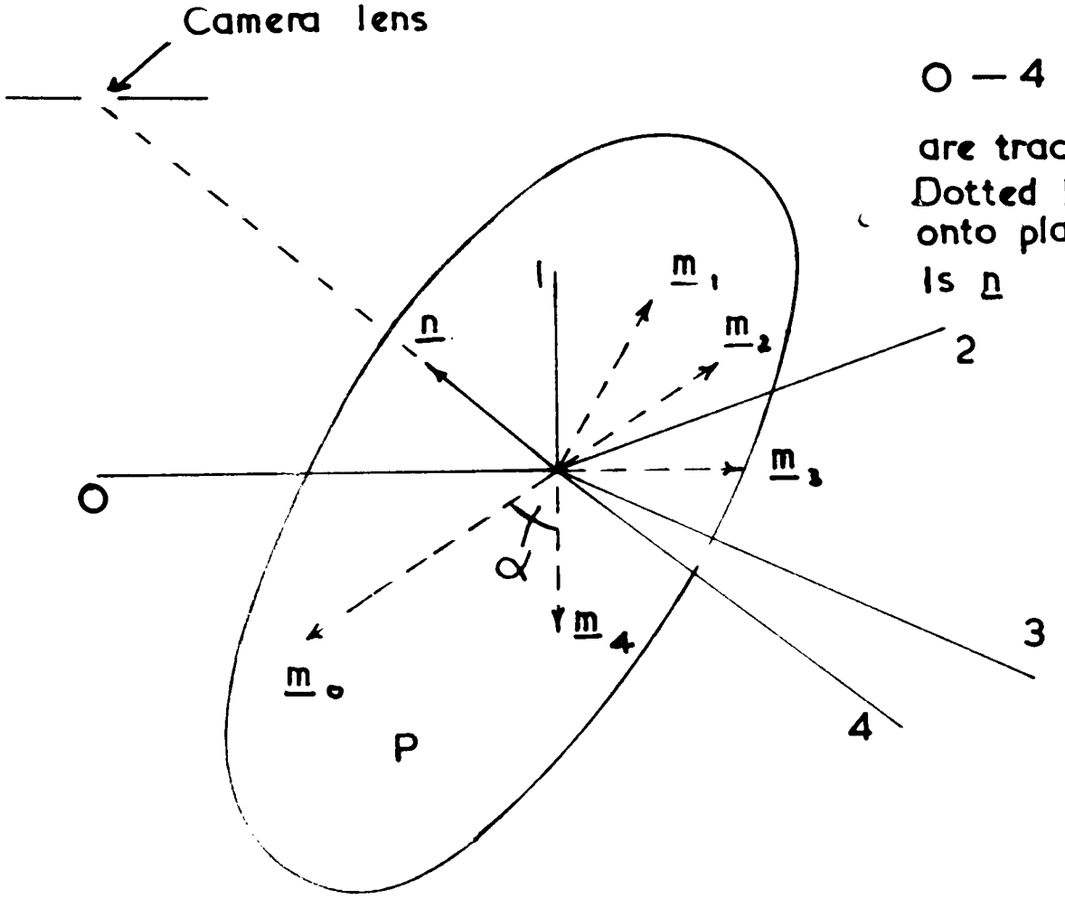

O — 4 (continuous lines) are tracks.
Dotted lines are projections onto plane P. Normal to P is n

FIG C4

APPENDIX C

Dip Correction Applied to Ionization Measurements

That a projection of a track onto any plane may be regarded (from the point of view of gap geometry) as an equivalent track with a higher bubble density (g) may be shown as follows:-

Fig. C.1. represents an "ideal" track. The gap length x is reduced to x sinθ when projected onto a plane whose normal makes the angle θ with the track as shown in the figure. The projected visible gap length y' is x sinθ - λ instead of x - λ. The distribution of y' is the same as that of y except that the gaps are shorter and the minimum visible has a value of x of λ cosec θ instead of λ. Consequently the effect of the dip is to reduce the number of visible gaps and increase the apparent bubble density of g', say. The distribution law may be written as:-

$n'(x) = Ae^{-g'x}$ where n(x) is the number of projected gaps $\geq$ x. This is the number of actual gaps $\geq$ x cosec θ so that $n'(x) = Ae^{-g'x} = Ae^{-gx \operatorname{cosec}\theta}$.

Therefore, any value of g' derived by use of the distribution law is identified with g cosecθ, and the dip correction required is just the average value of sinθ along the measured length of track.

Track Shuffling

As the ionization measurements were performed at a different time to those of the azimuth, dip and momentum, some confusion occasionally arose as to which track was which on the four prong events. A rule was made in the measurement of the ionization that all tracks were to be taken in strict clockwise order on the best view. When the output from the machine was compared with the azimuth, dip and momentum measurements for each track, therefore, the first step was actually to shuffle the measured values so that they were in the same order in both cases. The apparent track order on any view was the same as that in which they appeared on a plane (whose normal was parallel to the line joining the vertex to the camera lens) illustrated in Fig. C.4. The angle θ between the beam track and a secondary track was calculated:

$$\cos\theta_i = \frac{\underline{m}_i \cdot \underline{m}_o}{|\underline{m}_i| \, |\underline{m}_o|}$$

where $\underline{m}_j = \underline{a}_j + k\underline{r}_o \; ; \; \underline{m}_j \cdot \underline{r}_o = 0$

Measured quantities (g') and the error $\sigma(g')$ which were calculated for the projected tracks were put into the order of the α_j and the dip correction was applied.

Calculation of Dip Correction

The assumptions made were that:-

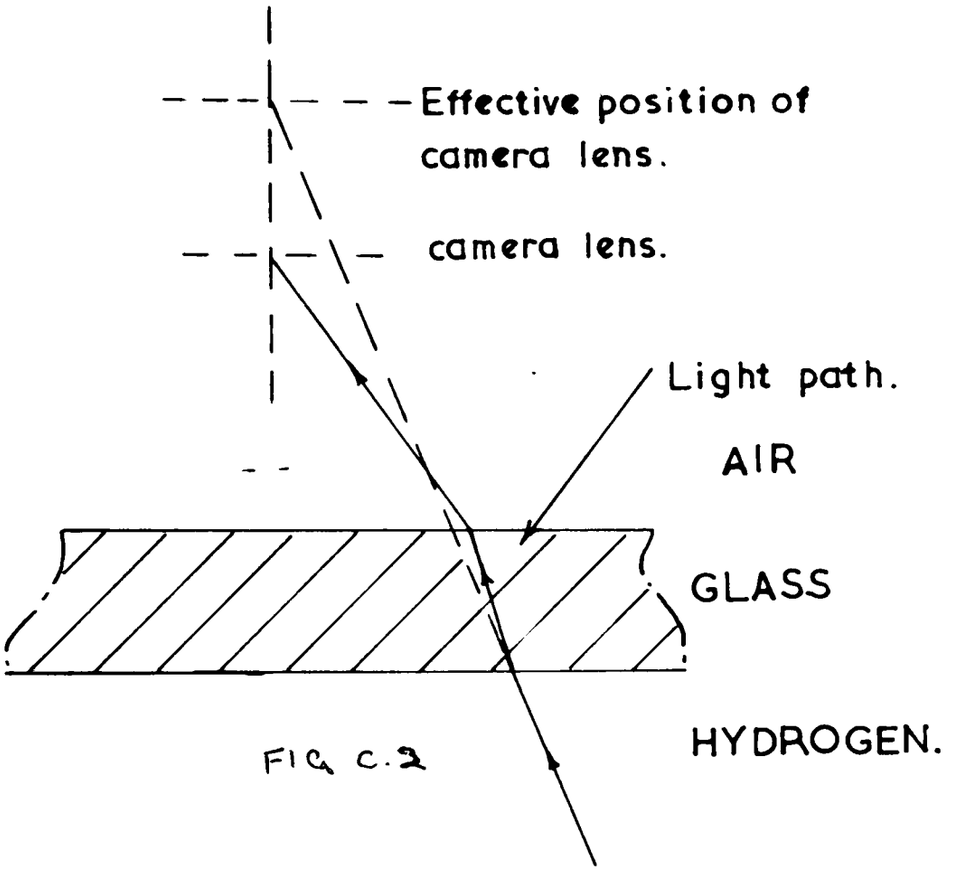
Effective position of
camera lens.
camera lens.
Light path.
AIR
GLASS
HYDROGEN.

FIG C.2

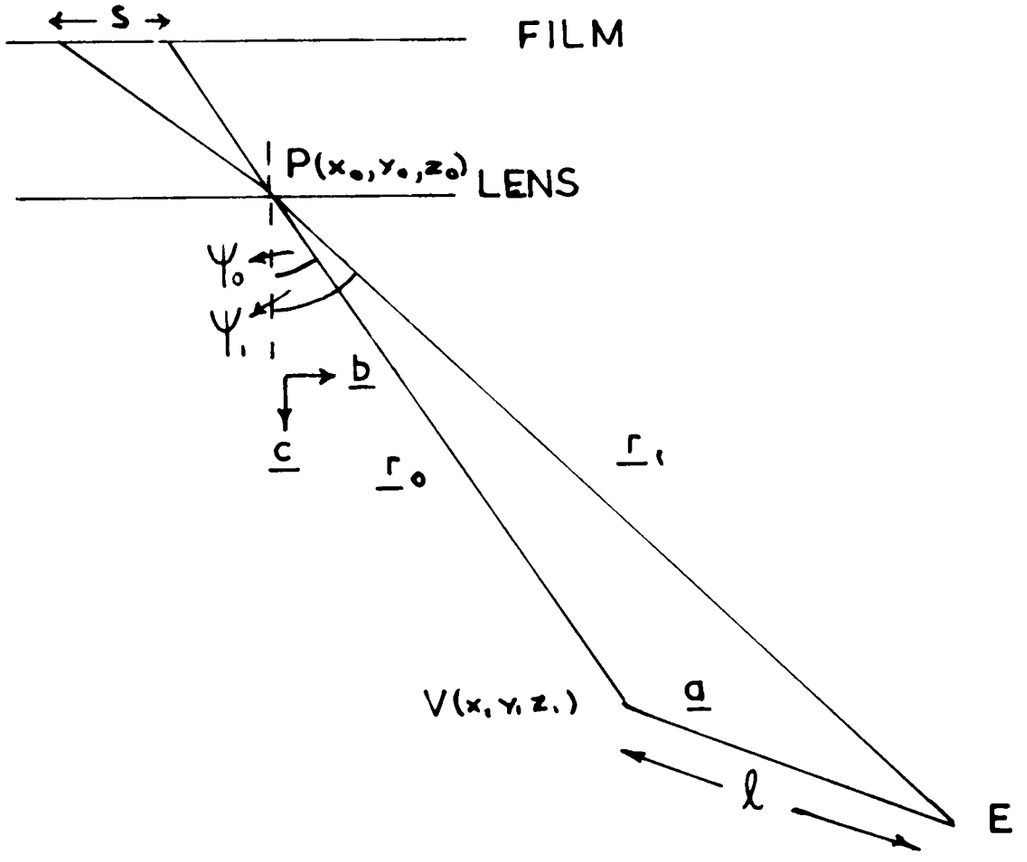
S
FILM
P(x₀,y₀,z₀)
LENS
ψ₀
ψ₁
b
c
r₀
r₁
V(x₁,y₁,z₁)
a
l
E

FIG. C.3

(a) The track was straight;

(b) Pinhole optics could be applied;

(c) The angle of view was small;

(d) The whole track of known length l was measured starting at the vertex.

The effect of (c) was that the front glass of the chamber could be neglected except that it adjusted the effective distance of the camera lens from its front surface. This is illustrated in Fig.C.2.

Fig. C.3. shows a straight track VE coming from a vertex $C(x_1, y_1, z_1)$. The diagram is drawn in the plane defined by the camera pinhole $P(x_o, y_o, z_o)$ and VE, and the correction to be applied to the ionization measurement was s/l (both defined in the figure).

The first step in the calculation was to rotate and translate the co-ordinate system so that the angle of azimuth (ϕ) for the track was zero, and the origin was at the camera lens. The unit vector $\underline{a}$ then had components ($\cos\lambda$, 0, $\sin\lambda$) where the track dip angle was λ, and the vectors $\underline{r}_o$ and $\underline{r}_1$ were also simple to calculate as the track length (l) was known. Calculation of the unit vector $\underline{c}$ was made from use of the fact that it lay in the plane PVE and was perpendicular to $\underline{b}$ which also lay in the plane.

The equations used were:

$$|\underline{b}| = 1 \; ; \; b_z = 0 \; ; \; \underline{b} \cdot (\underline{a} \times \underline{r}_o) = 0$$

$$|\underline{c}| = 1 \; ; \; \underline{b} \cdot \underline{c} = 0 \; ; \; \underline{c} \cdot (\underline{a} \times \underline{r}_o) = 0$$

It was then simple to calculate ψ_o and ψ_1 and so s.

$$\cos\psi_o = \frac{\underline{c} \cdot \underline{r}_o}{|\underline{r}_o|} \; ; \; \cos\psi_1 = \frac{\underline{c} \cdot \underline{r}_1}{|\underline{r}_1|}$$

$$s = v(\tan\psi_1 - \tan\psi_o)$$

where v was the distance of the film from the lens divided by c_3.

The correction was applied to the measurement performed on each view separately, and then a weighted mean was taken over the views for each track.

APPENDIX D

The Maximization of Functions of Many Parameters

A large part of the analysis of experimental results in high energy physics consists of a statistical investigation of theoretically predicted effects. As these effects become more difficult to detect, the need for a more sophisticated statistical analysis becomes apparent. A convenient method of obtaining the latter is that of maximum likelihood, and consists roughly of two types:-

(a) that in which a test of the relative merits of several well defined theories in describing the experimental results is to be made;

(b) that which provides a quantitative result for the best values of some parameters - which characterize the theory - for describing the experiment.

In this thesis, both types have been used, and in one case - that of the K**(1400) spin determination - (b) was first applied to find the best values for the density matrix elements for each of two hypotheses, and then (a) was used to estimate which hypothesis provided the better description.

In both (a) and (b), a likelihood function is constructed which either describes the exact ("direct") probability for a set of results or is constructed as follows. If $f(\alpha_i, x)$ is a function describing the expected distribution of the

quantities x whose form is fixed but whose exact "shape" depends upon the values of the parameters α_i, then the likelihood function is a product of this distribution over all N measured values of x.

$$F(\alpha_i, x) = \prod_{j=1}^{N} f(\alpha_i, x_j) \qquad \ldots\ldots (D1)$$

It is more usual, for numerical reasons, to refer to the log likelihood function $W(\alpha_i) = \ln.F(\alpha_i)$ since this is a monotonic function of F. To find the values of the α_i which maximize the value of F (or W) forms the major part of type (b) maximum likelihood calculations.

One might first think of making a computer evaluate W for several values of each parameter and then decide which was the maximum. However, to take a specific case, if the function had ten variables (α_i) and one calculated its value for 10 values of each, that would entail working it out 10^{10} times. Even at one microsecond a time (a gross under-estimate) this would take three hours. Consequently, in the examples in this thesis (the worst case was 16 parameters when the function required 6 seconds of Atlas time to evaluate) the method about to be described was applied. The assumptions:-

(a) that the function had only one stationary value in the vicinity of the current values of α, and

that this was a maximum;

(b) that the function was continuous in the same vicinity;

led to the requirement that the solution lay in that of solving the n equations:

$$\frac{\partial W}{\partial \alpha_i} = 0 \qquad \text{.... D2}$$

for the n parameters α_i.

A Taylor expansion of the first derivatives (D2) about the current values of $\alpha (\alpha_i^o)$ led to the equations:

$$\left(\frac{\partial W}{\partial \alpha_i}\right)_o + \sum_j \left(\frac{\partial^2 W}{\partial \alpha_j \partial \alpha_i}\right)_o \Delta\alpha_j \doteq 0 \qquad \text{....D3}$$

linear in the $\Delta\alpha_j$ which were the first order corrections to be applied to α_j. It was then simple to solve for the $\Delta\alpha_j$ which (when added to α_j) led to slightly better values. The process usually converged after about six or seven such iterations with the requirement that two successive values for the complete set of $\Delta\alpha_i$ were less than a required small amount ($\delta\alpha_i$).

The evaluation of the derivatives was a numerical one - very simply stepping the α_i by a fraction of $\delta\alpha_i$ and observing the change in W. It was only necessary to evaluate one half of the second derivative matrix as it was symmetrical $\left(\frac{\partial^2 F}{\partial \alpha_i \partial \alpha_j} = \frac{\partial^2 F}{\partial \alpha_j \partial \alpha_i}\right)$.

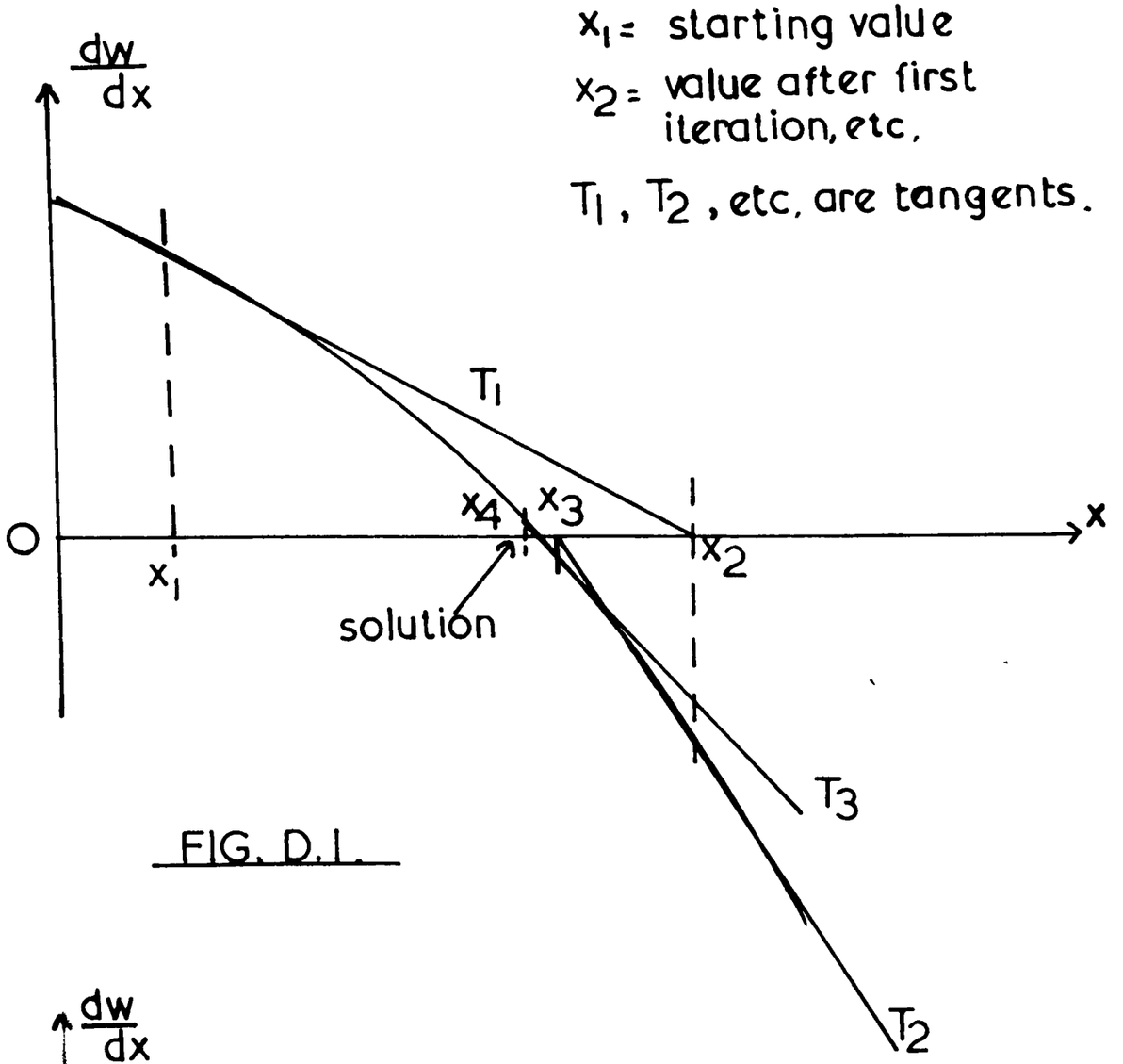

FIG. D.1.

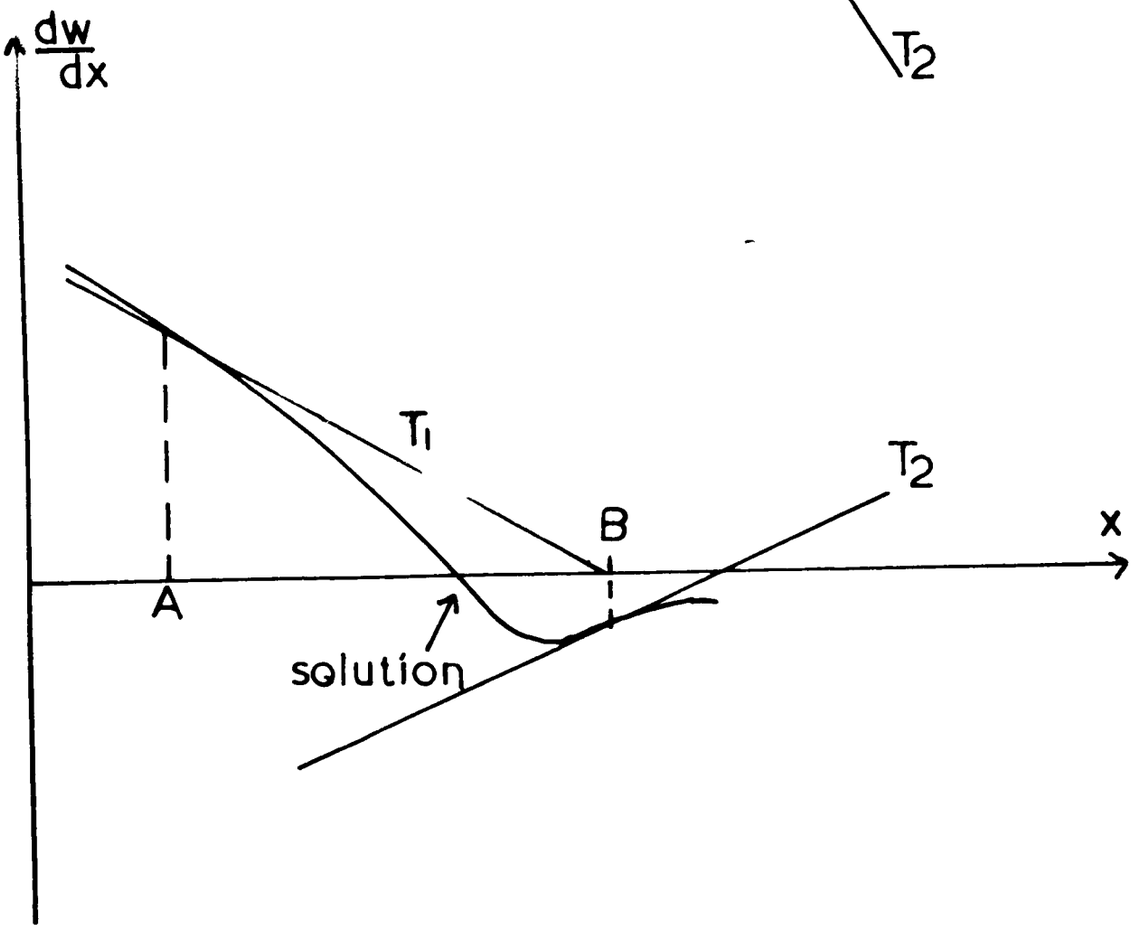

FIG. D.2. – Ill-conditioned derivative.

It is noted that a quadratic surface (to which a likelihood function approximates as the number of events - each of which provides a value for x - becomes larger[1]) has a maximum determined exactly by solution of the equations D3.

Difficulties Occasionally Encountered

Fig. D.1. illustrates graphically the nature of the method. It shows a derived curve $(\frac{\partial W}{\partial \alpha_i})$ as a function of one of the parameters - α_i. Fig D.2. shows a difficult case where one parameter becomes thrown right outside the required region by following the method exactly. It is realized that this can only happen if the derivative changes sign between iterations, so that a check was made that this did not happen unless the final derivative was smaller than some preset amount. If such a change of sign occurred, a note was made of the initial and final values of α_i (A and B on Fig D.2.) and the quantity α_i was stepped back to a position between these two limits by a weighted amount so that it was nearer to the point where the derivative had been smallest. At this point, evaluation of the derivative was repeated, and the above procedure again adopted - any new limits A and B being noted. The fact that the solution lay somewhere between A and B was slightly

modified by correlations with other parameters, but a subsequent iteration was not allowed to throw the parameter α_i outside the range AB by more than a preset percentage.

Another difficulty which rarely arose was that one iteration slightly overestimated one of the $\Delta\alpha$'s so that a step to the unphysical region occured (requiring the evalution of the log. of about -10^{-12}, say). For such a case, all the $\Delta\alpha$ were divided by two and the next iteration restarted. This was repeated as often as necessary.

Evaluation of Errors

Two methods were used to calculate the errors. The first relied upon the approximately Gaussion nature of the likelihood surface and lead to the result that the standard deviation of α_k should be H_{kk} where:

$$(H^{-1})_{ij} = -\frac{\partial^2 W}{\partial\alpha_i \partial\alpha_j} \qquad \ldots\ D4$$

Another method which was more applicable to those cases where the number N of measurements of the quantity x (see equation D1) was small relied upon the theorem that a suitable transformation for the parameter α_k would lead to the distribution of the likelihood function F becoming Gaussian. The standard deviation of this new parameter then corresponded to the points where the log likelihood obtained the value of numerically one half less than its maximum (W_{MAX}).

Therefore, adjustment of each parameter in turn in increasing and decreasing directions such that the value of W became (W_{MAX} - 0.5) led to the 65% confidence limits. The values of H_{kk} were used to estimate a starting position for α_k, and the change in its value in order to reach this point was

$$\delta\alpha_k \simeq \frac{(W(\alpha_k) - W_{MAX} + 0.5)}{(\partial W/\partial\alpha_k)}$$

Even though this method was a lot quicker than many others which could have been used, the time consumed in the case of the evaluation of resonance production cross-sections (see Chapter VII) was still very great. In order to evaluate one half of the second derivative matrix and all the first derivatives, over half an hour of computing time was required on a powerful computer. An approximate method in which the second derivatives were only calculated after every fifth iteration was therefore adopted in the more time consuming cases. Even so, the case just cited was not really feasible. It was certainly found that the higher derivatives only changed slightly in the neighbourhood of the maximum.

REFERENCES TO APPENDIX D

1. D. J. Hudson - Statistics Lectures II, C.E.R.N. 64-18

APPENDIX E

Definition of Kinematic Quantities

It is necessary to define some quantities that are later referred to, and in this connection it is instructive to consider how many independent quantities are required in the specification of a three body final state. Starting with the two body reaction:

$$A + B \longrightarrow C + D \qquad \ldots\ E1$$

where the masses of all particles are known, and the initial state is one of well defined momentum (e.g. $K^{-}p$ with stationary proton and K^{-} having 3.5 Gev/c momentum) one sees that six components of momentum (those of C & D are unknown. The conservation of four-momentum (imposing four constraints upon these variables) leads to a reduction in the number of independent variables to two which may be regarded, for instance, as the polar and azimuthal angles defining the final direction of the particles C and D in the overall centre of mass system (CMS). In our case, however, as the target was unpolarized, one of these angles was of no interest, so that a two body reaction could be completely specified by one scattering angle.

The inclusion of an extra particle in the final state

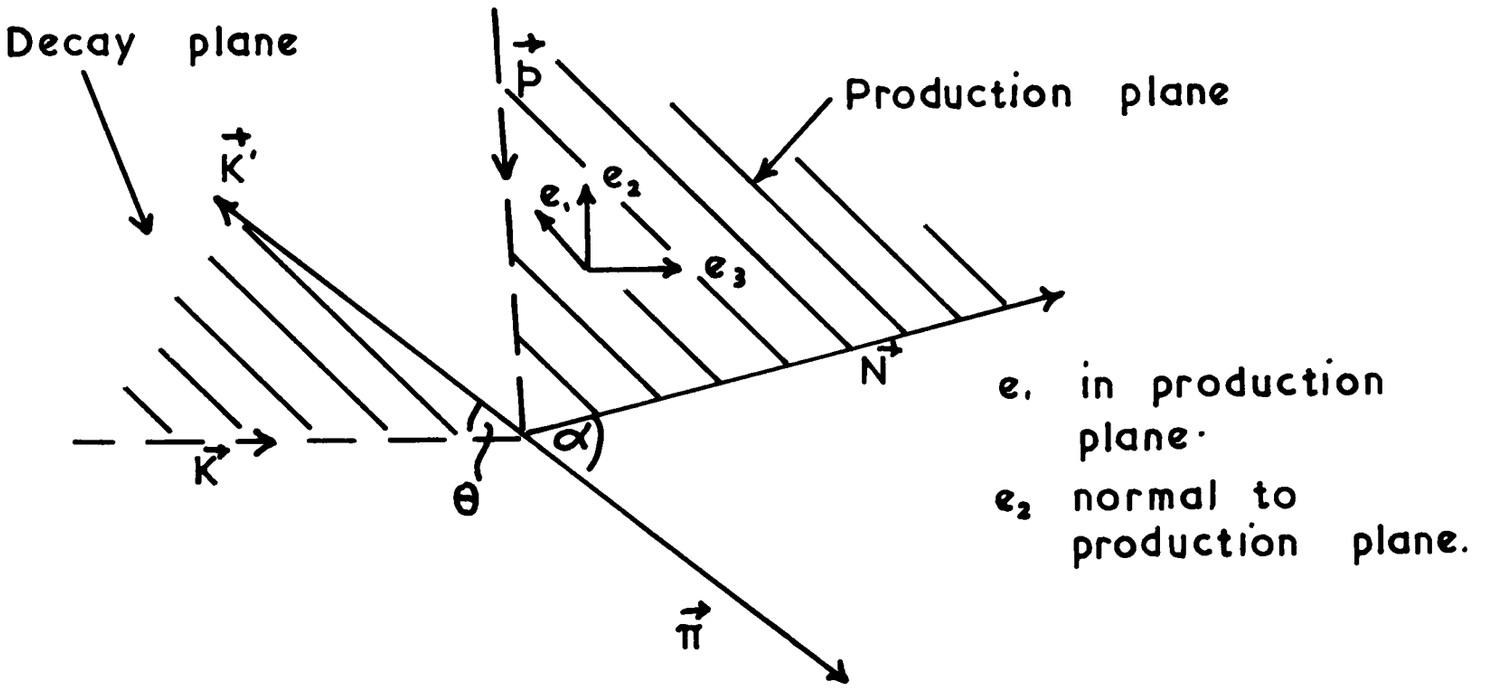

FIG. 1 (a)

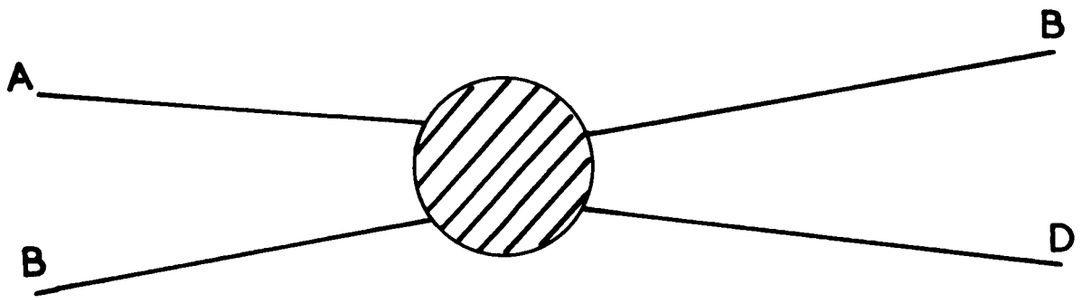

FIG. 1 (b)

$AB = m_a$
$BC = m_b$
$AD = m_c$
$DC = m_d$

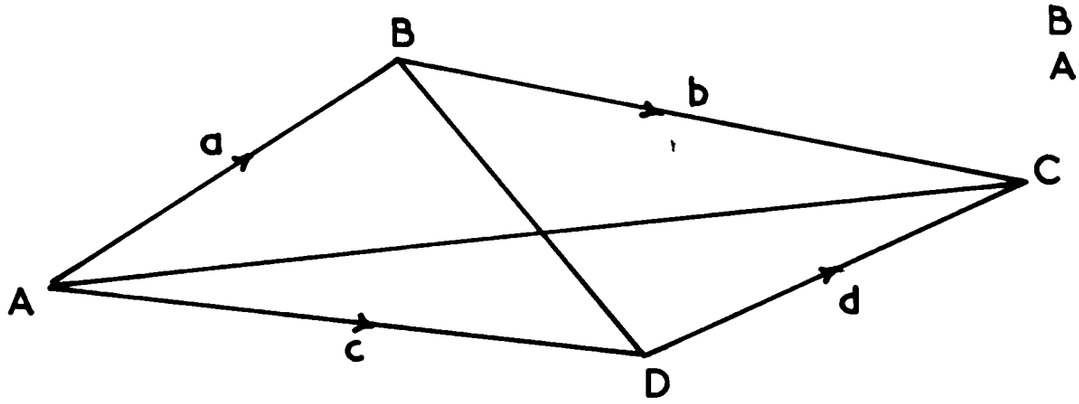

$BD = \sqrt{t}$
$AC = \sqrt{s}$

FIG. 1 (c).

introduces the need for the specification of a further three quantities. One may consider two of the particles as forming a system (C for instance) and their invariant mass may be regarded as one of the extra independent quantities. The other two may be taken as the azimuthal and polar angles describing the final direction of the two decay products of C in the CMS of C. These angles are usually referred to as the decay angles of C (θ_c and ϕ_c) and are defined below.

Decay Angles

Referring to the centre of mass system of the particles in C we may define a co-ordinate system as follows:-[1] Fig.1(a) shows the final 3 particle system in the rest frame of the K and π. The incoming particles K^- and p are drawn as dotted lines whilst the outgoing particles are drawn solid. The z-axis is taken along the incident K direction and the x-axis normal to this in the production plane. The y-axis parallel to the normal to the production plane then completes the right-handed system. Thus if $\vec{e}_1, \vec{e}_2, \vec{e}_3$ are unit vectors in the direction of the x,y,z axes respectively, using the notation implied by the reaction $K + P \rightarrow K' + N + \overline{\pi}$:

$$e_3 = \frac{\vec{K}}{|\vec{K}|}; \quad e_2 = \frac{\vec{p} \times \vec{N}}{|\vec{p} \times \vec{N}|}; \quad \vec{e}_1 = \vec{e}_2 \times \vec{e}_3 \quad \ldots\ldots \text{E2}$$

and the azimuthal and polar angles θ_c and ϕ_c in this system are:

$$\cos\theta_c = \frac{\vec{K}.\vec{K'}}{|K||K'|} : \cos\phi_c = e_2 \cdot \frac{\vec{K}\times\vec{K'}}{|K \times K'|} ; \sin\phi_c = e_2 \frac{\vec{K}\times\vec{K'}}{|K \times K'|} \quad \ldots\ldots \text{E3}$$

The angle χ in Fig.1(a) is loosely referred to as the decay angle. It is defined by $\cos\chi = \frac{\vec{K}.\vec{N}}{|K||N|}$. When this angle is referred to it will be identified specifically as α.

The Four-momentum Transfer ($\Delta^2 = -t$)

Another quantity occasionally referred to is the so-called square of the 4-momentum transfer (momentum transfer). This is, for instance, the difference in 4-momentum between A and D or B and C, etc, in the two body reaction: A + B $\rightarrow$ C + D represented in Fig.1(b). That this is Lorentz invariant may be seen as follows. If a,b,c and d are the 4-momenta of the four respective particles, the conservation of energy-momentum may be written as: a + b = c + d E4

Equation E4 may be represented as in Fig. 1(c) by a closed hypertetrahedron in four-space whose sides have lengths a,b,c and d. These lengths have magnitudes equal to the masses of the four particles and are therefore Lorentz invariant. This is also so if C has the invariant

mass of a pair of particles in the three body final state. Therefore the lengths of the diagonals of the tetrahedron whose squares are:

$$s = (a+b)^2 \; ; \; t = (c-a)^2 = (d-b)^2$$

are also invariant.

The first of these is the square of the total centre of mass energy, and the second the squared four momentum transfer to the particle c or d. The most usual case considered (for the reaction $K^- p \rightarrow KN\pi$) is that of the momentum transfer to the nucleon

$$t_N = (p_N - p_p)^2 - (E_N - E_p)^2$$

where the K and π are combined to make particle C and p is the 3-momentum and E the total energy of the incoming proton (or outgoing nucleon).

REFERENCES TO APPENDIX E

1. N. Schmitz: Proceedings of the 1965 Easter School for Physicists, Bad Kreuznach, April 1965, C.E.R.N. 65-24